

Public reporting burden for this collection of information is estimated to average 1 hour per response, including the time for reviewing instructions, searching existing data sources, gathering and maintaining the data needed, and completing and reviewing the collection of information. Send comments regarding this burden estimate or any other aspect of this collection of information, including suggestions for reducing this burden to Washington Headquarters Services, Directorate for Information Operations and Reports, 1215 Jefferson Davis Highway, Suite 1204, Arlington, VA 22202-4302, and to the Office of Management and Budget, Paperwork Reduction Project (0704-0188), Washington, DC 20503.

1. AGENCY USE ONLY (Leave blank)		2. REPORT DATE 1 December 1998	3. REPORT TYPE AND DATES COVERED Conference Proceedings	
4. TITLE AND SUBTITLE XXIII International Conference on Phenomena in Ionized Gases, VOL 5			5. FUNDING NUMBERS F6170897W0048	
6. AUTHOR(S) Conference Committee				
7. PERFORMING ORGANIZATION NAME(S) AND ADDRESS(ES) Universite Paul Sabatier 118 Route de Narbonne Toulouse Cedex 31062 France			8. PERFORMING ORGANIZATION REPORT NUMBER N/A	
9. SPONSORING/MONITORING AGENCY NAME(S) AND ADDRESS(ES) EOARD PSC 802 BOX 14 FPO 09499-0200			10. SPONSORING/MONITORING AGENCY REPORT NUMBER CSP 97-1013	
11. SUPPLEMENTARY NOTES One book of Invited Papers and five volumes of Proceedings and Contributed Papers				
12a. DISTRIBUTION/AVAILABILITY STATEMENT Approved for public release; distribution is unlimited.			12b. DISTRIBUTION CODE A	
13. ABSTRACT (Maximum 200 words) The Final Proceedings for XXIII International Conference on Phenomena in Ionized Gases, 17 July 1997 - 22 July 1997 kinetic, thermodynamics, and transport phenomena; elementary processes; low pressure glows; coronas, sparks, surface discharges, and high pressure glows; arcs; high frequency discharges; ionospheric magnetospheric, and astrophysical plasmas; plasma diagnostic methods; plasma surface effects; plasma processing; plasma flows; non ideal plasmas; waves and instabilities; non-linear phenomena; particle and laser beam interactions with plasmas; plasma sources of radiation; modeling; plasma for environmental issues; plasma thrusters; surface treatment; high pressure, non-thermal plasmas.				
14. SUBJECT TERMS EOARD, Space Environment, Pulsed Power, Astrodynamics, Coatings, Fluids & Lubrication, Electromagnetics, High Power Generation, Lasers			15. NUMBER OF PAGES Too Many to Count	
			16. PRICE CODE N/A	
17. SECURITY CLASSIFICATION OF REPORT UNCLASSIFIED	18. SECURITY CLASSIFICATION OF THIS PAGE UNCLASSIFIED	19. SECURITY CLASSIFICATION OF ABSTRACT UNCLASSIFIED	20. LIMITATION OF ABSTRACT UL	

NSN 7540-01-280-5500

Standard Form 298 (Rev. 2-89)
Prescribed by ANSI Std. Z39-18
298-102

**X
X
I
I
I**

F61708-97-W 0048

CSP 97-1013

**I nternational
C onference on
P henomena in
I onized
G ases**

Editors: M.C. Bordage and A. Gleizes

19981216 006



Proceedings

Contributed Papers

Late Papers

Vol. V

Organizers :

Centre de Physique des Plasmas et leurs Applications de Toulouse (CPAT)
Laboratoire de Génie Electrique de Toulouse (LGET)
From the Université Paul Sabatier, Toulouse France.

International Scientific Committee

R. d'Agostino	Italy
J. Allen	Great Britain
A. Bouchoule (Chairman)	France
E. Desoppere	Belgium
H. Kikuchi	Japan
E.E. Kunhardt	USA
J. Mentel	Germany
B. Milic	Yugoslavia
D. Morrow	Australia
A.H. Oien	Norway
A.A. Rukhadze	Russia
M. Sicha	Czech. Republic

Local Organizing Committee

J.P. Bœuf	M.C. Bordage (Sec.)
H. Brunet (co-Chair.)	J.P. Couderc
B. Despax	M. Dziadowiec
A. Gleizes	B. Held
F. Massines	L.C. Pitchford (co-Chair.)
Y. Segui	S. Vacquie
M. Yousfi	G. Zissis

Sponsors

Association pour le Développement de la Physique Atomique (ADPA)
International Union of Pure and Applied Physics (IUPAP)
Centre National de la Recherche Scientifique (CNRS)
Université Paul Sabatier (UPS) of Toulouse
Direction de la Recherche et Technologie (DRET)
Commissariat à l'Energie Atomique (CEA), Cycle de Combustible
Electricité de France through :

Club Arc Electrique, Club Chimie des Hautes Températures and Novelect ,
Conseil Régional de la Région Midi-Pyrénées
Conseil Général du Département de la Haute-Garonne
Mairie de Toulouse
CRT Plasma-Laser
Union Radio Scientifique Internationale (URSI)
US Department of Energy, US BMDO
US Air Force through the EOARD

The Local Organizing Committee wishes to express appreciation to the following corporations for their support :

AGA S.A.	Thomson Tubes Electroniques
Motorola Semiconducteurs S.A.	Schneider Electric
Osram-Sylvania Inc.	Philips Lighting (for the Penning Award)

FOREWORD

This volume is the fifth of five volumes which contain contributed papers that were accepted by the Local Organizing Committee of the XXIII ICPIG for presentation in poster sessions. These papers are to be listed in the INSPEC data base.

The contributions were submitted in camera-ready form by the authors. Therefore, the responsibility for the contents and the form of the papers rests entirely with the authors.

The first four volumes have been arranged by topics, the sequence of which corresponds to that of the respective poster sessions. The fifth volume is comprised of 'late' papers, those for which the authors registered after the deadline for printing of their papers.

The texts of the invited talks are to be published shortly after the conference in a special issue of Journal de Physique.

The editors would like to acknowledge the contributions of Mrs L. Fourmeaux, Mr J.M. Barachet and Mr J.P. Chauchepnat in the preparation of these volumes. The computer file of contributed papers and authors was prepared by C. de Peco, and her careful execution of this task is gratefully acknowledged.

August 1997

The Editors

For additional copies of this publication, please contact :

M.C. Bordage, CPAT, Université Paul Sabatier, 118 Route de Narbonne, 31062
Toulouse cedex 4 France

Printed in France, in the Université Paul Sabatier of Toulouse , 1997

Topic number	SCHEDULE FOR POSTERS
VOLUME 1 THURSDAY, JULY 17	
MORNING	
1	Kinetics, thermodynamics and transport phenomena (Part A)
2	Elementary processes (Part A)
6	High frequency discharges (Part A)
13	Waves and instabilities, including shock waves (Part A)
AFTERNOON	
1	Kinetics, thermodynamics and transport phenomena (Part B)
2	Elementary processes (Part B)
6	High frequency discharges (Part B)
12	Non-ideal plasmas. Clusters and dusty plasmas
13	Waves and instabilities, including shock waves (Part B)
18	Plasmas for environmental issues
VOLUME 2 FRIDAY, JULY 18	
MORNING	
3	Low pressure glows (Part A)
5	Arcs (Part A)
17	Numerical modeling (Part A)
AFTERNOON	
3	Low pressure glows (Part B)
5	Arcs (Part B)
11	Generation and dynamics of plasma flows
14	Non-linear phenomena and self-organization processes
17	Numerical modeling (Part B)
VOLUME 3 SATURDAY, JULY 19	
7	Ionospheric, magnetospheric, and astrophysical plasmas
16	Plasma sources of radiation
19a	Highly ionized, low pressure plasmas
19b	High pressure, non-thermal plasmas
VOLUME 4 MONDAY, JULY 21	
MORNING	
4	Coronas, sparks, surface discharges and high pressure glows (Part A)
8	Plasma diagnostic methods (Part A)
10	Physical aspects of plasma chemistry, plasma processing of surface and thin film technology (Part A)
AFTERNOON	
4	Coronas, sparks, surface discharges and high pressure glows (Part B)
8	Plasma diagnostic methods (Part B)
9	Plasma wall interactions, electrode and surface effects
10	Physical aspects of plasma chemistry, plasma processing of surface and thin film technology (Part B)
15	Particle and laser beam interaction with plasmas
VOLUME 5 LATE PAPERS	

CONTENTS

Topic 1 :

Kinetics, thermodynamics and transport phenomena.

MEASUREMENT OF ANOMALOUS TRANSPORT IN PLASMA Riccardi C., Gamberale L., Fattorini L., Chiodini G., Bevilacqua C., Fontanesi M.	V-2
MEASUREMENT OF ELECTRON TRANSPORT COEFFICIENTS IN THE C_3F_8 -AR MIXTURE B.H. Jeon, S.C. Ha, Y. Nakamura	V-4
THE CALCULATION OF THE VISCOSITY TENSOR FOR A MAGNETOPLASMA FROM THE STRESS BALANCE EQUATION Suchy K.	V-6

Topic 2 :

Elementary processes.

THE NUMERICAL ANALYSIS OF THE IONIZATION CROSS-SECTION OF A HYDROGEN-LIKE ATOM BY FAST ELECTRONS IN A HOMOGENEOUS ELECTRIC FIELD Krylov V.I., Pivkin V.V., Kriulina O.V.	V-8
CARBON OXIDATION CATALYSED BY A PLATINUM SURFACE : RECOMBINATION PROBABILITIES AND VIBRO-ROTATIONAL DISTRIBUTION IN CO Cacciatore M., Christoffersen E., Billing G.D.	V-10

Topic 3 :

Low pressure glows.

ELECTRON AND ION MOBILITIES IN SHOCK-HEATED PLASMA Abbas A., Basha T. S.	V-12
ROTATION OF A D.C. DISCHARGE PLASMA Abbas A., Basha T. S., Abdel-Maksoud A.S.	V-14
INVESTIGATION OF THE DISCHARGE FORMATIVE TIME IN NE AT 4 mBAR PRESSURE Jovanovic T., Radovic M., Stepanovic O., Maluckov C.	V-16
THE BEHAVIOUR OF THE BREAKDOWN TIME DELAY DISTRIBUTION IN NE AT 4 mBAR Radovic M., Jovanovic T., Maluckov C., Stepanovic O.	V-18

Topic 4 :

Coronas, sparks, surface discharges and high pressure glows.

SUPER-HIGH SPEED IONIZING WAVES IN LONG SHIELDED TUBES Sinkevich O.A., Gerasimov D.N.	V-20
--	------

HIGH PRESSURE MICROHOLLOW ELECTRODE DISCHARGES Schoenbach K.H., El-Habachi A., Shi W., Ciocca M.	V-22
PHENOMENA IN IONIZED GASES SUBJECTED TO IMPULSE VOLTAGES Tusaliu P., Tusaliu V., Tusaliu M., Tusaliu D.	V-24
PHENOMENA IN IONIZED GASES UNDER CONTROLLED ATMOSPHERE CONDITIONS Tusaliu P., Tusaliu V., Tusaliu M., Tusaliu D.	V-26
CONDUCTING PARTICLE INITIATED IMPULSE FLASHOVERS ON THE SPACER SURFACE IN COMPRESSED GASES Rao B.N., Dwarkanath K., Siddagangappa M.C.	V-28
PARTIAL DISCHARGES AS IONISATION SOURCE FOR ION MOBILITY SPECTROMETRY Soppart O., Baumbach J.I., Klockow D.	V-30

Topic 5 : Arcs.

CATHODE PHENOMENA IN HIGH PRESSURE ARC LAMPS Almeida R.M.S., Benilov M.S.	V-32
ANALYSIS OF THERMAL NON-EQUILIBRIUM IN A NEAR-CATHODE REGION OF AN ATMOSPHERIC-PRESSURE ARC Benilov M.S.	V-34
2D NUMERICAL MODELLING OF AN ARC JET THRUSTER Laufer B., Kaminska A., Dudeck M.	V-36

Topic 6 : High frequency discharges.

INVESTIGATION OF LOW PRESSURE AIR RF DISCHARGE Shishkin A.G., Shishkin G.G.	V-38
ELECTRON ENERGY DISTRIBUTION FUNCTION IN A AXIALLY INHOMOGENEOUS UHF ARGON PLASMA COLUMN Petrova Ts.	V-40
FEATURES OF HIGH-PRESSURE NON-SELF-MAINTAINED VOLUME DISCHARGE INSTABILITY IN A QUASIMONOCROMATIC MICROWAVE Sinkevich O.A., Sosnin V.E.	V-42

Topic 8 : Plasma diagnostic methods.

MEASUREMENTS OF ELECTRON ENERGY DISTRIBUTION FUNCTION IN POSITIVE COLUMN REGION OF DC-MAGNETRON SPUTTERING DEVICE Garamoon A.A., Al-Hassan A. A., Hassouba M.A., Elakskar F.F.	V-44
--	------

MEASUREMENTS OF PLASMA DENSITY : A COMPARISON BETWEEN RESONANCE CONES AND V-46
 LANGMUIR TECHNIQUES
 Riccardi C., Salierno M., Fontanesi M., Pierre Th.

STARK WIDTHS PREDICTIONS FROM REGULARITIES FOR TRIPLY AND QUADRUPLY-CHARGED V-48
 ION OFF-RESONANCES OF SEVERAL HEAVY ELEMENTS
 Puric J., Scepanovic M., Milosavljevic V., Cuk M.

Topic 9 : Plasma wall interactions, electrode and surface effects.

PECULIARITIES OF DISCHARGE FORMATION USING BLADE-SHAPED ELECTRODES IN A HF V-50
 (DF) LASER
 Zapol'sky A.F., Velikanov S.D., Evdokimov P.A., Kovalev E.V., Pegoev I.N.

Topic 10 : Physical aspects of plasma chemistry, plasma processing of surface and thin film technology.

A PULSED MICROWAVE DISCHARGING DEVICE FOR STUDIES ON PLASMA-WALL- V-52
 INTERACTIONS
 Baeva M., Luo X., Zhang Z., Schaefer J.H., Uhlenbusch J.

FORMATION OF LARGE MOLECULES AND AGGLOMERATES IN DC GLOW DISCHARGES IN V-54
 HYDROCARBONS
 Winter J., Leukens A.

MEASUREMENT OF SHEATH OSCILLATING CURRENT IN HIGH DENSITY PROCESSING PLASMA V-56
 Sawa Y., Shindo H., Fujii S., Horiike Y.

WAVE PATTERN MEASUREMENT IN HIGH DENSITY HELICONWAVE PROCESSING PLASMA V-58
 Shindo H., Sawa Y., Kawamura K., Furukawa M., Horiike Y.

Topic 11 : Generation and dynamics of plasma flows.

APPLICATION OF FFT TO EVALUATIONS OF VELOCITIES IN PLASMA JETS V-60
 Hlina J.

MODELLING OF DYNAMICS OF PENETRATION OF PLASMOIDS IN CROSS MAGNETIC FIELD V-62
 Korotaev K.N., Smirnov V.M., Savjolov A.S.

Topic 12 : Non-ideal plasmas. Clusters and dusty plasmas.

EXPANDING PLASMA LAYERS WITH TWO ELECTRON GROUPS AND DUST PARTICLES V-64
 Chutov Yu.I., Kravchenko A.Yu., Schram P.J.J.M., Yakovetsky V.S.

ON THE THEORY OF NONIDEAL PLASMAS
Kaklugin A.S., Norman G.E., Valuev A.A.

V-66

Topic 13 :
Waves and instabilities, including shock waves.

ELECTRON RESONANCE CONES IN INHOMOGENEOUS PLASMAS
Riccardi C., Salierno M., Fontanesi M., Pierre Th.

V-68

Topic 14 :
Non-linear phenomena and self-organization processes.

OBSERVATION OF SPONTANEOUS TURBULENT ELECTROSTATIC FLUCTUATIONS IN A
MAGNETOPLASMA
Riccardi C., Caspani D., Gamberale L., Chiodini G., Fontanesi M.

V-70

BIFURCATION ANALYSIS OF THE NEGATIVE CORONA DISCHARGE
Benilov M.S.

V-72

Topic 16 :
Plasmas sources of radiation.

MODELING OF LF BARRIER DISCHARGES IN A Xe EXCIMER LAMP
Oda A., Sakai Y., Sugawara H., Ventzek P.

V-74

NUMERICAL SIMULATION OF A PLASMA DISPLAY PANEL DISCHARGE OPERATED BY AC
PULSES
Hashiguchi S., Tachibana K.

V-76

DYNAMIC ELECTRICAL CHARACTERISTICS OF FLUORESCENT LAMPS
Vos T.P.C.M., Ligthart F.A.S., Van der Mullen J.A.M., Van Dijk J.

V-78

INVESTIGATION OF MICRO-PLASMA SOURCE OF RADIATION
Gostev V.A., Mamkovich V.V., Sysun V.I.

V-80

Topic 17 :
Numerical modeling.

STABILITY OF LOW-VOLTAGE DISCHARGE IN FINITE MAGNETIC FIELD
Temeev A.A., Sladkov O.S.

V-82

NEGATIVE CONDUCTANCE BECOMING EXCITED IN MAGNETIZED PLASMA AT HEAVY
GRADIENT OF DIRECTED ELECTRON VELOCITY
Temeev A.A.

V-84

CAPACITANCE AND CHARACTERISTICS OF THE BOUNDARY SHEATH UNDER VARIOUS
CONDITIONS
Valentini H.B., Herrmann F.

V-86

NUMERICAL STUDY OF THE WAVE-LENGTH DEPENDENCE ON THE THRESHOLD INTENSITY IN LASER INDUCED BREAKDOWN OF N ₂ Daoud J.M., El-Fotouh A. N., Gamal Y.E.	V-88
SELFCONSISTENT NUMERICAL MODELLING OF SURFACE WAVE SUSTAINED DISCHARGES Grosse S., Schluter H., Schluter M.	V-90
EFFECT OF KNUDSEN NUMBER ON MOMENTUM, HEAT AND MASS TRANSFER BETWEEN INJECTED PARTICLES AND NITROGEN THERMAL PLASMA Stefanovic P.L., Cvetinovic D., Pavlovic P.B., Kostic Z.G.	V-92
TOWARDS A GENERAL COLLISIONAL RADIATIVE MODEL van Dijk J., Hartgers A., Jonkers J., Herben P.G.J.M., van der Mullen J.A.M.	V-94
NUMERICAL MODELLING OF LOW PRESSURE ARGON/ MERCURY DISCHARGES : AN APPLICATION OF PLASIMO van Dijk J., Tas M.A., Jonkers J., Herben P.G.J.M, van der Mullen J.A.M.	V-96

Topic 19a :
Highly ionized, low pressure plasmas
(plasma thrusters, ion sources and surface treatment).

MICROWAVE SURFACE DISCHARGE THRUSTED HYPERSONIC FLIGHT IN THE ATMOSPHERE Glaskov V.V., Sinkevich O.A.	V-98
TRANSITION TO THE SUPERSONIC ION FLOW IN STATIONARY PLASMA THRUSTER Makowski K., Dudeck M.	V-100

ERRATUM
Topic 10 :
Physical aspects of plasma chemistry,
plasma processing of surface and thin film technology.

USE OF DYNAMIC ACTINOMETRY FOR THE DIAGNOSTICS OF A MICROWAVE H ₂ -CH ₄ -N ₂ PLASMA FOR DIAMOND DEPOSITION Chatei H., Bougdira J., Remy M., Alnot P.	V-102
---	-------

Topic 1

**Kinetics, thermodynamics and
transport phenomena.**

Measurement of Anomalous Transport in Plasmas

C. Riccardi, L. Gamberale, L. Fattorini, G. Chiodini, C. Bevilacqua and M. Fontanesi

Dipartimento di Fisica, Università di Milano,
Via Celoria 16, 20133- Milano, Italy

1. Introduction

It is well known that the particle transport phenomenon is the main cause of degeneration of a confined plasma. The analysis of the anomalous fluxes, i.e. fluxes produced by micro-fluctuations, is of great interest in elucidating the dynamics of such phenomenon. In this work the local particle flux produced by electrostatic fluctuations is measured by using digital correlation techniques. For this reason it is important to know how such a particle flux is distributed in space and how it behaves under different plasma conditions.

In this work we have analysed the electrostatic fluctuation-induced particle transport in the toroidal magnetoplasma Torello.

2. Diagnostic methods and results

The local particle flux is defined by

$$\Gamma(\underline{x}, t) = \langle n(\underline{x}, t) v(\underline{x}, t) \rangle \quad (1)$$

where $n(\underline{x}, t)$ is the instantaneous local plasma density, $v(\underline{x}, t)$ is the instantaneous mean velocity of the plasma particles contained in the Debye sphere centred at \underline{x} and $\langle \rangle$ is a well suited temporal average over a time domain $(t - T/2, t + T/2)$, where T is a time interval such that $1/T$ is a frequency much smaller than the smallest frequency of the density fluctuations.

It is customary to decompose $n(\underline{x}, t)$ and $v(\underline{x}, t)$ into two parts:

$$n(\underline{x}, t) = n_0(\underline{x}, t) + n'(\underline{x}, t) \quad (2a)$$

$$v(\underline{x}, t) = v_0(\underline{x}, t) + v'(\underline{x}, t) \quad (2b)$$

where $v_0(\underline{x}, t) = \langle v(\underline{x}, t) \rangle$, and $n_0(\underline{x}, t) = \langle n(\underline{x}, t) \rangle$ so that

$$\Gamma(\underline{x}, t) = \Gamma_0(\underline{x}, t) + \Gamma'(\underline{x}, t) \quad (3)$$

where

$$\Gamma_0(\underline{x}, t) = \langle n_0(\underline{x}, t) v_0(\underline{x}, t) \rangle \quad (4)$$

is called *normal particle transport flux* and

$$\Gamma'(\underline{x}, t) = \langle n'(\underline{x}, t) v'(\underline{x}, t) \rangle \quad (5)$$

is called *anomalous or fluctuation-induced particle transport flux* (cross products vanish by definition of $v'(\underline{x}, t)$ and $n'(\underline{x}, t)$).

If we consider a steady-state plasma the flux is independent of time and we can write

$$\Gamma'(\underline{x}) = \lim_{M \rightarrow \infty} \sum_{i=1}^M \frac{1}{MT} \int_{-T/2}^{T/2} n'(\underline{x}, \frac{iT}{2} + t) v'(\underline{x}, \frac{iT}{2} + t) dt \quad (6)$$

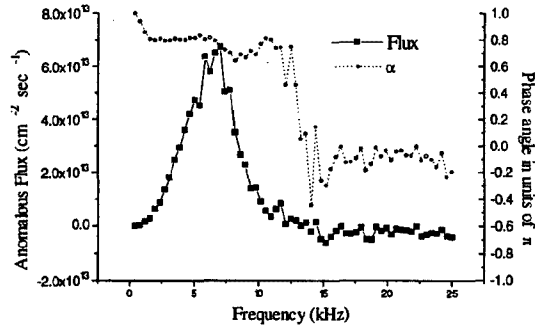


Fig.1: Spectral distribution of the anomalous flux and averaged phase angle in units of π between the density fluctuation and the floating potential measured at $r=3.5$ cm.

Since $v(\underline{x}, t)$ is the drift velocity and is given by

$$v'(\underline{x}, t) = \frac{E'(\underline{x}, t) \times B}{B^2} \cdot 10^8 \quad (7)$$

the anomalous flux can be written¹

$$\Gamma'_{\omega, d\omega}(\underline{x}) = \lim_{M \rightarrow \infty} \sum_{i=1}^M \frac{2 \cdot 10^8}{MTB} \int_0^\infty \frac{d\omega}{2\pi} k(\omega) \times \frac{B}{B} \cdot \text{Im}[n_i^*(\underline{x}, \omega) \phi_i'(\underline{x}, \omega)] \quad (8)$$

where $n(\underline{x}, \omega)$ and $\phi(\underline{x}, \omega)$ are the Fourier transforms of density and plasma potential respectively and $k(\omega)$ is the dispersion relation. The quantity

$$\Gamma'_{\omega, d\omega}(\underline{x}) = \lim_{M \rightarrow \infty} \sum_{i=1}^M \frac{2 \cdot 10^8}{MTB} k(\omega) \times \frac{B}{B} \text{Im}[n_i^*(\underline{x}, \omega) \phi_i'(\underline{x}, \omega)] \frac{d\omega}{2\pi} \quad (9)$$

can be viewed as the contribution to the anomalous flux of the fluctuations with frequency comprised between $\omega/2\pi$ and $(\omega+d\omega)/2\pi$.

Once the discretisation of the integrals is made we find (from now on we consider the radial component of the flux)

$$\Gamma'_{\omega, \Delta\omega}(\mathbf{x}) = \sum_{i=1}^M \frac{2 \cdot 10^8}{MB} k(\omega) \times \frac{B}{B} \cdot \text{Im}[n_i^*(\mathbf{x}, \omega) \phi'_i(\mathbf{x}, \omega)] \quad (10)$$

$$\omega_n = \Delta\omega \cdot n$$

$$\Delta\omega = \frac{2\pi}{T}$$

where $n=1, \dots, N$ and N is the number of subdivisions of the time interval T .

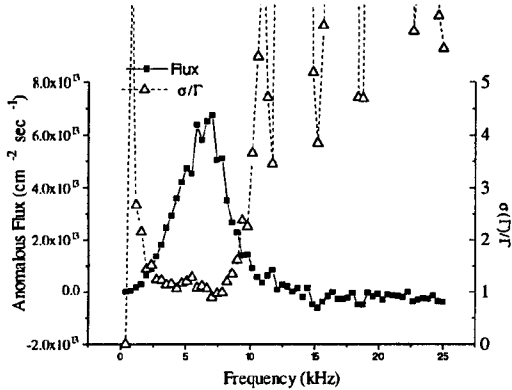


Fig.2: Spectral distribution of the anomalous flux and standard deviation normalised to the flux at $r=3.5$ cm.

The measurement is performed by synchronous acquisition on a digital oscilloscope on three pins (that we label 1, 2, 3) such that pins 1 and 2 are disposed along the radial direction and pin 1 and 3 in the B -direction and elongated by a distance of 0.6 cm. Pins 1 and 2 are floating potential probes whereas pin 3 is negatively biased to -18V and measures ion saturation

current I^+ , which is related to the plasma density to a good approximation by the formula

$$n'(\mathbf{x}, t) = \frac{n(\mathbf{x})}{I^+(\mathbf{x})} I^+(\mathbf{x}, t). \quad (11)$$

The experiment is carried out in the toroidal device Thorello (whose major and minor radii are $R=40$ cm and $r=8$ cm respectively) which produces magnetised hydrogen plasma in steady-state conditions. Typically obtained plasma parameters for a toroidal magnetic field of 1kG are: $T_e \approx 1$ eV, $T_i \approx 0.3$ eV, edge plasma density $\approx 10^9$ cm $^{-3}$, centre plasma density $\approx 10^{11}$ cm $^{-3}$, neutral gas pressure $P=10^{-4}$ mbar.

The data are composed by 32768 records with base time $\tau = 20$ μ sec, each containing the readouts of the three pins. In the analysis we have chosen $N=128$ and $M=256$.

Fig. 1 shows a typical flux spectrum together with the averaged phase angle between $\phi'(\mathbf{x}, t)$ and $n'(\mathbf{x}, t)$ in units of π . The main contribution to the flux is in the frequency range below 10kHz and is directed outward. Fig. 1 also shows that in the frequency range below 10 kHz the phase angle ranges between 0.6π and 0.8π , indicating the presence of dissipative effects (a value of 0.5 is expected when the drift-type electrostatic fluctuations² are collisionless). In Fig.2 the normalised standard deviation of the flux as a function of ω shows that in the frequency range below 10 kHz the measurement is statistically meaningful. On the contrary, when the frequency is above 10 kHz, $\phi'(\mathbf{x}, t)$ and $n'(\mathbf{x}, t)$ are completely uncorrelated and the signal has to be considered as statistical noise.

Fig.3 shows the integrated anomalous flux and the averaged (in ω) phase angle for different radial positions. The anomaly of the flux profile around $r=3.5$ cm is in correspondence with the shear layer. Such a behaviour in this region will be the argument of a future work.

The data analysed are in substantial agreement with the results of other groups^{3,4}.

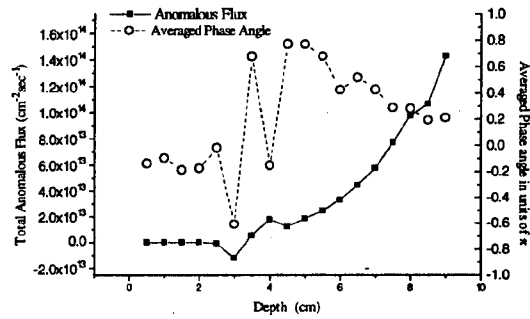


Fig.3: Integrated anomalous flux and integrated phase angle as a function of depth

References

1. Rowan, C.C. Klepper, C.P. Ritz, R.D. Bengston, K.W. Gentle, P.E. Phillips, T.L. Rhodes, B. Richards and A.J. Wootton, *Nucl. Fus.* **27** n. 7 (1987)
2. Riccardi, D. Caspani, L. Gamberale, G. Chiodini and M. Fontanesi, contribution at this Conference.
3. Ch. P. Ritz, Roger D. Bengston, S.J. Levinson and E. J. Powers *Phys. Fluids* **27** (12) 1984
4. Hidalgo *et al.*, *Nucl. Fus.* **31** n. 8 (1991), and references therein.

Measurement of electron transport coefficients in the C_3F_8 -Ar mixture

Byoung-Hoon Jeon, Sung-Chul Ha[†] and Yoshiharu Nakamura

Department of Electrical Engineering, Faculty of Science and Technology Keio University

3-14-1 Hiyoshi, Yokohama 223, Japan

[†]Department of Electrical Engineering, Dongguk University, 3 Pilldong Gunggu Seoul, Korea

1. Introduction

Perfluoropropane(C_3F_8) in the perfluoroalkanes, C_nF_{2n+2} ($n=1,2,3,4$), is frequently used as one of effective etchants in semiconductor etching processes and it is also used as gaseous media in gas discharge switches and radiation detectors[1]. And an accurate set of low-energy electron collision cross section data is required to the quantitative modelings of the related plasmas.

Pirgov and Stefanov[2] derived a momentum transfer cross section and a total vibrational excitation cross section for the molecule from the electron swarm data measured by Hunter *et al.*[3] by using a two-term approximation of the Boltzmann analysis, which may not be valid for molecules with large vibrational excitation cross sections. There are also new measurement of the ionisation and attachment cross sections for the molecules by Chantry and Chen[4].

It is, therefore, worth while at this stage to determine a new set of cross section data for the C_3F_8 molecule. To that purpose, we firstly measured the drift velocity, W , and the product of the gas number density and the longitudinal diffusion coefficient, ND_L , of electrons in C_3F_8 -Ar mixtures.

2. The method of measurement

The present measurement of the electron transport coefficients, W and ND_L , in 5.05% C_3F_8 -Ar mixture over the E/N range from 0.03 to 10 Td and gas pressure range from 1.33 to 122 kPa were carried out by the double

shutter drift tube with variable drift distance(1-10 cm), and the experimental apparatus and procedure were the same as used in the works[5].

The electron drift velocity W is derived from the relationship between the peak time of each arrival time spectrum of electrons(ATs) and the longitudinal diffusion coefficient D_L is determined from the relationship between the characteristic width of each ATs and the drift distance. An typical example of ATs in 5.05% C_3F_8 -Ar mixture is shown in Fig. 1.

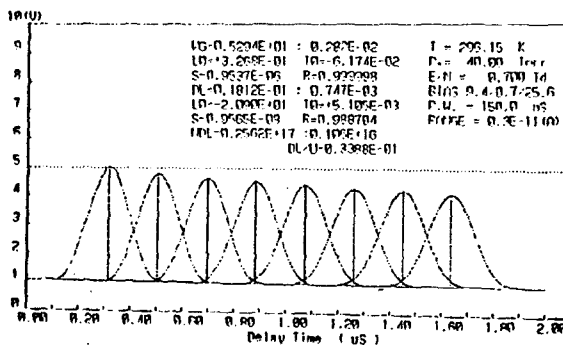


Fig. 1. An example for arrival time spectra of electrons measured in 5.05% C_3F_8 -Ar mixture

All measurements were carried out at room temperature, 300 ± 2 K. For the measurements spectrally pure C_3F_8 molecule gas(purity 99.99%) and Ar (99.9999%) were used, and the mix ratio of C_3F_8 -Ar mixtures was determined by the gas chromatography test.

3. The result of measurement

The results of the present measurements are summarized in Fig. 2 and 3. Each symbol shows the measured values of the transport coefficient determined

at several gas pressures. Typical scatters of the measured coefficients at each E/N were less than 1% for the drift velocity and less than 8% for the ND_L in the present measurement.

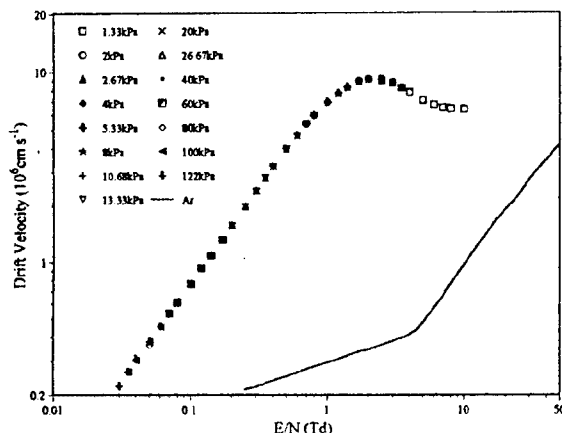


Fig. 2. W as a function of E/N in the 5.05% C_3F_8 -Ar mixture

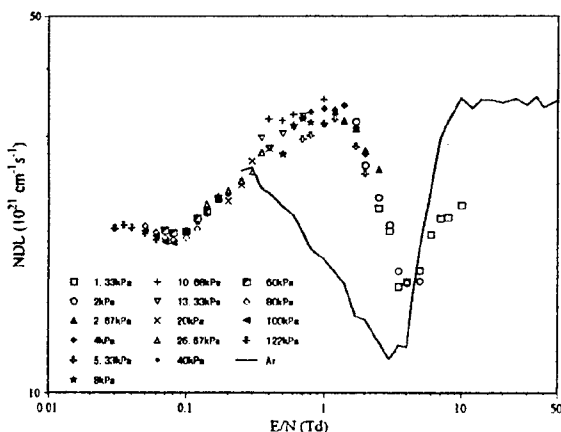


Fig. 3. ND_L as a function of E/N in the 5.05% C_3F_8 -Ar mixture

In both figures also shown are the respective transport coefficients in pure argon[5] by solid curve for comparison. The measured drift velocity in the mixture is enhanced more than an order of magnitude by adding the small fraction of C_3F_8 from that in pure argon and shows clearly the so-called Negative Differential Conductivity (NDC) indicating a strong contribution from the vibrational inelastic processes of C_3F_8 over the E/N range from 2 to 8 Td in the mixture. The measured ND_L in

mixture also show clear contribution of the molecular additive in argon.

4. Discussion

We have measured electron transport coefficients in the 5.05% C_3F_8 -Ar mixture over the E/N range from 0.03 to 10 Td.

We will continue the measurement of electron transport coefficients in this mixture for wider E/N range and also in the 0.5% C_3F_8 -Ar mixture and in pure C_3F_8 . After completion of the measurements, we will try to determine an accurate set of electron collision cross section for C_3F_8 molecule by comparison of measurement and calculation using a multi-term Boltzmann analysis[6] in the electron transport coefficients in C_3F_8 -Ar mixtures and in pure C_3F_8 molecule.

5. References

- [1] M. Hayashi : *Proc. 4th Symp. Inelastic Electron-Molecule Collisions* (New York: Springer, 1985)
- [2] P. Pirgov and B. Stefanov : *J. Phys. B* **23** (1990) 2879
- [3] S.R. Hunter and J. Carter and L.J. Christophorou : *J. Appl. Phys.* **58** (1985) 3001
- [4] P.J. Chantry and C.L. Chen : *J. Chem. Phys.* **90** (1989) 2585
- [5] Y. Nakamura and M. Kurachi : *J. Phys. D* **21** (1988) 718
- [6] K.F. Ness and R.E. Robson : *Phys. Rev. A* **33** (1986) 2068

The calculation of the viscosity tensor for a magnetoplasma from the stress balance equation

Kurt Suchy

University of Düsseldorf,
Universitätsstr. 1, D-40225 Düsseldorf, Germany

The fourth-order viscosity tensor can be obtained as the inverse of another fourth-order tensor, given by the stress balance equation [1]. For the inversion a suitable set of five orthogonal fourth-order projectors is most convenient. Of Braginskii's [2] five tensors only some are orthogonal and merely two are projectors, whereas the set of Hess [3] has both properties.

Second-order tensors

Gyrotropic second-order tensors with a common axial unit vector \mathbf{b} , e.g. electrical and heat conductivities for a magnetoplasma, have a common complete set of orthogonal projectors [4]

$$\mathbf{P}_0 := \mathbf{b}\mathbf{b}, \quad \mathbf{P}_{\pm 1} := \frac{1}{2}(\mathbf{I} - \mathbf{b}\mathbf{b} \pm i\mathbf{b} \times \mathbf{I}) \quad (1)$$

$$= \mathbf{P}_{\mp 1}^T = \mathbf{P}_{\mp 1}^* = \text{Re } \mathbf{P}_1 \pm i \text{Im } \mathbf{P}_1$$

with the orthonormality and completeness relations

$$\mathbf{P}_\mu \cdot \mathbf{P}_\nu = \delta_{\mu\nu} \mathbf{P}_\mu, \quad \sum_{\mu=-1}^1 \mathbf{P}_\mu = \mathbf{I} \quad (2)$$

where

$$\mathbf{I} = \mathbf{P}_0 + 2 \text{Re } \mathbf{P}_1 \quad (3)$$

is the unit tensor.

The momentum balance equation (and the balance equation for the heat flux) has the form (see [5] with (1) and (2))

$$\alpha \mathbf{a} + \beta \mathbf{b} \times \mathbf{a} = (\alpha \mathbf{I} + \beta \mathbf{b} \times \mathbf{I}) \cdot \mathbf{a}$$

$$= \left[\sum_{\mu} (\alpha - i\mu\beta) \mathbf{P}_\mu \right] \cdot \mathbf{a} = \mathbf{c} \quad (4)$$

and is solved by dot multiplication with the inverse tensor as

$$\sum_{\nu} \frac{\mathbf{P}_\nu}{\alpha - i\nu\beta} \cdot \sum_{\mu} (\alpha - i\mu\beta) \mathbf{P}_\mu \cdot \mathbf{a} = \mathbf{a} = \sum_{\nu} \frac{\mathbf{P}_\nu}{\alpha - i\nu\beta} \cdot \mathbf{c} \quad (5)$$

where the orthonormality and the completeness (2) of the set \mathbf{P}_μ has been employed. A set $\mathbf{P}_0, 2 \text{Re } \mathbf{P}_1, 2 \text{Im } \mathbf{P}_1$ would not be suitable for this procedure, since $2 \text{Im } \mathbf{P}_1 = \mathbf{b} \times \mathbf{I}$ is not a projector and $\text{Re } \mathbf{P}_1$ is not orthogonal with $\text{Im } \mathbf{P}_1$.

Fourth-order tensors

The stress balance equation [1] is of the form

$$\alpha \mathbf{U} + \beta [\mathbf{b} \times \mathbf{U} + (\mathbf{b} \times \mathbf{U})^T] = \mathbf{V} \quad (6)$$

with \mathbf{U} and \mathbf{V} as symmetric tracefree tensors. Because of these two properties we replace $\alpha \mathbf{U}$ by $\alpha D^{(4)} : \mathbf{U}$ with the fourth-order *reducer* [3]

$$D^{(4)} := I^{(2|2)} - \frac{1}{3} \mathbf{I} \mathbf{I} =: \mathbf{I} \circ \mathbf{I} - \frac{1}{3} \mathbf{I} \mathbf{I} \quad (7)$$

where the *symmetrizer* $I^{(2|2)}$ has been expressed with a Kronecker-like double-symmetrizing commutative ring product defined as

$$4\mathbf{a}_1 \mathbf{a}_2 \circ \mathbf{b}_1 \mathbf{b}_2 := (\mathbf{a}_1 \mathbf{b}_1 + \mathbf{b}_1 \mathbf{a}_1)(\mathbf{a}_2 \mathbf{b}_2 + \mathbf{b}_2 \mathbf{a}_2) \quad (8)$$

$$= 4\mathbf{b}_1 \mathbf{b}_2 \circ \mathbf{a}_1 \mathbf{a}_2$$

The five fourth-order symmetric projectors [3][4]

$$P_\lambda^{(4)} := \sum_{\mu} \sum_{\nu} \delta_{\lambda, \mu+\nu} \mathbf{P}_\mu \circ \mathbf{P}_\nu - \frac{\delta_{\lambda 0}}{3} \mathbf{I} \mathbf{I} = P_{-\lambda}^{(4)*} \quad (9)$$

are tracefree, orthogonal and complete:

$$\mathbf{I} : P_\lambda^{(4)} = 0, \quad P_\lambda^{(4)} : P_\kappa^{(4)} = \delta_{\lambda\kappa} P_\lambda^{(4)},$$

$$\sum_{\lambda} P_\lambda^{(4)} = D^{(4)}. \quad (10)$$

The tensor $\mathbf{b} \times \mathbf{U} + (\mathbf{b} \times \mathbf{U})^T$ in the stress balance equation (6) can be written for any (even nonsymmetric) \mathbf{U} as [4]

$$\mathbf{b} \times \frac{\mathbf{U} + \mathbf{U}^T}{2} + \left(\mathbf{b} \times \frac{\mathbf{U} + \mathbf{U}^T}{2} \right)^T = (2\mathbf{b} \times \mathbf{I} \circ \mathbf{I}) : \mathbf{U} \quad (11)$$

where the fourth-order tensor $2\mathbf{b} \times \mathbf{I} \circ \mathbf{I}$ has the spectral representation [4]

$$2\mathbf{b} \times \mathbf{I} \circ \mathbf{I} = -i \sum_{\lambda=-2}^2 \lambda P_\lambda^{(4)} = -2i \sum_{\lambda=1}^2 \lambda \text{Re } P_\lambda^{(4)} \quad (12)$$

With the spectral representations (10) for $D^{(4)}$ and (12) for $2\mathbf{b} \times \mathbf{I} \circ \mathbf{I}$ the stress balance equation (6) has the form

$$(\alpha D^{(4)} + 2\beta \mathbf{b} \times \mathbf{I} \circ \mathbf{I}) : \mathbf{U} = \left[\sum_{\lambda} (\alpha - i\lambda\beta) P_\lambda^{(4)} \right] : \mathbf{U} = \mathbf{V} \quad (13)$$

with the solution, analogous to (5),

$$\mathbf{U} = \sum_{\lambda} \frac{P_{\lambda}^{(4)}}{\alpha - i\lambda\beta} : \mathbf{V} \quad (14)$$

This was achieved with the orthogonality and the projector property (10) of the $P_{\lambda}^{(4)}$.

In contrast to the $P_{\lambda}^{(4)}$ (9) only some of Braginskii's tensors [2]

$$\begin{aligned} W_0^{(4)} &:= P_0^{(4)}, & W_1^{(4)} &:= 2 \operatorname{Re} P_2^{(4)} + \operatorname{Re} \mathbf{P}_1 \mathbf{I} \\ W_2^{(4)} &:= 2 \operatorname{Re} P_1^{(4)}, & W_3^{(4)} &:= 2 \operatorname{Im} P_2^{(4)}, \\ W_4^{(4)} &:= 2 \operatorname{Im} P_1^{(4)} \end{aligned} \quad (15)$$

are orthogonal and only $W_0^{(4)}$ and $W_2^{(4)}$ are projectors, analogous to the statements following (5) for the second order tensors $\operatorname{Re} \mathbf{P}_1$ and $\operatorname{Im} \mathbf{P}_1$. Therefore the solution method (13) (14) cannot be used with Braginskii's tensors $W_{\lambda}^{(4)}$ (15) instead of Hess' tensors $P_{\lambda}^{(4)}$ (9).

Explicit results for the stress tensor

To express the fourth-order projector $P_0^{(4)} = \mathbf{P}_0 \circ \mathbf{P}_0 + 2\mathbf{P}_{+1} \circ \mathbf{P}_{-1} - \frac{1}{3}\mathbf{I}\mathbf{I}$ (9) we need from (1) and (8) $\mathbf{P}_0 \circ \mathbf{P}_0 = \mathbf{P}_0 \mathbf{P}_0$ and

$$\begin{aligned} 4\mathbf{P}_{+1} \circ \mathbf{P}_{-1} &= 4\mathbf{P}_1 \circ \mathbf{P}_1^T = (\mathbf{P}_1 + \mathbf{P}_1^T)(\mathbf{P}_1^T + \mathbf{P}_1) \\ &= (\mathbf{I} - \mathbf{P}_0)(\mathbf{I} - \mathbf{P}_0). \end{aligned} \quad (16)$$

After some arrangements one obtains

$$P_0^{(4)} = \frac{3}{2} \left(\mathbf{P}_0 - \frac{1}{3}\mathbf{I} \right) \left(\mathbf{P}_0 - \frac{1}{3}\mathbf{I} \right) \quad (17)$$

and therefore with $\mathbf{P}_0 = \mathbf{b}\mathbf{b}(\mathbf{I})$

$$P_0^{(4)} : \mathbf{V} = \left[\mathbf{b}\mathbf{b} - \frac{1}{2}(\mathbf{I} - \mathbf{b}\mathbf{b}) \right] (\mathbf{b} \cdot \mathbf{V} \cdot \mathbf{b} - \frac{1}{3} \operatorname{trace} \mathbf{V}). \quad (18)$$

For the other four double contractions $P_{\lambda}^{(4)} : \mathbf{V}$ in the solution (14) we need the expressions for $(\mathbf{P}_{\mu} \circ \mathbf{P}_{\nu}) : \mathbf{V}$, cf. (9). The definition (8) of the ring product and the relation $\mathbf{P}_{\mu}^T = \mathbf{P}_{-\mu}$ (1) yields

$$2(\mathbf{P}_{\mu} \circ \mathbf{P}_{\nu}) : \mathbf{V} = \mathbf{P}_{\mu} \cdot \mathbf{V}^S \cdot \mathbf{P}_{-\nu} + \mathbf{P}_{\nu} \cdot \mathbf{V}^S \cdot \mathbf{P}_{-\mu} \quad (19)$$

with $\mathbf{V}^S := (\mathbf{V} + \mathbf{V}^T)/2$ as the symmetric part of \mathbf{V} .

With the definitions (1) and (9) we obtain

$$\begin{aligned} 2P_{\pm 1}^{(4)} : \mathbf{V} &= \mathbf{b}\mathbf{b} \cdot \mathbf{V}^S + \mathbf{V}^S \cdot \mathbf{b}\mathbf{b} - 2\mathbf{b}\mathbf{b} \cdot \mathbf{V}^S \cdot \mathbf{b}\mathbf{b} \\ &\quad \pm i(\mathbf{b} \times \mathbf{V}^S \cdot \mathbf{b}\mathbf{b} - \mathbf{b}\mathbf{b} \cdot \mathbf{V}^S \times \mathbf{b}) \end{aligned} \quad (20)$$

and

$$\begin{aligned} 4P_{\pm 2}^{(4)} : \mathbf{V} &= \mathbf{V}^S \cdot \mathbf{b}\mathbf{b} \cdot \mathbf{V}^S - \mathbf{V}^S \cdot \mathbf{b}\mathbf{b} \cdot \mathbf{b} \times \mathbf{V}^S \times \mathbf{b} + \mathbf{b}\mathbf{b} \cdot \mathbf{V}^S \cdot \mathbf{b}\mathbf{b} \\ &\quad \pm i(\mathbf{b} \times \mathbf{V}^S - \mathbf{V}^S \times \mathbf{b} + \mathbf{b}\mathbf{b} \cdot \mathbf{V}^S \times \mathbf{b} - \mathbf{b} \times \mathbf{V}^S \cdot \mathbf{b}\mathbf{b}) \end{aligned} \quad (21)$$

Combining $P_{\lambda}^{(4)} + P_{-\lambda}^{(4)} =: S_{\lambda}^{(4)}$ as well as $P_{\lambda}^{(4)} - P_{-\lambda}^{(4)} =: D_{\lambda}^{(4)}$ we write the solution (14) for the stress tensor as

$$\begin{aligned} \mathbf{U} &= \frac{1}{\alpha} P_0^{(4)} : \mathbf{V} + \sum_{\lambda=1}^2 \frac{\alpha S_{\lambda}^{(4)} + i\lambda\beta D_{\lambda}^{(4)}}{\alpha^2 + \lambda^2\beta^2} : \mathbf{V} \\ &= \frac{1}{\alpha} D^{(4)} : \mathbf{V} + \frac{\beta}{\alpha^2} \sum_{\lambda=1}^2 \lambda \left(iD_{\lambda}^{(4)} - \frac{\lambda\beta}{\alpha} S_{\lambda}^{(4)} \right) : \mathbf{V} \\ &\quad + 0 \left(\frac{\beta^3}{\alpha^4} \right) \\ &= \frac{1}{\alpha} P_0^{(4)} : \mathbf{V} + \frac{1}{\beta} \sum_{\lambda=1}^2 \left(iD_{\lambda}^{(4)} + \frac{\alpha}{\lambda\beta} S_{\lambda}^{(4)} \right) : \mathbf{V} \\ &\quad + 0 \left(\frac{\alpha^2}{\beta^3} \right) \end{aligned} \quad (22)$$

For a strong magnetic field ($\beta \gg \alpha$) the dominant term $P_0^{(4)} : \mathbf{V}$ (18) gives opposite contributions parallel and perpendicular to the direction \mathbf{b} of the magnetic field.

References

- [1] K. Suchy, C. Altman: J. Plasma Phys. 57 (1997) in print, eq. eqs. 2.11, 3.14
- [2] S.I. Braginskii: Rev. Plasma Phys. 1 (1965) 205-311, eq. 4.42
- [3] S. Hess: Springer Tracts in Modern Physics 54 (1970) 136-176, eqs. 3.7, 7.8
- [4] S. Hess, L. Waldmann: Z. Naturforschung 26a (1971) 1057-1071, eqs. A.2 through A.24
- [5] W.P. Allis: Handbuch der Physik 21 (1956) 383-444, eq. 12.2

Topic 2

Elementary processes.

THE NUMERICAL ANALYSIS OF THE IONIZATION CROSS-SECTION OF A HYDROGEN-LIKE ATOM BY FAST ELECTRONS IN A HOMOGENEOUS ELECTRIC FIELD

V.I.Krylov, V.V.Pivkin, O.V.Kriulina

Khabarovsk State Pedagogical University
Karl Marx street, 68, 680000 Khabarovsk, Russia

The differential ionization cross-section of the hydrogen-like atom by a fast electron in a homogenous electric field \vec{E} was obtained in the nonrelativistic Born approximation.

To determine differential cross-section asymptotes of the wave function proposed in the Ref.[1] were used.

A longitudinal (along \vec{E}) current density of the electrons calculated by these functions is zero, if the electrons are between their turning points in a homogenous electric field and the atomic nucleus, and this longitudinal current density is nonzero if electrons are on opposite side from the atomic nucleus (along \vec{E}).

We have chosen the direction of the external electric field \vec{E} along the z-axis: $\vec{E} = (0, 0, -E)$ and have assumed that this field exists in the region of the space with the coordinates $z > -L$ where L is the distance between an atomic nucleus and a homogenous electric field boundary.

When the energy of the scattered electrons $E_z > eEL$ we have used the wave functions Ψ_x [2]:

$$\Psi_x = A_x S^{-1/4} \exp \left[i \left(\frac{2\chi_z S^2}{3|\chi_z|} + \vec{k}_\perp \vec{r} \right) \right] \quad (1)$$

where the vector $\vec{\chi} = (\vec{k}_\perp, \chi_z)$ defines the current

density \mathbf{j} of electrons; $S = \frac{z}{\eta} + \frac{E_z}{eE\eta}$; $\eta = \left(\frac{\hbar^2}{2m_e eE} \right)^{1/3}$;

$E_z = \frac{\chi_z^2 \hbar^2}{2m_e} + eEL$; \vec{r} , $-e$, m_e are the radius-vector, the

charge and the mass of an electron. In a homogenous electric field there exist the final states of electron with $E_z \ll eEL$. The wave function asymptotes [1] of these states are

$$\psi(\vec{r}) = A_k \frac{\exp(i\vec{k} \cdot \vec{r})}{S^{1/4}} \begin{cases} \sin \left(\frac{2S^2}{3} + \frac{\pi}{4} \right), & \text{if } z < 0 \\ \exp \left(i \frac{2S^2}{3} + \frac{\pi}{4} \right), & \text{if } z > 0. \end{cases} \quad (2)$$

We assume that a homogenous electric field is considerably less then the atomic one therefore the normal state wave function of the atomic electron

can be written as $(\pi a^3)^{-1/2} \exp(-\frac{r_a}{a})$ (\vec{r}_a is the radius-

vector of the atomic electron, $a = \hbar^2 / (Ze^2 m_e)$).

Using these wave function (1), (2) for both a primary electron and final states of an atomic electron we can obtain the ionization cross-section $d\sigma$ of a hydrogen-like atom by a fast electron:

$$d\sigma = \frac{2}{\pi^2 Z^2} \frac{k}{k_0} |T|^2 d\Omega d^3 \vec{k}_a, \quad k^2 = k_0^2 - k_a^2 - 1$$

(we use the Coulombic units), where Z is the atomic number; $\vec{k}_0 = (\vec{k}_{0\perp}, \sqrt{2E_{0z}})$ and $\vec{k} = (\vec{k}_\perp, \sqrt{2E_z})$ are the initial and final wave vectors of a primary electron; $\vec{k}_a = (\vec{k}_{a\perp}, \sqrt{2E_{az}})$ is the wave vector of atomic electron, when it is in the final state; $d\Omega$ is the spatial angle element containing the vector \vec{k} ; $d^3 \vec{k}_a = k_a^2 dk_a d\Omega_a$; $d\Omega_a = \sin \theta_a d\theta_a d\varphi_a$, where φ_a is the angle between $\vec{k}_{a\perp}$ and $\vec{k}_{0\perp}$; θ_a is the angle between \vec{k}_a and z-axis.

The mathematical form of the T depends on the relation between E_z, E_{az} and eEL .

If $\varepsilon^{2/3} \ll E_{az}, E_z \ll eEL$, then

$$T = \frac{R_- \exp(-i[\gamma_1 - \gamma_{a1}])}{2q_+^2 (1 + Q_-^2)^2} - \frac{M_- \exp(i[\gamma_1 + \gamma_{a1}])}{2q_-^2 (1 + \lambda_-^2)^2} - \frac{R_+ \exp(-i[\gamma_1 + \gamma_{a1}])}{2q_+^2 (1 + Q_+^2)^2} - \frac{M_+ \exp(i[\gamma_1 - \gamma_{a1}])}{2q_-^2 (1 + \lambda_+^2)^2} + \frac{2L \exp(-i[\gamma_2 + \gamma_{a2}])}{q_+^2 (1 + Q_+^2)^2} - h_+ \frac{P_- \exp(-i\gamma_{a2})}{(1 + w_-^2)^2} - \frac{i}{2} h_- \left[\frac{P_-}{(1 + w_-^2)^2} \exp(i\gamma_{a1}) - \frac{P_+}{(1 + w_+^2)^2} \exp(-i\gamma_{a1}) \right],$$

where $\vec{q}_\pm = \vec{k}_\pm - \vec{k}_0$; $\vec{k}_\pm = (\vec{k}_\perp, \pm \sqrt{2E_z})$;

$$\bar{k}_{a\pm} = (\bar{k}_{a1}, \pm\sqrt{2E_{a2}}); \bar{Q}_{\pm} = \bar{q}_{\pm} + \bar{k}_{a\pm}; \bar{\lambda}_{\pm} = \bar{q}_{\pm} - \bar{k}_{a\pm};$$

$$\bar{w}_{\pm} = (\bar{q}_{\pm} + \bar{k}_{a1}, iq_{\pm} \pm k_{a2});$$

$$R_{\pm} = 1 + \frac{iQ_{\pm z}}{2\sqrt{1+Q_1^2}} \left(3 + \frac{Q_{\pm z}^2}{1+Q_1^2} \right);$$

$$M_{\pm} = 1 + \frac{i\lambda_{\pm z}}{2\sqrt{1+\lambda_1^2}} \left(3 + \frac{\lambda_{\pm z}^2}{1+\lambda_1^2} \right);$$

$$P_{\pm} = 1 + \frac{iw_{\pm z}}{2\sqrt{1+w_1^2}} \left(3 + \frac{w_{\pm z}^2}{1+w_1^2} \right);$$

$$L = 1 - \frac{iQ_{\pm z}}{2\sqrt{1+Q_1^2}} \left(3 + \frac{Q_{\pm z}^2}{1+Q_1^2} \right);$$

$$h_{\pm} = \left[\exp(-i\gamma_2) - \frac{i}{2} \exp(-i\gamma_1) \right] \frac{q_{\pm} \pm iq_{\pm z}}{q_{\pm} q_{\pm}^2} +$$

$$+ \frac{i}{2} \frac{q_{\pm} \pm iq_{\pm z}}{q_{\pm} q_{\pm}^2} \exp(i\gamma_1);$$

$$\gamma_{1,2} = \frac{\pi}{4} + \frac{k_z^2}{3\epsilon}; \gamma_{a1,2} = \frac{\pi}{4} + \frac{k_{az}^2}{3\epsilon}.$$

If $\epsilon^{2/3} \ll E_{a2} \ll \epsilon L < E_z$, then

$$T = \frac{1}{q_{\pm}^2} \left[\frac{1}{(1+Q_+^2)^2} (iR_+ \exp[-i\gamma_{a1}] + \right.$$

$$\left. + 2L \exp[-i\gamma_{a2}]) - \frac{iR_-}{(1+Q_-^2)^2} \exp(i\gamma_{a1}) \right],$$

when $\epsilon^{2/3} \ll E_z \ll \epsilon L < E_{a2}$, then

$$T = \frac{i}{q_{\pm}^2 (1+Q_+^2)^2} (R_+ \exp[-i\gamma_1] + 2iL \exp[-i\gamma_2])$$

$$- \frac{iM_-}{q_{\pm}^2 (1+\lambda_+^2)^2} \exp(i\gamma_1) + \frac{h_- P_+}{(1+w_+^2)^2} - \frac{h_+ P_-}{(1+w_-^2)^2}$$

and finally $T = \frac{4}{q_{\pm}^2 (1+Q_+^2)^2}$, if $E_z, E_{a2} > \epsilon L$.

All these expressions are reasonable if $k, k_a \gg 1$ which is in accordance with Born approximation.

We have used the numerical methods for the analysis of this cross-section.

The numerical results were compared with the cross-section $d\sigma = \frac{32k}{k_0 (Z\pi q_+^2 [1+Q_+^2])^2} d\odot d^3 \bar{k}_a$

(when $\bar{\epsilon} = 0$) and represented as the surfaces $\frac{d\sigma}{d\odot d^3 \bar{k}_a} \equiv F(\phi_a, \theta_a)$. These surfaces are shown in Fig.1-3.

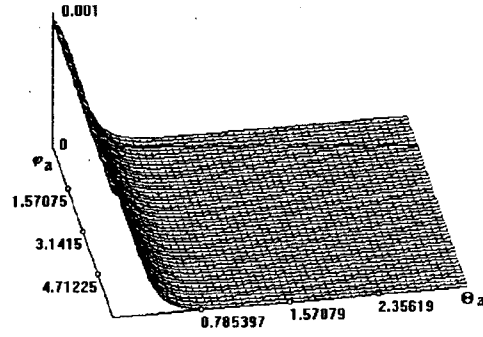


Fig.1. $\phi=0, \epsilon=0$,
 $\theta_0=1.37386, k_0=40.62019, \theta=1.48, k=40, k_a=7$.

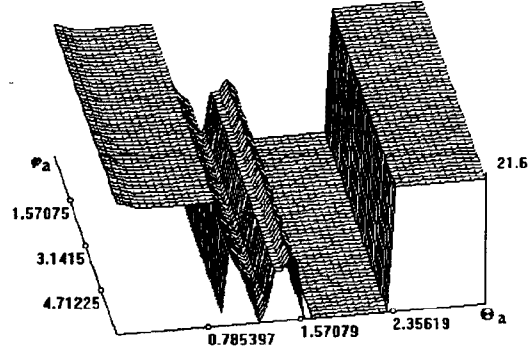


Fig.2. $\phi=0, \epsilon=0.01, L=1000$,
 $\theta_0=1.37386, k_0=40.62019, \theta=1.48, k=40, k_a=7$.

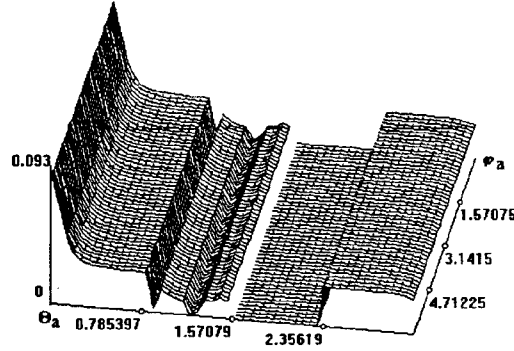


Fig.3. $\phi=0.001, \epsilon=0.01, L=1000$,
 $\theta_0=1.37386, k_0=40.62019, \theta=1.48, k=40, k_a=7$.

As may be seen from these diagrams, the ionization cross-section of the hydrogen-like atom by a fast electron in a homogenous electric field may be essentially different from the similar ones in the absence of this field.

The authors express their gratitude to A.A.Ruhadze for the discussion of the results.

REFERENCES

- [1] V.I.Krylov: *Kratkie Soob. Fiz. of the Lebedev Physics Institute* 8(1995). 90
- [2] V.I.Krylov: *Kratkie Soob. Fiz. of the Lebedev Physics Institute*. 11, 12 (1991) 61.

Carbon oxidation catalysed by a platinum surface: recombination probabilities and vibro-rotational distribution in CO

M.Cacciatore, E.Christoffersen*, G.D.Billing*

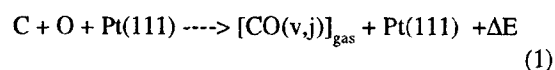
CNR-Centro chimica plasmi, Dipartimento di Chimica, Università di Bari, via Orabona N°4, 70126 Bari, Italy

(*)Chemistry Laboratory III, University of Copenhagen, Copenhagen, Denmark

1. Introduction

In this last few years a great deal of experimental and theoretical work has been done on the dynamics and kinetics of elementary heterogeneous reactions, such as the dissociative chemisorption of simple molecules and the atom recombination on surfaces [1]. These reactions are in fact of fundamental importance in a very broad field of technological applications, from classical catalysis to plasma/wall processes (including CVD, etching, deposition). The kinetics of such processes, in particular the processes due to the interaction of plasmas with solid target, is very complex, but nevertheless very often the rate determining step of the overall reaction scheme is an elementary reaction, such as the dissociative chemisorption of simple molecular species or the production of energetically active diatomic molecules (H_2 , CO, N_2 ,...) formed via atom recombination on the wall. Under operative conditions controlled by gas diffusion [2], gas-surface processes could also play a key role in the reaction kinetics not only in the gas/wall interface, but also in the bulk phase of the reactor. Despite their importance, collisional data, i.e. reaction probability or rate constants, relevant to gas/surface processes are rather sparse.

We have recently undertaken an extensive theoretical investigation on the CO formation catalysed by a platinum surface:



This reaction could be an efficient source of active CO molecules as well as an important loss mechanism of C and O atoms from the gas-phase. In this contribution we report some of the results obtained in our study.

2. Collisional model and Results

We have followed a semiclassical molecular dynamics approach [3] that has been applied for the description of several atom/molecule-surface interaction phenomena. According to this approach the C + O + Pt collision dynamics is described by simultaneously solving the Hamilton equations of motion for the carbon and oxygen atoms together with the time dependent Schrödinger equations for the (vibrational) motion of the surface Pt atoms. In our model a fraction of the energy released in the reaction can be directly transferred to the surface (phonons), while the remaining part, usually the largest one, can be redistributed among the rotational, vibrational and translational motions of the formed CO. In this work we have reexamined the potential energy surface used in previous studies [3] on the basis of the experimental determinations made on the vibrational normal modes of CO adsorbed on Pt(111) [4]. In the calculations we assume that the carbon and the oxygen atom recombines according to the Eley-Rideal mechanism. Therefore, reaction (1) is simulated by assuming the oxygen atom in a specific adsorption site in thermal equilibrium with the Pt surface (the surface temperature is kept constant, $T_s=300K$). The carbon atom hits the surface at different initial kinetic energies with an incident angle $\theta=45^\circ$ from the surface normal. One of the most important aspect of wall reactions is the influence of the geometry of the adsorption site on the catalytic behaviour of the surface. We have therefore explored such effect by placing the oxygen in different surface sites.

Some of the main results obtained in this study are reported in Table 1. Here the probabilities for the different reaction products are reported for three different oxygen adsorption sites and two impact energies, E_{kin} , of the carbon atom. In site $\{\alpha\}$ the oxygen is placed on top of a platinum atom, while the cartesian coordinates (Å) for site $\{\beta\}$ and $\{\gamma\}$ are ($x=-1, y=0, z=3$) and ($x=-2, y=0, z=3$) respectively (the top surface layer is in ($x,y,z=0$) plane).

Table 1a-b.: Reaction probabilities for the process:
$$C + O_{ad} + Pt \rightarrow \text{products}$$

for three different oxygen adsorption sites (see text).

 E_{kin} is the initial kinetic energy of the gas-phase carbon atom. The surface temperature is $T_s=300K$
1a: $E_{kin}=1.0eV$

Products:	(a)*	(b)	(c)	(d)	(e)	(f)
site { α }	0.06	0.39	0.05	0.01	0.49	0.00
site { β }	0.03	0.07	0.01	0.04	0.85	0.00
site { γ }	0.41	0.02	0.22	0.09	0.26	0.02

1b: $E_{kin}=2.0eV$

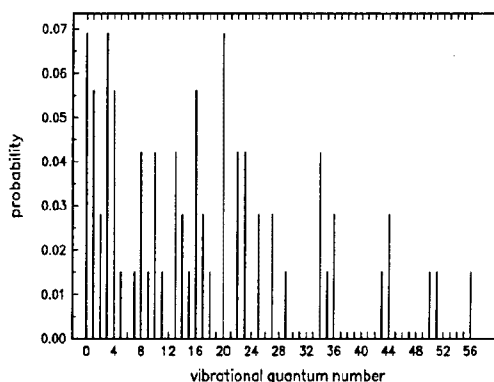
Products:	(a)	(b)	(c)	(d)	(e)	(f)
site { α }	0.08	0.53	0.06	0.05	0.28	0.00
site { β }	0.08	0.06	0.03	0.13	0.69	0.00
site { γ }	0.31	0.14	0.08	0.10	0.36	0.02

(*) (a) COgas; (b): COad; (c) Cad + Ogas; (d) Cgas+Oad (e) Cad + Oad; (f) Cgas + Ogas

From the results we notice that the O_{ad} site has a huge impact on the reaction probabilities, while the influence of the initial kinetic energy is small. The probability for CO formation when the sites { α } and { γ } are occupied is quite high, but nevertheless the two sites exhibit substantially different behaviours (the on top site is the most favourable site for CO chemisorption). In fact, the CO molecule remains bounded on the surface when Oad is adsorbed at the on top site, while in the { γ } site CO, initially formed on the surface, desorbs in the gas phase. It is worthwhile noticing that channel (e), i.e. the process $C + O_{ad} \rightarrow Cad + O_{ad}$ is a very effective one, while the probability for both the carbon and oxygen atom to be reflected in the gas-phase is negligible for all the conditions explored in the simulation.

A further important aspect of the recombination reaction (a) is the energy partitioning among the internal states of the desorbing CO molecules. The available energy for translational and internal energy excitation of CO is given by: $\Delta E_{exc} = D - E_b - \Delta E_{ph}$, where D is the CO dissociation energy at the surface, E_b is the binding energy of the adsorbed Oxygen, ΔE_{ph} is the energy loss to the wall. Under conditions of weak dynamical coupling with the surface phonons, and for weakly bounded surface states, a considerable

amount of energy can be available for CO excitation. Figure 1 shows a typical vibrational distribution of COgas in the final states.

Fig.1 Vibrational distribution for the reaction:
$$C + O_{ad} \rightarrow [CO(v,j)]_{gas}$$
 O_{ad} in on the { γ } site, $E_{kin}=1.0eV$


From Fig.1 we notice that the CO molecules desorb with a vibrational distribution in non thermal equilibrium. The results obtained in this work show that atom recombination on a Pt(111) surface can be regarded as an efficient collisional mechanism for the production of highly vibrationally excited CO molecules (in contrast with the electron-molecule collisions where the pumping up of vibrational quanta starts from the low-lying vibrational levels through a step-wise excitation mechanism). In addition to that, recombination processes on a clean Pt wall can be an efficient channel for the carbon and oxygen atom removal from the gas phase, under the collisional conditions considered in this work

3. References

- [1] Chem.Phys. Special issue vol. 205(1996), R.M.Hochstrasser and G.L.Hofacker eds
- [2] M.Boudard *Kinetics of Chemical Processes*, Prentice Hall (1968); G.Gordiets, M.C.Ferreira, J.Nahorny, D.Pagnon, M.Touzeau and M.Vialle J.Phys.D29(1996)1021
- [3] M.Cacciatore and G.D.Billing Surface Sci. 232(1990)35; M.Cacciatore and G.D.Billing, Pure and Appl.Chem. 68(1996)1075; G.D.Billing and M.Cacciatore Chem.Phys.Lett 113 (1985) 23
- [4] A.M.Lahee, J.P.Toennies and Ch.Wöll Surface Sci. 177(1986)371

Topic 3

Low pressure glows.

ELECTRON AND ION MOBILITIES IN SHOCK-HEATED PLASMA

A. Abbas and Tawhida S. Basha

Physics Department, Faculty of Science, Assiut University, Egypt

Abstract. A new experimental technique is reported in which the mobility of electrons in a hot argon plasma was measured in an electric shock tube. The ion mobility was deduced from the electron mobility. The result obtained for the electron mobility is in good agreement with theory for voltage gradient less than 10^3 Vm^{-1} . Although, the results of the ion mobility are not as good as expected with theory, however, it is in close agreement with other reported data.

1. Introduction

A high velocity plasma, produced in an electric shock tube [1] is allowed to flow between filament metal electrodes and to interact with an external transverse magnetic field. The open-circuit voltage and the current flowing between these electrodes allowed the mobility of electrons to be measured and ion mobility to be deduced, as a function of gas temperature, where thermal equilibrium is assumed.

The main utility of this paper lies in the fact that it permits mobilities by a new method to be obtained for effective gas temperature suitable for MHD power generators [2], in hot gases such as fusion energy [3] and perhaps elsewhere as well.

2. Theory

The electron mobility μ_e is given by

$$\mu_e = \omega_e \tau_e / B_z = \left(\frac{\pi}{8k m_e} \right)^{1/2} \cdot \frac{e}{T_e^{3/2}} \cdot \frac{1}{\sum_j n_j Q_j} \quad (1)$$

where ω_e is the electron cyclotron frequency, τ_e is the mean collision time for electrons, B_z is the applied magnetic flux density, T_e is the electron temperature n_j is the number density of the j th particle species and Q_j is the velocity averaged cross-sections of the j th particle species. For highly-ionized plasma in thermal equilibrium, it can be shown that for argon, the ratio of the ion mobility to electron mobility is given by [4],

$$\mu_i \approx [\mu_e / 270] \quad (2)$$

3. Experimental Work

The glass shock tube, Fig. (1), is of circular cross-section with a 5-cm diameter. The magnetic field was provided by an iron-core Oxford electromagnet that was capable to produce magnetic flux densities between 0.06 and 0.91 Tesla, uniformly distributed over a circular area of 5-cm diameter. The basic pressure was varied between 14 and 140 Pa. The energy input to the driving section was in the range from 112.5 to 1012.5 J, which produced shock Mach number in the range from 3 to 20. The measurements were made by measuring the open-circuit MHD voltage of the shock-

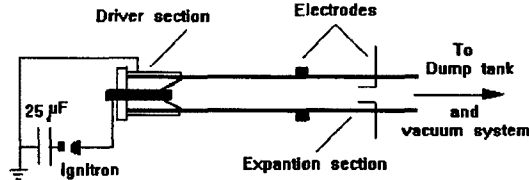


Fig.(1). The electrode assembly and shock tube.

heated gas, induced between tungsten electrodes, carefully machined, so that their faces were flush with the inner wall of the tube. The measurements were continued by measuring the current flow between two parallel filament electrodes for voltages electromagnetically induced between these filaments. The filaments were loaded by carbon-film resistors, in the resistance range 0.5 to 500 Ω .

4. Results and Discussion

The variation of the open-circuit MHD voltage versus the applied magnetic flux density, is shown in Fig. (2).

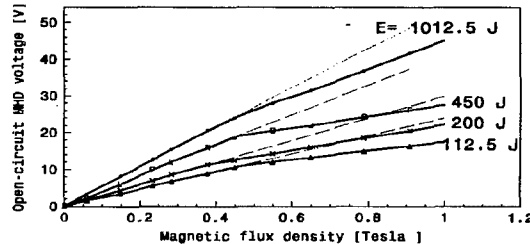


Fig.(2). Open-circuit MHD voltage for shock-heated argon plasma, with different input energy.

Normally, for uniform plasma properties, the induced e.m.f. generated within the plasma is given by

$$V_{o.c.} = v_s B_z d \quad (3)$$

where $V_{o.c.}$ is the induced open-circuit MHD voltage, v_s is the flow velocity and d is the electrodes separation. However, owing to the existence of a viscous boundary layer at the wall of the shock tube, it can be shown that [5],

$$v_s B_z d / V_{o.c.} = (1 + \xi) + \xi \omega_e^2 \tau_e^2 B_z^2 \quad (4)$$

$$\text{where } \xi = \frac{4 a Y}{\pi Z \left(\frac{1}{\delta} - 1 \right)} \frac{\sigma_M}{\sigma} = \text{const.}$$

Y and z represent the the effective length of the conducting plasma and the radial dimension which determine the conducting area respectively, a is a constant equals to $1 + \frac{\delta \sigma^*}{Y \sigma_{bl}} = \text{const.} = a$, δ is the

displacement thickness of the boundary layer, σ_{bl} is its average conductivity perpendicular to B_z , and σ^* is the free-stream electrical conductivity. A plot of $v_s B_z d / V_{0,c}$ against B_z^2 should yield a straight line with a slope of $\xi \omega_e^2 \tau_e^2$ and an intercept of $(1 + \xi)$. The result of a sample at a measuring station of 38 cm. from the ring electrode, for different electron temperature, is shown in Fig.(3). Using the statistical technique of the least

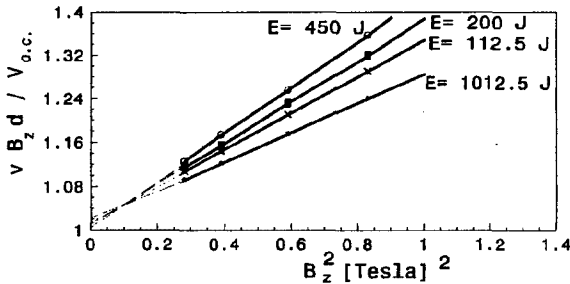


Fig.(3). $v_s B_z d / V_{0,c}$ vs B_z^2 , at different input energy.

square method, the slopes and the intercepts have allowed us to estimate μ_e with electron temperature T_e , on the assumption that thermodynamic equilibrium has been reached in the free stream. Table (I) shows the experimental results of μ_e with temperature, reduced to the standard gas number density $2.69 \times 10^{25} \text{ m}^{-3}$ according to the hydrodynamic shock relations [6] across the shock front, together with the theoretical values of μ_e according to equation (1), where Normand's [7] cross-section measurements for Q_i has been used. Also, Table(I) shows the electron mobility using the data of Nielsen [8] and Kirshner *et al* [9].

Table(I). Electron mobility in argon reduced to the standard gas number density, $2.69 \times 10^{25} \text{ atoms m}^{-3}$. For $E < 10^3 \text{ Vm}^{-1}$, μ_i is in unit of $[\text{m}^2 \text{ V}^{-1} \text{ s}^{-1}]$

T_e (°K)	μ_e present experiment	μ_e Theory Ref.[7]	μ_e Refs.[8]& [9]
1000	0.68	0.78	0.022
1450	0.64	0.68	0.019
2000	0.62	0.62	0.0166
2650	0.63	0.59	0.0141
3300	0.57	0.38	0.0126
3700	0.59	0.57	0.0119
3850	0.54	0.56	0.0116
4870	0.56	0.55	0.0091
6200	0.51	0.54	0.0089
7500	0.52	0.52	0.0077
9000	0.47	0.49	0.0074

Table(I) shows that the electron mobility, in the present experiment, is in good agreement with the theoretical data using Normand's electron-atom collision cross-section and electron-ion long range interaction.

According to equation (2), the ion mobility of positive ions A^+ , in their own gas, is shown in Table (II).

Table(II). Ion mobility in argon reduced to the standard gas number density, $2.69 \times 10^{25} \text{ m}^{-3}$. For $E < 10^3 \text{ Vm}^{-1}$, μ_i is in unit of $[10^{-3} \text{ m}^2 \text{ V}^{-1} \text{ s}^{-1}]$.

T (°K)	μ_i Present Experiment	μ_i Theory Ref.[10]	μ_i Mason <i>et al</i> Refs.[11]	μ_i Dalgarno Ref.[12]
1000	2.53	0.072	0.318	0.095
1450	2.37	0.059	0.328	0.081
2000	2.3	0.051	0.332	0.070
2650	2.33	0.044	0.327	0.063
3300	2.11	0.039	0.322	0.056
3700	2.19	0.037	0.320	0.054
3850	2.00	0.036	0.319	0.053
4870	2.26	0.032	0.304	0.044
6200	1.89	0.029	0.300	0.042
7500	1.93	0.026	0.290	0.038
9000	1.74	0.024	0.287	0.036

The ion mobility, in the present experiment, is higher by a factor in the range from 6 to 8 in comparison with Mason *et al* data. This result is in close agreement with Mason data, taking into consideration that we deduced the ion mobility for highly-ionized plasma, where ion-neutral interaction is ignored, while Mason experiment was carried out in zero-field and only elastic collisions between ions and neutrals were considered.

The research for determination the electron mobility is carrying out on other gases such as H_2 , He, Ne,.....etc., using the present experimental technique.

References

- (1) T.S. Basha: Acta Physica Slov., **43** (1993) 271.
- (2) M.E. Taalat: Pro. 25th intersociety Energy conversion, Eng. Conf., Reno, NV, USA, **2** (1990) p.462
- (3) S. K. Guharay: ICTP Spring College on Fusion Energy, Trieste (1981) 281.
- (4) M. Sakuntala, Von Engel, and R.G. Fowler: Phys. Rev., **118** (1960) 1459.
- (5) T.S. Basha: Ph.D. Thesis, Assiut Univ., (1989).
- (6) A. Abbas, and T.S. Basha: Bull. Fac. Sci., Riyadh Univ., Saudi Arabia, **5** (1973) 129.
- (7) C.E. Normand: Phys. Rev., **35** (1930) 1217.
- (8) R.A. Nielsen: Phys. Rev., **50** (1936) 950.
- (9) J.M. Kirshner, and D.S. Tofollo: J. Appl. Phys., **23** (1952) 594.
- (10) K.T. Compton, and I. Langmuir: Rev. Mod. Phys., **2** (1930) 218.
- (11) E.A. Mason, L.A. Viehland, H.W. Ellis, D.R. James, and E.W. McDaniel: Phys. Fluids, **18** (1975) 1070.
- (12) A. Dalgarno: Phil. Trans., Series 250 A (1958) 426.

ROTATION OF A D.C. DISCHARGE PLASMA

A. Abbas, Tawhida S. Basha, and A.S. Abdel-Maksoud
Physics Department, Faculty of Science, Assiut University, Egypt

Abstract. The behaviour of the rotation of a glow discharge plasma has been investigated experimentally in argon in magnetic flux density from 0.22 to 0.64 Tesla. The radial distributions of the electric field, the electric potential and electron density have been obtained. The results of the energy stored in rotation show that the effective dielectric constant is in good agreement with theory at relatively high magnetic flux density. The drift velocity obtained from the energy stored measurements, is in good agreement with theory based on ion free motion rather than the boundary effects in viscous rotating plasma.

1. Introduction

There is a considerable interest in rotating plasmas [1-3], since the resultant particle drift stores electrical energy and this indicate that the plasma behaves like a capacitor with relatively high effective dielectric constant. Rotating plasma have many advantages such as impurities can be centrifuged as reported by Bonnevier[4]. Hydrogen pellet-rotating plasma interaction was currently carried out by Jorgensen and Sillesen [5], with fusion reactor refueling in mind. Rotating plasma with a d.c. discharge [6-7] needs more attention. There is no sufficient information in the literature on the field, ion-density distributions and variation of dielectric constant with magnetic fields. In this paper, measurements on these behaviours, in a rotating d.c. glow discharge, are reported.

2. Experimental Measurements

The homopolar device, used in this experiment, is as described elsewhere [8]. It consists of two coaxial copper electrodes of cylindrical geometry as shown in Fig. (1). The diameters of the inner and outer electrodes are 2.05 and 12 cm. respectively, the axial length is 3.5 cm. and the radial interelectrodes spacing is 4.2 cm.

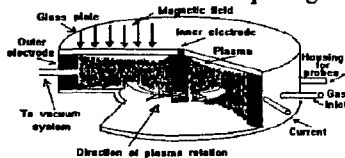


Fig. (1). The schematic diagram of the homopolar device.

The theoretical capacitance of the vessel is, therefore, 1.1pF. The discharge vessel was placed in an axial magnetic field which was varied between 0.22 and 0.64 Tesla. The distribution of the magnetic flux density, within the vessel, was such that, in the equatorial plane, the magnetic field has its maximum value B_0 at the inner electrode and then decreases to $0.975 B_0$ at the outer electrode. The discharge was powered by a 1.2 kV stabilized d.c. supply, and the outer electrode was chosen as the cathode to maintain the glow discharge in the normal mode, while the discharge current was kept constant at 50 mA. The measurements were made with high-purity argon, in the pressure range from 10 to 100

Pa. The polarity of the applied magnetic field was reversed and the average of at least three readings was taken as the experimental point. The electric field distribution in the rotation mode was obtained by measuring the potential difference between double floating cylindrical tungsten probes, of 0.038cm. diameter, insulated by thin glass tube except their tips and separated by 0.5cm. The axes of the probes were made parallel to the circumference of the equipotential surfaces. By moving the double probes radially, the variation of the electric field was detected. The radial electric potential was measured directly between a single probe and the outer earthed electrode.

The radial distribution of the ion density was measured by the known technique of the floating double probe, with their axes were made perpendicular to the direction of the rotation. The probe response was recorded on an X-Y recorder. At low pressure (less than 10Pa) and high magnetic field, a very sharp increase in the probe current was observed. This was attributed to the contract of the discharge; the measurements in the contracted mode was excluded.

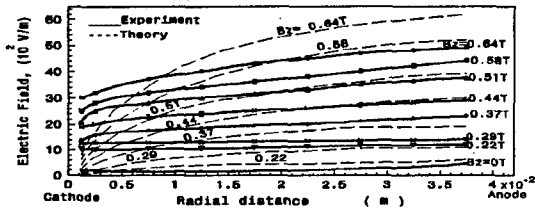
By applying a direct short circuit to the terminals of the vessel, the effective dielectric constant of the rotating plasma can be detected accurately from the voltage measured across the plasma and the charge drawn out during the first quarter cycle of the resulting "Crowbar" transient. The average drift velocity can then be derived from the kinetic drift energy stored in the rotation.

3. Results and Discussion

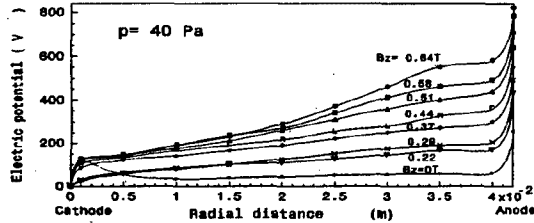
The radial distributions of the electric field and the electric potential are shown in Figs.(2) and (3). The electric field in Fig(2) is estimated theoretically, (dashed curves), using the relation [9],

$$|E_r| = |\eta j_r - v_\theta \cdot B_z| \quad (1)$$

where η is the plasma resistivity, j_r is the radial current density, v_θ is the azimuthal drift velocity and B_z is the axial magnetic flux density. Although, uniform electron density is not assumed, the resistivity is taken to be uniform through the flow. It can be seen that good agreement between the experiment and the theory is obtained within the considered approximation.



Fig(2). The experimental and theoretical radial distributions of the electric field, at a pressure of 100 Pa, and different B_z .



Fig(3). The radial distribution of the electric potential at a pressure of 40 Pa, and different values of the magnetic field.

The radial ion density distribution, in the rotation mode, is shown in Fig. (4). It is interesting to note that

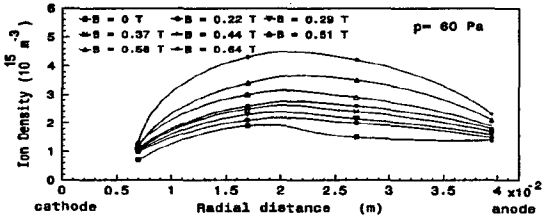


Fig. (4). The radial ion density distribution, at $p = 60$ Pa.

the charged particles redistributed themselves, in the vicinity of the homopolar electrodes, and they accumulate towards the positive electrode. This is because, the region filled with plasma can act very effectively as a virtual anode [9], cable of emitting the necessary ion current; with increasing the ion densities and a decrease in the electron temperature as a result of increasing the electron-atom collision frequency. Stored energy measurements were done by using a low-inductance "Crowbar" circuit as given elsewhere [10]. The energy stored may be estimated according to the following relation,

$$W_e = \frac{1}{2} C_M V_o^2, \text{ where } C_M = \frac{i_o^2}{\omega i_o V_o}, \therefore W_e = \frac{i_o^2 V_o}{2 \omega i_o} \quad (2)$$

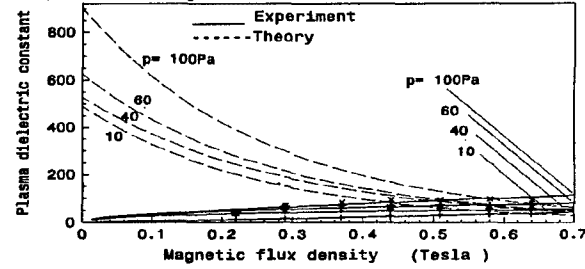
where C_M is the effecting capacitance of the discharge vessel, V_o is the voltage measured across the plasma at the instant of the short circuit, i_o and i_o' are the peak values of the current at the first quarter cycle and at the first three-quarter cycle respectively, and ω is the damped angular frequency.

The plasma dielectric constant K_{exp} measured experimentally may be estimated from the formula,

$$K_{exp} = \frac{9.1 \times 10^{11} i_o^2}{\omega i_o V_o} \quad (3)$$

Fig (5) shows K_{exp} in the rotation mode together with the theoretical values K_{theor} of the rotating plasma, of mass density $\rho = n_i M$, where n_i is the average density,

$$K_{theor} = 1 + \frac{36 \pi \times 10^9 \rho}{B_z^2} \quad (4)$$



Fig(5). Variation of the experimental and the theoretical plasma dielectric constant at different values of pressure.

At higher values of the applied magnetic fields, Fig.(5) shows good agreement between the experimental and the theoretical plasma dielectric constant, where fringing is completely neglected. At low magnetic fields, the measured ion density, enters equation (4), exceeds the number ion density in the rotation region, also, ion leakage should be considered. The kinetic drift energy stored, in ordered rotation of the plasma, may be regained if losses are neglected, as

$$W_e = \pi l \int_0^r n_i M v_o^2 r dr = N_i \frac{M v_o^2}{2} \quad (5)$$

Equations (2) and (5), give the average drift velocity of the rotating plasma as shown in Fig.(6). These results were compared with theory; first the theory of ion drift: $v_o = E \times B / B^2$, where E_r is obtained from the measured electric field in the positive column. The result is shown as dashed curves, the second theory is the viscous flow theory [9], for the drift velocity.

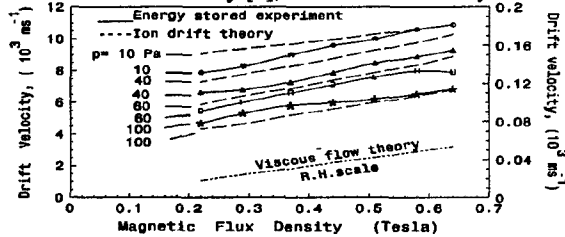


Fig.(6). The drift velocity vs the magnetic field; the scale of the theory of the viscous flow is on R.H. side.

$$v_o = \frac{J_r(r_2) B_z r_2}{4 \mu r} \left[r^2 \ln \left(\frac{r_2}{r} \right) - r_1^2 \left(1 - \left(\frac{r}{r_2} \right)^2 \right) \right] \quad (6)$$

where μ is the viscosity of the conducting fluid; its value is taken from data given in [11]. We can see that the experimental drift velocity obtained from the energy stored is in good agreement with the ion drift theory.

References

- [1] L.W. Jorgensen, and A.H. Sillesen, Plasma Phys., 21 (1978) 345.
- [2] G.D. Abardzhaniya, Physica Scripta, 38 (1988) 59.
- [3] B. Lehnert, Nucl. Fusion, 11 (1971) 485.
- [4] B. Bonnevier, Plasma Phys., 13 (1971) 763.
- [5] L.W. Jorgensen and A.H. Sillesen, Plasma Phys., 22 (1980) 771.
- [6] S.A. Diamond and D.L. Turcotte, Phys. Fluids, 14 (1971) 928.
- [7] A. Abbas, IL Nuovo Cimento, 54B (1979) 197.
- [8] T.S. Basha, and A. Abbas, J. Physical Society of Japan, 62 (1993) 4255.
- [9] W. B. Kunkel, R. Baker, A. Bratenahi, and K. Halbach, Phys. Fluids, 6 (1963) 699.
- [10] A.S.M. Abdel-Maksoud, M.Sc. Thesis, Phys. Dept., Assiut Univ., Egypt (1991).
- [11] S. Chapman and T.G. Cowling, "The Mathematical Theory of Non-uniform Gases", Cambridge Univ. Press, 2nd Ed. (1960) Chap. 12.

Investigation of the discharge formative time in Ne at 4 mbar pressure

T. Jovanović, M. Radović*, O. Stepanović* and Č. Maluckov*

Fac. of Medicine, Inst. of Physics, Univ. of Niš, PF 174, 18001 Niš, Yugoslavia

*Department of Physics, Faculty of Philosophy, Univ. of Niš, PF 91, 18001 Niš, Yugoslavia

1. Introduction

According to Kiselev [1] the discharge formative time is in opposition with the pressure. For the low pressure it could have a significant value [2]. The characteristics of electrical breakdown in diodes with changeable gap (interelectrode distance) d are investigated in papers [3, 4]. The results of measurement of the electrical breakdown formative time in Ne at 4 mbar pressure for the gap from 0.1 to 19 mm are presented in this paper, especially the effect of discharge displacing from the gap, for extremely small gaps, was investigated. In Fig. 1 this situation is schematically presented. The zone of negative light is indicated in case when it is in the gap A: and in the case when it is displaced from it B:.. The typical gap is indicated in Fig. 1.

In this experiment, when the volume of the tube is much larger than the interelectrode volume, there is no possibility of finding a system on the left side of the Paschen minimum. In present geometry, there is always possibility of existing the pd -min (but somewhere out of the gap). The forming of this kind of discharge is somewhat difficult as it is shown in this paper.

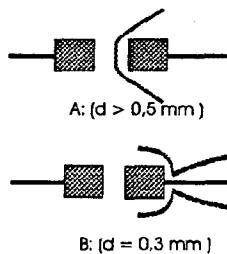


Fig. 1. The position of the negative light being in (A) or out of the gap (B).

By increasing the gap, the glow is coming back to interelectrode space and further increase of the gap is followed by the increase of the mean value of the total electrical breakdown time delay (t_d) and the formative time (t_f). That is the case up to pd values of 6 mbar cm

and then, for the further increase of the gap, the formative time began to decrease due to the greater possibility of some other processes (as it could be the resonant transfer of the excited energy through the interelectrode space or increasing the yield of the fotoelectrons created).

2. Experiment

The discharge is formed between the two Cu cylindrical electrodes facing each other by their basis which diameter is 1 cm. The facing sides of the electrodes have the Au electrolytically coated surfaces. The gap could be externally changed from zero to 20 mm. For each gap the value breakdown voltage and the time delay were measured. As with the statistical behavior, the time delay were determined as the mean values of the 200 independent measurements at the same conditions. From this, the critical electrical field in the gap as U/d was estimated and the formative time as the difference between the total time delay and his standard deviation (this is due to the statistical theory of the electrical breakdown [5]).

Personal computer (PC 486) with the custom made interface was used for controlling the basic parameters of the experiment, for acquisition of the data and their analyses. The principle scheme and measurement is the same as in [6]. The current flow time ($t_g = 1$ s), as well as the gas relaxation time between the two consequent measurements ($\tau = 2$ s) were kept constant, so as to make the initial concentration of the discharge carries constant during the measurements.

3. Results and discussion

The measured values of the breakdown voltage versus the gap are shown in Fig. 2, where the quasi Paschen minimum on the gap of about 2 mm can be seen. The values of the critical electric field in the gap are presented the same figure, and the strong decreasing on the left and the quasi-constant field on the right side from the U_p -minimum value is evident. For the gap d which corresponds to this minimum (0.1-4 mm), there are no

significant changes of the total time delay or the formative time. Further increasing of the gap, i.e. from 4 mm up to 15 mm, is followed by the increasing of the total breakdown time delay (see Fig. 3.). But for the values $d > 14$ mm, ($pd > 6$ mbar cm) there is a significant decreasing of the total time delay.

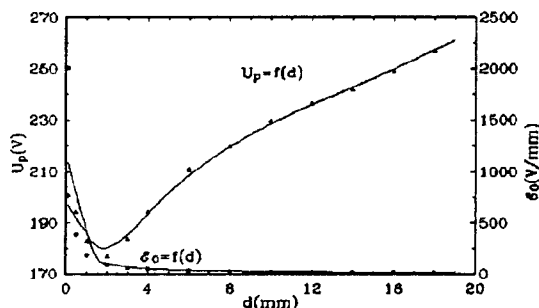


Fig. 2. Breakdown voltage U_p and the critical field ϵ_0 in function of gap in Ne at 4 mbar.

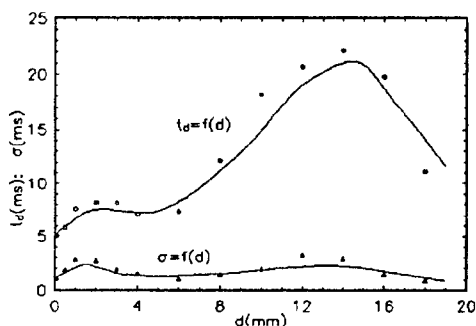


Fig. 3. The total discharge time delay and its standard deviation as the function of the gap.

The calculated values of the formative time and the mean formative velocity are presented in Fig. 4. It is obvious that the formative time is the dominant part in the total time delay in Ne for the present conditions. This dependence on the gap shows the expected increasing for the pd values up to 6 mbar cm and the significant decreasing for the bigger values, which is not a characteristic for the low pressure discharge forming. We assumed that the reason for this may be in the greater efficiency of the first electron avalanche and/or the

transport of the resonant energy via the photons in the gas and/or the increasing of the number of photons with enough energy for releasing the electrons reaching the cathode. All mentioned processes are efficient for the intermediate and high pressures.

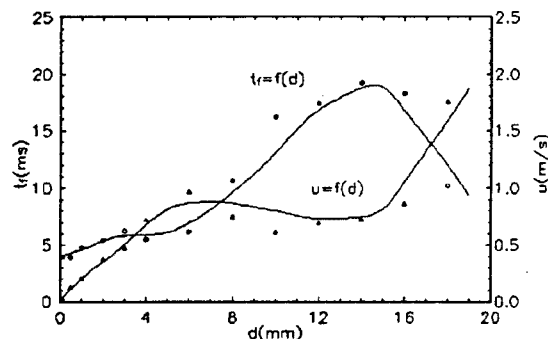


Fig. 4. Formative time and the mean formative velocity depending on the gap in Ne on 4 mbar.

Further investigations of this kind have to be done to show which of mentioned mechanisms is dominant under these circumstances.

Acknowledgments

The authors would like to thank the Ministry of Science and Technology of the Republic of Serbia which contributed significantly to the realization of this investigation by a financial support.

References

- [1] Y.V. Kiselev, 7th Int. Conf. On Phen. In Ionized Gases, Beograd (1965) 838-43.
- [2] M.K. Radović and Dj.A. Bošan, J. Phys. D: Appl. Phys. 20 (1987) 639-41.
- [3] Y. Shibuya, 3rd Int. Conf. On Gas Discharges, (1974) 132.
- [4] M.K. Radović, T.V. Jovanović, Dj.A. Bošan and V.Ž. Zlatić, Contributed papers of 18th Yug. Summer school and Int. Symp. on Phys. Of Ionized Gases, (1996) 391-3
- [5] J.M. Meek and J.D. Craggs, "Electrical Breakdown of Gases", John Wiley and Sons, Chichester, New York, Toronto, 1978.
- [6] Dj.A. Bošan and T.V. Jovanović, J. Phys. D: Appl. Phys. 25 (1992) 436-41.

The behaviour of the breakdown time delay distribution in Ne at 4 mbar

M.Radović, T.Jovanović*, Č.Maluckov and O.Stepanović

Department of Physics, Fac. of Philosophy, Univ. of Niš, PF 91, 18001 Niš, Yugoslavia

*Fac. of Medicine, Inst. of Physics, Univ. of Niš, PF 174, 18001 Niš, Yugoslavia

1. Introduction

As the result of the statistical behaviour of including microprocesses, the electrical breakdown is of a stochastic nature itself. One of the important characteristics of the electrical breakdown is the time delay t_d , which consists of two contributions, statistical time delay t_s and the formative time t_f . Being of the statistical nature, the measured values of time delay occurred with the characteristic distribution, which, as shown by von Laue [1], may be written as:

$$\ln(N/n) = -(t_d - t_f) / \langle t_s \rangle$$

where n is a number of the t_d longer than the actual time, N is a total number of measured values, and the $\langle t_s \rangle$ is a mean value of the statistical time delay.

This distribution is the subject of interest in many papers [2]. In most of reports, the single discharge mechanism had resulted in to characteristic quasi Poisson distribution. In some cases, the complex distribution may occurred as presented in [3].

The specific distributions of the electrical breakdown time delay values in Ne at 4 mbar pressure as the function of the gap are presented in this paper. The shapes of the established distributions are somewhat unexpected, but under these circumstances they indicate the complex nature of the discharge formation mechanism.

2. Experiment

The measurements of the time delay were performed with the Ne filled diode at the pressure of 4 mbar and 300 K temperature. The volume of the diode tube is about 300 cm³ and the cylindrical electrodes have the Au electroplated coated surfaces. Gap was externally changed from zero to 19 mm. The personal computer (PC 486) with the custom made interface was used for controlling the basic parameters of the experiment (as the time of discharge glow and the relaxation time of the diode between the two successive breakdowns), for acquisition of the data and for their analyses.

The electrical details of the circuit and the experiment procedure were described earlier [4]. The applied

overvoltage was 5% and the distributions were established on the basis of the 1000 independent and successive measurements under the other experimental conditions being constant.

3. Results and discussion

The established time delay distributions are presented in Figs. 1 and 2 as the histograms with the bar width of 0.5 ms. The actual gaps are indicated in figures. The shape of distribution indicates that there is not only the movement of the distribution towards the greater values of the time present but also is a change that distribution.

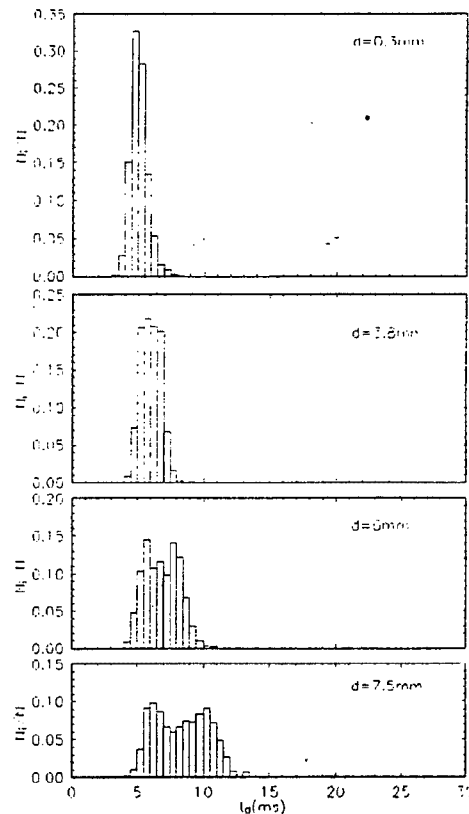


Fig.1. Time delay values distributions for the gap indicated on the pictures.

We assumed that this can be understood only as two different breakdown macroscopic channels with the possibility of the same order of magnitude. The channel 1 being actual for the small gap is losing his possibility with increasing the gap and the channel 2 which becomes more and more of interest with that increasing. The both channels characterized the movement of the pic toward the greater t_d with the gap increasing and that indicates that the transport phenomena like movement of the positive ion throughout the gap with the strong diffusion towards the walls are included.

From the first pic movement for the d values from 4 to 10 mm, and the elapsed time delay (and the formative time) which is about 1 ms an can be calculated the ambipolar diffusion coefficient or the ion mobility. Under the presumption that the ambipolar diffusion is an actual processes, the values of the D_a coefficient of $180 \text{ cm}^2\text{s}^{-1}$ are calculated. That value is in relatively good agreement with the actual reference data. However according to the applied electrical field of about 300 V/cm in the gap, the positive ion mobility can be calculated and the $2 \text{ cm}^2 \text{ V}^{-1}\text{s}^{-1}$ value is obtained. That value can not be accepted as the real one, so the mobility of the positive Ne ions directly throughout the gap is not the valid presumption.

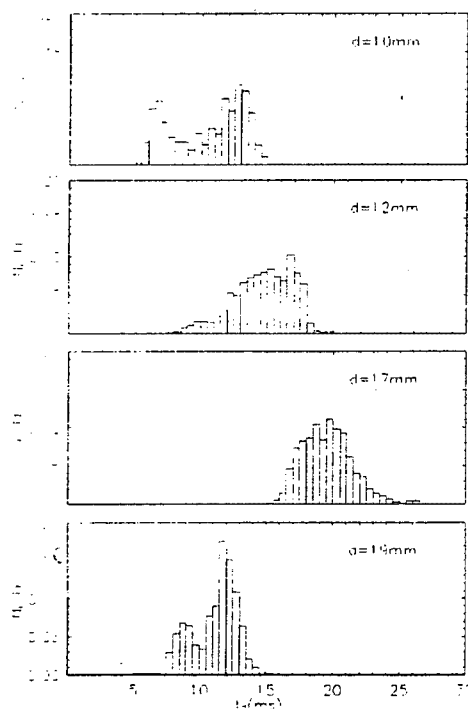


Fig.2. The time delay value distribution for the gap indicating in figure.

Further data analysis can be made using the Laue-grams. One of them, for the gap of 10 mm is shown in Fig.3. From the Laue-gram, it can be seen that the mean value of t_d (having the $\ln(n/N)$ values of -1) for the both macroscopic breakdown channels is 12 ms, with the great difference in the formative time which is, for the faster (first) channel about 5 ms and for the slower one about 11.5 ms. One can assume that, for the present diode geometry and the overvoltage applied, the more than one avalanche is needed for the discharge formatting.

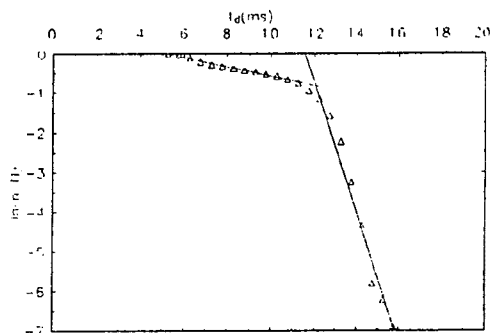


Fig.3. Laue-grams for the time delay data values for the gap length $d=10 \text{ mm}$ in Ne at 4 mbar.

For $d > 17 \text{ mm}$, t_d decreases and it is presented as distributions in Fig. 2 ($d = 19 \text{ mm}$).

Acknowledgments

The authors would like to thank the Ministry of Science and Technology of the Republic of Serbia which contributed significantly to the realization of this investigation by a financial support.

References

- [1] M. von Laue, Ann. der Physik 9 (1925) 721-32.
- [2] H.Tagashira and S.Sakamoto, J. Phys. D: Appl. Phys, 2 2 (1969) 1193.
- L.Nastase, 12th Int. Conf. on Phen. in Ionized Gases, (1976) 93.
- M.Radović and Dj.Bošan, J. Phys. D: Appl. Phys,20 (1987) 639-41.
- M Pejović et al., J. Phys. D: Appl.Phys 24 (1991) 779-81.
- [3] J.M.Meek and J.D.Crages,"Electrical Breakdown of Gases", John Wiley and Sons, Chichester (1978).
- [4] Dj. Bošan and T.Jovanović, J.Phys D: Appl. Phys, 25 (1992) 436-41.

Topic 4

**Corona, sparks, surface discharges
and high pressure glows.**

SUPER-HIGH SPEED IONIZING WAVES IN LONG SHIELDED TUBES

O. A. Sinkevich and D.N. Gerasimov

Moscow Power Engineering Institute, Heat Phys. Dept.,
Krasnokazarmennaja, 14, Moscow, 111250, Russia, fax (095)3611620

Last decade the propagation of ionizing waves - or some times called electrical breakdown waves - of super-high velocities (with velocities up 1/3 of the light velocity) in shielded tubes are intensively investigating [1,2,3,4,5] both experimentally and theoretically. These waves are carrying electrical potential from the high voltage electrode to the grounded electrode and are effectively ionizing gas. These experiments are closely connected with laboratory modeling of streamer propagation and return stroke in the lightning or the long spark and give the base for several new technologies. There were investigated both cathode and anode - directed waves, waves in long shielded cylinder with circular cross-section and in conical tubes. It was found dependence of the ionizing wave velocity from an applied electrical potential of the high voltages electrode, pressure of gas, and electrical capacitance per the unit of length of the discharge tube. The mechanism of wave propagation is closely connected with ionization processes inside the narrow structure of the wave front where the electrical field has the typical sliton shape [3,4,5]. The several models of ionizing wave including processes of electron drifts and diffusion, of electron runaway, gas photoionization are discussed and compared with experiments (see, for example, the review [1] and [5]). Some attempts were made to find the well known for gas discharges similarity for the wave velocity from the radius of the discharges tube and gas pressure product [2].

The main goal of our investigation is to find quite simple formulas for the most advantage variables of the ionizing wave (the distributions of concentration of electrons and the electric potential along the ionizing wave, and the velocity of ionizing wave) which could reproduce the typical experimental dependence of these variables from parameters of installation. Now we are generalizing our early results [3] taking in a count several new phenomena in such waves and on the theoretical model of supper-high velocity ionizing waves. For investigation of super - high velocity wave propagation the numerical code was developed. Our numerical model is based on the continuity equation for electron (n_e) and on the proposed earlier in our work [3] non-linear equations describing evolution of the electrical potential (φ), using cross-section averaging of the basic equations and equations for processes on the boundaries. Using this numerical model it is possible to investigate evolution of waves and to trace dependence of the propagation speed from main parameters: voltages, gas pressure, radii of discharge tubes.

Below we are presenting new self-similar analytical solution of our equations, neglecting by electron flux along the wave front in the continuity equation for electrons:

$$\frac{\partial n_e}{\partial t} = n_e V_i(E),$$

$$\frac{\partial \varphi}{\partial t} = \frac{\partial}{\partial z} \frac{\sigma}{C_l} \frac{\partial \varphi}{\partial z},$$

$$E = -\nabla \varphi.$$

Here

$\varphi(z,t) = \langle \varphi(r,z,t) \rangle$, $n_e(z,t) = \langle n_e(r,z,t) \rangle$ is the electrical potential and the concentration of electrons correspondingly averaged over the tube cross-section, C_l is electrical capacitance per the unit of length of the discharge tube, $\sigma = e \mu_e n_e(E)$ is plasma conductivity. Other values have there well-known meanings.

The self-similar analytical solution the above equations is based on approximation of the frequency of impact ionization

$$V_i(E) = V_i(E_m) = \text{Const, if } E > E_{cr}$$

$$V_i(E) = 0, \quad \text{if } E \leq E_{cr}.$$

where E_m is the maximum of strength of the electric field, E_{cr} is depended from the approximation of the frequency of impact ionization and type of gas.

Using this approximation we had found needed formulas for the distributions of concentration of electrons and the electric potential along the ionizing wave, the velocity of ionizing wave (W) propagating in long shielded cylinder.

$$n_e = n_f \exp\left(-\frac{V_i(E_m)}{W} \xi\right),$$

$$\varphi = \varphi_0 \exp\left[-\frac{W^2 C_l}{e \mu_e v_i(E_m) n_f}\right] \cdot \quad (1)$$

$$\exp\left(\frac{v_i(E_m)}{W} \xi\right),$$

$$W = \sqrt{\frac{C_l}{e \mu_e v_i(E_m) n_i}} \quad (2)$$

Here φ_0 is the applied potential of high voltage electrode, $\xi = z - Wt$ is the self-similar variable. The point where $\xi = 0$ is corresponded the maximum of strength of the electric field inside the wave front structure. It should be marked that our formula for the wave velocity (2) has very simple physical meaning and could be easy used for the wave velocity estimation.

The self-similar analytical solution of our equations helps to investigate influence different parameters - geometrical parameters of discharge tubes, capacity of the shielded tube per unity of length, type of gas, and so on - on propagation of the ionizing wave. Our formula for velocity well reproduce the typical experimental non-monotone dependence of near-light ionizing wave on the gas pressure and dependence from electrical capacity per unity of length of the shielded tube [1]. It is clear seen from comparisons theoretical results with experimental data that the strict similarity for the wave velocity from the radius of the discharges tube and gas pressure product is not exist. Obtained for shielded tubes formula (2) is also in reasonable correlation with results were received in streamer propagation investigations [6] if the related distributed capacitance is used.

For investigating non self-similar regimes of high - velocity ionizing wave propagation our numerical code was used. Investigating non self-similar regimes of super - high velocity wave propagation one could find condition when waves are become self-similar. It is also possible to find the dependence condition of self-similarity ionizing wave propagation from main parameters of an installation. Using this numerical model it is also possible to investigate evolution of non-self-similar waves and to trace dependence of the propagation speed from main parameters: voltages, gas pressure, radii of discharge tubes and so on. Our preliminary estimations show that our new results could be used for high-voltages breakdown wave propagating in free atmosphere and directing by the laser beam [1] when the laser beam preionize air and guide the ionizing wave. The processes on the boundaries of discharge channel are producing free-organized, self-sustained shielded regimes and are forming conditions similar to condition on the boundary of shielded discharge tubes. Certainly, in such free-organized, self-sustained shielded discharge channels the cross-section of channel is varying along

distance of streamer propagation and propagation of breakdown waves reveals a typical three-dimensional phenomenon.

CONCLUSION

New self-similar analytical solution of the cross-section averaged continuity equation for electron and the proposed earlier in our works [3,4] non-linear equation describing evolution for the electrical potential is presented. This self-similar analytical solution is based on approximation of the frequency of impact ionization. Using this self-similar solution for distributions of electron concentration and of electric potential along the ionizing wave the velocity of ionizing wave had found. For investigating non self-similar regimes of high-velocity ionizing wave propagation new numerical code was developed. From computer simulation it had found conditions when the regime of the ionizing wave was become self-similar and one could use above relations. Using our model for high-voltages breakdown wave propagating in free atmosphere when the laser beam preionize air and guide the ionizing wave are discussed.

REFERENCES

- [1] L.M. Vasilyak, S. V. Kostuchenko, N.N. Kudrjavitsev, I.V. Filugin: *Usp. Fis. Nauk*, **165** (1994) 263.
- [2] E.I. Asinovsky, A.N. Lagarkov, V.V. Markovets, I.M. Rutkevich: *Plasma Sources Sci. Technology*, **3** (1994) 556.
- [3] O. A. Sinkevich, Yu.V. Trofimov: *Dokl. Akad. Nauk. (Reports Acad. Sci. USSR)*, **243** (1979) 597.
- [4] O. A. Sinkevich, Yu.V. Trofimov: In book "The Problems of Physic and Technique of Nanosecond Discharges. Nanosecond Generators and Breakdown in Distributed Systems". Inst. High Temp., Acad. Sci. USSR, Moscow, 1982, 55.
- [5] A.N. Lagarkov, I.M. Rutkevich: "Electric Breakdown Waves in a Bounded Plasma", Nauka, Moscow, 1989.
- [6] R.F. Fernsler: *Phys. Fluids*, **27** (1984) 1005.

High Pressure Microhollow Electrode Discharges

K H. Schoenbach, A. El-Habachi, W. Shi, and M. Ciocca

Physical Electronics Research Institute
Old Dominion University, Norfolk, VA 213529

1. Discharge modes

Experimental studies on microhollow cathode discharges [1], gas discharges between a plane anode and a cathode with submillimeter opening of diameter, D , and a submillimeter electrode gap of length, d , have shown that three distinct modes of operation exist [2]. At pressures, p , such that pd is on the left hand side of the Paschen minimum, and at low currents where space charge formation can be neglected, the discharge develops between the anode and the outer face of the cathode. The current-voltage characteristic of this predischage has a positive slope. With increasing current the charge density in the cathode opening becomes large enough to modify the electric field. A virtual anode is formed on axis, and the electrons emitted from the ring shaped cathode are begin to oscillate through this virtual anode. This "pendulum" effect causes a drastic increase in ionization efficiency, and consequently a higher current at lower sustaining voltage. In this mode, the genuine hollow cathode discharge mode, the plasma column expands with increasing current, and consequently the cathode fall width decreases until it becomes so small compared to the hole diameter, that the "pendulum" motion ceases to exist. In this third phase of the discharge at high currents, the discharge behaves like an abnormal glow discharge with a current-voltage characteristic with, as in the predischage mode, positive slope.

Similarity relations for hollow cathode discharges predict the possibility to extend the discharge operation to higher pressures, p , by reducing the hole diameter, D [3]. An upper limit for hollow cathode discharge operation is stated as $pD = 10$ Torr cm [4]. In order to test the validity of this relation and its limit at high pressure for discharges in argon we have reduced the hole diameter from initially 700 μm [1] to 350 μm and 200 μm , respectively, and varied the pressure up to values of 900 Torr, corresponding to a pD -value of 18 Torr cm. Current-voltage curves for discharges between a plane anode and a cathode with a circular opening of $D = 200$ μm , and an anode-cathode distance of $d = 250$ μm are plotted in Fig. 1. The characteristic shape of the I-V curves is in the entire pressure range that expected for hollow cathode discharges. However, as photographs of the discharge, and deviations from the similarity relation [3] at higher pressure indicate, the hollow cathode

discharge begins, at several hundred Torr, to change from a hollow cathode discharge into what we believe is a "pulseless" partial discharge [5].

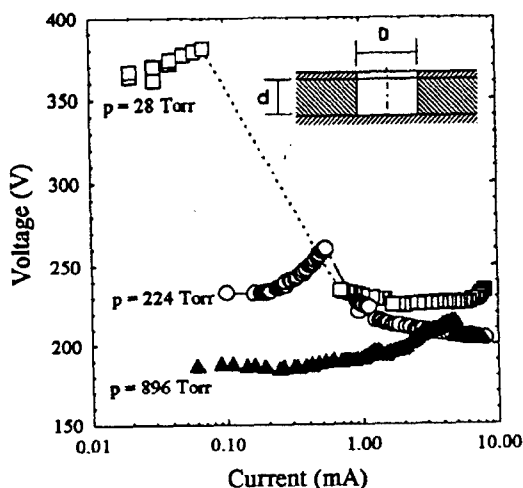


Fig. 1 Current-voltage characteristics of hollow electrode discharges in argon at pressures of 28 Torr, 224 Torr, and 896 Torr. The hollow electrode geometry is shown in the insert.

At low pressure (< 100 Torr) the discharge develops as described in reference [1] and discussed in paragraph one of this paper. At pressures exceeding 100 Torr (which in our experiment corresponds to the pd value at the Paschen minimum) a ring shaped plasma close to the cathode edge is observed in the low current range. With increasing current, the plasma ring disappears and the center plasma fills the cathode hole opening. At high pressure (> 400 Torr) the ring shaped plasma and an intensely radiating plasma column, generally off-axis, inside this ring coexist over the entire current range. The discharge in this pressure range is assumed to be of the "partial discharge" type, a glow discharge which is typical for short gaps [5].

2. Excimer emission

The condition for excimer emission is the presence of high energy electrons in the discharge (nonequilibrium discharge) and, because of the three-body reaction required for excimer formation, the possibility of high pressure operation. High pressure

concentration of high energy electrons [6]. This seems to hold also for high pressure hollow cathode discharges and for partial discharges. Spectral measurements in the wavelength range below 200 nm in both argon (126 nm) and xenon (172 nm) have shown the presence of excimer. The spectrum of hollow electrode discharge in xenon at 760 Torr and a current of 5.75 mA is shown in Fig. 2.

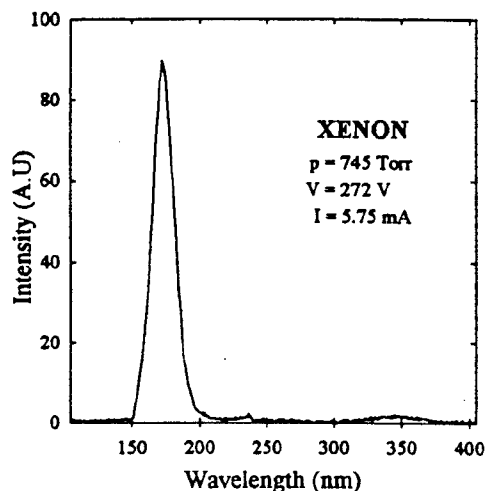


Fig. 2. Spectrum of Xe_2^* excimer

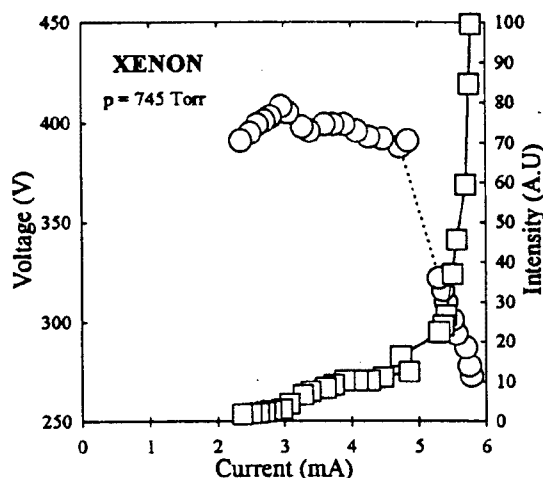


Fig. 3. Discharge voltage and Xe_2^* emission versus discharge current.

The excimer emission is strongly dependent on pressure. The intensity of the xenon excimer emission increases by three orders of magnitude when the pressure is varied between 100 Torr and 760 Torr. The strongest increase is observed in the range at atmospheric pressure where the intensity increases exponentially by one order of magnitude over a 100

mbar range. The strong dependence on pressure is consistent with the pressure dependence of the excimer formation, a three-body reaction.

The excimer emission is also strongly dependent on the current-voltage characteristic of the discharge. This is shown for a Xe discharge at 745 Torr, where the excimer line intensity is plotted in relation to the current-voltage characteristic of the discharge (Fig. 3). The intensity of the excimer radiation increases with current whenever the discharge is in a mode with negative differential resistivity. In ranges with positive slope of the current voltage characteristics the intensity increases only slightly or not at all when the current is increased. This holds not only for discharges in xenon, but also for argon discharges, where the excimer emission is at 126 nm.

3. Conclusion

The reduction of the hole diameter and the gap of microhollow electrode discharge to submillimeter values has allowed us to extend the pressure range of these discharges to atmospheric pressure. At pressures close to atmospheric the discharge seems to change from a hollow cathode discharge to a partial discharge. The fact that the discharges are nonthermal allows their use as direct current excimer lamps. The resistive behavior of these discharges (this holds at least for argon discharges) allows furthermore to arrange these discharges in parallel without individual ballast, and, consequently, to generate large area, unsegmented, direct current flat panel excimer lamps.

4. References

- [1] Karl H. Schoenbach, R. Verhappen, T. Tesson, F.E. Peterkin, and W.W. Byszewski, *Appl. Phys. Lett.* **68**, 13 (1996).
- [2] A. Fiala, L.C. Pitchford, and J.P. Boeuf, XXII ICPIG, Hoboken, NJ, 1995, Contr. Papers 4, p. 191.
- [3] D.J. Sturges and H.J. Oskam, *J. Appl. Phys.* **35**, 2887 (1964).
- [4] J.W. Gewartowski and H.A. Watson, *Principles of Electron Tubes*, D. Van Nostrand Co, Inc, Princeton, NJ, 1965, p. 562.
- [5] R. Bartnikas and J.P. Novak, *IEEE Trans. Electrical Insulation* **27**, 3 (1992).
- [6] Kan-ichi Fujii, *Japanese J. Appl. Phys.* **16**, 1081 (1977).

This work is supported by DOE, Advanced Energy Projects Division.

PHENOMENA IN IONISED GASES SUBJECTED TO IMPULSE VOLTAGES

P. TUŞALIU *

V. TUŞALIU **

M. TUŞALIU **

D. TUŞALIU **

* University of Craiova, Lăpuş Street, no.5, Craiova, Romania, Fax: +40-51-145.763

** National College of Craiova, Romania

Abstract

The prebreakdown phenomena of impulse corona, corona propagation and leader propagation in the standard rod gap in air have been studied for spacings of up to 30cm. The variations occurring in the measured quantities of corona-current amplitude, time of occurrence, corona-propagation time, corona speed, number and length of steps in the leaders, leader-propagation time and leader speed are correlated to the variations in the conditions of gap length, applied voltage, humidity and irradiation. The results of the prebreakdown phenomena have been shown to explain the characteristics of impulse breakdown of the rod gap. The final part of this study contains an adequate numerical programs concerning at Phenomena in ionised gases subjected to impulse voltages.

Keywords: phenomena in ionised gases; corona; radiation effects; impulse testing.

1. INTRODUCTION

The mechanism of breakdown of atmospheric air in nonuniform-field gaps subjected to impulse voltages has been the subject of numerous investigations in the past [1]. The use of still and time-resolved photography has permitted correlation between the variations in time of the physical form of the impulse discharge and the variations in time of the current flowing in the gap to be investigated [1-5]. Three distinct successive phases have thus been identified in the discharge process: they are the corona phase, the leader phase and the main stroke. For a point-point gap, when an impulse voltage of sufficient amplitude is applied to the gap, localised impulse corona appears on both electrodes at approximately the same instant [1]. The anode corona extends much further into the gap than the cathode corona, the size of the positive corona being five to six times larger than the size of the negative corona. [...]

The main objective of the present work was to study the prebreakdown phenomena in rod-rod gaps in air under impulse voltage and at spacings of up to 30cm. It was desired to examine how the prebreakdown phenomena of corona and leader formation were affected by variations in humidity, applied voltage, polarity, irradiation and spacing. To this end, the oscillograms of the applied voltage were supplemented by oscillograms of the current flowing in the gap before breakdown. The time of occurrence of the impulse-corona current and its amplitude; the effective corona-propagation time and effective corona velocity; the average leader formation time and average leader speed; and the number and length of the steps in the leader could thus be evaluated from the current oscillograms, and could be correlated to the various parameters of humidity, voltage, polarity, etc. Linear multiple regressions performed on a computer

permitted the separation of the effect of each of the parameters on any of the measured quantities.

2. EXPERIMENTAL ARRANGEMENTS

The impulse voltage of the 1/50 μ s waveshape was produced by a 400kV impulse generator with a total capacitance of 6300pF. The voltage was measured with a 300pF capacitive divider. The experimental gap was enclosed in a cylindrical steel vessel, which was 3m high and 1.7m in diameter. The humidity in the vessel could be set to any value between zero and 25g/m³, and the temperature could be adjusted between -5°C and +30°C. All measurements were made at atmospheric pressure. The impulse voltage was fed into the vessel via a porcelain bushing fixed on the roof of the vessel. The electrodes used were standard rods; i.e. square cross-section rods of 1.27 \times 1.27cm, with their ends cut square. The high-voltage electrode was suspended vertically along the axis of the cylindrical vessel, and it extended halfway down the vessel. The high-voltage electrode was so hollow as to allow the insertion of a 1mg Ra₂₂₆ needle when irradiation of the gap was required. The lower electrode was insulated both from its supporting tripod and the earthed vessel. The lower rod was completely shielded except for a length of 3cm at its tip. A 75 Ω coaxial cable extended from it to the oscillograph, where it was terminated with a 75 Ω resistance and earthed. Any current flowing in the gap could thus be measured by the voltage drop across the terminating resistance.

3. IMPULSE CORONA

The time T_1 of occurrence of the corona-current pulse varied between 0.6 μ s and 3.1 μ s, and the pulse was then either before or after the peak of the voltage wave, which occurred at 1.7 μ s. Table 1 shows the values of the time delay T_1 obtained for various gap

conditions at voltage levels V_{11} , giving a 50% probability of breakdown at a humidity of 11g/m^3 .

Table 1

Gap length	Time delay T_1 of corona pulse			
	Positive impulse, irradiated	Negative impulse, irradiated	Positive impulse, un-irradiated	Negative impulse, un-irradiated
cm	μs	μs	μs	μs
5	0.6	1.2	2.2	1.1
10	0.8	3.1	1.1	2.4
20	1.1	1.0	0.8	2.9
30	1.4	-	1.2	2.1

The time delay T_1 varied with gap length, polarity and spacing, but have no obvious correlation with these parameters. Regression analyses showed that the time delay T_1 was independent of humidity but that it decreased with increasing applied voltage. The decrease was to be expected, since the corona-inception level would be reached sooner with a higher applied voltage, the waveshape remaining constant. The time delay T_1 decreased by up to three times the proportional increase in voltage.

4. EFFECTIVE CORONA PROPAGATION

It was observed that, when breakdown of the gap occurred, the corona-current pulse was followed by another pulse, which started a gradual increase in current up to breakdown. It has been suggested that this second pulse of current is associated with a second corona discharge developing at the cathode due to the arrival there of sizeable positive-corona streamers. It has been also suggested that the second corona burst is usually sufficient to induce an increase in the electric field in front of the anode, previously reduced by the positive-corona burst, to such an extent as to initiate a positive leader at the anode and to lead to breakdown. From these considerations, the period of time T_c elapsing between the first and the second current pulse could be defined as the effective corona-propagation time; i.e. the time required to build up the positive corona and to project it towards the opposite electrode with sufficient intensity to produce an effective ionisation centre there.

5. LEADER PHASE

From the enlarged current oscillograms, the average number N of steps in the current buildup was determined for each 'series' of measurements; i.e. for impulse voltages of a given amplitude and for identical conditions of the gap. It was observed that, at low applied voltages, the average number of steps was fairly large but that it decreased with increasing voltages. It also appeared that the number of steps was not affected by humidity but depend only on the applied voltage. When the values of N obtained for the same conditions of gap length, polarity and irradiation, but for different

humidities, were plotted against applied voltage, the points were observed to lie approximately on the same curve irrespective of the humidity at which they had been obtained. From these curves, the values N_{11} of the average number of steps existing at the reference voltages V_{11} were obtained (Table 2). It was found that, for a given gap length, N_{11} had approximately the same value irrespective of the polarity and conditions of irradiation. It was also found that the number of steps increased almost linearly with increasing gap length, the average value of N_{11} being approximately three for the 5cm gaps and 15 for the 30cm gaps.

Table 2

Gap length	Average number of steps in leader current at reference voltages			
	Positive impulse, irradiated	Negative impulse, irradiated	Positive impulse, un-irradiated	Negative impulse, un-irradiated
cm				
5	4	3	3	3
10	6	5	5	6
20	11	11	11	14
30	16	-	15	14

It was observed that the average length of step increased approximately linearly with increasing applied voltage but was independent of humidity. A measure of the effect of applied voltage on the average step length was provided by the slopes $\Delta L/\Delta V$ of the best straight lines. The values of the slopes ranged from $+0.02\text{cm/kV}$ to 0.09cm/kV for the various conditions of the gap. The maximum step length observed was 5 cm, which was obtained at an overvoltage of approximately 50% above V_{11} .

6. CONCLUSIONS

The present work has stressed the importance of the first corona burst in the process of impulse breakdown of rod gaps. It has been seen that the first corona burst determines the initiation of the positive leader, which is the necessary and, in most cases, sufficient precursor to breakdown. The variations occurring in the 50% breakdown voltages of the rod gap with varying conditions of humidity, polarity and irradiation could thus be explained largely by the size of the first corona pulse.

References

- [1] Matthews, J., T., Saint-Arnaud, R., Proceedings IEE, vol. 118, No. 10, October, 1971
- [2] Nitta, T., Kawane, K., Yamada, N. Influence of humidity on the prebreakdown phenomena of atmospheric air. Elect. Engng., Japan, 1966, 86.
- [3] Tuşaliu, P., and others. Contact and blow-out Chamber Assembly for I.U.P. - 27.5kV/1250A breaker. Author's certificate of innovation no. 628/1987, Bucharest, Romania.
- [4] Tuşaliu, P., Ciontu, M. Aspects concerning the reestablishment oscillatory voltage at disconnecting of kilometric defect. Seventh International conference on "Switching arc phenomena", Lodz, Poland, 1993.
- [5] Tuşaliu, P., Ciontu, M., Tuşaliu, V. About High-Voltage Insulating of 750kV Circuit Breaker. Symposium on Electrical Insulation, June 16-19, 1996, Montreal, Quebec, Canada.

PHENOMENA IN IONIZED GASES UNDER CONTROLLED ATMOSPHERE CONDITIONS

P. Tusaliu*, V. Tusaliu**, M. Tusaliu**, D. Tusaliu**

* University of Craiova, Lapus Street, nr. 5, CRAIOVA 1100, ROMANIA, Fax: +40-51-145.763

** National College of Craiova, ROMANIA

ABSTRACT

The study presents the characteristics of impulse breakdown of standard rod gaps under controlled-atmosphere conditions [1-5]. The effect of humidity, polarity and irradiation on the 1/50 μ s impulse voltage breakdown and time lag of standard rod gaps has been determined for a range of spacing from 5cm to 30cm and a range of humidities from 1g/m³ to 24g/m³. An anomalous condition is reported for a 5cm unirradiated gap under positives impulses in which the slope of the humidity characteristic is opposite to that normally obtained. It is shown that, although the time lag is independent of humidity, the probability of breakdown in the sigmoid region is not independent of humidity. In finally, this study presents an adequate numerical program concerning at characteristics of impulse breakdown of standard rod gaps under controlled-atmosphere conditions.

KEYWORDS: Phenomena in ionized gases, Radiation effects, impulse testing.

1. INTRODUCTION

The main object of this work has been to determine the influence of humidity on the break-down voltage of rod-rod gaps in atmospheric air using 1/50 μ s waves of both polarities for spacings in the range 5-30cm. The absolute breakdown voltage was also determined for the conditions specified, and measurements were made with and without irradiation. These measurements formed part of a larger work which included measurement of prebreakdown phenomena and are reported in another paper [2]. The time lag to breakdown, i.e., the collapse of the applied voltage, was recorded oscillographically in each case and is used to determine the effect of the other parameters on the total time lag. These measurements were mainly on gaps of lengths greater than those in the present investigation and did not include the effects of irradiation [2]. It is clear, however, that measurements of the effect of polarity, and hence humidity, which is polarity dependent, will depend on the geometry of the gap used. This geometry is determined by the position of the ground plane, enclosure walls and high-voltage bushing, so that a given set of measurements is applicable only to the particular geometry used. It has been reported [2] that the discharge products produced by sparking inside an enclosed volume affected the measurements, but in the

present work no such effect was detected in spite of runs involving 100 sparkovers at 0-5min intervals. It is possible that the continuous ventilation provided by air recirculation was responsible for removing any such effect.

2. EXPERIMENTAL TECHNIQUES

The impulse voltage was produced by a 20-stage stage 400 kV 1/50 μ s impulse generator with a total capacitance of 6300pF [1-2]. The voltage was measured with a 300pF capacitive divider which also served as the wavefront capacitor. The experimental gap was enclosed. In a steel vessel having the shape of a cylinder 3m in height and 1.7m in diameter. The humidity in the vessel could be set to any value between zero and 25g/m³, and the temperature could be adjusted between -5° C and +30° C. Although there was provision for varying the pressure between 1torr and 1500 torr, only atmospheric pressure was used. The impulse voltage was fed into the vessel via a porcelain bushing at the top which extended 1m into the vessel. The electrodes used were standard rods; i. e. square cross-section rods of 1.27 X 1.27cm with their ends cut square. The high-voltage electrode was suspended vertically along the axis of the cylindrical vessel and extended halfway down the vessel. The high-voltage electrode was hollow to allow the insertion of a 1mg Ra₂₂₆ needle when irradiation of the gap was required. The lower electrode was insulated from both its supporting tripod and the earthed vessel, and was completely shielded except for a length of 3cm at its tip. The currents were determined by examining the voltage across a 75 Ω series resistor and displaying the waveform on an oscillograph using suitable screening and protective circuits. The basic technique consisted of applying a number of impulse voltages of a given amplitude to the gap. The voltage levels were chosen so that the range of breakdown probability expended from zero to 100%. The measurements taken at one level of voltage for a particular condition of the gap constituted a 'series', and the measurements taken over the complete range of voltage levels for the same gap condition constituted a 'run'.

3. EXPERIMENTAL RESULTS AND DISCUSSION

Effect of humidity on 50% breakdown voltage. For each particular condition of spacing, polarity and irradiation, the relationship between the 50% breakdown

voltage V and the absolute humidity H showed no tendency other than one of a linear nature. Table 1 shows the breakdown voltage V_{11} at a humidity of 11 g/m^3 and Table 2 shows the slope of the humidity characteristic expressed as a percentage of V_{11} . Measurements could not be taken on the irradiated 30cm gap under negative polarity because the voltages required exceeded the rating of the capacitance divider. It was observed that, in all cases except one, the slope dv/dH was positive; i.e. an increase in humidity produced an increase in the 50% breakdown voltage (Table 2). This is in agreement with the observations of numerous workers. In one case (5cm gap under positive impulse and without irradiation), however, the slope was negative, indicating a decrease in V as the humidity increased. This is referred to subsequently as the anomalous case. With the exception of this, the rod-gap performance under positive impulses was fairly uniform. The spacing and conditions of irradiation had very little effect on the humidity correction, which had an average value of $+0.8\%$ per g/m^3 . It is therefore surprising that the anomaly should occur with positive impulses.

Table 1

ROD-ROD-GAP BREAKDOWN VOLTAGE AT HUMIDITY OF 11 g/m^3

Gap length	Rod-rod gap breakdown voltage			
	Positive impulse, irradiated	Negative impulse, irradiated	Positive impulse, un-irradiated	Negative impulse, un-irradiated
cm	kV	kV	kV	kV
5	54.6	56.1	58.8	58.0
10	95.9	89.6	92.3	92.1
20	146.6	183.3	164.5	174.0
30	193.2	—	209.6	258.5

Table 2

EFFECT OF HUMIDITY ON BREAKDOWN ON ROD-ROD GAPS

Gap length	Humidity correction			
	Positive impulse, irradiated	Negative impulse, irradiated	Positive impulse, un-irradiated	Negative impulse, un-irradiated
cm	% per g/m^3	% per g/m^3	% per g/m^3	% per g/m^3
5	0.53	0.37	-0.72	0.31
10	0.94	0.55	0.92	0.56
20	0.89	1.29	0.72	0.83
30	0.96	—	0.55	0.64

4. VARIATION OF BREAKDOWN VOLTAGE WITH SPACING, POLARITY AND IRRADIATION

The polarity of the applied impulses had practically no effect on V_{11} for the unirradiated gaps at shorter spacings (Table 1). For the 20cm and 30cm gaps, however, the negative breakdown voltage was, respectively 6% and 23% higher than the positive value. This polarity effect can only be ascribed to the proximity of the earthed vessel: the field is intensified at the high-voltage electrode and reduced at the earthed electrode. This reduces the breakdown voltage when the high-voltage electrode is negative, as it is the field is near the positive electrode that largely determines the flashover of a rod-rod gap. It is readily understood that the asymmetry increases with gap spacing.

5. CONCLUSIONS

The effect of humidity on the breakdown voltage of the standard rod gap is of the order of 1% per g/m^3 , but there are variations with polarity, gap length and irradiation. In general, the departures from this figure are more pronounced at the smaller spacings.

The anomalous behaviour of the 5cm unirradiated gap under positive impulses is attributed to a humidity-dependent space-charge effect which is affected by irradiation. This aspect is far from being resolved, and it is fortunate that it is confined to the lower range of spacings.

The curve showing the absence of an effect of humidity on the time-lag/voltage characteristic is of interest in insulation co-ordination, since it also illustrates the significance of the probability of breakdown in the sigmoid region. If a rod gap is being used as a protective gap under these conditions, humidity reduces the effectiveness of the rod gap as a protective device by reducing the probability of breakdown.

To assess the practical aspects of this limitation, it would be necessary to compare similar humidity characteristics for the insulation in question

References

- [1] Matthews, I.E., Saint-Arnaud, R. Proc. IEE, Vol. 118 no. 10, October, 1971.
- [2] Carrara, G. A statistical aspect of the co-ordination of two gaps. IEEE Trans., 1965, PAS-84.
- [3] Tusaliu, P., and others. Contact and Blow-out Chamber Assembly for IUP-M-27.5 kV/250A breaker. Autor's certificate of innovation no. 628/1987, Bucharest, Romania.
- [4] Tusaliu, P. Ciontu, M. Aspects concerning the reestablishment oscillatory voltage at disconnecting of kilometic defect. Seventh International Conference on "Switching arc phenomena", Lodz, Poland, 1993.
- [5] Tusaliu, P., Ciontu, M. High voltage repartition over the extinction chamber of switches analysed with help of system theory.

CONDUCTING PARTICLE INITIATED IMPULSE FLASHOVERS ON THE SPACER SURFACE IN COMPRESSED GASES

B. Nageshwar Rao, K. Dwarkanath, and M. C. Siddagangappa*

Central Power Research Institute,
*Indian Institute of Science, Bangalore, India

Abstract: The influence of a conducting particle on the surface of solid insulator spacer placed in nonuniform field subjected to lightning impulse voltages is investigated for different air and SF₆ gas pressures. The discharge initiation and propagation is related to gas pressure, position of the particle and the polarity of impulse voltage in compressed air, whereas anomalous discharges were observed in SF₆.

1.0 Introduction

The insulating spacers are necessary in Gas Insulated Systems. Charges produced during system operation are deposited on the insulator surface and modify the electric field and thus influence the dielectric strength of the system. Surface charges play an important role in the initiation and propagation of spacer flashovers[1]. The investigations are underway to explain the role of surface charges in determining the reliability of compressed gas insulated systems. Lightning impulse FOV characteristics under uniform electric field conditions with a metallic particle representing the charge source is reported by the authors elsewhere [2]. The present experimental investigation is to study the role of surface charges in the initiation and propagation of discharges on insulating spacer surfaces in compressed air and SF₆ subjected to nonuniform electric field conditions.

2.0 Experimental setup and procedure

The experimental investigations were carried out in a steel chamber which can withstand pressures upto 10 bars having hv feeder bushing rated for 450 kV ac and 1050 kV Impulse voltages. A rod-plane nonuniform field electrode geometry (nonuniformity factor $\eta = 0.21$) was used in the experiments. The high voltage electrode was a cylindrical brass rod of diameter 12 mm with hemispherical tip and the other electrode was plane 120 mm Bruce electrode connected to ground. The impulse voltages (1.2/50 μ sec) applied to the system were provided by 4 stage, 500 kV, 15 kJ, Marx Generator. The experimental details and procedure is reported elsewhere [2].

3.0 Results and discussion

A cylindrical PMMA spacer of length 30 mm and dia 50 mm was centrally positioned between rod-plane electrodes. A steel wire of diameter 1 mm and length 5 mm, was glued to the insulator surface at different positions measured from the bottom electrode. The positive and negative impulse breakdown strengths (V_b) of spacer with a conducting particle at different locations for various compressed air pressures is shown in figure 1. The experimental results clearly indicate the influence of a of conducting particle on the values of breakdown voltage.

For negative polarity voltages the lowest V_b obtained are, when the conducting particle on the spacer surface is close to plane electrode ($d = 2$ mm). Perhaps, under negative impulse field conditions applied to rod electrode, the particle when situated very near to plane electrode attains positive polarity of the plane electrode either by induction or through conduction bridged by micro discharges resulting in point - rod electrode configuration and hence drastically reducing breakdown strength of the system. However as the particle position gets nearer to the rod electrode ($d = 22$ mm) progressive improvement in V_b values suggests that the metallic particle switches over to induction by the polarity of the rod electrode and acts as an extended rod electrode increasing the point - plane gap distances.

For positive impulse applications, the presence or the position of the conducting particle on the spacer does not significantly affect the V_b values as is evident from figure 1. During experimentation it has been experienced that every time polarity is reversed the flashover occurred initially at low V_b values and breakdown voltages raised with increasing number of voltage applications reaching saturation. Similar trend was noticed in the studies for rod diameter of 6 mm (nonuniformity factor $\eta = 0.125$, results not shown) keeping the other conditions common. At pressures above 200 kPa positive impulse breakdown voltages saturate due to combination of charge spread on

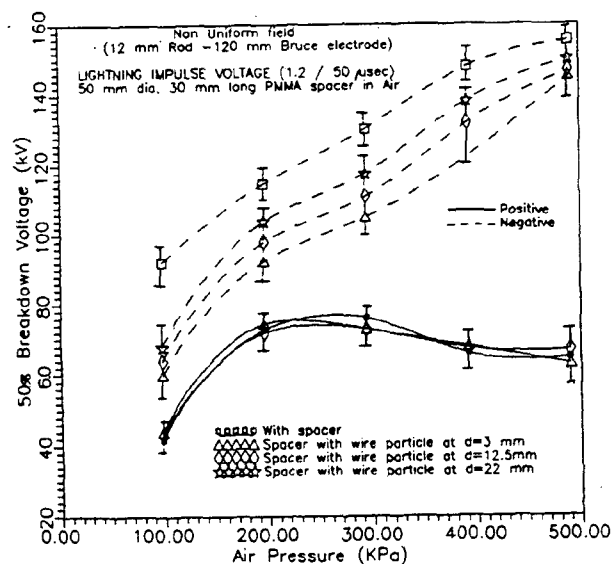


Figure 1. Breakdown voltage as a function of Air pressure, for 30 mm long, 50 mm dia PMMA spacer

the surface adjacent to rod electrode and suppression of prebreakdown currents. Probably the saturated V_b data suggests role played by maximum accumulated surface charges on the spacer. Similar accumulated charge controlled spacer surface flashover behaviour has been reported by Takaaki et al [3].

Even for nonuniform field condition the discharges were visually observed to originate from the conducting particle and propagates along the spacer surface, similar to the discharge initiation process observed in uniform field conditions [2]. The intermittent carbonized tracks seen on examination, left by the discharges in different directions on the spacer surface to originate from the location of particle; strongly suggest that the breakdown process is controlled by spacer surface conditions.

Preliminary data of positive impulse breakdown characteristics are plotted in figure 2, for 30 mm long, 50 mm diameter PMMA spacer in nonuniform field without and with particle at different positions for SF₆ gas pressures. With the inclusion of conducting particle on spacer surface, there is no consistency in the breakdown data (V_b) pattern. Discharge initiations seem to be governed by additional factors [5]. Observed tracking patterns are not always originated from the location of conducting particle on the spacer surface. Surface discharges in SF₆ gas appears to be largely controlled by memory of the charge accumulated pattern decided by the immediate past discharge due to breakdown.

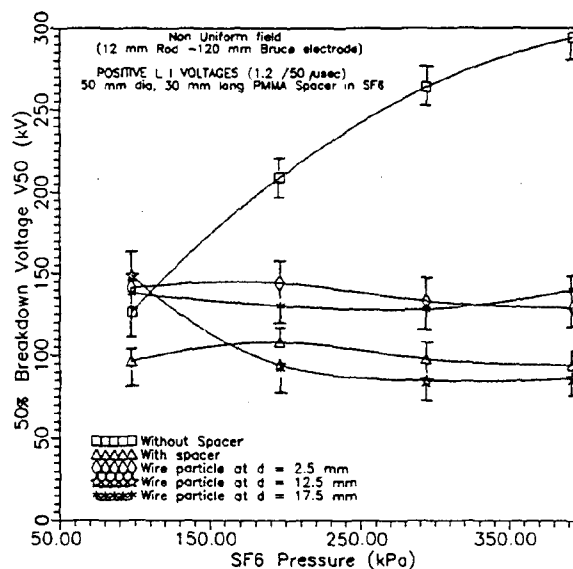


Figure 2. Breakdown voltage as a function of SF₆ gas pressure, for 30 mm long, 50 mm dia PMMA spacer

4.0 Conclusions

In compressed air insulation system, the surface flashover conditions are also determined by the possible charges accumulating and their locations on insulator spacers under nonuniform field conditions. Apparently, in SF₆ insulation system with spacers, the mechanisms of surface discharges are yet to be understood clearly to explain the anomaly in the breakdown data.

5.0 Acknowledgements

The authors wish to thank the management of Central Power Research Institute, Bangalore, for the permission to publish this paper. Thanks are due to Prof. M.S.Naidu, Chairman, High Voltage Department, Indian Institute of Science, for his interest in this work.

6.0 References

- [1] Alan H. Cookson, Proceedings of the 3rd Intl. Conf. on applications of dielectric materials, Tokyo, Japan, pp 369 -376, 1991
- [2] B. Nageshwar Rao, K. Dwarkanath and M. C. Siddagangappa, Submitted at ISH'97 conference Montreal, Canada, July 1997.
- [3] Takaaki Tsukiji and Toshiyuki Matsumoto, Conf. Record of 1983, Interfacial Phenomena in Pract. Ins. Syst., IEEE Pub 83, CH 1946-3, 1983
- [4] H.T. Wang and R.G. Van Heeswijk, Conf. Record of the 1990, IEEE Intl. Symposium on Ele. Ins., Toronto, Canada, pp 247 -247, 1990.
- [5] N.Giao Trinh, Garry Mitchel and Claire Vincent, IEEE Trans. on Power Delivery, Vol.3, No.1, Jan 1988, pp 16-25 (See discussions).

Partial Discharges as Ionisation Source for Ion Mobility Spectrometry

Oliver Soppart, Jörg Ingo Baumbach, Dieter Klockow

Institut für Spektrochemie und Angewandte Spektroskopie (ISAS), Bunsen-Kirchhoff-Str. 11,
44139 Dortmund, Germany

Abstract

Ion mobility spectrometers (IMS) are analytical instruments for rapid and sensitive detection of gaseous pollutants. The high mobility and range of applications of these instruments are partially restricted by limitations of the ionisation sources used. Partial discharges are proposed as an alternative to the commonly used ^{63}Ni β -radiation sources and UV-lamps. A suitable geometry and its characteristics are discussed and an IMS with partial discharge ionisation is described.

Introduction

During the last two decades ion mobility spectrometry has been increasingly employed for sensitive detection of organic compounds in air. A separation of previously ionised compounds is achieved by means of their different mobilities within an electric field. Collection of the charge of these ions on a faraday plate delivers a time resolved signal, the ion mobility spectrum.

The traditional fields of operation were detection of narcotics and explosives. Here ^{63}Ni β -radiation sources and sometimes UV-lamps were employed as ionisation sources.

Nowadays new applications as the quality assessment of SF_6 in gas insulated substations exhibit limitations such as internal corrosion or public acceptance of radioactive sources and require new ionisation sources. A possible effect, which may be exploited are partial discharges occurring in a highly inhomogeneous electric field.

Partial Discharges in a Point-to-Plane Geometry

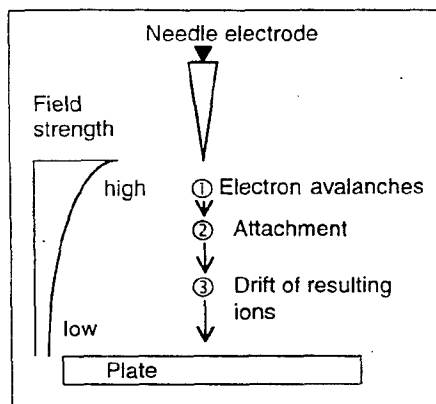


Fig. 1: Point-to-plane geometry

Geometry

One of the classical geometries to generate partial discharges in a gas consists of a point in the vicinity of a plane, technically realised with a needle electrode and a plate (Fig.

1). Sufficient voltage applied between the two electrodes generates a highly inhomogeneous electric field, which exceeds the dielectric strength of the gas in the surrounding of the needle (①). The electron avalanches formed there drift towards the subsequent region of lower electric field to be attached to neutral molecules forming ions (②), which then continue (③) the drift to the plate. These ions may be analysed with ion mobility spectrometry, requiring only a suitable interface.

Employment of Partial Discharges for Ion Mobility Spectrometry

Especially for the analysis of SF_6 , the common ionisation sources fail. The possible occurrence of corrosive by-products restricts the use of radioactive material and the very strong UV-absorption of the matrix SF_6 makes photoionisation impossible. Hence, a partial discharge ionisation source was developed, replacing the plate shown in Fig. 1 by a fine meshed grid. This grid permits the drift of the ions generated in the partial discharge through the spacing between the wires into the drift region attached below it. The separation process occurring there is based on different mobilities of different ions in an electric field after formation of ion swarms by use of a periodically opened shutter grid. This allows an observation of the further behaviour of ions generated in partial discharges at ambient pressure and a detection of trace compounds in the matrix gas (SF_6). A further description of the spectrometer may be found in [1].

Requirements for a partial discharge ionisation source

As partial discharges are a non linear effect, the determination of suitable operating conditions is of considerable interest. Above the inception voltage, the ionisation rates are adjustable with the voltage (Fig. 2). For ion mobility spectrometry, only a small portion of the gas contained in the ionisation chamber is to be ionised, resulting in ionic currents in the range below a Nanoampere. Operation with higher currents suffers from parasitic effects like coulombic repulsion or clustering. For the point-to-plane geometry discussed here, this current is produced for voltages only slightly above the inception voltage for partial

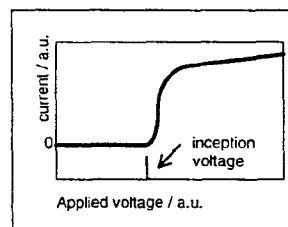


Fig. 2: Current generated by partial discharges

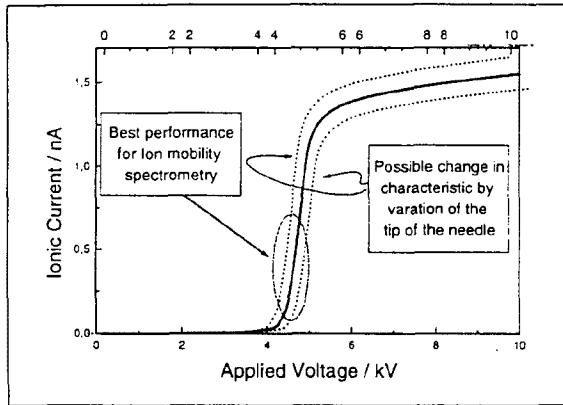


Fig. 3: Characteristic of point-to-plane geometry

discharges. Fig. 3 shows the ionic current in the experimentally used geometry. The operating range for best performance is indicated. Because of the steep characteristic in this range, even small changes of the inception voltage lead to serious variations in the amount of ions generated. As this may be induced by small variations of the tip of the needle, a regulation would be conceivable.

Stabilisation of the ionic current

Stable conditions for ion mobility spectrometry are defined by a constant generation rate for ions. In a strongly electronegative gas as SF_6 , the overall balance of charge is virtually unaffected by charge transfer reactions. This allows to use the total charge accumulated during acquisition of each spectrum as a reference for the ion generation by the ionisation source. This can be easily realised with an analogue low pass filter connected to the signal output of the spectrometer. The resulting signal was used as input for the regulating circuitry. The characteristic contains a proportional and integral component to achieve a sufficiently fast and precise stabilisation of the ion generation. Additionally, the data acquisition software was updated, halting data acquisition during short instabilities.

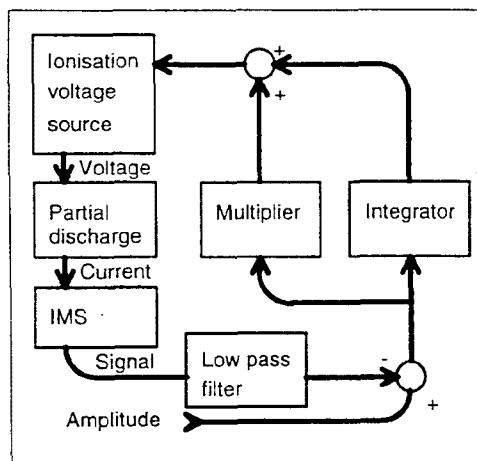


Fig. 4: Sketch of the stabilisation unit

Characterisation of ions generated by partial discharges

The ionisation unit described here is capable of delivering a constant amount of ions into the drift region of an IMS, allowing a characterisation of ionic species by means of their mobilities. Such an experiment allowed to distinguish between two different ion generated by partial discharges (Fig. 5). The corresponding mobilities are indicated in the figure, the ions are supposed to be SF_6^- and SF_5^- , respectively.

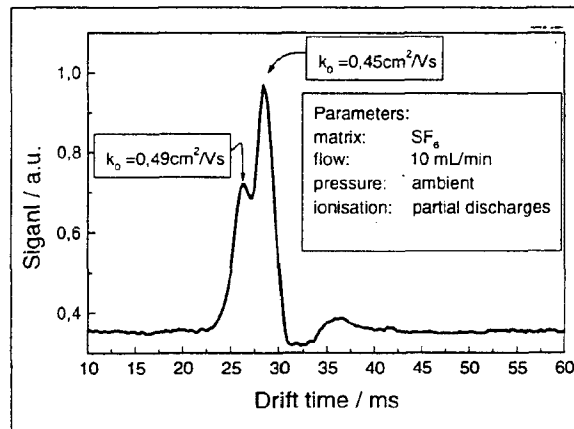


Fig. 5: Mobility spectrum of negative ions generated by partial discharges

Conclusions

An unconventional ionisation source was developed for ion mobility spectrometry, avoiding the use of radioactive material or UV-transparent windows. A suitable operating range was determined and stabilised with a regulation unit. The feasibility of this ionisation source for ion mobility spectrometry was demonstrated. For further studies, a combination of the partial discharge ionisation source with an ion mobility spectrometer and a mass spectrometer is scheduled.

Acknowledgement

The authors would like to thank the Deutsche Forschungsgemeinschaft / Gesellschaft für technische Zusammenarbeit (DFG/GTZ) for financial support. The steady and efficient assistance we received from the Lehrstuhl für Hochspannungstechnik und elektrische Anlagen (LSHA) der Universität Dortmund is highly appreciated.

Reference

- [1] Baumbach, J.I.; v. Irmer, A.; Klockow, D.; Alberti Segundo, S.M.; Sielemann, St.; Soppart, O.; Trindade, E.: Characterisation of SF_6 Decomposition Products caused by Discharges in Switchgears using Ion Mobility Spectrometry. - Proceedings of the 4th International Workshop on Ion Mobility Spectrometry, Cambridge, August 1995

Topic 5

Arcs.

Cathode phenomena in high-pressure arc lamps

R. M. S. Almeida and M. S. Benilov
Departamento de Física, Universidade da Madeira
Largo do Município, 9000 Funchal, Portugal

1. Introduction

Design of cathodes of high-pressure discharge lamps could be facilitated if physics of near-cathode phenomena were well understood and an appropriate theoretical model developed [1]. An adequate calculation model of near-cathode phenomena is an important constituent of any model of the lamp on the whole (e.g., [2]).

The aim of this contribution is to analyze near-cathode phenomena in high-pressure arc discharge lamps by means of the approach suggested in [3]. The main attention is paid to case of a mercury plasma at the pressure of 30 atm and a tungsten cathode.

2. Macroscopic length scales and mean free paths

The near-cathode layer includes a space-charge sheath adjacent to the cathode surface where deviations from quasi-neutrality occur and a quasi-neutral ionization layer without ionization equilibrium.

If thermal equilibrium maintains in the ionization layer, ionization is governed by the heavy-particle temperature, which is relatively low, and the plasma in the near-cathode layer is weakly ionized. The ionization layer will be in thermal equilibrium if the thickness of the ionization layer is greater than the length of electron energy relaxation. Otherwise there is no equilibrium and the plasma may be strongly ionized.

The scale of thickness of the ionization layer is represented by the recombination length $d = \sqrt{2D_a/k_{re}n_{coo}^2}$, where k_{re} is the recombination rate constant, n_{coo} is the number density of the charged particles at the edge of the ionization layer, and D_a is the coefficient of ambipolar diffusion.

The length of electron energy relaxation is estimated using the formula $\lambda_u = [\sqrt{\delta}(\lambda_{ei}^{-1} + \lambda_{e0}^{-1})]^{-1}$, where λ_{ei} and λ_{e0} are the mean free paths for electron-ion and electron-neutral collisions, respectively, and the parameter δ characterizes the energy exchange between an electron and a heavy particle.

The hierarchy of the length scales and various mean free paths for the case $T_e = T_h$, where T_e is the electron temperature, is as follows:

$$\lambda_{e0} \leq \lambda_{i0} \ll \lambda_{00} \leq h \ll \lambda_u \ll d \leq \lambda_{ii} \sim \lambda_{ei} \sim \lambda_{ee} \quad (1)$$

0.01 0.02 0.2 0.4 5 55 65

the heavy-particle temperature, T_h , here and further is set equal to 4000 K, the numbers below are values in μm ; h is the Debye length, λ_{i0} , λ_{00} , λ_{ii} , and

λ_{ee} designate mean free paths for collisions ion-atom, atom-atom, ion-ion, and electron-electron. While obtaining these values, the Saha equation of ionization equilibrium and the formula of Hinnov and Hirshberg have been used. The average cross section for electron-neutral atom collisions was obtained by integration of the momentum-transfer cross section given in [4], and those of ion-atom and atom-atom collisions were set equal to $10^{-18} m^2$ and $10^{-19} m^2$, respectively. The ionization degree in this case is quite low ($1.8 \cdot 10^{-6}$).

Condition $\lambda_u \ll d$ is satisfied, so these estimates are self-consistent and these regimes can realize.

The latter, however, does not mean that regimes with $T_e \neq T_h$ cannot realize. Consider, for example, the case $T_e = 7000 K$. The hierarchy is

$$\lambda_{e0} \leq h \sim \lambda_{i0} \ll \lambda_{ii} \leq \lambda_{00} \sim d \leq \lambda_{ei} \sim \lambda_{ee} \ll \lambda_u \quad (2)$$

0.01 0.02 0.1 0.2 0.4 6

Since $d \ll \lambda_u$, the estimates are self-consistent and these regimes can realize. The ionization degree is $1.8 \cdot 10^{-3}$. With the increase of electron temperature the ionization degree will increase, while the scale ordering will suffer no significant change.

Thus, one should conclude that a regime of a weakly ionized plasma in thermal equilibrium and a regime of a moderately to strongly ionized plasma with differing temperatures of the electrons and of the heavy particles are both possible. The question is which one of them realizes in the range of current densities typical for arc lamps.

3. Regimes with a weakly ionized plasma in thermal equilibrium

In these regimes, distributions of the number densities of the ions and electrons and of the electric field strength in the near-cathode plasma may be described by the system of hydrodynamics equations and the Poisson equation. The dominating mechanisms of ionization and recombination must now be specified.

The neutral atoms may be ionized by electron impact, by impact of a neutral atom, and by a photon (photoionization). Recombination may occur by the respective inverse processes.

Three-body recombination rate constants have been obtained by means of the formula of Hinnov and Hirshberg for the case of an electron as a third body and by means of the extended J. J. Thomson theory of three-body recombination for a neutral atom as a third body. Considering a typical radiative recombination rate constant of $10^{-18} m^3/s$, we conclude that three-body recombination with a neutral atom as a

third body and radiative recombination are unessential as compared to three-body recombination with an electron as a third body. With account of the principle of detailed balancing, one can conclude that dominating mechanisms of ionization in the considered conditions is ionization by electron impact (cf. [2]).

An asymptotic solution of the system of hydrodynamics equations and the Poisson equation has been constructed, the ratio h/d was considered as a small parameter. Analytic solutions have been obtained for each zone, including the sheath and the ionization layer, and for the voltage drop in the near-cathode layer.

On the basis of this solution, a conclusion has been made that regimes with a weakly ionized plasma in thermal equilibrium can hardly realize because of two reasons: first, the electric field necessary to support the required current density is quite strong and would heat the electrons appreciably; second, such a field would induce an unrealistically high (of order of several kilovolts) voltage on the near-cathode layer.

4. Regimes with a moderately or strongly ionized non-equilibrium plasma

According to estimates (2), the Debye length in these regimes is comparable to the ion mean free path. One can consider the sheath in the simplest approximation as collision free for the ions.

One can use the model suggested in [3], with the current density as input parameter, all other parameters will result from the calculations.

The near-cathode voltage drop U calculated by means of this model for the surface temperature of 3000 K is shown in Fig. 1. The voltage drop corresponding to the current density of 10^6 A/m^2 is about 10 V, which does not look unreasonably high.

The electron temperature in the ionization layer increases with the increase of the current density but remains below 9000 K, see Fig. 1. Hence the plasma remains moderately ionized in the whole range of the current densities considered.

One can conclude that regimes of a diffuse current transfer to cathodes of arc lamps [1] may be explained by means of the model [3] as regimes with moderately ionized plasmas.

In solving the problem of the heat regime of the cathode one obtains a non-unique solution [5]: a solution with a smooth distribution of the temperature over the cathode surface, describing the diffuse regime of current transfer to the cathode surface, and one or more solutions describing regimes with spots. A one-spot solution is described by the model [3].

Consider, for example, a solution given by the model [3] for a spot with the current of 1.7 A. The voltage drop is 17.3 V in the space-charge sheath and 3.7 V in the ionization layer. The spot temperature is 4850 K, which is above the melting temperature of tungsten. The spot radius is about 26 μm . The

electron temperature is about 47000 K. Fraction of the ion current is 0.16 and the ratio of the current density of the counterdiffusing plasma electrons to the total current density is 0.33.

One can conclude that the hot-spot regimes of current transfer to cathodes of arc lamps may be explained by means of the model [3] as regimes with strongly ionized plasmas.

5. Conclusions

Analysis by means of the model [3] indicates that the diffuse mode of current transfer to cathodes of high-pressure arc lamps may be explained as the regime with a moderately ionized plasma and the hot-spot mode may be explained as the regime with a strongly ionized plasma; the regime of a weakly ionized plasma with the electron temperature close to the heavy-particle temperature is unlikely to realize.

Quantitative results of the present work should be considered as preliminary until the theoretical model has been refined and the effect of non-ideality of the plasma has been clarified.

The authors are grateful to Prof. J. Mentel for useful discussions. The work has been supported by F.E.D.E.R. and the program *Praxis XXI*. One of the authors (MSB) appreciates financial support of the Alexander von Humboldt-Stiftung during his research stay at the Ruhr-Universität Bochum.

REFERENCES

- [1] J. F. Waymouth, *J. Light & Vis. Env.*, **6**, 53 (1982).
- [2] E. Fischer, *Philips J. Res.*, **42**, 58 (1987).
- [3] M. S. Benilov and A. Marotta, *J. Phys. D: Appl. Phys.*, **28**, 1869 (1995).
- [4] S. D. Rockwood, *Phys. Rev. A*, **8**, 2348 (1973).
- [5] M. S. Benilov, *Phys. Rev. E*, **48**, 506 (1993).

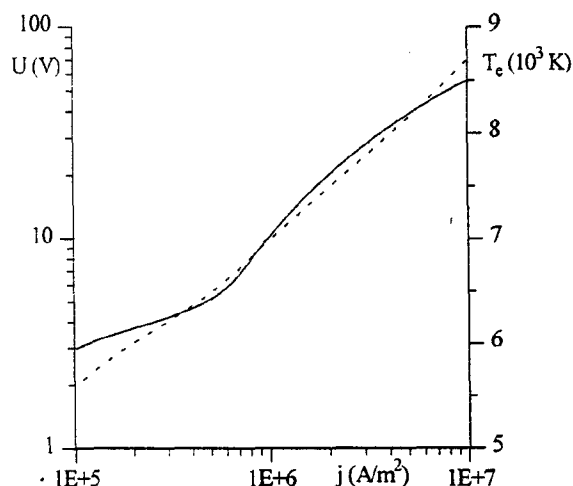


Fig. 1. The near-cathode voltage drop (full line) and the electron temperature in the ionization layer (broken line).

Analysis of thermal non-equilibrium in a near-cathode region of an atmospheric-pressure arc

M. S. Benilov

Departamento de Física, Universidade da Madeira, Largo do Município, 9000 Funchal, Portugal

1. Introduction

One of key questions in understanding physics of cathodic parts of atmospheric-pressure arc discharges is the question of the electron temperature: whether it deviates from the heavy-particle temperature and if it does, in which region this deviation is localized. Unfortunately, experimental investigation of non-equilibrium phenomena near cathodes of atmospheric-pressure arc discharges (e.g., [1–3] and references therein) is far from complete and no answer to this question has been obtained yet.

Even the most recent theoretical models are essentially different as far as the electron temperature is concerned. In particular, in the models [4, 5] the electron temperature is assumed to be in equilibrium with the temperature of heavy particles. In the models [6–8] a deviation of the electron temperature from the heavy-particle temperature is taken into account, however is assumed to be localized in a layer of a thickness of order of $100 \mu m$. Electron temperatures calculated exceed substantially the heavy-particle temperature and are of order of $2 \cdot 10^4 K$. In [9], electron temperatures in excess of $4 \cdot 10^4 K$ have been calculated, the electron energy equation was treated in an integral balance form.

The aim of this contribution is to analyze qualitatively the electron energy equation in the near-cathode region. In particular, validity of the above-mentioned theoretical approaches is considered.

2. Electron energy equation

We write this equation under the assumption that collisions between charged particles dominate over their collisions with neutrals and that mean velocities of all species are much smaller than respective thermal velocities:

$$\nabla \cdot (\alpha_e \nabla T_e) + \nabla \cdot \left[\left(\frac{5}{2} + \gamma_e \right) \frac{k T_e}{e} \mathbf{j}_e \right] + \mathbf{j}_e \cdot \mathbf{E} - \frac{3e^2 n_e^2 k}{\sigma_e m_i} (T_e - T_h) + w_e^{(e)} = 0. \quad (1)$$

Here γ_e is the dimensionless thermal-diffusion coefficient of electrons and $w_e^{(e)}$ is a rate of change of electron energy due to reactions, all other designations are conventional. The particle mass m_i of all ion species is assumed to be the same.

Quantities below terms of Eq. (1) represent estimates of their relative orders. Here $\alpha = \lambda_u/L$,

$\lambda_u = \sqrt{m_i/m_e}/n_e Q_{Coul}$ is the length of electron energy relaxation, L is a local macroscopic length scale, $\beta = j/en_e C_i$, j is the electric current density, C_i is the thermal velocity of ions, Q_{Coul} is a characteristic Coulomb cross section.

In the case $\lambda_u \ll L$ and $j \ll en_e C_i$, the fourth term of Eq. (1) is dominating. One gets $T_e \approx T_h$, i.e., the plasma is in thermal equilibrium.

In the case $\lambda_u \ll L$ and $j = O(en_e C_i)$, the third and fourth terms of Eq. (1) are dominating. Employing Ohm's law, one finds that Eq. (1) is reduced to the equation of local balance between the Joule heating and the energy transferred in elastic collisions with ions. It follows that

$$T_e - T_h = \frac{m_i j^2}{3e^2 n_e^2 k}. \quad (2)$$

3. Application to near-cathode region of atmospheric-pressure arcs

We divide the near-cathode region into the space-charge sheath, the ionization layer, and the expansion zone. The sheath is treated in available models either as collision-free (e.g., [6–9]) or as collision-dominated [5]. In the collision-free model the sheath is described kinetically and the question of whether thermal equilibrium holds in the sheath does not arise. In the collision-dominated model this question arises however is not crucial, since ionization (which is the process most strongly affected by variations of electron temperature) is not essential in the sheath. Therefore, the sheath is excluded from the subsequent estimates.

An idea of a scale of thickness of the ionization layer can be obtained by considering the case when only singly charged ions are present: in this case, the above scale may be set equal to the recombination length d , which is of order of $10 - 50 \mu m$ [9]. The expansion zone is an adjacent to the cathode spot plasma region of an extension of order of the spot radius r_* , in which the current density is reduced from high values typical for the spot to substantially lower values. Assuming that the spot radius is of order of $1 mm$, one finds that $r_* \gg d$.

If $\lambda_u \ll d$ and $j_c \ll en_e C_i$ (here j_c is a characteristic current density in the spot), the plasma is in thermal equilibrium both in the ionization layer and in the expansion zone. This is the case in which the approach [4, 5] is justified.

If $\lambda_u = O(d)$ and $j_c \ll en_e C_i$, thermal equilibrium maintains in the expansion zone but is violated

in the ionization layer. Since the thickness of the ionization layer is much smaller than the spot radius, one can employ the electron energy equation (1) in a one-dimensional form. A boundary condition at the edge of the layer is $T_e = T_h$. Governing processes are electron heat conduction and energy exchange due to elastic collisions with ions; convective enthalpy transport, thermal diffusion, work of the electric field, and the change of electron energy due to reactions are smaller effects. The approach employed in [7, 8] is justified in the considered case.

If $\lambda_u = O(d)$ and $j_c = O(en_e C_i)$, thermal equilibrium is violated both in the ionization layer and in the expansion zone. In the latter, the electron temperature is governed by Eq. (2). The difference $T_e - T_h$, being substantial in the inner part of the expansion zone where $j = O(j_c)$, decreases proportionally to j^2 as the distance from the spot increases. Distribution of the electron temperature in the ionization layer is described by Eq. (1) in a one-dimensional form with the boundary condition supplied by Eq. (2).

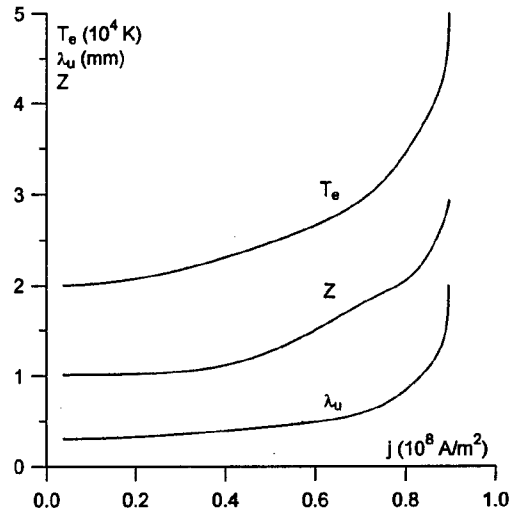
If $\lambda_u = O(r_*)$ and $j_c = O(en_e C_i)$, thermal equilibrium is violated both in the ionization layer and in the expansion zone. Distribution of the electron temperature in the expansion zone is governed by Eq. (1), in which the electron current density j_e is replaced by the total current density j . In the ionization layer, the electron energy equation in the first approximation is reduced to equation of constancy of the electron heat flux. If one assumes that $\lambda_u/d \gg eU_D/kT_e$, then the flux of energy brought in the ionization layer by emitted electrons is smaller than characteristic values of the electron heat flux inside the ionization layer, and one finds that the electron temperature is in the first approximation constant in the ionization layer. In order to find this constant, one should consider the electron energy equation in the second approximation, which amounts to considering an integral balance of the electron energy. The integral balance approach employed in [9] is justified in this case.

In order to find out which case realizes for some or other particular arc, it is convenient to calculate T_e as a function of j by means of Eq. (2), in which n_e is considered as an equilibrium value corresponding to the considered T_e . Evidently, the deviation $T_e - T_h$ found in this way for a given $j = j_c$ characterizes a relation between j_c and $en_e C_i$.

Results of calculation for argon at the pressure of 1 atm and $T_h = 2 \cdot 10^4$ K are shown in the figure. Also shown are the length of electron energy relaxation λ_u and the average charge number of the plasma Z . No solution exists when j_c exceeds a certain critical value, which is approximately $0.896 \cdot 10^8$ A/m². Two solutions exist when j_c is below this value, only lower one being shown on the graph.

In most models, values of the current density in the cathode spot exceed 10^8 A/m². No solution exists for these values. Even for lower values the difference

$T_e - T_h$ is quite appreciable [which corresponds to $j_c = O(en_e C_i)$]; for example, $T_e - T_h$ at $0.5 \cdot 10^8$ A/m² is approximately $5 \cdot 10^3$ and the average charge number is 1.27. The length of electron energy relaxation is 0.44 mm, i.e., is comparable to the spot radius.



4. Conclusions

Estimates for a 1 atm argon plasma show that at current densities typical for cathode arc spots thermal non-equilibrium is quite appreciable and occurs not only in the ionization layer, but also in the expansion zone. Since the length of electron energy relaxation is comparable to the spot radius, the approximation of local balance between the Joule heating and the energy transferred in elastic collisions cannot be used and one should treat a multi-dimensional electron energy equation in order to find a distribution of the electron temperature in the expansion zone. In the ionization layer, one can apply the integral balance approach.

The work has been supported by FEDER and by the program PRAXIS XXI.

REFERENCES

- [1] S. Pellerin, K. Musio, B. Pokrzywka, and J. Chapelle, *J. Phys. D*, **27**, 522 (1994).
- [2] J. Haidar, *J. Phys. D*, **28**, 2494 (1995).
- [3] X. Zhou and J. Heberlein, *Plasma Chemistry and Plasma Processing*, **16**, 229S (1996).
- [4] R. Morrow and J. J. Lowke, *J. Phys. D*, **26**, 634 (1993).
- [5] J. J. Lowke and J. C. Quartel, *Aust. J. Phys.*, **50**, No. 3 (1997; to appear).
- [6] K. C. Hsu and E. Pfender, *J. Appl. Phys.*, **54**, 3818 (1983).
- [7] C. Delalondre and O. Simonin, *Coll. de Physique*, **51**, C5-199 (1990).
- [8] B. Rethfeld, J. Wendelstorf, T. Klein, G. Simon, *J. Phys. D*, **29**, 121 (1996).
- [9] M. S. Benilov and A. Marotta, *J. Phys. D*, **28**, 1869 (1995).

2D Numerical Modelling of an Arc Jet Thruster

B. Laufer, A. Kaminska
Institute of Electric Power Engineering
60-965 Poznan, ul. Piotrowo 3A, Poland

M. Dudeck
Laboratoire d'Aerothermique
4 ter, Route des Gardes, 92190 Meudon, France

1. Introduction

Numerical modelling of plasma arc jets is a developing area since few years. This development results in the increase of applications of plasma generator (for example, the satellite propulsion system or the plasma wind tunnel) and in the need of less expensive control method of plasma parameters.

The cathode of thruster used at the Laboratoire d'Aerothermique, is made of zirconium and consists in an 2 mm diameter implant in a copper water-cooled support. The anode is constituted of a copper nozzle with a cylinder constrictor of 4 mm diameter and 5 mm long. The angle of the nozzle is 30° and it is 44 mm long. The electric arc is created in the constrictor only. In the constrictor, the gas is heated by Joule effect: strong velocity and temperature radial gradients appear. During the expansion phase, in the nozzle, the pressure and the temperature decrease rapidly while the velocity increase. Others strong axial gradients are observed.

Modelling this kind of plasma involve to solve numerically a set of equations in which all the main physical processes are take into account. But because of the large variety of plasma generator construction and specific conditions of the flow, several methods are used [1-3]. These methods differ in the form of the plasma flow equations, in the discretization scheme, the numerical grid and the solver algorithm.

In this paper, the plasma flow in the thruster is modelled using the conservative integral form of the conservation equation of mass, electron, momentum, energies and current density. The first steps of the study by a finite volume method are presented.

2. Numerical method and plasma equations

The set of plasma flow equations can be expressed under different forms: the integral or differential conservative form, and the differential non-conservative form. Although either formulations are physically correct, numerical experiments and comparisons [4] show that the use of non-conservative formulations gives generally less accurate results than conservatives ones, particularly in the presence of strong gradients.

In the finite volume method is the name given to the technique by which the integral formulation of the

conservation laws is discretized directly in the physical space by integrating the equations over a control volume. In the other well-used method, the finite difference one, the differential form of the equations is discretized in an infinitesimal volume around the grid node. In fact, only the first method expresses the exact conservation of relevant properties because of the recovering of the physical domain by all control volumes.

Because of the presence of strong gradients in the plasma flow, the finite volume method is more suitable. Under the assumptions of stationary processes, single ionised argon plasma and non local thermodynamic equilibrium, the plasma can be describes by the conservation equations of mass, electrons, momentum, heavy species and electrons energies, and current density:

$$\oint_S \rho \vec{v} \cdot d\vec{S} = 0 \quad (1)$$

$$\oint_S (n_e \vec{v}_e - D_A \vec{\nabla} n_e) \cdot d\vec{S} = \int_V \dot{n}_e \cdot dV \quad (2)$$

$$\oint_S (\rho \vec{v} \otimes \vec{v} + pI - \vec{\tau}) \cdot d\vec{S} = 0 \quad (3)$$

$$\oint_S (\rho_h \vec{v}_h H_h - k_h \vec{\nabla} T_h - \vec{\tau} \cdot \vec{v}_h) \cdot d\vec{S} = \int_V q_h \cdot dV \quad (4)$$

$$\oint_S (\rho_e \vec{v}_e H_e - k_e \vec{\nabla} T_e - \vec{\tau} \cdot \vec{v}_e) \cdot d\vec{S} = \int_V q_e \cdot dV \quad (5)$$

$$\oint_S \vec{j} \cdot d\vec{S} = 0 \quad (6)$$

where: ρ , ρ_h , ρ_e are the gas, heavy species and electron mass densities respectively, n_e is the number of electrons, \vec{v} , \vec{v}_h , \vec{v}_e are the velocities of fluid, heavy species and electrons respectively, T_h , T_e are the heavy species and the electrons temperatures, p the pressure, I the unity matrix, H_h , H_e are the heavy species and the electron enthalpies, \vec{j} is the current density, D_A the

ambipolar diffusion coefficient, k_h and k_e are heavy species and electron thermal conductivities, \dot{n}_e the electron source term. The forces tensor τ has components:

$$\tau_{ij} = \mu \left[(\partial_j v_i + \partial_i v_j) - \frac{2}{3} (\bar{\nabla} \cdot \bar{v}) \delta_{ij} \right]$$

where μ is the viscosity.

The heavy species heat source q_h includes the collisional energy exchange term and the electron heat source q_e includes the ohmic heating, the radiative and collisional losses of energy (which means that a chemical model as been establishes).

3. Discretization scheme

The accuracy of the calculation depends on the discretization scheme. In a two dimensional problem, the value in one cell has to be linked to the values in surrounding cells. More the number of surrounding cell is important, higher is the order of accuracy of the scheme. High order schemes allow to avoid some numerical problems as false diffusion and then, to employ a coarser grid. It is also proved that discretization schemes do not give the same results in the presence of strong gradients. Some of them are better in this kind of situation.

For modelling the thruster, an accurate scheme giving a good description of the fast variations of the physical quantities is therefore necessary. The T.V.D. (Total Variation Diminishing) of Yee-Harten has been choose. It is of second order of accuracy, can fit shocks without oscillations of the solution and an entropy condition avoid non physical solutions [7]. After discretization, the set of algebraic equations can be written under a pentadiagonal matrix form. Using a 100×100 grid, a 10000×10000 matrix containing approximately 50000 non zero elements is obtained. Then, the matricial system has to be solve employing a numerical algorithm.

4. Solver algorithm

The matricial system obtained after the discretization is solved. The convergence of the calculation depends on the solver algorithm. The direct methods could not be employed because of the non linearity of the problem. The iterative methods like Jacobi's or Gauss-Seidel's are too much time expensive in these problems. In this case, two methods are well appropriated: the Alternating Direction Iteration (ADI) and the Strongly Implicit Procedure (SIP) [8].

To solve the pentadiagonal matrix obtained, the ADI method is used [9]. Because solving directly a pentadiagonal matrix is too expensive, the ADI method consist in factoring the matrix in such a way that, finally, a tridiagonal matrix has to be solve.

5. Conclusion

The plasma flow in an arc jet thruster has been modelling by a finite volume method, using the conservative integral form of the conservation equations. The discretization scheme and the solver algorithm are discussed and Yee-Harten discretization scheme and ADI solver have been chose.

The results for the velocities, pressure, temperature and densities will be presented for thermal equilibrium and chemical non equilibrium case.

6. References

- [1] R.F.G. Meulenbroeks, R.A.H. Engeln, M.N.A. Beurskens, R.M.J. Paffen, M.C.M. van de Sanden, J.A.M. van der Mullen, and D.C. Schram: Plasma Sources Sci. Technol., 4 (1995) 74-85
- [2] P.C. Sleziona, M. Auweter-Kurtz, and E.W. Messerschmid: AIAA Paper 95-2110 (1995)
- [3] T.W. Megli, H. Krier, and R.L. Burton: AIAA Paper 95-1961 (1995)
- [4] C.A.J. Fletcher: Computational Techniques for Fluid Dynamics, Springer-Verlag vol. 1 (1991) 237-261
- [5] B.P. Leonard: Comput. Methods in App. Mech. and Eng., 19 (1979) 59-98
- [6] T. Hayase, J.A.C. Humphrey, and R. Greif: Journal of Comput. Physics, 98 (1992) 108-118
- [7] S. Osher and S. Chakravarthy: SIAM J. Numer. Anal., 5 vol. 21 (oct. 1984) 955-983
- [8] H.L. Stone: SIAM J. Numer. Anal., 5 vol.3 (sept. 1968) 530-558.
- [9] D.W. Peaceman and H.H. Rachford, Jr., J. Soc. Indust. Appl. Math., 3 (1995) 28-41

Topic 6

High frequency discharges.

Investigation of Low Pressure Air RF Discharge

A.G.Shishkin¹⁾ and G.G.Shishkin²⁾

¹⁾ Dept. of Computational Mathematics & Cybernetics, Moscow State University, 119899, Vorobjovy Gory, Moscow, Russia

²⁾ Research Institute of Applied Mechanics & Electrodynamics of Moscow State Aviation Institute, 125871, Moscow A-80, Volokolamskoe shosse, 4, Russia

1. Introduction

Capacitively coupled RF discharges are receiving increasing attention due to their wide application in microelectronics, engineering industry, plasma chemical reactions, medicine and other areas. Usually in capacitive RF discharges on an alternating current the power is coupled to the plasma through parallel plate electrodes. However, this wide-spread configuration is not always convenient. In this contribution the capacitively coupled RF discharge configuration where one of the electrodes is the case of the metallic chamber is considered. Such type of the discharge was used in our experiments on high biological cleansing of materials and instruments from microorganisms.

To estimate theoretically the parameters of the discharge plasma the self-consistent mathematical model based on drift-diffusion approximation is developed. The parameters of the discharge are investigated experimentally and theoretically for high frequency case when the frequency of RF source ω_{RF} is much greater than the ion plasma frequency ω_{pi} . The numerical and experimental results are shown to be in a good agreement.

2. Theory

The schematic plot of gas discharge chamber is given in Fig.1. The plasma assumed to have no spatial gradients in y and z directions. The model of the capacitive RF discharge used in the present contributions is based on continuum equations of change.

The basic assumptions are the following ones [1-3]. Electron and ion motion is assumed to be collisionally dominated so that electron and ion momentum balance equations reduce to expressions incorporating drift and diffusion. Electrons are assumed to have Maxwell-Boltzmann distribution. Electrons, positive and negative ions are the charged species in a gas which is nominally air.

Thus the model is based on the self-consistent solution of the electron and ion continuity and momentum transfer equations and the equation of the balance of electron thermal energy. These are coupled with Poisson's equation for a given potential waveform between electrodes.

Electron and ion kinetic coefficients were taken from [4,5]. The equations were numerically solved by Sharfetter - Gummel method [6,7]. The calculations have been done for different RF frequencies, voltage, electron temperature for helium and air. The calculated results were compared with experimental ones.

3. Experiment

The experimental setup included the following systems: gas discharge chamber, vacuum systems, electrotechnical unit, RF generator, control and measuring units.

Gas discharge chamber of volume 2 l was made from stainless steel and served as an electrode. The second electrode was located in the central section of the chamber (Fig.1). As an energy source RF generator operated at frequency f_{RF} of 13.56 and 27.12 MHz with output power 100 W was used.

To measure the electromagnetic fields intensity in the surrounding space selective and panoramic noise analyzers with sensitivity up to 1 μ V were used.

By the spectroscopic and probe measurements the spatial distributions of electron temperature T_e , density n_e , pressure p , potential V , integral intensity of optical radiation and other parameters were determined. Probe measurements were carried out across and along the chamber. Some experimental results of measurements are presented in Table 1.

4. Discussion

Through measured values of discharge current, voltage and phase shift between them the discharge impedance was calculated. From the results of measurements one can conclude that with the increase in pressure the active and capacitive resistances drop, i.e. the discharge impedance diminishes in magnitudes.

In our conditions the increase in applied power usually led to the rise of discharge impedance while the voltage was maintained at a steady level. That is typical for glow discharge. The discharge impedance depends strongly as well on the generator frequency, residual pressure, form of electrodes and their relative location and on a number of other factors.

The vibrational temperature of nitrogen molecules in the main state was determined by measuring the relative intensities of electron-vibrational bands. It follows from the experimental results that gas temperature is about 450-500 K whereas the oscillating temperature is about 4500-500 K. It is also necessary to note that the glow intensity is maximal in electrode sheaths.

The comparison of experimental results and those calculated numerically using the model developed allows to draw a conclusion about their good agreement. For example, in Fig.2 the spatial variation of potential is shown. The solid line presents the results calculated numerically and circles - the measured values. One can see rather close coincidence of theoretical and experimental. This is also confirmed by the Table 1 where measured and calculated electron density and temperature are presented. The given values are relevant to the point

located in 1 mm distance from the electrode. The indices «1» - «3» correspond to three different values of gas pressure $p = 0.01, 0.1$ and 1 Torr, respectively.

Thus the general features of capacitively coupled RF discharges, for instance, the existence of the space charge sheaths, are well appeared in our study. The space charge sheaths in front of the electrodes lead to a DC bias voltage between the bulk plasma and these electrodes. Ions are accelerated out of the bulk towards the electrodes during the whole RF cycle due to this bias voltage. The continuous flux of energetic ions perpendicular to the electrodes and materials located on their surfaces leads to the heating of materials. That was necessary in our experiments for cleansing of tools. Furthermore, in such discharges it is possible to sustain discharge between electrodes with isolated material and instruments located on them.

5. Acknowledgements

The authors would like to acknowledge the assistance of A.M.Repin in part of the experimental work.

6. References

- [1] D.B.Graves: J. Appl. Phys., **62** (1987) 88.
- [2] Y. Oh, N.Choi, D.Choi: J. Appl. Phys., **67** (1990) 3264.
- [3] S.K.Park, D.J.Economou: J. Appl. Phys., **68** (1990) 3094.
- [4] A.D.MacDonald *Microwave Breakdown in Gases* (John Wiley & Sons), N.Y., 1966.
- [5] J.A.Dutton: J. Phys. Chem. Ref. Data, **4** (1975) 577.
- [6] D.I.Sharfetter, H.K.Gummel: IEEE Trans. Electron. Devices, **ED-16** (1969) 64.
- [7] J.-P.Boeuf: Phys. Rev. A, **36** (1987) 2782.

	Experiment	Theory
T_{e1} [eV]	6.5	6.09
T_{e2} [eV]	4.7	4.51
T_{e3} [eV]	3.2	2.85
n_{e1} [cm ⁻³]	$0.5 \cdot 10^{10}$	$0.37 \cdot 10^{10}$
n_{e2} [cm ⁻³]	$2.23 \cdot 10^{10}$	$1.99 \cdot 10^{10}$
n_{e3} [cm ⁻³]	$2.2 \cdot 10^{10}$	$4.2 \cdot 10^{10}$

Table 1 Comparison of experimental and numerical values of electron temperature T_e and density n_e for different gas pressures ($p = 0.01, 0.1$ and 1 Torr).

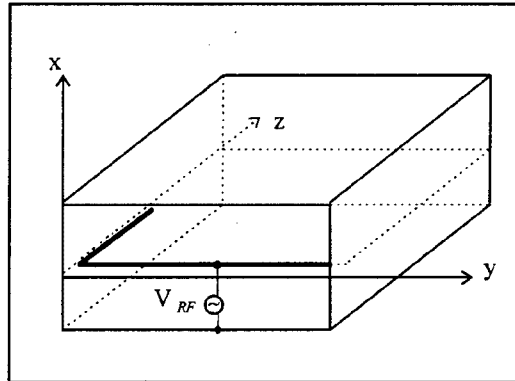


Fig.1 Schematic plot of gas discharge chamber

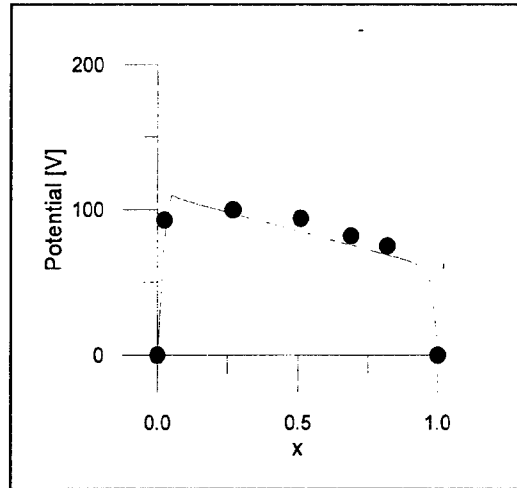


Fig.2 Calculated (solid line) and measured (circles) potential variation between electrodes for air discharge. Here $f = 13.56$ MHz, $V_{RF} = 328$ V, $p = 0.1$ Torr.

Electron Energy Distribution Function in an Axially Inhomogeneous UHF Argon Plasma Column

Ts. Petrova

Faculty of Physics, Sofia University, BG-1164 Sofia, Bulgaria

1. Introduction

Theoretical models of UHF discharges sustained by travelling electromagnetic waves consist of two parts—kinetic and electrodynamic. The first one points out plasma parameters and the second part focuses on the wave behaviour. It is the purpose of the present work to obtain the electron energy distribution function (EEDF) in an axially inhomogeneous UHF argon plasma column sustained by an electromagnetic wave of frequency $\omega/2\pi = 2.45$ GHz. The plasma column together with the dielectric discharge tube and a metallic enclosure is an integral part of the waveguiding structure. The length of the plasma column is usually much larger than its diameter. The whole system extends axially and, under travelling wave conditions it is axially nonuniform since the plasma density decreases away from the launcher. The calculations are applied to study the axial structure of plasma column with a radius $R = 0.45$ cm, contained in a dielectric tube of thickness $d = 0.15$ cm and permittivity $\epsilon_d = 4.8$ surrounded by vacuum and a metal enclosure of radius $R_1 = 2.0$ cm at gas pressure of 1.8 Torr and gas temperature $T_n = 300$ K [1].

2. Basic relations

The basic relations for the kinetic part are: (i) the Boltzmann equation, (ii) particle balance equations, (iii) electron energy balance equation; and for the electrodynamic part: (iv) a local wave dispersion relation and (v) the wave energy balance equation.

The EEDF has been calculated from the homogeneous electron Boltzmann equation by using the two terms Legendre polynomial expansion. This equation includes by appropriate collision integrals the action of elastic and several inelastic electron-atom collisions, electron-electron and electron-ion collisions and the impact of a UHF electric field [2,3]

$$E_{\text{eff}} = \frac{E_0}{\sqrt{2}} \frac{v_m(u)}{\sqrt{v_m^2(u) + \omega^2}},$$

where v_m is electron-neutral collision frequency for momentum transfer and E_0 is the root-mean-squared field. A model of two blocks of effective excited levels for argon (Ar 3s with $\epsilon_1 = 11.548$ eV and Ar 4p with $\epsilon_2 = 12.907$ eV) has been used taking into account follow-

ing elementary plasma processes: electron-electron and electron-ion collisions, excitation from the ground state, step-wise excitation and deexcitation, direct and step-wise ionization, imprisonment of the radiation, ambipolar diffusion and dissociative recombination.

The EEDF must satisfy the particle balance equations for electrons, excited atoms, atomic and molecular ions as well as the electron energy balance equation. From this set of equations it is possible to derive all plasma characteristics (mean electron energy, effective electron-neutral collision frequency for momentum transfer v_{en} , mean power θ required for sustaining an electron-ion pair in the discharge, and the densities of excited atoms considered, atomic and molecular ions) as functions of the electron density. From the local wave dispersion relation, the dependence of the electron density on the wave number (the so called *phase diagram*) can be obtained. The wave energy flux carried by the wave is dissipated by the electrons and is expended for elastic and inelastic collisions, diffusion and recombination. The wave energy balance equation with the values of θ and v_{en} , calculated from the kinetic equations, yields the axial distribution of the local electron number density. Using this connection between kinetics and electrodynamics it is possible to obtain the axial distribution of the EEDF as well as all plasma and wave characteristics selfconsistently, namely the wave number, wave power and all wave field components, the population of the excited atoms, atomic and molecular ions etc.

3. Results and discussion

Figure 1 shows the corresponding axial variation of the isotropic distribution as a function of the electron kinetic energy. The end of the plasma column is denoted by $z = 0$. As can be seen, the EEDF remarkably differs from the Maxwellian one, but near the exciter, where the electron density is high, the EEDF tends to Maxwellian.

In our former studies [4] the mean power θ required for sustaining an electron-ion pair in the discharge has been calculated, using the Maxwellian EEDF. Moreover, in [5] the relation between the electron density and the wave power per unit column length absorbed by the electrons Q has been postulated to be in the form $Q \propto n_e^{1+\beta}$ with an appropriate constant β and to be independent on the axial position. In fact this postulated relation of the electrodynamic code replaces the all kinetic part of the model. Such an approach is

applicable only in limited ranges of gas pressures. Using the model briefly presented above this limitation is avoided and the longitudinal dependence of both $\theta(z)$ and $Q(z) = \pi R^2 n_e(z) \theta(z)$ can be correctly described.

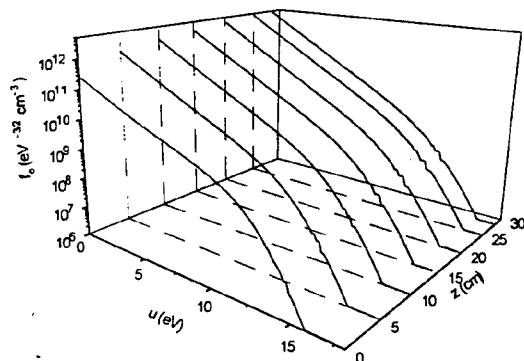


Fig. 1. Axial distribution of EEDF at $p = 1.8$ Torr

The results for the EEDF (normalized with respect to unity) presented below illustrate the ability of the numerical code to operate at different discharge conditions. The isotropic distribution as a function of the kinetic energy, shown in Fig. 2, sensitively depend on the electron density. Similar results have been obtained in [6], where the effects of the electron-electron collisions has been investigated. As can be expected at high electron density the distribution function is Maxwellian.

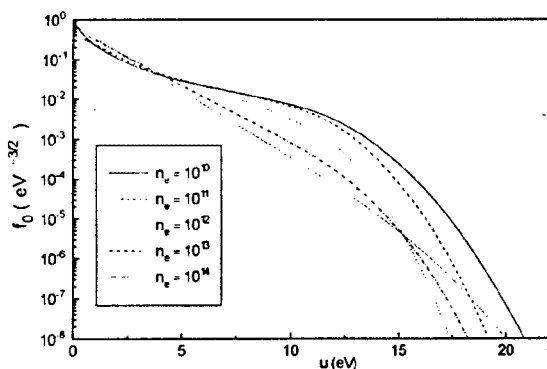


Fig. 2. EEDF at $p = 1.8$ Torr at different electron densities

The results presented in Fig. 3 have been obtained for an electron density $n_e = 10^{12} \text{ cm}^{-3}$ at different gas pressures. The low energy part of the isotropic distribution is not sensitive when the gas pressure changes, while the high energy part (above the first excitation potential) remarkably changes with the gas pressure variation. Namely the high energy part plays an important role in the calculation of the rate constants for all inelastic processes. Taking into account that the threshold energy

for direct ionization is 15.755 eV one can see from Fig. 3 that the role of this process is negligible small at higher pressures. This yields a strongly nonlinear dependence $\theta(n_e)$ (comparing the calculated one with a Maxwellian electron energy distribution function [4]) because of the increasing of the relative contribution of the step-wise processes at higher pressures.

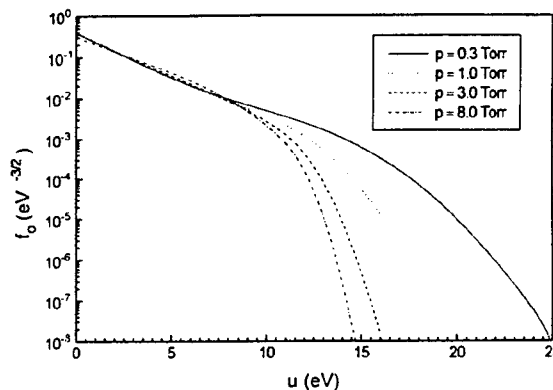


Fig. 3. EEDF for $n_e = 10^{12} \text{ cm}^{-3}$ at different gas pressures.

Acknowledgments

This work was supported by the National Fund for Scientific Research under Grant No. F-471/94.

References

- [1] A. Gamero, J. Cotrino, A. Sola, V. Colomer: J. Phys. D: Appl. Phys., **21** (1988) 1275
- [2] R. Winkler, in *Microwave Discharges: Fundamentals and Applications*, eds. C. M. Ferreira and M. Moisan (Plenum, New York, 1993) p. 339
- [3] C. M. Ferreira, J. Loureiro: J. Phys. D: Appl. Phys., **17** (1984) 1175
- [4] E. Benova, Ts. Petrova, A. Blagoev, I. Zhelyazkov: J. Appl. Phys., **79** (1996) 3848
- [5] I. Zhelyazkov, E. Benova: J. Appl. Phys., **66** (1989) 1641
- [6] P. A. Sá, J. Loureiro, C. M. Ferreira: J. Phys. D: Appl. Phys., **25** (1992) 960

FEATURES OF HIGH-PRESSURE NON-SELF-MAINTAINED VOLUME DISCHARGE INSTABILITY IN A QUASIMONOCROMATIC MICROWAVE

O.A.Sinkevich and V.E.Sosnin

Heat Physics Depart., Moscow Power Eng. Institute,
14, Krasnokazarmennaya, Moscow, Russia, 111250
fax: (095) 3628938; e-mail: senkevich @ postbank.rospace.ru

Non-equilibrium microwave plasma generated by a powerful microwave drive, due to its advantages over common discharges (such as high plasma production efficiency remote discharge ignition and so on), is an attractive medium for various plasma-assisted technologies, far beyond the scope of common plasma applications (see, for example [1]). Generally, the main problem is to create and to maintain uniform large-scale plasma, and the most suitable way to generate such plasma consists of employing microwave powers below breakdown threshold, i.e., form a so-called non-self-maintained (nsm) discharge that requires some sort of external preionization. However, the time of uniform plasma evolution in a microwave is restricted to development of different thermal, kinetic and ionization-field instabilities, resulting in formation of an intricate spatial structure.

All earlier theoretical studies of microwave plasma instabilities (see references in [1]) were relevant to a plane monochromatic microwave drive, and the received increment expression has singularity in the zone of resonant instability (RI) [2], which is a consequence of the adopted model. Since singularity is integrable, transition to considering a quasimonochromatic microwave, or a microwave packet allows to avoid the above difficulty and obtain correct values for the increment in RI region.

1. Ionization-field instability

According to the above reasoning we represent the unperturbed microwave as

$$E_0' = \frac{1}{2} \int d\omega E_\omega \exp(ik_\omega z - i\omega t) + c.c.,$$

$$E_\omega = (E_{x\omega}, iE_{y\omega}, 0).$$

Utilized quasimonochromatic approximation means that the expansion coefficients $E_{x\omega}, E_{y\omega}$ are essentially nontrivial only in the vicinity $|\Delta\omega|$ of some given frequency ω_0 so that the integral field can be roughly treated as plane monochromatic wave that propagates in z direction

$$E_0' = \frac{1}{2} E_0 \exp(ik_0 z - i\omega_0 t) + c.c.$$

Below we find solution for the particular situation when the expansion coefficient $E_{i\omega} = E_{i0} f(\omega)$,

$$f(\omega) = \frac{\alpha \sin(\alpha(\omega - \omega_0))}{\pi \alpha(\omega - \omega_0)}; \quad f(\omega) \text{ goes over into}$$

δ -function as $\alpha \rightarrow \infty$. The main reason for such choice of $f(\omega)$ is that this form is the most convenient for further manipulations and allows to derive resulting increment in explicit form. As for the applicability of a final expression to different more realistic situations we believe that all results will remain intact since maximum increment is determined by increment behavior near already mentioned singularity and therefore the particular adopted form for $f(\omega)$ can not seriously affect final expression.

We consider plasma layer with the concentration, that is smaller than the critical one, as being warmed by a plane quasimonochromatic microwave and study linear evolution of arbitrary plasma perturbations. For times, smaller than the time of overheating processes, the system, governing plasma evolution, includes the following equations:

1. Equation for plasma density n :

$$\frac{\partial n}{\partial t} = D_a \Delta n + (v^i - v^a) n + Y,$$

where v^i, v^a are the frequencies of ionization and accommodation, assuming that $v^i = v^i(|E_a|)$, where E_a is the instant amplitude of the quasimonochromatic microwave. The term Y models the action of a external source of ionization.

2. Equation for the electric field E' in general form:

$$\Delta E' - \nabla \nabla E' - \frac{1}{c^2} \frac{\partial^2 E'}{\partial t^2} = \frac{4\pi}{c^2} \frac{\partial j'}{\partial t},$$

$$j' = -enV_e'.$$

3. Equation for electrons movement describing vast electrons oscillations in the microwave drive in the form:

$$\frac{dV_e'}{dt} = -\frac{e}{m} E' - v_e V_e',$$

(Other notifications are generally accepted [1,2].)

The problem is considered with an initial plasma perturbation of arbitrary form: $t = 0$, $n = n_0 + \delta n_0$, where n_0 is the uniform plasma background (for non-self-maintained discharges $v^a > v^i$), δn_0 is the initial plasma perturbation.

Accomplishing original problem linearization in respect to stationary background $f = f_0 + df$, $f = n, E', V_e'$ and resolving the linearized system with the use of Laplace transformation in t and r one can easily receive for the case of high-pressure MD ($\omega / v_e \ll 1$) the following solution:

$$\delta n(r, t) = \left(\frac{1}{2\pi i} \right) \int_{\sigma-i\infty}^{\sigma+i\infty} dp \delta n_{0p} \exp(pr + \gamma_{in} t), \text{ where}$$

e

$$\gamma_{in} = (v^i - v^a) + D_a p^2 + Z X_p^{-1} \alpha_0 v^i,$$

$$Z = -i \frac{4\pi}{\omega_0} \sigma, \quad \alpha_0 = \frac{d \ln v^i}{d \ln |E|},$$

$$X_p^{-1} = B \frac{1}{\omega' + \omega_0} (\beta(\omega_0) -$$

$$- \exp(-i\alpha(\omega' + \omega_0)) \beta(\omega')),$$

$$\beta(\omega) = 1 + R c^2 / \omega^2 \epsilon_0, \quad R = e_x p_x^2 + e_y p_y^2,$$

$$e_i = E_{i0}^2 / E_0 E_0^*, \quad i = x, y,$$

$$B = \frac{c}{2ip_z \sqrt{\epsilon_0}}, \quad \omega' = \frac{p^2 c}{2ip_z \sqrt{\epsilon_0}},$$

where δn_{0p} is the Laplace transform for the initial plasma perturbation. Strictly speaking the above expression for increment γ_{in} holds when $\text{Im}(\omega') \leq 0$; in the opposite case γ_{in} has similar form.

There are several items of interest:

-unlike the increment in monochromatic microwave (see, for example [2]) the obtained increment has no singularity;

-the maximum increment for a definite volume plasma belongs to RI domain ($\omega' + \omega_0 \approx 0$) and explicitly depends on microwave parameter $|\Delta\omega| = 1/\alpha$, for example in circular-polarized microwave; $p \parallel k_0$, $|p| \approx 2\omega_0 / c$:

$$\gamma_{in} = \frac{1}{4} \left(\frac{\omega_p^2}{\omega_0 v_e} \right) \frac{\alpha_0 v^i (\alpha \omega_0)}{\sqrt{\epsilon_0}},$$

where ω_p is the plasma frequency; in real situations $\alpha_0 \approx 10$, $\alpha \omega_0 \approx 10 + 100$, and therefore it is possible that $\gamma_{in} \gg v^i$;

-the increment form suggests simple way to suppress the discussed instability by utilizing a microwave with the broad band to decrease $\alpha \omega_0$.

The same result probably will be achieved if to use periodic pulsed drive. Note that the development of instability establishes in the high-pressure plasma intricate pattern with spatial spacing $\approx c / 4\omega_0$, so if this structure appears due to this instability (the difference in spacing can be easily explained by known doubling scale phenomenon in the nonlinear stage), the proposed method can be utilized to stabilize plasma in microwave plasma-assisted technologies.

2. References

1. High-Frequency Discharge in Wave Field. Gor'ri: IPF AN SSSR, 1988.
2. Sinkevich O.A. and Sosnin V.E. J. Phys. D: Appl. Phys: **29** (1996) 2609.

Topic 8

Plasma diagnostic methods.

Measurements of Electron Energy Distribution Function in Positive Column Region of DC-Magnetron Sputtering Device.

A.A.Garamoon, A.Abu Al-Hassan*, M.A.Hassouba* and F.F.Elakskar

Phys. Dep. Faculty of Science, Azhar University, Nasr City, Cairo, Egypt.

*Phys. Dep. Faculty of Science, Benha University, Nenha, Egypt.

Abstract

The electron energy distribution function (EEDF) in the positive column region of a DC-magnetron sputtering device were measured. The distribution was found to be Maxwellian in the pressure range of 0.5-6 torr for Ar and He gases. Electrons were have a chance to thermalize themselves due to the long plasma life time in this region. Electron density and temperature were also determined using different techniques.

Introduction

Positive column is the best understood region of the DC-glow discharge. However, recent published investigations were devoted toward describing the mechanism of the positive column on the basis of a consequent kinetic treatment of the electron components (Dietrich et al. 1993 [1]; Toudet, 1995 [2]; Kaneda, 1990 [3]). Thus, further investigation of the EEDF is of great interest (Kimura et al. 1995 [4] & Behnke 1992 [5]). Further more, experimental measurements of the distribution function, in particular in DC-magnetron, received little attention in the literature's. In 1996, Elakshar et al. [6] studied the EEDF in the cathode fall-negative glow regions of the magnetron. They concluded that the distribution function deviates from being Maxwellian as a result of the short plasma life time in these regions.

The purpose of the present work is to investigate the EEDF in the positive column region of DC-magnetron sputtering device using Ar & He gases.

Experimental Setup

The DC-magnetron device consists of two electrodes, copper anode and aluminum cathode each of 5 cm diameter and separated by about 3-6 cm distance apart. A permanent magnet was placed under the cathode to confine the gas discharge in the space between the two electrodes. The device was operated by 400-700 V at current density of about 10-12 A/m². A large vacuum vessel were located at the center of the vessel. The vessel was evacuated to 10⁻⁵

torr using rotary and diffusion pumps. The EEDF was determined by measuring the electron current second derivative using Langmuir single probe. The probe was placed in the positive column region and can be moved either radially or axially.

Results and Discussion

Figures (1) [a],[b] show the EEDF in the positive column region for both Ar & He glow discharges. Maxwellian distribution functions are obtained which compared with the theoretical one at the same energy, having a temperatures of 4.6-7 eV & 5.8-8.8 eV, respectively. Figures (2) [a], show a more sensitive test for the presence of Maxwellian distribution i.e. by plotting the semi-log curves of the second derivative of the electron current against the probe voltage, a straight lines are obtained. These straight lines prove that there was only one group of electrons in the positive column region, unlike the two groups of electrons found in the cathode fall region (Elakshar et al., 1996 [6]).

The electrons would have a chance to redistribute their energy and thermalize themselves in a Maxwellian distribution function. The self collision time t_c is given by (Spitzer, 1967 [7]) :-

$$t_c = m_e^{0.5} (3kT_e)^{3/2} / [17.94N_e e^4 Z^4 \ln L]$$

The plasma life time, in the positive column region, is about an order of magnitude longer than t_c within the used pressure range in both Ar & He discharges.

Electron density N_e was estimated by integrating the EEDF in Fig. (1)

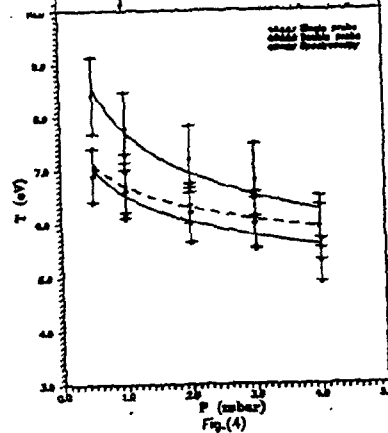
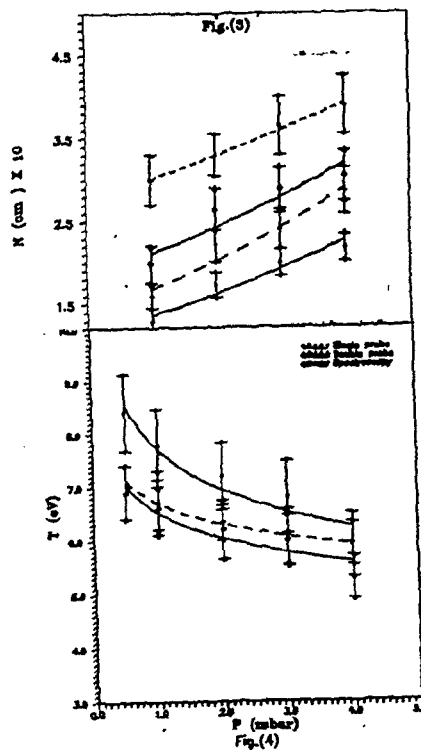
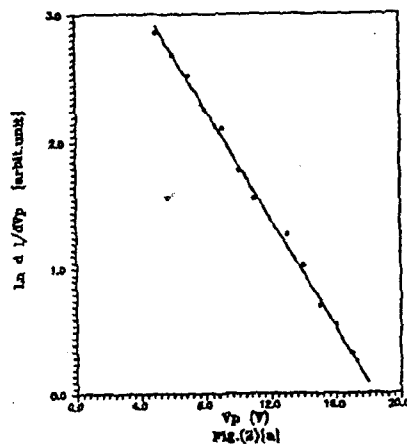
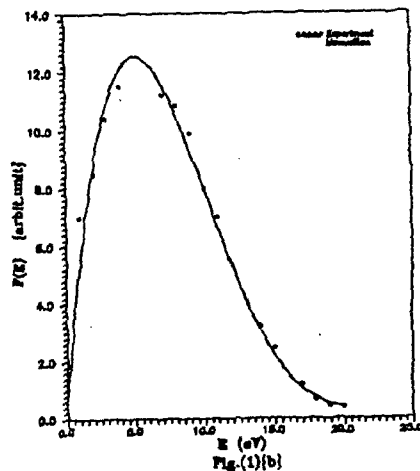
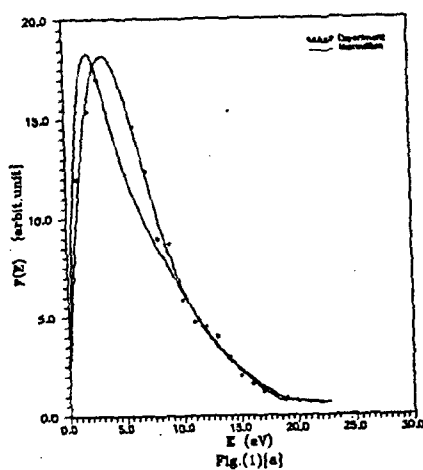
$$N_e = \int_0^{\infty} F(E) dE. \text{ Values of } N_e \text{ were}$$

also compared with those estimated using different methods e.g. double probe, Langmuir single probe and log-log method. Figure (3) shows values of N_e by different methods for both gases as a function of the gas pressures.

The estimated values of T_e , using Figs. (1) & (2), were compared with those determined by spectroscopic (line/line intensity ratio) technique (Fig. 4). For He gas, lines 5016 & 3389 Å were used instead of the lines 5048 & 4713 Å. Line 3389 Å is among the very few lines for which the influence of secondary processes can be computed using reliable cross-section values. The intensity of the 5016 Å line is influenced only by less than 10 % of the secondary processes. Unfortunately this is generally difficult to do for most levels and for other gases due to lack of atomic data.

References

- [1] M.Dietrich et al. XXI ICPIG, Bochum (1993).
- [2] E.I.Touder, J.Phys. D., 28, 75, (1995).
- [3] T.Kaneda, T.Kubota and J.S.Chang, J.Phys. D., 23, 500, (1990).
- [4] T.Kimura, A.Kano and K.Ohe, Phys.Plasma, 2, 4659, (1995).
- [5] J.Behnke and J.B.Golubowski, Optika & Spektroskiba, 73, 65, (1992).
- [6] F.Elaksher et al., ICPP 96, Nagoya, (1996).
- [7] L.S.Spitzer "Phys. of Fully Ionized Gases" (1967).



Measurements of plasma density: a comparison between resonance cones and Langmuir techniques

C. Riccardi, M. Salierno, M. Fontanesi

Dipartimento di Fisica-Universita' degli Studi di Milano
Via Celoria, 16 - 20133 Milano - Italy

Th. Pierre

Laboratoire de Physique des Milieux Ionisés
URA 835 C.N.R.S. , Université de Nancy I, B.P. 239
54506 Vandoeuvre-les-Nancy Cedex - France

1. Introduction

Electron resonance cones can be used to diagnose the plasma density and electron temperature [1]. The main vantage of a diagnostic based on resonance cones is that it gives a local and direct measurement of plasma parameters, with respect to the usual Langmuir diagnostic. The aim of this work is to compare the two diagnostic methods and to show the feasibility of the resonance cones technique.

2. Purpose and results

Resonance cones in a magnetized plasma can be excited by an oscillating point source. Following the theory, the θ_c cone half-angle, i.e. the surface where the wave potential becomes singular, depends on the principal plasma parameters, like electron density and temperature. In the cold collisionless plasma approximation, the angle is given by the following formula:

$$\sin^2 \theta_c = (f_{pe}^2 + f_c^2 - f^2) / f_{pe}^2 f_c^2,$$

where f , f_{pe} and f_c are respectively the exciting, the electron plasma and the electron cyclotron frequencies. Exciting the cone at a given frequency f , and for a fixed magnetic field value B (and consequently f_c), from the experimental value of θ_c it is possible to estimate f_{pe} and so to obtain the value of the electron plasma density n_e . The introduction of thermal effects makes the theory more complex and induces both the apparition in the wave signal profile of a set of secondary peaks near the main one, both the shift of the cone angle. The angular distance between two consecutive secondary peaks is also related to the electron temperature. Consequently from the recorded wave signal, the plasma density and the electron temperature can be calculated. The experimental set up for resonance cones consists in a double probe with two pins, one of which is the emitter (fig.1), fed by a signal generator, and the other is the receiver. To avoid a phenomenon of reciprocal shadow inside the plasma, the pins of the probe have been positioned perpendicularly with respect to the magnetic field lines. A radial movement of the probe permits the estimation of the plasma density in different radial positions.

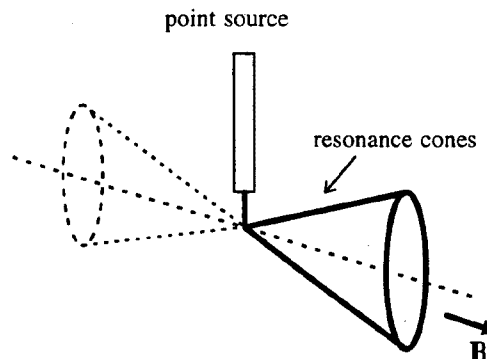


Fig.1 Resonance cones system configuration

In order to compare the density measurements based on resonance cones with those obtained through a Langmuir probe, a pin of the double probe has been also used to collect the Langmuir characteristics.

The experiment is performed in the toroidal magnetoplasma Thorello; typical working parameters are the follows: $P \approx 10^{-5}$ mbar, toroidal magnetic field $B = 1$ kG, $T_e \approx 1$ eV, $T_i \approx 0.3$ eV, edge plasma density $\approx 10^9 \text{ cm}^{-3}$, centre plasma density $\approx 10^{11} \text{ cm}^{-3}$.

The electron temperature effects are negligible for $\theta_c = 90^\circ$; so it is possible to work without such effects arranging the detection system in order to detect only resonance cones with $\theta_c = 90^\circ$. Having fixed pins, the measurement of the electron plasma frequency is carried out sweeping the signal frequency, individuando the signal maximum amplitude which corresponds to the electron plasma frequency.

By repeating measurements at different radial positions, a density radial profile can be obtained.

Fig.2 shows a comparison between a density profiles obtained through the Langmuir method with that got by the resonance cone angle. It can be seen that the density profile relevant to the resonance cone method (cones), agrees with that obtained with the Langmuir method based on the analysis of the electron saturation current (e-dens-lang).

It is known in fact that the Langmuir probe method gives two different plasma density values when it is considered, as reference current, the ion saturation current I^+ or the electron one I^- .

In particular it can be seen that density values got from I^+ , are generally greater than those obtained from I^- .

The difference between the n_e evaluated through Γ^+ and Γ^- current can be due to the high dependence of Langmuir method on the sheath area A_s that collects the current and to the presence of the magnetic field.

The presence of plasma in fact induces, around the probe, the formation of a sheath which thickness and dimensions are proportional to the potential difference applied to the probe.

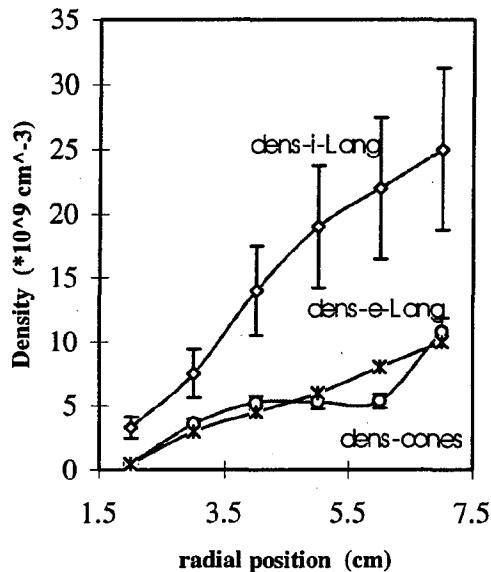


Fig.2 Density profiles

So for calculating the density, instead of considering the probe geometrical area A_p , it should be considered the effective area A_s that collects the charges.

Observing that $A_s > A_p$, it is clear that the n_e value obtained evaluating the effective area can give lower density values. The main difficulty is just the estimate of the sheath dimension. Consequently the n_e value can overestimated if obtained from Γ^- .

As concerns electron saturation current, even if there are no problems for the sheath, we must consider the effects due to the magnetic field that can modify the n_e value. Magnetic field intensity can be in fact a limitation to the Langmuir method for two mainly reasons: the reduction of the electron saturation current and the geometry of the probe with respect to the magnetic field line slope. The magnetic field of Thorello is so that for reading the Langmuir characteristic neither the model in absence of field nor that one for high fields are applicable, being for our case $\rho_e \ll d$ and $\rho_i \ll d$ ($\rho_{e,i}$ are the electron and ion larmor radius and d is the diameter of the probe). Indeed an accurate analysis performed by Piel [2] shows that, increasing B , the density got through the cylindrical probe, increases becoming more and more different from that one obtained from the plane probe, which value remains almost constant.

The effect of the magnetic field is not only correlated to the probe geometry but also to the orientation of the

probe surface with respect to the same magnetic field directions. For these mainly reasons it is important to consider methods which are not affected by complicated phenomena. The advantage of the density measurement through the resonance cones is so evident: measurements based on resonance cones do not depend on the system geometry, i.e. the characteristics of the launching system or the surface area of the detecting system and on the magnetic field intensity. Indeed it permits, in a more direct way, a "local" measurement of the density.

As concerns our measurements it is easy to realize that near the chamber edge, where the density gradient is high, it is not possible that the plasma density is of the order of 10^{10} cm^{-3} , as shown in the graphic relevant to Γ^+ . So that in our plasma the density measured by the electron saturation current seems to be more corrected than that given by the ion saturation current.

The main limit of applicability of the density diagnostic based on resonance cones is represented by the presence of high density fluctuations. It can be noticed that while the Langmuir method, using electron saturation current, can be applied again in plasmas with not negligible density fluctuations (an average value of the Γ^- current can be taken, for the resonance cones the diagnostic is no more applicable because the density fluctuations destroy the cone shape inducing a global broadening of the signal, not permitting a precise localisation of the mean resonance peak).

3. Conclusions

The based diagnostic on electron resonance cones permits a local and direct measurement of the plasma density. With respect to the usual langmuir diagnostic the resonance cones method used for the evaluation of the plasma density is not affected by the effective probe area, the probe geometry and on magnetic field effects. The only obstacle to this method is presented by high density fluctuations which can destroy the resonance cone envelope making impossible the determination of the maximum peak.

4. References

1. C.Riccardi, M.Salierno, P.Cantu', M.Fontanesi, Th.Pierre, Journal De Phys. IV,5 C6-67 (1995)
2. K.Hansen, T.Klinger, A.Piel, Rev.Sci.Instrum. 65 2615 (1994).

STARK WIDTHS PREDICTIONS FROM REGULARITIES FOR TRIPLY AND QUADRUPLY-CHARGED ION OFF-RESONANCES OF SEVERAL HEAVY ELEMENTS

J. Purić, M. Šćepanović*, V. Milosavljević and M. Ćuk

Faculty of Physics, University of Belgrade, P.O.Box 368, 11001 Belgrade, Yugoslavia

* Faculty of Sciences and Mathematics, University of Montenegro, 81 000 Podgorica, Yugoslavia

1. Introduction

Stark widths dependencies on the upper level ionization potential within spectral lines originating from ns-np off-resonance transition ($n=n_0+1$, where n_0 is the main quantum number of ground energy level of a corresponding emitter) of several doubly, triply, quadruply and quintuply charged ions [1-4] have been found and discussed. After being well established using existing theoretical calculations the dependencies have been used to predict additional Stark broadening data for triply charged ion off-resonance's of the following elements: Ca, Ti, Ga, Ge, As, Kr, Zr, Nb, Mo, In, Sn, Sb, Te, and Bi; and quadruply charged ion off-resonances of the following elements: Ge, Nb, Mo, Sn, Sb and Bi.

The procedure for Stark broadening data predictions was described elsewhere [5-7]. A comprehensive set of Stark broadening data [1-4] of the investigated ion off-resonance spectral lines has been used here to demonstrate the existence of Stark widths data regularities within this group of spectral lines. Namely, Stark parameters dependencies on the upper level ionization potential of the investigated lines originating from ns-np off-resonance transition arrays of the following doubly (Ar, Al, Si, P, S and Cl); triply (C, N, O, Ne, Mg, and Si); quadruply (C, F, O, Ne, Al and Si); quintuply (F, N, Ne, Na, Si and P) charged ions have been found and discussed.

Different kinds of regularities within Stark parameters of the given spectra can be explained on the bases of their dependence on the upper level ionization potential [5-7]. A general form of that dependence in the case of the particular transition array along the Periodical table of the elements is

$$w = N_e f(T) z^c a \chi^b \quad (1)$$

where w is the line width in angular frequency units; χ is the corresponding upper level ionization potential expressed in eV; z is the rest core charge of the emitter seeing by the electron undergoing transition. Coefficients a , b and c are independent of the temperature, ionization potential, and the electron density for a particular transition.

2. Results and discussion

It has been verified that the Eq.(1) is appropriate for all the investigated ns-np transitions in the above mentioned group of the ions at different temperatures and electron densities. Namely, it was found that the best fit can be obtained if $f(T)$ is approximately taken as $T^{-1/4}$ instead $T^{-1/2}$ [10].

As an example, the reduced Stark width

$$w^* = w \sqrt[4]{T} z^c = a \chi^b, \quad (2)$$

as the function of the inverse value of the upper level ionization potential χ of the corresponding transition is given in Fig. 1.

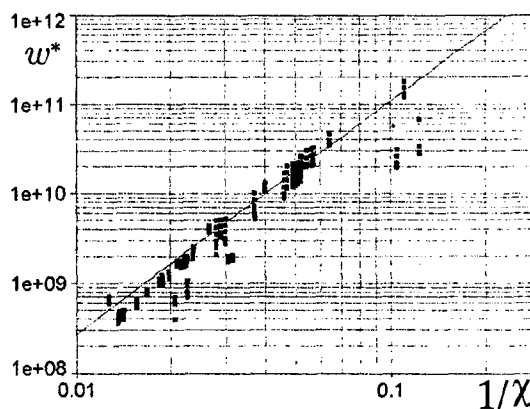


Fig. 1.

By a comparison of the above described regularities and those presented elsewhere [8] (Figures 1 - 7) one can conclude that the method used here differs in the choice of the variable conveying atomic structure information. Prior work (see Ref. [6] and Refs. therein) was based on the hydrogenic model. Consequently, it used integer principal quantum numbers instead of the upper level ionization potential. Although both parameters take into account the density of states perturbing the emitting state, the advantages of the present method are: (i) χ based trend analyses achieve better fits; (ii) in χ values the lowering of the ionization potential [9] is taken into account, predicting merging with continuum when the plasma environment causes a line's upper state ionization potential to approach zero;

and (iii) the ω dependence on χ is theoretically expected [5-7].

Using the existing Stark parameters data for the investigated lines originating from different ions the corresponding coefficient a, b and c from Eq. (1) are found as $a = 4.30 \times 10^{13}$, $b = 2.60$ and $c = 4.18$. The corresponding correlation's factors were almost equal to unity. Therefore, the Eq. (2) can be used to calculate Stark widths of the triply and quadruply charged ion off-resonance's of different elements along the Periodic table of the elements not calculate so far taking T and χ in K and eV, respectively. The results obtained by the above described procedure several triply and quadruply charged ions are given in Table 1. All data are normalized at an electron density $N_e = 1 \times 10^{23} \text{ m}^{-3}$ for different temperatures.

Table 1. Stark full half widths $(n_0+1)s - (n_0+1)p$ off-resonance's of several triply and quadruply-charged ions for an electron density $N_e = 1 \times 10^{23} \text{ m}^{-3}$ at different electron temperatures

Emitter $\lambda[\text{\AA}]$	Temperature in 10^5 K				
	0.5	1	2	4	8
Ca IV 2858.2	0.0265	0.0223	0.0187	0.0157	0.0132
Ti IV 2103.7	0.0402	0.0338	0.0284	0.0239	0.0201
Ga IV 1338.1	0.0079	0.0067	0.0056	0.0047	0.0039
Ge IV 3677.8	0.3886	0.3268	0.2748	0.2311	0.1943
As IV 3216.9	0.2449	0.2059	0.1732	0.1465	0.1225
Kr IV 2609.5	0.1179	0.0992	0.0834	0.0701	0.0589
Zr IV 2287.3	0.0685	0.0576	0.0485	0.0407	0.0343
Nb IV 2182.0	0.0456	0.0384	0.0323	0.0271	0.0228
Mo IV 2061.0	0.0241	0.0203	0.0171	0.0143	0.0121
In IV 1810.2	0.0227	0.0191	0.0161	0.0135	0.0114
Sn IV 1437.5	0.0124	0.0105	0.0088	0.0074	0.0062
Sb IV 3736.3	0.4126	0.3469	0.2917	0.2453	0.2063
Te IV 3586.3	0.3485	0.2931	0.2465	0.2073	0.1743
Bi IV 3684.7	0.3977	0.3344	0.2812	0.2365	0.1988
Ge V 1116.8	0.0051	0.0429	0.0036	0.0030	0.0026
Nb V 1877.3	0.0464	0.0390	0.0328	0.0276	0.0232
Mo V 1748.8	0.0209	0.0176	0.0148	0.0125	0.0105
Sn V 1302.1	0.0145	0.0122	0.0102	0.0086	0.0072
Sb V 1226.0	0.0091	0.0076	0.0064	0.0054	0.0045
Bi V 2682.0	0.2784	0.2341	0.1968	0.1655	0.1392

3. Conclusion

Stark parameters dependence on the upper level ionization potential, after being well established within particular ns-np off-resonance transition array can be used for prediction of the parameters for the corresponding ion off-resonance of heavier elements where not available so far. The electron-impact widths predicted by intratransition arrays regressions analyses are of the same accuracy as the accuracy of the results

used in the course of the calculation of coefficients a, b and c from Eq.(1) in order to generate widths for heavier elements ion off-resonance's. This method is computationally simple, involving each line's upper level ionization potential and one multiplicative and one exponential fitting parameter per the investigated group of spectral lines originating from ns-np off-resonance transition arrays for the given emitter temperatures and electron densities. Such method is conducive to the method's incorporation into mathematical simulations of stellar atmosphere opacities.

4. References

- [1] H.R. Griem, Spectral Line Broadening by Plasmas New York:Academic (1974)
- [2] M.S. Dimitrijević, A & AS, 76, (1988) 53
- [3] M.S. Dimitrijević, A & AS, 100, (1993) 237
- [4] M.S. Dimitrijević, Astro.Lett. and Communications 28 (1993) 385
- [5] J.Purić, M. Ćuk, M.S.Dimitrijević, A.Lesage, ApJ, 382, (1991) 353
- [6] J.Purić, M.H.Miller, A.Lesage, ApJ, 416, 82 (1993) 825
- [7] J.Purić, Proc. of Invited Lectures III of XXI Int.Conf. on Phen. Ion. Gases, (eds. G.Ecker, U.Arend, J.Boseler), Ruhr-Universität Bochum (Arbeitsgemeinschaft Plasma Physik) (1993) 34.
- [8] M. S. Dimitrijević and S. Sahall Brechot, A & AS, 95, (1992) 109
- [9] D.R. Inglis, E.Teller, ApJ, 90, (1939) 439
- [10] J.Purić and M.Šćepanović, to be published (1997)

Topic 9

**Plasma wall interactions, electrode
and surface effects.**

Peculiarities of Discharge Formation Using Blade-Shaped Electrodes in a HF(DF) Laser

A F Zapol'sky, S D Velikanov, P A Evdokimov, E V Kovalev, I N Pegoev

Russian Federal Nuclear Center - All Russian Scientific Research Institute of Experimental Physics
607190, Mira prosp. 37, Sarov, Niznii Novgorod Region, Russia
Tel.: (831-30) 56646, Fax: (831-30) 54565, E-mail: zapolsky@otd13.vniief.ru

1. Introduction.

The electric parameters of pulse and pulse-periodic electric-discharge lasers depend greatly on the method used for discharge formation in the laser active volume. In this process uniformity and stability of a discharge are conditioned not only by the parameters of an exciting electric signal but also by the configuration of an electrode system in a discharge chamber, which is very important when discharge formation takes place in active mixtures with electronegative components, such as SF_6 , and also in small discharge gaps.

Nonuniformity not only affects the laser energy obtained with one-shot initiation, but also limits the extreme repetition rate of the output pulses, which caused some decrease in the average power of pulsed-periodic lasers. For example, the pulse-periodic HF(DF) laser described in [1] utilised the discharge formed in such an electrode system where the cathode was a collection of pins, separated electrically by resistors, and the anode was a plate with the special profile. The discharge was formed steady enough (without spark channels) in this configuration. But its appreciable nonuniformity led to the lower laser electric efficiency as compared with the case of flat electrodes with the special profiles.

Experimental results performed in the present report reveal the further progress of our investigation [2] and are indicative about peculiarities of discharge formation using a blade-shaped electrodes in an active medium of a HF(DF) laser. The influence of some modifications in the electrode system on uniformity and stability, and consequently on energy of lasing, is described for one-shot initiation.

2. Apparatus

The installation, which was used in our study, was implemented around an electric-discharge laser with UV preionization of a working mixture.

The electrodes producing the main and preionizing discharges were mounted into a discharge chamber, which windows were made of CaF_2 . The external resonator consisted of the mirrors with corresponding reflectivity of $r_1=0.96$ and $r_2=0.5$ at the working wavelength. It could be adjusted parallel to the windows of the discharge chamber. The high-voltage source supplying the discharge was a voltage-doubling Fitch generator, the total capacity of which was $C = 8.9 \text{ nF}$;

the duration of the initiating signal did not exceed $t = 50 \text{ nsec}$.

The main discharge was excited by the 260 mm along and 18 mm wide Stappaerts electrodes made of aluminium. The distance between the electrodes was unchangeable and equal to $d = 8 \text{ mm}$, but the electrodes could be replaced following the conditions of our experiment. The electrodes used for preionization discharge were tungsten wires with a 1 mm diameter and were placed on either side of the anode at the distance about 2 mm. Separating resistors were used to connect these electrodes with the main cathode. The spark channels appeared while the resistors were being charged by the Fitch generator output provided the UV preionization.

When the investigations of the flat electrodes with the special profile were finished, the cathode was replaced with the electrode which was a collection of blades. The longitudinal profile of each blade repeated the cross section of the flat electrode. The blades were parallel each other and perpendicular to the resonator axis. The width of each blade was $\Delta \approx 0.3 \text{ mm}$. They were placed with the step $\alpha \approx 1 \text{ mm}$. Their tops were flat areas with the width about 0.2 mm and their edges were rounded with the radius of curvature $r = 30 \dots 50 \text{ }\mu\text{m}$. The height of the blades measured up to the flat part of the tops was $H = 3 \text{ mm}$.

3. Experimental results

In our investigations the discharge was formed in the active mixture of the $\text{SF}_6 + \text{D}_2 = 6:1$ composition.

The discharge glow was recorded both over the end face of the discharge chamber and over the lateral side of the active volume of the laser. We have changed the pressure of the working mixture at the fixed charging voltages of the Fitch generator.

At the same time the laser energy was measured as well as the laser beam cross-section, which sizes repeated practically the sizes of the discharge glow.

Attention was paid to the fact that the discharge was formed with the peculiarities characteristic for each configuration of the electrodes.

So, for the flat electrodes with the special profile, the discharge glow was diffusive and bright near the anode, and it became weaker at the distances of 0.5...1.0 mm from the cathode. The width of the laser beam increased gradually from about 7 mm near the cathode to about 9

mm near the anode; the height was about 7 mm.

For the blade-shaped cathode and flat anode, the discharge starting on the cathode blades was formed as bright streams, which converged into the diffusive discharge at the distance of from two to three steps between blades. Meanwhile, the integrated discharge glow observed over the end face of the chamber was uniform as well as the laser beam cross-section, the width being about 10 mm and the height about 8 mm.

When both of the electrodes mounted in the chamber were blade-shaped, the flat discharge streams also appeared near the anode, but they were weaker than near the cathode. The diffusive discharge occupied still smaller area of the discharge gap, though the lasing was uniform along the whole discharge height, and the width of the laser beam increased up to about 12 mm.

At the same time the dependencies of the laser energy on the pressure of the working mixture were obtained for the several fixed charging voltages of the Fitch generator.

Fig.1 a) represents the sizes of the laser beam cross-section, and Fig.1 b) shows the dependencies of the laser energy obtained for the various combinations of the electrodes in the discharge chamber.

The dependencies shown in Fig.1 b) indicate that the laser energy increased by about 30% and the pressure of the working mixture, which was optimum for lasing, increased by 20% when the flat electrodes with the special profile were replaced with the two blade-shaped. In this way the range of the pressure of the working mixture for which the formation of the spark channels didn't yet take place was broadened from $P_{\text{mix}} = 0.14 \div 0.22$ atm to $P_{\text{mix}} = 0.1 \div 0.26$ atm, which proved a significant improvement of the discharge uniformity.

Measurements of the discharge voltage and current indicated that the obtained increase in efficiency of lasing was due to the more effective consumption of the energy stored in the capacitors of the Fitch generator. This phenomena can be accounted for strengthening of the electric field near the sharp edges of the blade-shaped electrodes. According to the paper [3] the electric field must be approximately five times greater than in the case of flat electrodes. In this process enhanced electron emission ensures some decrease of the maintaining voltage of a volumetric discharge, hence, the unused energy stored in the capacitors of the generator becomes smaller.

So, the carried out experimental investigations have proved that the use of blade-shaped electrodes with special surface profiling is equivalent to some increase in the voltage feeding a discharge, which makes it possible to increase the efficiency of a chemical laser. Here, discharge burning becomes more stable without any deterioration in its uniformity.

It is necessary to note that discharge broadening

provided the more complete utilisation of the electrode area, and an improvement in the useful surface of an electrode is of particular interest in the case of pulse-periodic electric-discharge lasers.

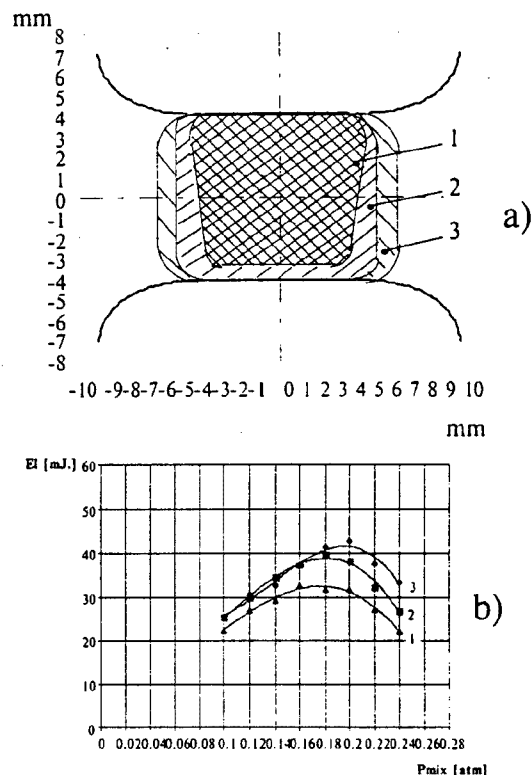


Fig.1 a) The laser beam cross-sections ($P_{\text{mix}} = 0.2$ atm); b) Dependencies of the laser energy (E_l) on the mixture pressure (P_{mix}) for the different combinations of the electrodes

$\text{SF}_6 : \text{D}_2 = 6 : 1$; $U_{\text{charg}} = 20$ kV;

1 - two flat electrodes,

2 - flat anode and blade-shaped cathode,

3 - two blade-shaped electrodes.

References

1. Rudko R I, Drozdowicz Z, Linhazes S, Bua D *Rev.Sci. Instrum.*, 53, 4, 452, (1982)
2. Velikanov S D, Zapol'sky A F, Frolov Yu N. *Physical Aspects of Operation of Reperitively Pulsed Closed-Circuit HF, DF Laser* (To be published in *Proceedings of the International Conference "lasers 96"* December, 1996, Portland, USA).
3. Bugaev S P, Kochkarev A V, Monlyov V I, Paychin V M *Pribori i Technica Experimenta (Moscow)* 2 160 (1974)

**Physical aspects of plasma chemistry,
plasma processing of surface,
and thin film technology.**

A Pulsed Microwave Discharging Device for Studies on Plasma-Wall-Interactions

M. Baeva*, X. Luo, Z. Zhang**, J. H. Schaefer and J. Uhlenbusch

*Department of Physics, Technical University Varna, 9010 Bulgaria

**Institute of Physics, Chinese Academy of Science, Beijing, China

Institute of Laser and Plasma Physics, University of Duesseldorf, Germany

1. Introduction

Microwave excited discharges are today finding increasing applications in the industrial plasma processing technologies. Mostly a dielectric window made of quartz glass or ceramic materials is used to couple the microwave energy into the discharge volume. Simultaneously it separates the outer atmosphere from the low pressure discharge chamber. It is commonly observed, as the microwave power is increased, the discharge tends to drift in direction of the source until a hot layer of plasma finally is built up at the coupling window. This is called window-burning effect. The hot plasma layer prevents the further coupling of the microwave energy to the inside of the discharge. The processing plasma may additionally be deteriorated by the sputtered window materials. Due to the high temperature it could even lead to the destruction of the window. Plasma-wall (plasma-window) interactions thus are of great practical interest.

In the following we present a plasma source

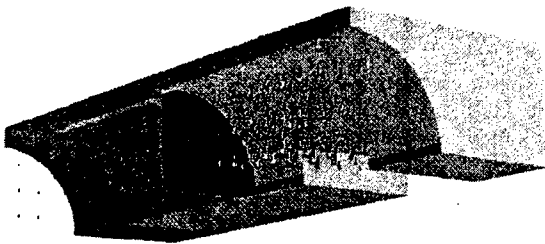


Fig 1 Distribution of electric field strength in the cylindrical cavity (only a quarter section is drawn)

excited by a pulsed microwave discharge. By a variation of the pulse length and pulse repetition rate we are able to adjust a controllable window-burning state. Diagnostic investigations can then be made under reproducible conditions.

2. Experimental setup

As is shown in Fig. 1, the discharge chamber consists of a cylindrical microwave resonant cavity of 9 cm in dia. and 10.2 cm in length. At the one end there is the coupling window made of quartz glass, at the other end a slider short-circuits the microwave. Four lateral windows are fixed for diagnostic purposes. The microwave pulses generated by a magnetron of the type YJ-1600 capable of producing up to 6 kW power are coupled through the quartz window into the discharge chamber. Using a homemade switched power supply, the pulse duration can be changed from cw to 50 μ s and

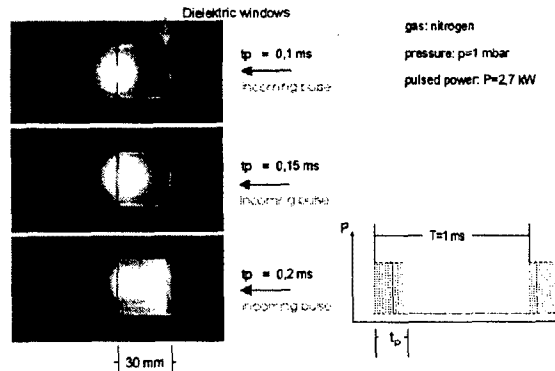


Fig 2 Plasma state as function of pulse width t_p .

the repetition frequency from DC up to 10 kHz. Fig. 1 displays also the electric field distribution as calculated using the MAFIA codes. A standing wave is developed in the cavity. The discharge ignites in the center of the vessel where the maximum of the electric field is established. As shown in Fig. 2, the shape and position of the discharge can be easily controlled by changing the parameters of the microwave pulses like the peak power, duration and repetition frequency. Under extreme conditions the hot plasma is produced immediately at the coupling window.

3. N₂ discharge

For microwave discharges in non reactive N₂ the double probe configuration is a suitable and convenient method to measure the electron densities, for it has no need for a well-defined ground electrode in the plasma. Fig. 3 shows the spatial distribution of the electron density in an N₂ discharge. The values are averaged over the time. The maximum appears in the center, where the electric field distribution also has its maximum.

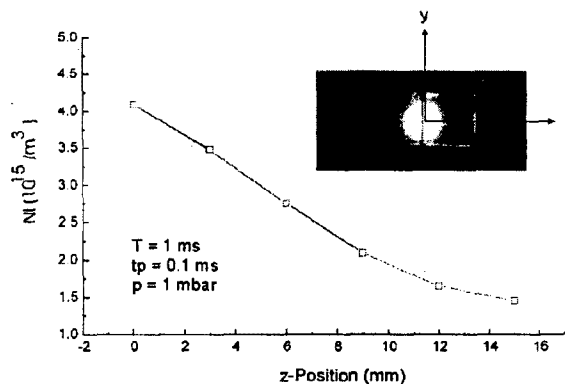


Fig 3 Axial distribution of electron densities (time averaged) from probe measurements for $t_p=0.1$ ms, only the values for $z>0$ are plotted.

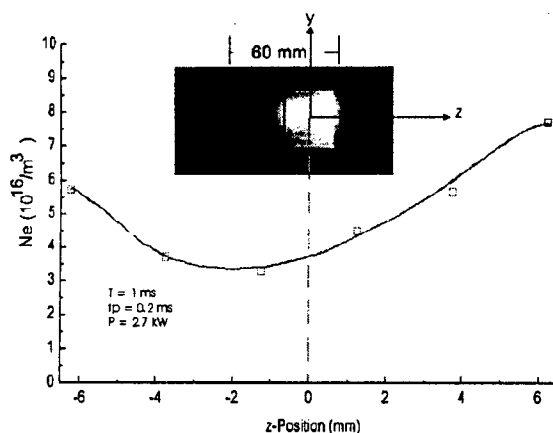
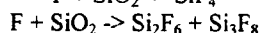
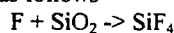


Fig 4 Axial distribution of electron density (taken at the pulse maxima) from HCN-Laser-interferometer data for $t_p=0.2\text{ms}$

Fig. 4 shows electron density measured by using an HCN-FIR-interferometer. The change in phase shift across a region with and without a plasma is measured. This in turn can be related to the change in the index of refraction and hence to the electron density. The values shown are taken at the peak of the microwave pulses. With the increased input of the pulses compared to the case of probe measurements, the discharge now has moved to the coupling window. Consequently, we measured a higher electron density approaching the cut-off density in the region near the coupling window.

4. Ar-CF₄ discharge

Plasma etching is a key process for removing material from surfaces. One of the most important application of plasma etching is the removal of patterned silicon or polysilicon films. Halogen atoms (F, Cl, Br) are almost always used for this purpose. CF₄ is the most commonly used feedstock gas among others. We filled our device with a gas mixture of Ar/CF₄=1/9. F atoms are known to etch SiO₂, although the pure chemical etch rate is small compared to that in etching silicon. The main reactions are as follows



The density of the F atoms has been measured by means of the optical actinometry. The pair of the commonly

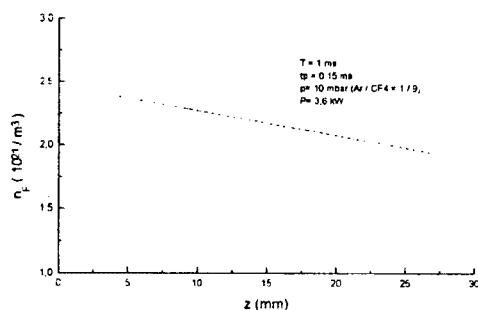


Fig 5 Axial distribution of F-density

used spectral lines at 703.7 nm for F and 750.4 nm for Ar have been chosen. The drop of the F- density due to the etching of the SiO₂ coupling window has been observed. Etching rate can be derived and is found to be good in consistent with that given in [1]. Fig. 5 shows the spatial distribution of the F atoms in the discharge chamber. A decreasing gradient of the density n_F towards the window can be seen, while n_F remains constant in radial direction.

5. Theoretical modelling of the gas breakdown

For our case the cascade-induced ionization mechanism is accepted to lead to breakdown. The governing equations describing the physical picture of the problem are [2]:

$$\frac{\partial n_e}{\partial t} = \left(\nu_{ion} - \nu_{att} - \frac{D}{\Lambda^2} \right) n_e - \nu_{rec} n_e^2 \quad (1)$$

$$\frac{\partial \epsilon}{\partial t} = \frac{e^2 E^2 \nu_e}{m_e (\omega^2 + \nu_e^2)} - \left(\frac{\partial \epsilon}{\partial t} \right)_{loss} \quad (2)$$

These equations are coupled, moreover they should be considered simultaneously with the Boltzmann equation, whose solution is the time- dependent electron energy distribution function. At breakdown the electrons gain energy equal to the ionisation frequency ν_{ion} . For a square pulse of duration t_p Eq.(1) is integrated to give the electron density. With n_e one can estimate the average F-atom number density [1], which is of interest for the process of the plasmas etching. Following [1]:

$$\frac{dn_F}{dt} = K_{eff} n_{CF_4} n_e, \quad (3)$$

where K_{eff} is the rate coefficient taking into account both attachment and dissociation processes in the discharge plasma. Some results obtained for Ar/CF₄ gas mixture and input parameters are presented in the table below. These predicted values are in a good agreement with the experimental results.

$(E/N) = 9.6 \cdot 10^{-16} \text{ V.cm}^2$	$D/\Lambda^2 = 1.46 \cdot 10^5 \text{ s}^{-1}$
$K_{ion} = 6.55 \cdot 10^{-11} \text{ cm}^3/\text{s}$	$n_e/n_{e0} = 2.19 \cdot 10^9$
$K_{att} = 6.43 \cdot 10^{-11} \text{ cm}^3/\text{s}$	$n_F = 2.55 \cdot 10^{15} \text{ cm}^{-3}$
$K_{eff} = 1.18 \cdot 10^{-11} \text{ cm}^3/\text{s}$	$n_{e0} = 45 \text{ cm}^{-3}$

6. Conclusions

A pulsed microwave discharge of cylindrical geometry has been developed and experimentally investigated. The plasma properties can be easily controlled by changing the pulse parameters. It is especially convenient for studies of the plasma-wall interactions with the coupling window. Various diagnostic methods like Langmuir probe, interferometry, optical spectroscopy and actinometry have been carried out on discharges of N₂ or Ar/CF₄. A quantitative description of the etching procedure is given.

References

- Lieberman, M.A., Principles of Plasma Discharges and Materials Processing, (John Wiley & Sons, Inc, 1994)
- Smith D.C., Meyerand R.G. Jr, Laser radiation induced gas breakdown, in "Principles of laser plasmas", Ed. G.Bekefi, (John Wiley & Sons, Inc, 1976)

Formation of Large Molecules and Agglomerates in DC Glow Discharges in Hydrocarbons

J. Winter

Inst. Experiment. Phys. II

Ruhr-University, D-44780 Bochum, Germany

A. Leukens

Inst. of Plasma Phys.

Research Center Jülich, D-52425 Jülich, Germany

1. Introduction

DC glow discharges are attractive tools for the plasma-assisted treatment of large surface areas. The set-up is simple and large processing systems can be built at comparatively moderate cost. DC glow discharges in hydrocarbon and other reactive gases (diborane, silane, ...) have been used successfully for the deposition of surface coatings. They are widely used for the wall conditioning of fusion devices [1,2] where the glow discharge has some hollow cathode character due to the torus-shaped vacuum vessel, which is used as a cathode. In this study we investigate the formation of large molecules (neutral radicals, cationic and anionic species) and agglomerates in a low pressure hollow-cathode glow discharge by plasma-ion mass spectroscopy.

2. Experimental Arrangement

The apparatus consists of an UHV vacuum chamber of cylindrical shape (0.6 m diameter, 0.6 m height). It contains a "liner" of SS sheet metal of the same geometry which is electrically isolated from the vessel. It is kept at ground potential in these studies (as is the vacuum vessel). A coil shaped anode (8 mm SS tube, 6 windings, 12 cm total length) protrudes up to the vessel center. It can be used for coupling of RF power, which has not been utilized in this study, however. The system is equipped with a turbomolecular pump via a variable conductance and a mass flow controlled gas injection system. Key diagnostics for this study is a BALZERS plasmamonitor (PM) for energy and mass dispersive plasma-ion mass spectroscopy. The PM can be biased with respect to the ground potential. It is localized at an equatorial position of the vessel as are a retarding field analyzer (RFA) and Langmuir probes. The flux determination and the mass and energy transmission

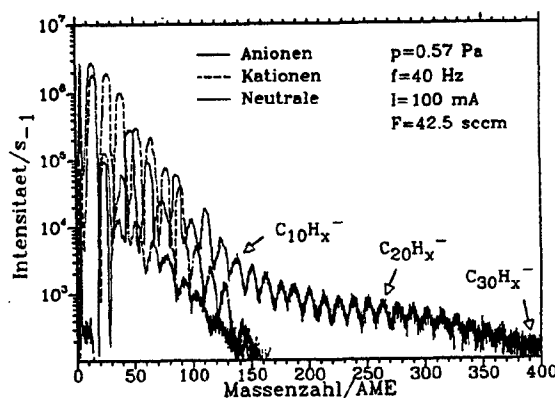


Figure 1: Anions, cations and neutrals from a pulsed glow discharge in Methane (pressure $p = 0.57$ Pa, flow rate $F = 42.5$ sccm, current density $j = 10 \mu\text{Acm}^{-2}$, modulation frequency 40 Hz).

of the PM have been calibrated utilizing measurements with the RFA in inert gas discharges [3].

3. Results and Discussion

Similar to earlier investigations [3] the formation of cations up to about 150 amu is observed in Methane plasmas, see fig. 1. The data in fig. 1 are presented with low resolution to facilitate the identification of different C_n -groups. The cations are sampled during the discharge and are accelerated from their production region in the negative glow through the sheath potential into the extraction hood of the PM. At pressures below 1 Pa they are essentially monoenergetic with an energy corresponding to that of the cathode fall potential (measured by probes). The intensity distribution of the C_3 , C_4 , ..., C_n groups

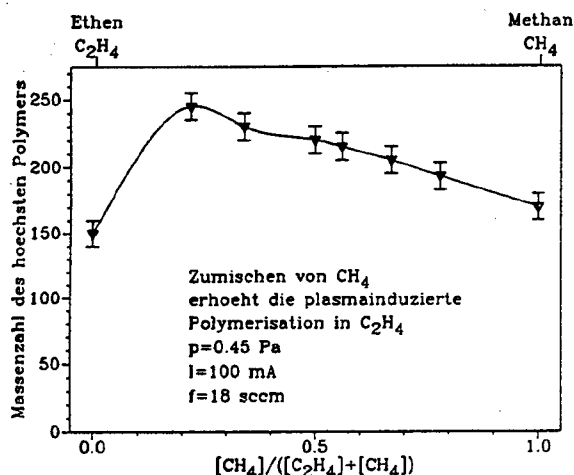


Figure 2: Highest mass numbers of cations observed in dc glow discharges in CH_4 - C_2H_4 mixtures as a function of the molar CH_4 fraction in the working gas.

shows a logarithmic decay with increasing mass, indicating a successive ion-molecule reaction path of the type $\text{C}_x\text{H}_y^{(+)} + \text{CH}_4 \rightarrow \text{C}_{x+1}\text{H}_z^{(+)} + n\text{H}_2$. A similar decay rate is found for the neutrals, which are a factor of about 8 less abundant than the cations.

For the measurement of the anionic species, the discharge was operated in a pulsed mode, modulated at acoustic frequencies. The hood of the PM was biased positively (a few V) during the afterglow to extract the negative ions. As can be seen from fig. 1, anions are observed up to about 400 amu. Beyond 120 amu their decay rate is much slower than at lower masses where it is similar to that of cations and neutrals. This points to a different reaction path for high mass anions.

Time dependent measurements of selected anions as a function of the "plasma on time" and the fact that much higher masses are found than for cations and neutrals points to the fact that anions are not only formed during the afterglow but also in the negative glow region during the regular plasma discharge.

The importance of the CH_3^+ -ion for starting and promoting the cation formation becomes evident from an experiment in which CH_4 - C_2H_4 mixtures were investigated. Plotted in fig. 2 is the largest observed mass number as a function of the methane fraction in the working gas.

A small (10%-20%) addition of methane to the ethene working gas promotes the formation of large molecules and clusters, for the same external conditions. At large CH_4 fractions the maximum size of the molecules decreases again. We tentatively explain this behaviour via the formation of significant fractions of saturated hydrocarbon ions from CH_4 , promoting the polymerization with the unsaturated

background gas. At high concentrations of CH_4 the increased reactivity of the double bond in Ethene may become rate determining.

Model calculations solving the rate equations with available and extrapolated rate constants for ion-molecule reactions and electron attachment reactions are in progress.

References

- [1] J. Winter, *Plasma Phys. Contr. Fusion* **38**, 1503 (1996).
- [2] J. Winter, in: *Physical Processes of the Interaction of Fusion Plasmas with Solids*, W. Hofer, J. Roth (Eds.), Academic Press 1996, pp. 217.
- [3] T. Rose, *Report KFA Jülich, Jül-2662* (1992)

Measurement of Sheath Oscillating Current in High Density Processing Plasma

Yoshio SAWA, Haruo SHINDO, Syuitsu FUJII* and Yasuhiro HORIIKE**

Department of Applied Physics, Tokai University, Hiratsuka, Japan 259-12

*ADTEC Co. Ltd., Fukuyama, Japan 721

**Department of Electrical Engineering, Toyo University, Kawagoe, Japan 350

1. Introduction

End point detection is one of key technologies in ULSI etching process, and conventionally it has been done by optical emission spectroscopy. However, some severe problems have still remained, such as low reproducibility of emission line intensity and degradation of optical path of measurement system. Recently a new technique for end point detection has been reported [1,2], and thereby the sheath oscillating current is employed to know the electron density in plasma. The method is quite advantageous in that the measure is directly related to the sheath width of the RF electrode, but at present it is only applicable in low plasma density region.

In this work, a new method was studied by superimposing a pulse voltage to the bias. The behavior of the sheath oscillating current was experimentally and theoretically investigated. It was possible to excite the oscillation by superimposing the pulse voltage even in high density plasma region. Specifically, the displacement current in sheath was measured by superimposing a pulse voltage to the sheath bias, and the behavior of current oscillation after the pulse voltage applied was studied in detail. At the same time, the displacement current was numerically calculated using the sheath equations.

2. Experimental

In Fig.1, the experimental apparatus is shown; the plasma source is a typical one of ICP (inductively coupled plasma), and the etching stage placed at 10 cm down from the ICP antenna was excited by a pulse voltage with 20 ns rising time as well as the DC bias voltage. The displacement current in sheath was detected by a commercially available sensor (HERCULES; Adolf-Slaby-Institute) [1], and the frequency of this current oscillation was

analyzed by a FFT (fast Fourier transformation). The distance between the sensor and the stage was fixed at 5 cm in this experiment. The dominant frequency was measured for Ar plasma at various RF power, pressures and Vdc.

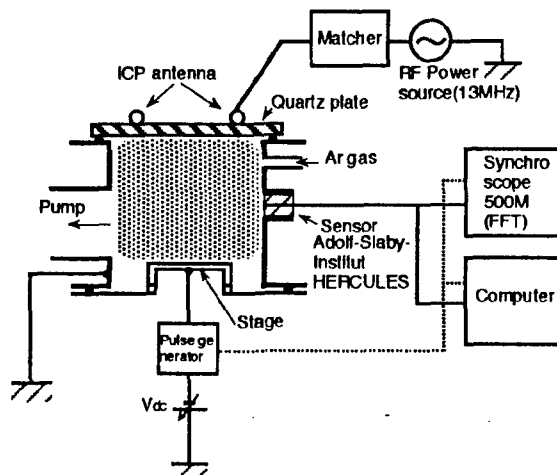


Fig.1 Experimental apparatus

3. Results and discussions

Typical FFT spectrum showed several peaks at low frequency corresponding to the harmonics of 13MHz of ICP power source but no notable peak at high frequency region when no pulse voltage is applied to the stage. When a pulse voltage was applied, however, a clear peak appeared at FFT spectrum above 100 MHz frequency region. This newly appeared peak can be ascribed to the sheath oscillating current, because the frequency of the peak is shifted to higher region with an increase in RF source power.

In Fig.2, the frequency at which the FFT spectrum has a peak is plotted for the RF source power in the condition of 20 mTorr, and

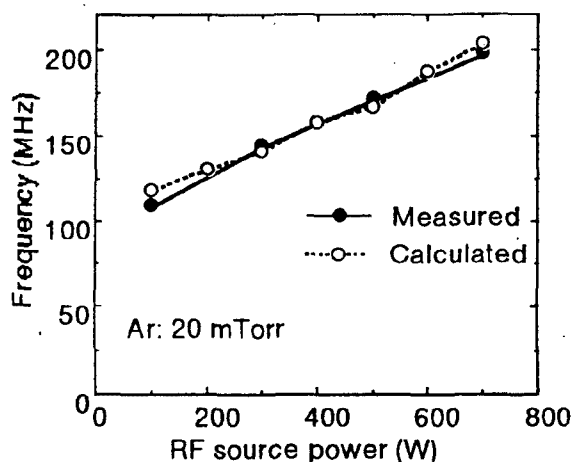


Fig.2 Frequency vs RF source power

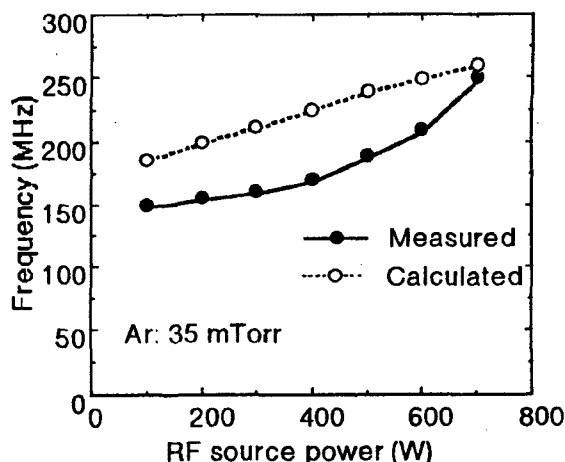


Fig.3 Frequency vs RF source power

the frequency is clearly shifted to higher region with the RF power. Since the electron density increases with an increase in RF power, the frequency of the oscillation increases with the RF power. The oscillation of sheath displacement current is interpreted as a serial circuit resonance of sheath capacitance and plasma bulk inductance[1,2], and then the oscillating frequency depends on the plasma frequency and the sheath width as well.

In Fig.2, the calculated result is also shown for comparison. The calculation is based on the fluid equation[2] with using the electron density and temperature measured by Langmuir probe. They are quite consistent with each other, stating that the measurement of sheath oscillating current is succeeded.

In Fig.3, the variation of the oscillating frequency is also plotted for the RF power in the condition of 35 mTorr. In this high pressure condition, a fairly big discrepancy is seen between the measured and calculated; the calculated frequency is higher than the measured. The discrepancy may be explained as below; the 1/2 power law proposed by Godyak[3] is used in this analysis for the voltage dependence of the sheath width. However, at such higher pressure as 35 mTorr the collision effect in the sheath may become important, and thus the sheath width rather obeys the mobility limited law than the 1/2 power law, meaning that the sheath is actually wider and the oscillating frequency becomes lower. Further, the oscillation at such higher pressure involves a strong dumping, and this may make the frequency measure

ment difficult.

In Fig.4, an oscillation of sheath displacement current calculated at 35 mTorr is shown; a strong dumping is seen.

References

- [1] M. Klick, Proc. 10th Int. Collo. on Plasma Process, Antibes, p341, 1995.
- [2] Y. Sawa, Proc. 3rd Int. Conf. on Reactive Plasmas, Nara, Japan, p67, 1997.
- [3] V. Godyak and N. Sternberg, Phys. Rev. A **42**(1990)2299.

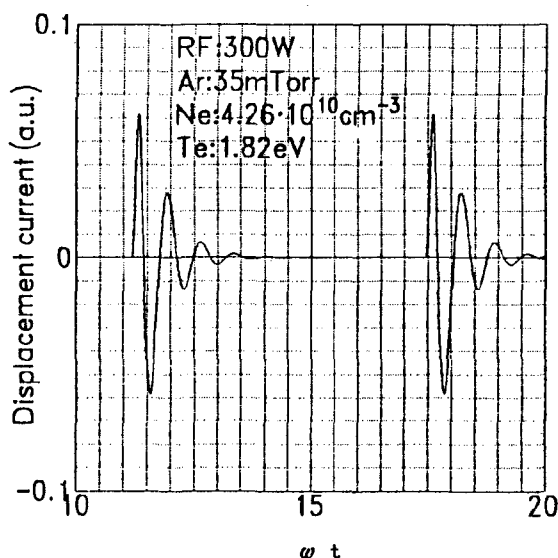


Fig.4 Oscillation of displacement current at 35 mTorr.

Wave Pattern Measurement in High Density Heliconwave Processing Plasma

Haruo SHINDO, Yoshio SAWA, Katsufumi Kawamura*,
Masakazu Furukawa* and Yasuhiro HORIIKE**

Department of Applied Physics, Tokai University, Hiratsuka Japan 259-12

*Canon Sales CO. INC., 2-12-23 Kounan, Minatoku, Japan 108

**Department of Electrical Engineering, Toyo University, Kawagoe, Japan 350

1. Introduction

In the deep submicron ultralarge-scale-integrated circuit (ULSI) etching process, numerous requirements of the plasma, such as fine pattern fabrication with high aspect ratio, uniformity in large-diameter wafers, high etch rate and low damage, are becoming increasingly critical. The requirements have promoted development of low-pressure and high density plasma, such as magnetron and ECR plasmas. In these plasmas, however, several crucial problems, such as gate oxide breakdown and notching in polysilicon etching, rise up in conjunction with employing relatively high magnetic field.

Recently helicon wave plasma[1] and inductively coupled plasma(ICP)[2] have been intensively studied, because the both plasmas only need low or no magnetic field. In these plasmas, it was found that propagation or spatial distribution of wave fields were highly correlated to etching characteristics of Si and SiO₂. [3] These were clarified in investigations of etching in various spatial region. [4] Thus it is important to know the propagation mode of helicon wave and to reveal related plasma characteristics. These subjects are extremely important in conjunction with low damage etchings. However, little work has been reported on this subject.

In this work, the helicon wave propagation was experimentally studied, and the related plasma characteristics are subsequently discussed. In particular, it is pointed out that the wave nearby the two-turn antenna behaves peculiarly and this is responsible for plasma produced.

2. Experimental

In Fig.1, the experimental apparatus is shown; the plasma source is a typical heliconwave plasma (MORI200) equipped with

two-turn $m=0$ antenna through 100 mm diameter quartz belljar. The plasma thus produced was transported into the reactor chamber of 150 mm diameter and the distribution profile of plasma was adjusted by the dual magnetic coils.

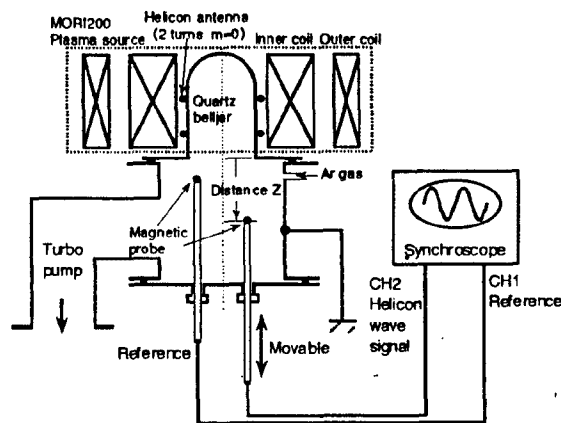


Fig.1 Experimental apparatus

The propagation mode of heliconwave was measured by a pair of magnetic probes immersed in plasma; the one was fixed as a reference and another was axially moved and the signal amplitude of the movable probe was plotted for the distance. The wave pattern was thus obtained at various conditions. The measured RF field was $B\hat{e}\Delta$ and they are shown for the distance Z with the origin of the belljar end. In this coordinate system, the positions of two-turn heliconwave antenna are $Z=-15$ and -3 cm, and thus the axial distance of the antenna loop is 12 cm.

3. Results and discussions

Typical wave pattern measured by the

magnetic probe is shown in Fig.2 where the inner coil current is taken as a parameter with no current of the outer. The magnetic field by the inner coil has the positive direction to the reactor chamber. At the coil current of 10 A, the wave propagation with a dumping is clearly seen from the antenna region of $Z = -15$ to -3 cm. As the coil current is increased, however, the wave propagation is fairly distorted, especially in the antenna region; at the coil current of 20 and 30 A, the waves are not clear and its amplitude is rather small there but the wave with the highest amplitude appears just downward the antenna.

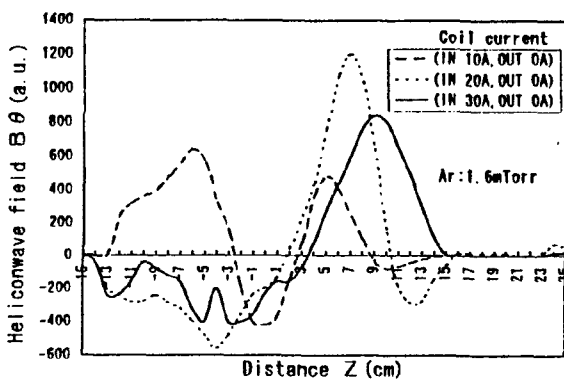


Fig.2 Measured wave patterns

This states that the two antenna loops works to generate the wave at the current of 10 A, but the top antenna does not work at the currents of 20 and 30 A, and the wave is generated by the bottom antenna alone. This wave behavior possibly has a strong influence to the plasma characteristics.

The helicon wave has the higher phase velocity, hence the longer wavelength at higher magnetic field.[5] Therefore, at the high magnetic field like 20 or 30 A coil current as in Fig.2, the helicon wavelength becomes longer than the axial distance of the antenna, and then the different wave generation mode appears. In this wave generation mode, the wave field at the down stream is rather higher than at the antenna region. This makes the plasma behavior different.

In Fig.3, the wave patterns measured at another condition are shown, where the inner coil current is fixed with 20 A but with different outer coil currents. The magnetic field by the outer coil has the negative direction. the wave propagation mode in Fig.3 has the same tendency as in Fig.2.

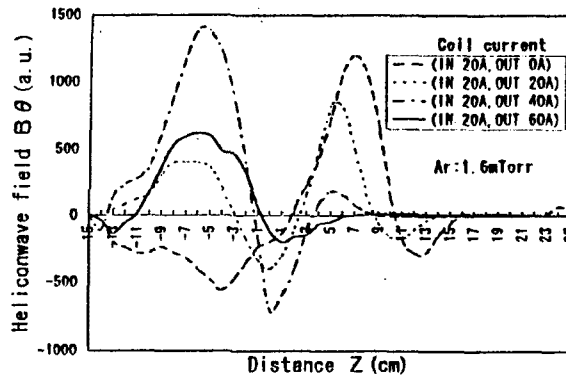


Fig.3 Measured wave patterns

In Fig.4, the helicon wavelength obtained from the wave patterns is plotted for the condition of Fig.3. As the outer coil current is increased, the wavelength becomes shorter and eventually shorter than the axial distance of the antenna. This makes the propagation mode different.

References

- [1] A.J.Perry, D.Vender and W.Boswell: J. Vac. Sci. Technol. B9 (1991) 310.
- [2] J.Hopwood, C.R.Guarnieri, S.J.Whitehair and J.J.Cuomo: J. Vac. Sci Technol. A11 (1993) 147.
- [3] N.Jiwari, T.Fukasawa, A.Nakamura, K.Kubota, H.Shindo and Y.Horike: Jpn. J. Appl. Phys. 33(1994)4454.
- [4] T.Fukasawa, A.Nakamura, H.Shindo and Y.Horike: Jpn. J. Appl. Phys. 33 (1994) 2139.
- [5] F.F.Chen: Introduction to Plasma Physics, Plenum press, New York, 1984, p131.

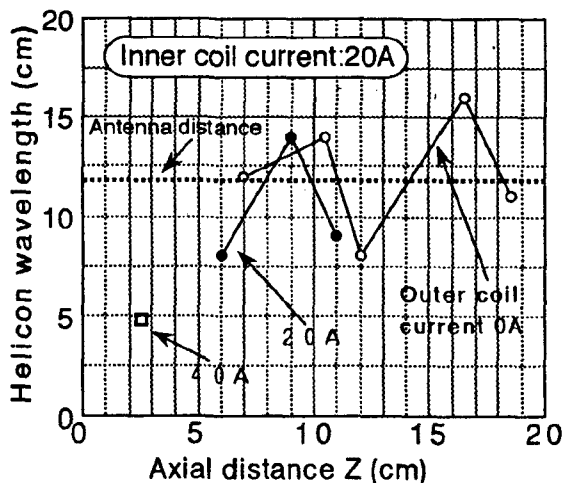


Fig.4 Measured wavelength for the distance

Topic 11

Generation and dynamics of plasma flows.

Application of FFT to evaluations of velocities in plasma jets

Jan Hlína

Institute of Electrical Engineering, Academy of Sciences of the Czech Republic
Dolejšková 5, 182 02 Praha 8, Czech Republic

1. Introduction

The fast Fourier transform (FFT) is widely used for investigations of various oscillation processes in plasma jets. The FFT performed on time series representing some physical quantity in the system yields a matrix of complex numbers. The real and imaginary parts of these numbers contain an information about the amplitudes and phase angles belonging to the elementary oscillators into which the measured signal can be decomposed. The amplitudes are often used to show the frequency spectra of the signal, while the application of phases resulted from the FFT has been studied much less. Phase angle relations in multichannel records of the arc jet optical emission were used to indicate transitions between various turbulence stages in the jet by Hlína and Neníčka [1]. Another possible application of the phase angles relating to detection points situated along the axis of the plasma flow is described in this contribution and it consists in evaluations of the gas velocity. The evaluation procedure was first mentioned by Hlína *et al.* [2] when it was applied to another type of the arc jet. Velocities in plasma jets are measured by many methods including laser Doppler anemometry, applications of Pitot tubes, various types of probes, plasma scattered laser light *etc.* An interesting method based on the convective transport of luminosity fluctuations generated by arc root movements was introduced by Coudert *et al.* [3]. The time delay between the signals representing the light emitted from two points situated along the plasma flow was evaluated using numerical techniques in order to eliminate the signal modulation caused by other effects than the arc root fluctuations. The approach based on the FFT and resulting phase angle relations described in this contribution enables to evaluate the velocity respecting the character of various oscillation processes present in the plasma jet.

2. Results

The measurement method was tested on a plasma jet generated by a dc plasma torch 67 mm long, with the nozzle exit diameter 8 mm and operated with argon. The results reported here were acquired at the arc current 175 A. The integral light emitted along the plasma jet axis was detected by an array of 8 photodiodes and registered by A/D boards. The measurements included the arc voltage records. The changing character of the frequency spectrum as a function of the gas flow rate in the range 10 l/min-200 l/min ac-

quired by means of the FFT from the record of the plasma optical emission 3 mm above the nozzle exit is shown in Fig.1.

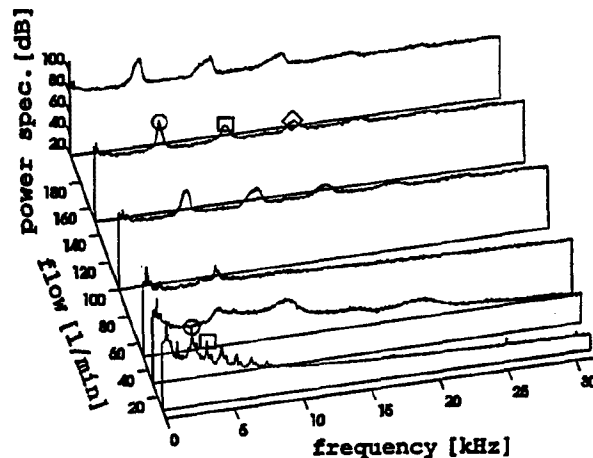


Fig.1. Spectrum of optical emission 3 mm above the nozzle exit as a function of the gas flow rate.

In Fig.2 there are spectra of the arc voltage records which show the correspondence with the optical spectra in the range of higher gas flow rates and on the contrary the absence of significant lines at small flow rates.

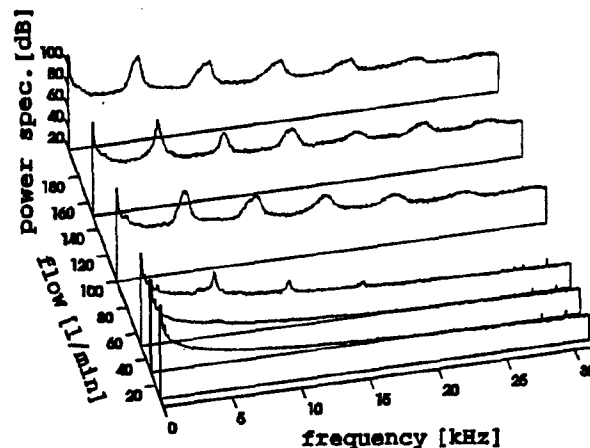


Fig.2. Spectrum of the arc voltage as a function of the gas flow rate.

When the FFT of the 12th order (using 4096 data points) is applied to the signals detected by two of the diodes and the difference of the phase angles relating to these points is plotted as a function of the

frequency, the linear character of the dependence is remarkable either in a limited part of the frequency range (Fig. 3 - gas flow rate 10 l/min) or in the whole range (Fig. 4 - gas flow rate 150 l/min).

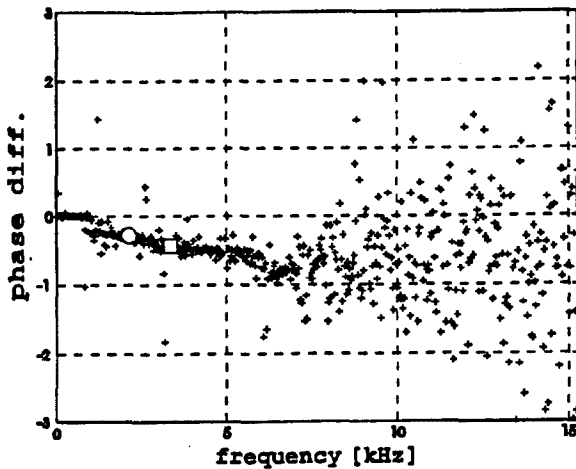


Fig.3. Phase difference between the detection points 1.6 and 2.4 mm above the nozzle exit as a function of frequency. Gas flow rate 10 l/min. The marks indicate the frequencies shown also in Fig.1.

The velocity v is given by the tangent of the straight line (drawn in Fig.4 and clearly seen between 1 and 7 kHz in Fig.3) approximating this linear dependence as $v = 2\pi d \Delta f / \Delta \varphi$, where d is the distance of the points, Δf the frequency and $\Delta \varphi$ the phase increments. The velocities determined in this way for the input flow rates 10-200 l/min are in Fig. 5.

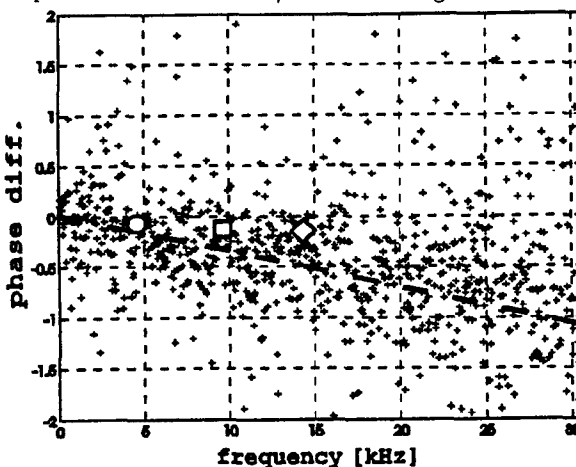


Fig.4. Phase difference between the detection points 0.8 and 2.4 mm above the nozzle exit as a function of frequency. Gas flow rate 150 l/min. The marks indicate the frequencies shown also in Fig.1.

3. Conclusion

The method used here for evaluations of the gas velocity in a plasma jet is based on an assumption that the oscillations of the plasma at least in a limited frequency range are carried by the gas flow and thus the time delay (represented here by the phase angle difference) between two points along the flow may be

used to determine the velocity. Fig.3 indicates that the frequency spectrum includes lines of many types. The oscillations with frequencies up to 1 kHz are well correlated and show a zero phase shift between the detection points, while in the frequency range over 7 kHz the recorded signal contains solely the noise and the phase relations become random. The phase differences related to significant spectral lines (indicated by marks in Fig.1) agree with the general linear character of the plot between 1 and 7 kHz and the respective oscillations may be therefore considered to be carried with the gas flow. The low frequency hydrodynamic oscillations at low flow rates do not penetrate the arc chamber which is proved by the arc voltage spectra. The phase difference close to zero was found for the significant lines determining the character of the frequency spectra at high flow rates though they occur in the frequency range where the lines with lower amplitudes show average values of phase shifts corresponding to the gas velocity. This gives evidence for a global character of these oscillations which also influence significantly the thermal transport in the plasma torch, as it was shown by Krejčí *et al* [4]. The results show that possible application of the here presented method for the measurement of velocities in plasma jets must respect carefully the character of oscillations in the plasma jet. Another factor important for a successful application of the method is the distance of detection points which must be sufficient with respect to the expected gas velocity and sampling rate and at the same time it must be enough small so that the phase relations might be still evaluated.

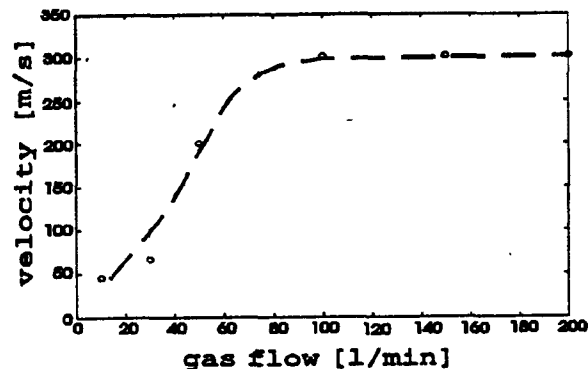


Fig.5. Velocity in the plasma jet as a function of the gas flow rate.

4. References

- [1] J. Hlína, V. Něníčka: Acta Technica CSAV 41 (1996), 15-32
- [2] J. Hlína, J. Gregor, J. Šenk: Acta Technica CSAV 41 (1996), 373-383.
- [3] J. F. Coudert, M. P. Planche, P. Fauchais: Plasma Chem. and Plasma Proc. 15 (1995), 47-67
- [4] L. Krejčí, V. Dolínek, B. Růžička, V. Chalupová, S. Russ: Plasma Chem. and Plasma Proc. 13 (1993), 601-612

Modelling of dynamics of penetration of plasmoids in cross magnetic field

Korotaev K.N. Smirnov V. M. Savjlov A. S.

Department of Plasma Physics, Moscow State Engineering and Physics Institute
115409, Moscow, Russia

The interaction of directed flows of plasma with cross magnetic field was considered by numerical modelling [1], analytically [2], experimentally [3]. This problem is of interest in application to research laboratory plasma, and in studying interaction of solar wind with the magnetosphere of the Earth. In the present work results of modelling of interaction of a clot of plasma with magnetic field are given for the ratio of the plasma energy density to the density of the magnetic field energy in range of $0.7 \cdot 10^{-4}$ - $0.7 \cdot 10^{-2}$. The plasmoid is simulated by large particles "macroions" and "macroelectrons". Each of them has the spherically symmetric form. The potential energy of electrical interaction between particles with numbers i and j (U_{ij}) is determined by the formula:

$$U_{ij} = e^2 \cdot \frac{Z_i \cdot Z_j}{\sqrt{r_{ij}^2 + R_p^2}}.$$

Where r_{ij} is the vector of distance between particles, R_p - radius of the particle, Z_k - electrical charge of the particles, with number k . The energy of magnetic interaction between particles with numbers i and j (U_{mj}) is determined by the formula:

$$U_{mj} = \frac{e^2}{c^2} \cdot \frac{V_i \cdot V_j \cdot Z_i \cdot Z_j}{\sqrt{r_{ij}^2 + R_p^2}}.$$

Where V_k - the velocity of the particle with number k . The total energy U_t of the simulated plasmoid is determined by the formula:

$$U_t = \sum_{i=1}^N \frac{M_i \cdot V_i^2}{2} + \sum_{k=1}^N \sum_{l=1}^N (U_{pk} + U_{ml}).$$

The model permits to simulate the plasma clot as in the mode of one electron atoms, where there is only one electron per every ion and in the many-electron mode which permits more completely simulate the effects with developed function of electron distribution. Evolution of the plasmoid striking the magnetic barrier is considered. This problem in our opinion bears a relation to processes on the border between the magnetosphere and magnetopause where primary plasma flow during interaction with magnetopaus can be splitted on some slot-hole flows oriented along magnetic field. Modelling of splitting by the method of large magnetoactive particles is possible basically,

however in the present version the model would require too many particles. This problem bears also relation to processes after injection of a working substance into a closed magnetic system. The parameters of the model were chosen from the following reasons:

1. Radius of a particle $R_p = N \cdot R_i$ ($N \sim 0.5 - 5.0$), where R_i - the larmour radius of ions.
2. Degree of overlapping $\alpha = 1-5$ ($\alpha = n/n_1$ and

$$n_1 = \frac{N_p}{\frac{4}{3} \pi \cdot R_p^3}, \text{ where } n - \text{the density of plasma,}$$

n_1 - the average density in the particle, N_p - the number of elementary particles in a large particle).

3. The ratio of ion to electron weights $m_i/m_e = 9.85$ (the ion is 200 times lighter then proton).
4. The number of particles in the task was 10 - 50 pairs. The following cases are considered: $n < n_c$,

$$n > n_c \text{ and } n > n_m \left(n_c = \frac{B \cdot V \cdot \epsilon_0}{4\pi \cdot h \cdot e} \right) \text{ coincides with}$$

$$[2] \text{ and } n_m = \frac{B^2}{8\pi \mu_0 c^2 m_i}, \text{ where } B - \text{magnetic}$$

induction, V - speed of a plasmoid, h - thickness of a plasmoid. Figures 1,2,3 shown the time evolution of the total U_t , kinetic E_k , potential U_p , and magnetic energies of the plasma clot where the limit of time measurements is the quarter of the larmour period of the model electron. In all three cases the initial density of the plasmoid was $n=100$ [1/cm³], and the velocity of the plasmoid perpendicular to the magnetic field $V_0=300$ [km/sec]. For modelling of the plasmoid, 27 pairs of the model particles (ions and electrons) were used. The simulated plasmoid had originally the form of parallelepiped.

During movement of the clot, the energy in its decelerating for head part is replenished at the expense of other parts of a clot converging the "head", while elongation of the configuration of the clot along the magnetic lines is supported due to charge flow along the field lines. The clot is extended also in the direction perpendicular to the magnetic field and velocity of the clot. Compression of the clot in the direction of movement permits it to penetrate into the

magnetic field for which $n < n_c$ at the expense of increase of density of particles.

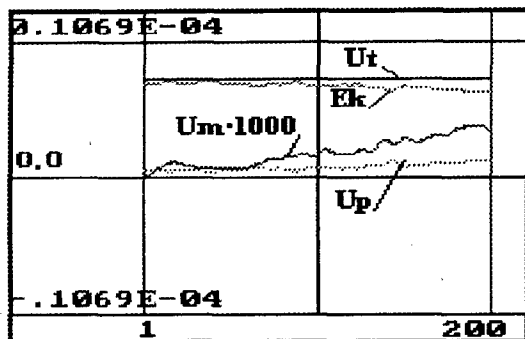


fig.1. - time dependence of energy of the plasma clod, when the value of the magnetic field of the barrier $B=5 \cdot 10^{-4}$ [T] is higher than the critical value corresponding to reflection of the plasmoid.

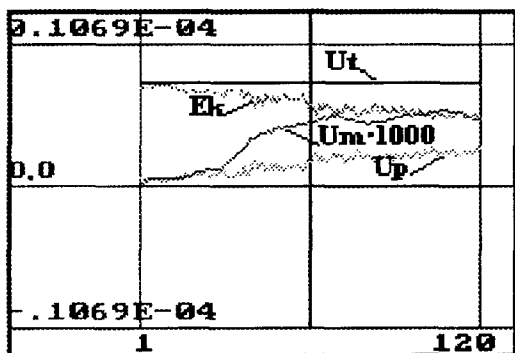


fig.2. - time dependence of energy of the clod penetrating through the magnetic barrier $B=9 \cdot 10^{-5}$ [T] with formation of an electrostatic shell and organization of a drift field of polarization.

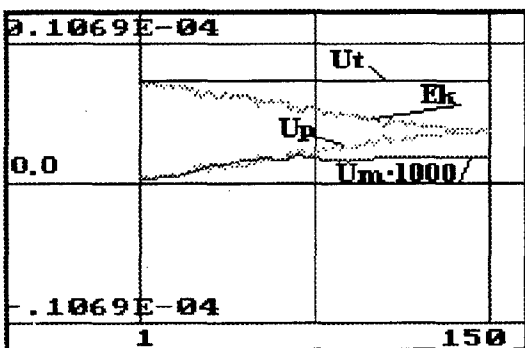


fig.3.- time dependence of energy of the clod which forms an electrostatically magnetic shell ensuring joint electrostatically-magnetic penetration into the magnetic barrier $B=5 \cdot 10^{-5}$ [T], when the condition $n > n_m$ is satisfied (magnetic field is frozen in the plasmoid).

In the model the dissipative processes are not considered, therefore the energy of directed movement perpendicular to the field lines transforms partially in the energy of movement along the lines, potential energy of the field of polarization. At movement of the plasmoid in a cross magnetic field, there is development of fluctuations of various frequencies which difficultly to identified due to fluctuations of all physical parameters. The figure shown permit to identify some of them as the plasma frequency ω_p , electron-cyclotron and ion-cyclotron frequency of the model clod. It is necessary to note very good fulfilment of the law of the total energy U_t conservation in the model (the total energy - is shown by the horizontal stright line U_t in figures 1, 2, 3).

Borders of applicability of the model, besides the mentioned necessity of large number of particles for modelling of splitting of the flow on the magnetospher is the following restrictions:

- Complete pushing of the magnetic field out of plasma cannot be achieved because of discrete character of large particles.
- Impossibility, of uniform density in the model results in significantly enhanced energy necessary for moving the electron component in such if to compare with real plasma.
- Ratio of ions and electrons masses cannot be taken close to the real value, therefore both the scale of the boundary layers, time of the electron reaction on movement of ions change.
- Discrete behaviour of large particles leads to essential fluctuation of parameters of the clod. Nevertheless the results of calculations show, that the model in borders of it's applicability, shows effects admitting physical interpretation, gives the law of energy conservation, and permits modelling of physically essential effects of interaction of plasmoid with magnetic barriers using personal computers.

References

- Miguel Galvez: "Computer simulations of finite plasma streams convected across a magnetized vacuum." *Phys. Fluids B*, 1(1989)2516.
- Joseph E. Borovsky: "Limits on the cross-field propagation of streams of cold plasma", *Phys. Fluids* 30(1987)2518.
- Lindberg L.: *Astrophysics and Space Science* 55(1978)203.

Topic 12

**Non ideal plasmas.
Clusters and dusty plasmas.**

EXPANDING PLASMA LAYERS WITH TWO ELECTRON GROUPS AND DUST PARTICLES

Yu. I. Chutov, A. Yu. Kravchenko, P. J. J. M. Schram*, V.S. Yakovetsky

Department of Physical Electronics, Taras Shevchenko Kiev University, Volodymyrska Str. 64, 252017 Kiev, Ukraine

* Department of Physics, Eindhoven University of Technology, Postbox 513, 5600 MB Eindhoven The Netherlands

Introduction

Expanding plasmas with dust particles have been intensively investigated in recent years [1-9] including investigations of relaxation problems in such plasmas [5-9]. However these investigations have been carried out under the assumption of an equilibrium initial state although non-equilibrium plasmas can be realized in many cases, for example, by an interaction of laser radiation with solid state surfaces, in particular in laser fusion.

The aim of this work is the computer modeling of an expansion of bounded plasma layers with dust particles and with two groups of electrons with different temperatures which can be realized by an interaction of laser radiation with solid state surfaces..

Model

Uniform quasi-neutral plasma layers with the initial size L and sharp boundaries consist of two groups (cold and hot) of electrons with initial densities n_{eo}^c and n_{eo}^h and with different initial temperatures T_{eo}^c and T_{eo}^h , respectively, as well as ions with density n_{io} and temperature T_{io} . The quasi-neutrality condition gives the following relation between densities of electrons and ions:

$$n_{io} = n_{eo} = n_{eo}^c + n_{eo}^h.$$

This plasma layers can expand into a vacuum due to the self-consistent electric field. Non-charged dust particles with radius R_d and density n_d appear in this plasma layer at the initial time. Therefore the plasma relaxation takes place both by this plasma expansion and by the collection of electrons and ions from the plasma on dust particles. The plasma is considered to be collisionless because the plasma relaxation time is much less than the electron-ion collision time due to the choice of the parameters of the plasma and the uncharged dust particles.

Various parameters of this relaxing plasma have been numerically simulated using the PIC method and taking into account the dynamics of

the dust particle charge in the framework of the orbit-limited-probe theory without the assumption about equilibrium of electrons and ions. Coulomb collisions of electrons and ions with dust particles are taken into account in the framework of the method of stochastic differential equations. In some cases, the electron and ion collection by dust particles and the Coulomb collisions have also been simulated by the Monte Carlo method.

3. Results

Typical results of the computer modeling are plotted in Fig. 1 - 3 for different numbers $N_d = n_d L_\delta$ of dust particles in a Debye sphere at $R_d = 0.32$, $(T_{eo}^h / T_{eo}^c) = 10$, $T_{io} = T_{eo}^c$ and $m_i / m_e = 256$ which last value is taken to obtain higher simulation precision. Here R_d and the spatial coordinates X are divided by the initial Debye length L_δ of the cold electrons, the time t is multiplied by the initial ion plasma frequency ω_{oi} .

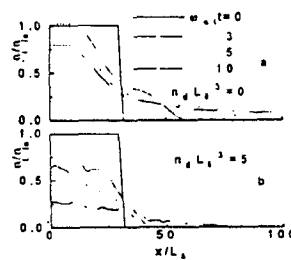


Fig. 1

The influence of dust particles on the plasma expansion is clearly seen from Fig. 1 in which the spatial distributions of the ion density

n_i divided by the initial ion density n_{io} are shown for various times after the start of the plasma expansion in case of plasma expansion without dust particles (upper part) and in case of plasma expansion with dust particles (lower part). In the first case, we have the usual plasma expansion with a rarefaction wave propagating

into the central part of the plasma layer. Therefore the decrease of the ion density in the same layer point starts only after this point has been reached by the rarefaction wave. In case of plasma expansion with dust particles (lower part of Fig. 1) the decrease of the ion density starts in all points of the plasma layer due to the ion collection by dust particles. Besides, this decrease is faster than in the case of plasma expansion without dust particles.

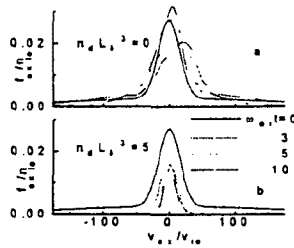


Fig. 2

The influence of dust particles on electrons is clearly seen from Fig. 2 in which the X-components of the mean (for positive values of the spatial X-axis) electron velocity distribution function are shown for various cases corresponding to Fig. 1. As can be seen from Fig. 2, this function is non-equilibrium initially, because the plasma layer consists of two groups of electrons. In the case of a plasma without dust particles, this function evaluates due to a transfer of electron energy to ions by the self consistent electric field during the plasma acceleration. All electrons participate in this energy transfer and therefore the non-equilibrium character of this function as well as the special properties of this non-equilibrium are preserved during the plasma expansion without dust particles (Fig. 2a). However, in the case of a plasma with dust particles fast electrons can be collected by dust particles only due to their negative electric charge. Therefore these fast electrons vanish just after the start of the plasma expansion and the electron velocity distribution function is like Maxwellian.

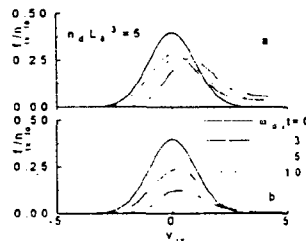


Fig. 3

As can be seen from Fig. 3, there is also some difference between the evolution of the mean ion velocity distribution function during the

plasma expansion for these two cases. In the case without dust particles the ion acceleration takes place due to the self consistent electric field along the X-axis during the plasma expansion. Therefore there is some shift of the mean (for positive values of the spatial X-axis) ion velocity distribution function to the right. In the case of plasma without dust particles, this shift is smaller because fast electrons are just collected by dust particles and their contribution to the ion acceleration is smaller than in the case of plasma without dust particles.

4. Conclusion

Computer modeling of expanding plasma layers with dust particles shows that dust particles can strongly influence different phenomena accompanying this expansion. This influence is caused by the selective collection of electrons and ions by dust particles with self-consistent negative electric charge. First of all, these particles can change the initial energy distribution functions of electrons and ions due to the selective collection of electrons and ions.

Acknowledgment

This work was partially supported by INTAS in the framework of contract No 94-2959 and by a grant from the Ukrainian Committee of Science and Technology

References

- [1] Lonngren K.E. Planet Space Sci. 1990. V.38, N 11. P.1457-1459
- [2] Luo H., Yu M.Y. Phys. Fluids. 1992. V. B4. - P.1122-1125
- [3] Yu M.Y., Luo H. Physics Letters. 1992. V.A161. P.506-509
- [4] Yu M.Y., Luo H. // Phys. Plasmas. - 1995 - V.2, No 3. - P. 591-593
- [5] Chutov Yu., Kravchenko A., Schram P. // Physica.- 1996.- V.B128. - P.11-20
- [6] Chutov Yu.I., Kravchenko A.Yu., Schram P. / J. Plasma Phys. -1996 - V.55. P. 87-94
- [7]. Chutov Yu.I. at al. Invited papers of PFNL'96 September 17-19, 1996, Sendai, Japan. Abstracts of PFNL'96, p.71
- [8]. Chutov Yu.I., Kravchenko A.Yu., Schram P. Contributed papers of ICPP'96, 9-13 September 1996, Nagoya, Japan. Abstracts of ICPP'96, p.318
- [9]. Chutov Yu.I., Kravchenko A.Yu., Schram P. Contributed papers of ICPDP'96, 21 - 25 October 1996, Goa, India. Abstracts of ICPDP'96, p.93.

On the Theory of Nonideal Plasmas

A.S. Kaklugin, G.E. Norman, A.A. Valuev

Moscow Physical Society, PO Box 110, Moscow 121019, Russia

Fax: 095 1357995 e-mail: henry@aha.ru

Collective phenomena and plasma waves are the base, the essence, and the starting point of any gas plasma theory [1-4]. However, these concepts are not used in the theory of nonideal plasmas [5,6]. So there is a barrier between the treating of ideal and nonideal plasmas. However, plasma waves do exist in nonideal plasmas (s. [7] and refs. therein) and it is possible to develop nonideal plasma theory starting with plasma waves, just as in the gas plasma case. It is the incorporation of nonideal plasma in conventional plasma theories that is the goal of the present report.

1. Damping decrements

It is often assumed that the range of plasma wave existence is limited by the inequalities

$$k < k_0 \approx \alpha \kappa \quad (1)$$

$$\gamma < \gamma_0 < 1 \quad (2)$$

k is the wave number, $\kappa = 1/a_e$, the electron Debye radius $a_e = (kT/4\pi n_e e^2)^{1/2}$, T is temperature, n_e is electron number density, the nonideality parameter $\gamma = e^2 n^{1/3}/kT$ and $n = 2n_e$. The inequality (1) results from Landau damping, $\alpha \approx 1$. The inequality (2) is due to collision damping. The fact that plasma waves were neglected in [5,6] may be attributed to the violation of (2) in the nonideal plasma region.

In ideal plasmas, the collision damping decrement Γ_c is determined by the Landau collision integral, and its correct form is

$$\Gamma_1/\Omega_e = (1/6)\gamma^{3/2} \ln(\Lambda_1^2 + 1) \quad (3)$$

where $\Omega_e = (4\pi e^2 n_e/m)^{1/2}$, $\Lambda_1 = 1/[(4\pi)^{1/2} \gamma^{3/2}]$, and the screening length a_e is taken as an upper cut-off distance. The equation (3) takes into account weak long range multiparticle interactions. As γ grows, a_e becomes less than the mean interparticle distance $n^{-1/3}$ and the latter begins to play the role of the screening distance [8]. Then, short range interaction between charged particles is predominant, the collisions become strong and almost binary, and the Landau collision integral should be replaced by the Boltzman collision integral. In this case, collision damping has the same functional form but with a_e replaced by $n_e^{-1/3}$

$$\Gamma_2/\Omega_e = 1/6 \gamma^{3/2} \ln(\Lambda_2^2 + 1), \quad (4)$$

where $\Lambda_2 = (9/4)\gamma^{-2}$. Thus, at small γ , the quantity Γ_c/Ω_e increases as $\gamma^{3/2}$ according to (3) and at large γ it decreases as $\gamma^{-1/2}$. A maximum between these two branches of the damping decrement can be evaluated by sewing the equations (3) and (4) at $a_e = n_e^{-1/3}$. This estimate gives a value of $(\Gamma_c/\Omega_e)_{\max} \approx 0.1$ at $\gamma \approx 1$.

The withdrawal of the collision restriction (2) is explained by the fact that a_e becomes less than $n_e^{-1/3}$. The inequality (1) should also be modified

$$k < q_0 = (6\pi n_e)^{1/3} \quad (5)$$

where q_0 is the Debye wave number [9]. In a Debye plasma, $q_0 \gg \kappa$ and the restriction (1) is stronger than (5). As γ grows, the inequality reverses $q_0 < \kappa$.

Landau damping is determined by the electrons moving with velocity equal to the phase velocity of the wave. In a Debye plasma, this corresponds to the electron thermal velocity. In nonideal plasma, the minimum phase velocity increases and the number of electrons contributing to Landau damping decreases. They correspond to the tail of the Maxwell distribution. Hence, the maximum value of Landau damping decreases as γ grows.

The range of plasma waves existence is presented in Fig. 1. Account was taken of the fact that according to [3], the Landau damping decrement $\Gamma_L(k_0) = \omega(k_0)$ when $k_0 = 2.34\kappa$ and $\omega(k_0)/\Omega_e = 3.5$.

Two regions can be distinguished in Fig. 1. In the first, where the lines are parallel to the one marked by unity, Landau damping dominates. The region where the isolines are vertical is dominated by collision damping.

From the definition of q_0 , it follows that the fraction of the collective degrees of freedom $s/3n_e = 1/3$ at $\gamma = \gamma_L = 0.3$ ($q_0 = k_0$ for $\gamma = \gamma_L$). The value $1/3$ means that only longitudinal waves are considered.

Thus, the number of collective degrees of freedom in a nonideal plasma is greater than in a Debye plasma, since in that case, they are no longer limited by Landau damping.

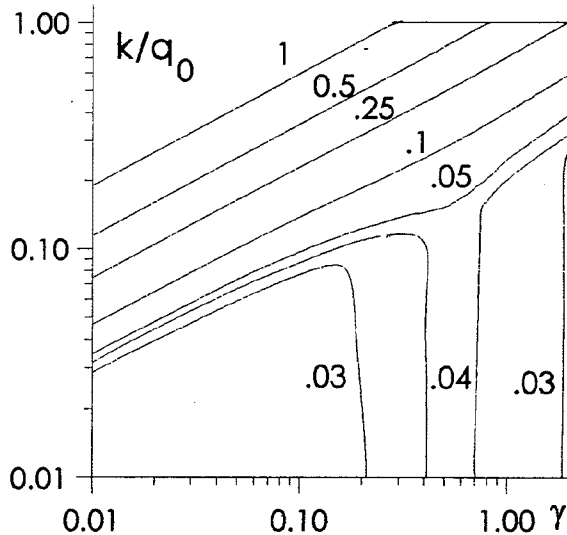


Fig. 1. Isolines $(\Gamma_c + \Gamma_L)/\omega = \text{const}$

The figures near the lines denote the values of const . The horizontal line corresponds to $k = q_0$.

2. Oscillation modes

Each collective degree of freedom corresponds to a normal oscillation mode, that is, to an oscillatory motion of a collective variable [10]

$$\rho_k(t) = \sum_j^N \exp(-ikx_j(t))$$

with a certain frequency $\omega(k)$.

In the nonideal plasma, the case is much more complicated, because we deal with a system of interacting oscillators with nonlinear coupling. To derive the motion equation for collective excitations in nonideal plasma, one should use the smallness of plasma wave damping. Then, similarly to [10], the Hamiltonian of the system has the form

$$H = H_{os}(\rho_k) + \Delta H_{kk'} + \Delta H_{os-in} + H_{in}(q, p) \quad (6)$$

where $H_{os}(\rho_k)$ is the Hamiltonian of the collective degrees of freedom, $H_{in}(q, p)$ is the energy of the individual degrees of freedom, and $\Delta H_{kk'}$ and ΔH_{os-in} represent relatively small interactions between different collective degrees of freedom and between collective and individual degrees of freedom, respectively.

Differentiating (6) with respect to ρ_k , one can obtain the equations of motion of the collective degrees of freedom. Then, following Tatarskii [11], who studied a system of coupled oscillators at small evolution times, one can reduce these equations to those of the Langevin form

$$\ddot{\rho}_k = -\omega_k^2 \rho_k + \Gamma_{eff} \dot{\rho}_k + y \quad (7)$$

where Γ_{eff} is the effective friction coefficient, which includes both collision and Landau dampings, and y is the δ -correlated random force

$$\langle y(t)y(t') \rangle = 2D_p \delta(t - t'),$$

D_p is the diffusion coefficient in p space.

The equations (7) are not coupled with respect to different k and can be treated as usual equations for a stochastic oscillator.

The corresponding estimates of plasma wave dispersion and damping decrement are in agreement with the results of molecular dynamics simulations [12].

3. Individual degrees of freedom

Differentiating (6) with respect to the coordinates of individual degrees of freedom, one can obtain the motion equations of individual quasiparticles. According to (6), two force terms appear. The first is due to the strong pair interaction of the electrons with other charges at short distances and the second is the action of the collective high frequency electric field.

Each force term results in a corresponding electron "collision" frequency item. Thus, the total effective scattering frequency ν_{eff} can be written in the form

$$\nu_{eff}/\Omega_e = \nu_c/\Omega_e + \xi \quad (8)$$

where ν_c is the electron-charge collision frequency and ξ is the fraction of collective degrees of freedom or the

ratio of the energy of the collective fluctuations to the electron thermal energy. For a Debye plasma $\xi = 0.17\alpha^3\gamma^{3/2}$ and for a nonideal plasma, $\xi = 1/3$. This estimate agrees with molecular dynamics results [12].

4. Energy of electric field fluctuations

The potential energy of the system of charged particles is proportional to the mean squared intensity of the electric field, including the collective field. The collective field energy is important for evaluation of certain properties of a nonideal plasma (see e.g. Section 3). However, to obtain thermodynamic functions, it is necessary to calculate the difference between the potential energies of the real system and of the noncorrelated system of charged particles. The derivation is rather complicated but can be performed analytically. The following expression for the internal correlation energy E/nkT is obtained [13]:

$$E/nkT = -2\pi^{-1/2}\gamma^{3/2} \arctg(q_0/\kappa) \quad (8)$$

For $\gamma \ll 1$, equation (8) gives the Debye-Hueckel limiting law. Further development of the thermodynamics can be done in the framework of the approaches some of which were considered in [5,6].

5. Acknowledgement

The authors acknowledge stimulating discussions with prof. A.Rukhadze and prof. M.Nezlin.

6. References

- [1] E.M.Lifshitz, L.P.Pitaevskiy: Physical Kinetics. Moscow, Nauka, 1979
- [2] A.F.Aleksandrov, L.S.Bogdankevitch, A.A.Rukhadze: Foundations of Plasma Electrodynamics. Moscow, High School, 1978.
- [3] G.Bekefi: Radiative Processes in Plasmas. New York, Wiley, 1966
- [4] L.Spitzer, Jr.: The Physics of Fully Ionized Gases. New York, Interscience, 1967.
- [5] V.E.Fortov, I.T.Yakubov: Nonideal Plasma. Moscow, Energoatomizdat, 1994.
- [6] Ebeling W., Forster A., Fortov V.E., Gryaznov V.K., Polishchuk A.Ya Thermophysical properties of hot dense plasmas. Teubner-Texte zur physik. Bd 25. Stuttgart: Teubner, 1992.
- [7] A.S.Kaklyugin, G.E.Norman, A.A.Valuev: Proc. Intern. Conf. Physics of Strongly Coupled Plasmas. Ed. W.D.Kraeft & M.Schlages. Singapore, World Scientific, 1996, p.435
- [8] V.M.Zamalin, G.E.Norman, V.S.Filinov. Monte Carlo Method in Statistical Thermodynamics. Moscow, Nauka, 1977.
- [9] J.M.Ziman: Principles of the Theory of Solids. Cambridge University Press, 1964.
- [10] D.Bohm: General Theory of Collective Coordinates. New York, Wiley, 1959.
- [11] V.I.Tatarskii: Uspekhi Fiz. Nauk, 151 (1987) 273
- [12] I.V.Morozov, G.E.Norman, A.A.Valuev: Plasma Waves in Nonideal Plasma. Molecular Dynamics. This Conference.
- [13] A.S.Kaklyugin. High Temp., 23 (1985) 217.

Topic 13

**Waves and instabilities,
including shock waves.**

Electron resonance cones in inhomogeneous plasmas

C. Riccardi, M. Salierno, M. Fontanesi
Dipartimento di Fisica-Universita' degli Studi di Milano
Via Celoria, 16 - 20133 Milano - Italy

Th. Pierre
Laboratoire de Physique des Milieux Ionisés
URA 835 C.N.R.S. , Université de Nancy I, B.P. 239
54506 Vandoeuvre-les-Nancy Cedex - France

1. Introduction

Resonance cones in the range of lower and upper hybrid frequencies are investigated experimentally in inhomogeneous magnetized plasmas.

The analysis has been performed both in linear and toroidal devices and was aimed to the study of some phenomena involved with the cones propagation in inhomogeneous plasma, like cone reflection close to the electron plasma layer, cone scattering due to the presence of density fluctuations and cone deflection due to geometrical effects.

A resonance cone can be excited by an oscillating point source. It can be shown that in a cold homogeneous magnetized plasma the wave potential generated through a point source becomes singular along a cone called "resonance cone", whose axis is parallel to the static magnetic lines, whose vertex is the point source and whose opening half-angle θ_c is related to the plasma parameters.

In this paper we analyse the propagation of electron resonance cones excited in the lower branch ($0 < f < \min(f_{pe}, f_{ce})$) (where f_{pe} is the electron plasma frequency and f_{ce} is the electron cyclotron frequency).

The analysis aims to study the cone propagation under different plasma conditions and in presence of inhomogeneities, which affect and sometimes prevent the cone propagation in the plasma.

The experimental investigation has been performed in linear (MIRABELLE) and toroidal devices (THORELLO), in which magnetized low density plasmas are produced.

2. Experimental results

Fig.1 shows the typical map relevant to the propagation of an electron resonance cone excited in the lower branch inside the plasma column of MIRABELLE; in the abscissa is represented the axial coordinate ($200 \text{ mm} < z < 400 \text{ mm}$) while in the ordinate the horizontal one ($-75 \text{ mm} < x < 75 \text{ mm}$). The detected signal amplitude is shown in arbitrary unit in the z coordinate.

The point source is located in $x=0 \text{ mm}$, $z=325 \text{ mm}$ (column centre is in $x=y=0 \text{ mm}$, $z=325 \text{ mm}$).

The signal is detected by a Langmuir probe and sent to a network analyser. The data have been detected along a

longitudinal plane (x,y) symmetric with respect to the emitting source, so it has been possible to detect the two divergent cones propagating from the source: one (left cone) propagates along the versus of the magnetic field (which is z) and the other (right cone) in opposite versus.

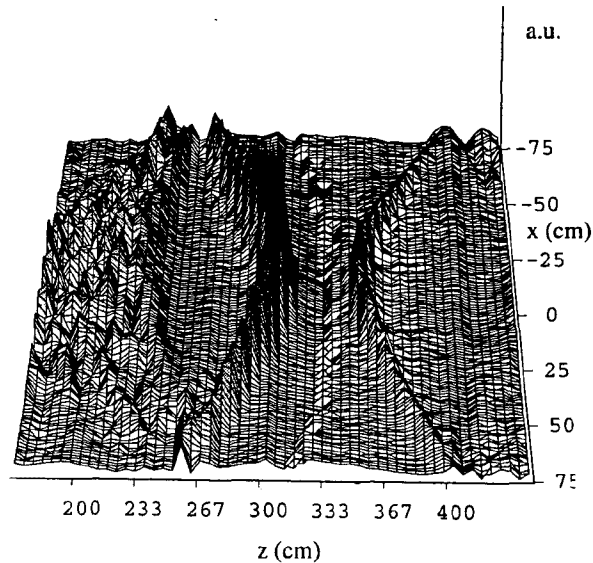


Fig.1 Resonance cones for $f=475 \text{ Mhz}$, detected in Mirabelle.

For the cone propagating to the left, it can be seen the reflection effect.

From the theoretical analysis^[3], the reflection of a resonance cone excited in the L.B. occurs on the electron plasma layer (f_{pe} layer), which corresponds to a local density n_e obtained from the resonance condition between the electron plasma frequency and the exciting frequency $f=f_{pe}(n_e)$.

It can be seen that while the diverging cones propagating from the source to the electron plasma layer exhibit a well defined cone structure (fig.1), the propagation of the reflected cone toward the focalization area ($x=0 \text{ cm}$; $z=223 \text{ cm}$) becomes less localised so that the cone does not converge into a focal point, but in a broadened region around it.

This phenomenon is due to a non-perfect symmetry of density transversal (perpendicular to the magnetic field) profile; the two branches departing from the source are reflected in different radial positions ($x_1 \neq x_2$) around $x = \pm 75$ mm. The non perfect symmetry of the density profile generates two different effects: the global radial shift of the convergent cone with respect to the symmetry axis ($x=0$ cm) of the divergent cone, and a delocalized focal region.

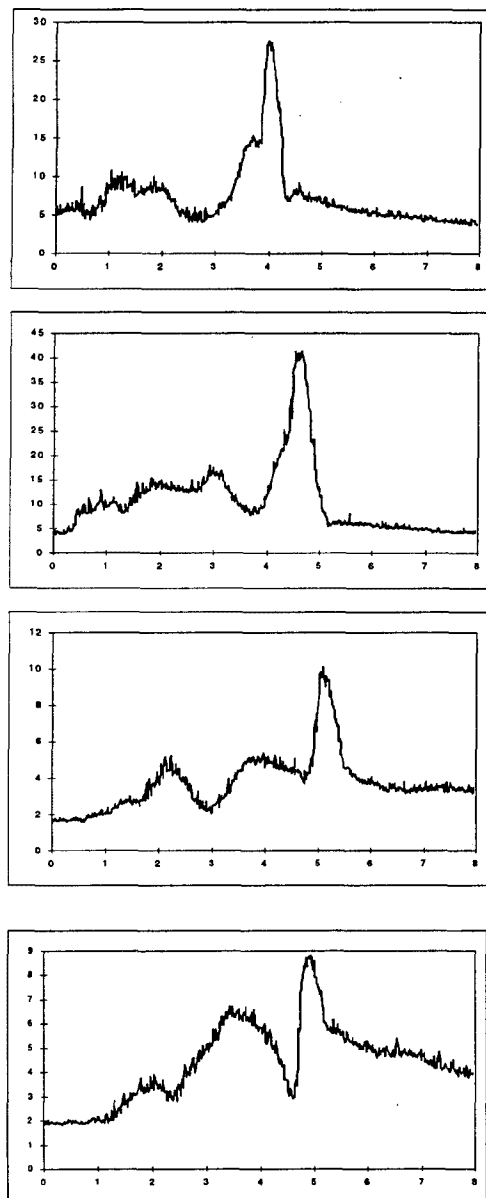


Fig.2 Resonance cones vs radial position in a.u., detected in Thorello for different frequencies : from the top $f=350;450;505;515$ Mhz.

The energy relevant to the reflected converging cone instead of being focalized, and consequently presenting a maximum, is distributed among a set of secondary

peaks. Another phenomenon which prevents the cone focalization is related to the presence of density fluctuations, which are also the main obstacle to the propagation and consequently to the detection of resonance cone.

For what concerns the analysis of toroidal effects, in fig. 2 are shown the cone amplitudes as a function of the radial position for several values of the exciting frequency. The emitting source and the probe are both in the equatorial plane of the chamber and they can move along the radial section of the plasma column.

We have observed as follows: only a resonance peak appears and there is a radial shift of the cone increasing the exciting frequency. At the frequency of $f=505$ Mhz, the resonance peak reverses its radial shift.

As the distance between the source and the probe is 15 cm and the source is placed 2.5 cm from the chamber edge, where density gradient is high, we can explain the lack of the second resonance peak supposing that the cone propagating towards the edge side of the chamber has been subject to one or more reflections on the edge plasma layer before detection.

These reflections can induce a partial wave delocalization and a signal modulation as shown in the same figure. The radial cone shift with the frequency is in agreement with L.B. theory: the cone angle increases when the exciting frequency increases.

The reason for which this shift is not very evident compared to the cone propagation in the linear device could be due to the presence of a weak toroidal magnetic field gradient.

In fact, as theory shows, the resonance cone propagation is highly sensitive to the magnetic field variation.

3. Conclusions

In the linear device the cone propagation and the effects induced by a density gradient have been analysed: the cone reflection on peculiar plasma layers and the bending of the cone generatrices has been observed.

The analysis of the cones propagation has been performed varying the signal frequency.

In the toroidal device the cone propagation has been shown to be highly influenced by the geometry, i.e. the curvature of the toroidal magnetic field lines, and by the strong radial density gradient.

4. References

1. Fisher R.K. and Gould R.W., Phys. Fluids **14**, p.857 (1971).
2. Pierre Th., Leclert G. and Braum F., Rev. Scient. Instrum. **58**, 6 (1987).
3. Ohnuma T. *IEEE Trans. Plasma Sci.* **PS6** (12), p. 471 (1978).

Topic 14

**Non-linear phenomena and
self-organization processes.**

Observation of spontaneous turbulent electrostatic fluctuations in a magnetoplasma

C. Riccardi, D. Caspani, L. Gamberale, G. Chiodini and M. Fontanesi

Dipartimento di Fisica, Università di Milano,
Via Celoria 16, 20133- Milano, Italy

1. Introduction

This paper concerns the analysis of the electrostatic fluctuations in the toroidal magnetoplasma Thorello. The research is focused on the characterisation of the turbulent regime, associated with destabilised drift-type waves. This study is performed by measuring the frequency spectra and by evaluating the presence of nonlinear wave interactions through the estimate of the bicoherence coefficients of density fluctuations.

The destabilisation of drift waves driven by density gradient has been subject of theoretical analyses¹ based on the collisional model. They showed that a coherent drift mode can destabilise and generate a turbulent spectrum for the ion gyroparameter satisfying the following relation:

$$\beta = (k_{\perp} \rho_i)^2 \ll 1,$$

where ρ_i is the ion gyro-radius calculated at the electron temperature. In our plasma for a magnetic field value of 2kG, the typical ion gyroparameter is lower than 0.1, so that drift waves are destabilised.²

2. Experimental results

The experiment is carried out in the Toroidal device Thorello which produces magnetised hydrogen plasma in steady-state conditions. Typically obtained plasma parameters for a toroidal magnetic field of 2kG are: $T_e \approx 1$ eV, $T_i \approx 0.3$ eV, edge plasma density $\approx 10^9$ cm⁻³, centre plasma density $\approx 10^{11}$ cm⁻³, neutral gas pressure $P = 10^{-4}$ mbar.

In fig.1 the radial behaviour of the density fluctuations normalised to the medium density evaluated from the ion saturation current is shown.

The relative density fluctuations reach the maximum value (25%) in the plasma edge and decrease going towards the plasma center where they assume the value of 5%.

These fluctuations are to be ascribed to the presence of drift waves driven by density gradient in the plasma edge. The statistical dispersion of such modes has been analysed in previous works^{2,3}.

The wave frequency power spectra of such fluctuations are obtained by Fourier transforming the signals relevant to the ion saturation current.

Signals are sampled at 10 μ s, as the typical measured frequency range of the fluctuations is below 50 kHz.

Fig.2 shows the frequency spectra measured in different radial positions at the plasma edge, where the relative

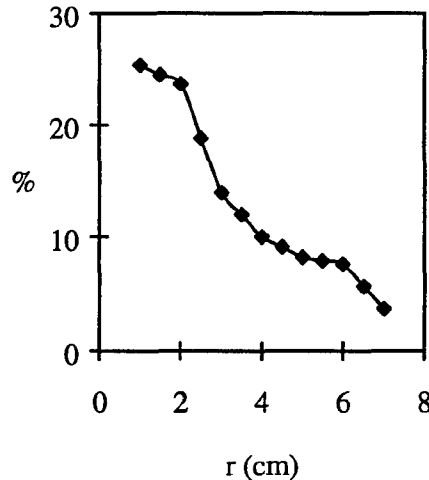


Fig.1: density fluctuations normalised to the medium density as a function of the radial position.

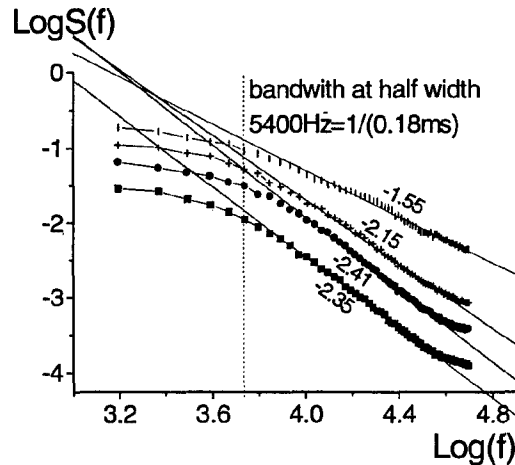


Fig.2: Frequency spectra at different radial positions: ■ 1cm, ● 1.5cm, ▲ 2cm, ◆ 3cm.

density fluctuations are quite large.

The spectra can be fitted in the frequency range above 5 kHz by a power law characterized by a spectral index b , as follows:

$$S(f) \propto \frac{1}{(f)^b}$$

where b is of the order of 2. It turns out that density fluctuations are characterized by a turbulent regime.

The experimental data are in agreement with previous measurements performed in other linear and toroidal devices^{4,5}.

Turbulence can be caused by nonlinear interactions between destabilised drift waves. To investigate the occurrence of a non linear mechanism in the fluctuation spectra we have estimated the bicoherence coefficient following the procedure described in reference 6.

The normalised bicoherence coefficient gives information on the degree of phase coherence among three different frequency modes ω_1 , ω_2 , $\omega_1 + \omega_2$, regardless from their amplitude. A statistically different from zero value would indicate that there exists a waves dynamical interaction in the system that couples non linearly the three modes, or may reflect phase relation between modes describing quasi-static, long-lived structures.

We have computed the bicoherence coefficient on different time scales and we have found that a typical time scale exists for which the degree of phase coherence among the three modes is large indicating that this effect is produced by wave dynamical interactions rather than a time stationary process. The most convenient analysis tool for discriminating between dynamic and static processes is that of bicoherence wavelet transform and will be the argument of a future work.

In fig.3 the bicoherence coefficient has been plotted as a function of ω_1 and ω_2 .

For $B=2$ kG the main bicoherence peak reaches the value 0.33 ($\sigma^2(b) \approx 0.01$) and the non-linear interaction occurs in the rectangle defined by the frequency ranges $f_1=(0-30)$ kHz and $f_2=(0-5)$ kHz, i.e. the non-linear wave-wave interaction is significant over the whole frequency range (Fig. 3).

By repeating this analysis for different plasma parameters (magnetic field and plasma density) we have obtained very similar bicoherence spectra indicating that the non-linear behaviour depends mainly on the magnetic field intensity and on the radial position.

The bicoherence coefficient is high in the edge ($x=1$ cm) where the total integrated bicoherence reaches values higher than unit ($b^2 \approx 3$), showing a nonlinear interaction between more than three waves. Moving towards the center ($x > 3.5$ cm) the total integrated bicoherence lowers at about $b^2 \approx 0.2 + 0.3$. For this reason we can conclude that the characteristics of drift waves in the edge and in the plasma center are different.

It can be noticed that the bicoherence and the density fluctuations amplitude have a similar behaviour: the nonlinear interaction between waves is strong in the

plasma edge ($x < 3$ cm), where the density fluctuations are large.

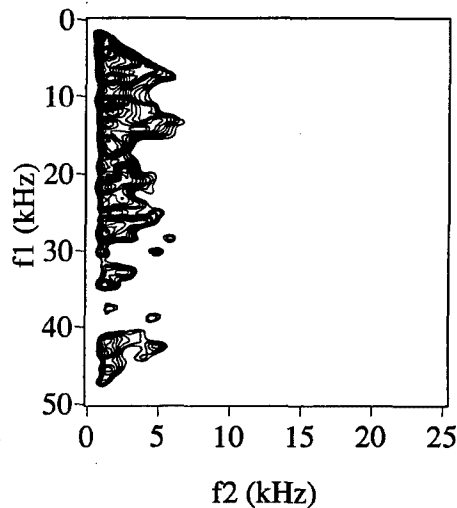


Fig.3: bicoherence coefficient plotted as a function of f_1 and f_2 .

3. Conclusions

In conclusion we see that the turbulent regime develops mainly in the plasma edge due to the destabilisation of drift modes. In presence of turbulent density fluctuation spectra are characterised by a power law in agreement with other measurements.

The amplitude of these fluctuations is large and the bicoherence analysis shows a large presence of three-wave coupling, so that the turbulence can be regarded as a nonlinear interactions of drift-type modes. Contrary, in the plasma inner the nonlinear interactions are negligible and the level of the relative density fluctuations is low.

4. References

1. Kauschke, G. Oelerich-Hill and A. Piel, Phys. Fluids B 2, (1990).
2. C. Riccardi, D. Xuantong, L. Gamberale, D. Caspani, L. Fattorini, M. Fontanesi, Proc. of the 23rd EPS Conf. on Contr. Fus. and Plasma Phys., Kiev (Ukraine) 1996.
3. C. Riccardi, D. Xuantong, M. Salierno, L. Gamberale, M. Fontanesi, submitted to Phys. Plasmas (1997).
4. J.M. Beall, J.K. Kim, E.J. Powers, J. Appl. Phys., 53 p.3933 (1982).
5. G. Prasad, D. Bora, Y.C. Saxena, S.D. Verma, Phys. Plasmas, 1 p.1832 (1994).
6. J.K. Kim, E. J. Powers, IEEE Transactions on Plasma Science, PS 7, p.120 (1979).

Bifurcation analysis of the negative corona discharge

M. S. Benilov

Departamento de Física, Universidade da Madeira, Largo do Município, 9000 Funchal, Portugal

1. Introduction

Interesting current structures were observed on spiral corona cathodes in an electrostatic precipitator configuration in recent experiments [1]: part of the cathode was dark with bright points, another part was luminous with longitudinal dark strips. The bright points seem to correspond to the spots on the surface of a corona cathode in electron-attaching gases, described in [2]. The dark strips were interpreted by the authors [1] as current-free zones. Later, the current-free strips on cylindrical and spiral cathodes have been observed in two- and three-dimensional steady-state computer simulation [3].

The basic question concerning these current-free strips is whether they appear due to (1) current contraction or (2) the specific discharge geometry. The second hypothesis implies that a regime with a more or less uniform current distribution over the cathode surface does not exist in the discharge configuration considered, thus the regime with the strips is the only possible in this situation. The first hypothesis implies that the geometrical factor is not decisive and the regime with a uniform current distribution over the cathode surface exists, however it is unstable and does not realize in the physical and computer experiments, while the regime with the strips is stable and realizes. If this hypothesis is correct, the current-free strips belong to self-organized structures, similarly to the normal spots on glow cathodes and to the arc spots.

In the computer simulation [3], regimes of both types (with a nearly uniform distribution of the electric current over the cathode surface and with current-free strips) have been observed, depending on parameters of the discharge. This indicates that the effect of the geometrical factor is weak, which supports the first hypothesis. Note that equations considered in [3] are not very different from those in the framework of which the normal spots on glow cathodes can be described: both sets of equations include the Poisson equation and the equation(s) of continuity of mobility-dominated flux of the charge carriers. This also confirms to the first hypothesis.

The aim of this contribution is to perform the bifurcation analysis of the corona discharge on a negative electrode and to find out on the base of this analysis whether the current-free strips appear due to current contraction or due to the specific discharge geometry. A procedure is similar to that applied in [4] to the problem of the normal current spot on a glow cathode.

2. The model

We consider the computational model of a negative corona discharge in air at atmospheric pressure suggested in [3, 5]. The model is based on a steady-state description of the discharge and is simple enough to be tractable in multidimensional situations. In brief, this model may be described as follows. It is assumed that ionization of neutral particles is localized in a thin active zone adjacent to the corona cathode surface. The positive ions drift to the surface. The electrons attach rapidly to molecules to form negative ions which leave the active zone and drift to the grounded electrode. The plasma outside the active zone is described by the conventional system of equations (e.g., [6]) consisting of the Poisson equation, the equation of current continuity, and Ohm's law

$$\epsilon_0 \Delta \varphi = en_-, \quad \nabla \cdot \mathbf{j} = 0, \quad \mathbf{j} = -e\mu_- n_- \nabla \varphi. \quad (1)$$

Here n_- and μ_- are the number density and the mobility of the negative ions, other designations are conventional.

Boundary conditions for these equations are

$$\varphi = -U, \quad en_- = c\bar{\alpha}; \quad \varphi = 0; \quad j_n = 0. \quad (2)$$

The first and the second boundary conditions apply to the edge of the active zone, the third one applies to the surface of a (grounded) outer electrode, and the last one to an insulating part of the inner surface of the discharge tube; U is the voltage applied to the corona cathode, c is a given constant, and $\bar{\alpha}$ is the effective ionization coefficient ($\bar{\alpha} = \alpha - \eta$, where α and η are the ionization and attachment coefficients, respectively) considered as a given function of the local electric field. The first condition implies that a voltage drop in the active zone is neglected as compared to the total voltage applied. The second condition accounts in an approximate way for production of charge carriers in the active zone and is central in the model [3, 5]. Supposing that the thickness of the active zone is much smaller than dimensions of the corona cathode, one can assume in calculations that the first and the second boundary conditions apply to the cathode surface.

3. Bifurcation analysis

We proceed within the framework of the assumption that the current-free strips appear due to current contraction, i.e., that the first hypothesis described in the Introduction is correct. This means that the geometrical factor is not decisive and the considered problem has a solution describing the regime with a more

or less uniform current distribution over the cathode surface, and one or more solutions describing regimes with the current contraction (with the current-free strips).

In the simplest case, one can completely exclude the geometric factor by considering a cylindrical or spherical geometry. For definiteness, we shall consider the cylindrical geometry, i.e., assume that the discharge tube consists of two concentric cylindrical electrodes and the insulating ends. The regime with a uniform current distribution over the cathode surface is described by a one-dimensional solution $\varphi = \varphi(r)$, and solutions describing regimes with the current contraction are multidimensional: $\varphi = \varphi(r, \theta, z)$. Thus, the hypothesis that the current-free strips appear due to current contraction amounts to the claim that the problem (1), (2) in the cylindrical configuration has one- and multidimensional solutions simultaneously.

In accordance to the results of [7,8], it is natural to assume that regimes with the current contraction, if they exist, under variation of the voltage continuously join the regime with a uniform current distribution over the cathode surface. In mathematical terms, this means that the one-dimensional solution has bifurcation points in which multidimensional solutions branch off. Thus, one should find the one-dimensional solution and carry out its bifurcation analysis.

The one-dimensional solution of the problem (1), (2) in the cylindrical geometry is well-known (e.g., [9] and references therein). Designate by U_0 and by $\varphi_0(r)$, respectively, a value of the applied voltage and a distribution of the electrostatic potential that correspond to one of the bifurcation points. Represent solutions in the vicinity of this point (i.e., for U close to U_0) in the form $\varphi(r, \theta, z) = \varphi_0(r) + \psi(r, \theta, z)$. In the vicinity of the bifurcation point function ψ is small and the problem may be linearized. A linear non-homogeneous boundary-value problem appears, non-homogeneity being introduced by the difference $U - U_0$. Since this problem describes the vicinity of a bifurcation point, its solution must be non-unique. This means that the corresponding homogeneous problem also has a non-unique solution, i.e., is degenerate. After separation of variables, one gets an eigenvalue problem for an ordinary differential equation of the third order describing the radial part of this solution, U_0 being an eigenvalue.

This problem was solved numerically in the following way. A finite difference scheme of the fourth order of accuracy was applied. The determinant of the resulting system of linear algebraic equations was evaluated by means of the variant of the Gaussian elimination technique. Such an evaluation was made for a given geometry of the discharge and for varying U_0 . A change of sign of the determinant would indicate passing through a bifurcation point.

Calculations have been performed in the range of U_0 of up to 200 kV. The geometrical parameters

were chosen similar to those of [3]: the radius of the corona cathode was taken equal to 3 mm or to 15 mm, the radius of the grounded anode was 15 cm, and the height of the discharge tube was 15 cm. Five modes were taken into account in each of the directions θ, z (i.e., bifurcation points were sought in which first 24 harmonics branch off).

No change of the determinant sign was detected in the whole range of conditions studied. In other words, bifurcation points are absent, which indicates that multidimensional solutions probably do not exist.

4. Concluding remarks

The performed analysis shows that there are no bifurcation points on the one-dimensional steady-state cylindrically symmetric solution obtained in the framework of the model [3,5] of the corona discharge. This indicates that regimes with the current contraction probably do not exist in the framework of the considered model. One can conclude that the current-free strips on the corona cathode surface appear due to the specific discharge geometry rather than due to the current contraction. The fact that the weak geometrical factor can produce a finite effect is probably explained by the strong dependence of the current density at the corona onset on the local electric field.

5. Acknowledgments

The work has been supported by FEDER and by the program PRAXIS XXI. Part of the work has been performed in the Ruhr-Universität Bochum and supported by the Alexander von-Humboldt Stiftung. The author is grateful to W. Egli and U. Kogelschatz for providing additional information on the experiment [1] and the simulation [3,5].

REFERENCES

- [1] W. Egli, O. Riccius, U. Kogelschatz, R. Gruber, and S. Merazzi, in *Proc. 6th Joint EPS-APS International Conference on Physics Computing*, 535 (1994).
- [2] L. B. Loeb, *Electrical Coronas* (University of California Press, Berkeley, 1965).
- [3] W. Egli and U. Kogelschatz, *Contr. papers of XXII Int. Conf. on Phenomena in Ionized Gases*, vol. 1, 119 (1995).
- [4] M. S. Benilov, *Sov. Phys. - Tech. Phys.* **33**, 1267 (1988).
- [5] W. Egli and U. Kogelschatz, *Helvetica Physica Acta* **68**, 203 (1995).
- [6] R. S. Sigmond, in *Electrical Breakdown of Gases*, ed. by J. M. Meek and J. D. Craggs (Wiley, Chichester, 1978).
- [7] M. S. Benilov and N. V. Pisannaya, *Sov. Phys. - Tech. Phys.* **33**, 1260 (1988).
- [8] M. S. Benilov, *Phys. Rev. A* **45**, 5901 (1992).
- [9] R. T. Waters and W. B. Stark, *J. Phys. D* **8**, 416 (1975).

Topic 16

Plasma sources of radiation.

Modeling of LF barrier discharges in a Xe excimer lamp

A.Oda, Y.Sakai, H.Sugawara and P.Ventzek
Hokkaido University, Sapporo 060 Japan

1. Introduction

An excimer lamp is an important UV light source for photochemical technologies [1,2]. One of the efficient large volume stable discharges for obtaining high power uv light is barrier discharges [2].

In this article, a simulation is presented, the goal of which is to understand the discharge characteristics (e.g., spatio-temporal evolution of the electron and excimer (xenon dimer) concentrations, electric field, and efficiency of the UV output) in LF (low frequency) Xe plasma discharges between the dielectric barrier electrodes.

2. Model

Fig.1 is the electrode configuration for this work. The electron swarm parameters used in the simulation are calculated using the Boltzmann equation. Using these parameters the concentrations of electrons and ions are calculated by the following equations as, for electrons

$$\frac{\partial n_e}{\partial t} = S_e + \frac{\partial}{\partial x} \left(-W_{Te} n_e + D_L \frac{\partial n_e}{\partial x} \right)$$

and for ions,

$$\frac{\partial n_{+,j}}{\partial t} = S_{+,j} + \frac{\partial}{\partial x} \left(W_{T+,j} n_{+,j} + D_{L+,j} \frac{\partial n_{+,j}}{\partial x} \right)$$

(j : Xe⁺, Xe₂⁺)

Here, the S_e and $D_{L+,j}$ are written as functions of the electron energy determined by an energy conservation equation for electrons.

The local field $E(x,t)$ is a sum of the external field E_{ex} and space charge distorted field E_{in} as

$$E(x,t) = E_{ex}(t) + E_{in}(x,t)$$

$E_{in}(x,t)$ is found by solving the following equations.

$$\text{div } D = \rho, \quad D = \epsilon E, \quad E = -\text{grad } V$$

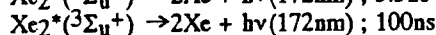
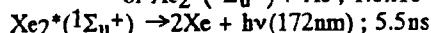
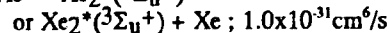
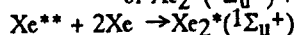
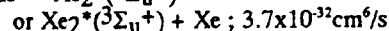
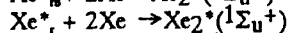
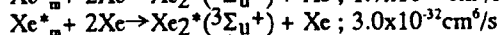
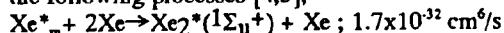
The charges accumulated on the ground and the powered electrode are calculated by time integrating the flux of electrons and ions incident on the electrodes. The charges on the barrier surface are assumed to recombine only when hetero-charges arrive.

The discharge current i_g is written as

$$i_g(t) = \frac{eS}{d} \int_{d/2}^{d/2} (n_+(x,t) \cdot W_{T+}(x,t) - n_e(x,t) \cdot W_{Te}(x,t)) dx$$

Here S is the electrode area.

The reaction processes among electrons, ions, ground state and excited neutral species are taken from [3-5]. Particularly important processes are for generation and extinction of Xe₂^{*}. We use the following processes [4,5].



For our standard case, the Xe pressure, p_0 , is 50Torr, and the frequency and peak values of the power source are 100kHz and 6.375kV respectively.

3. Results and discussion

Fig.2 contains the discharge voltage V_g and current i_g , and power voltage V_s waveforms. The phase of i_g coincides with that of V_g , though the phase shift between V_g and V_s is seen by $\pi/2$ due to presence of the dielectric barriers.

The electron and ion concentration in the discharge bulk is found to be an order of 10^{12} cm^{-3} .

The E at the cathode is enhanced up to 800 V/cm, while the anode side is 200V/cm as shown in Fig.3. As the result of the E enhancement, the electron temperature at the cathode side is around 4eV compared to the anode side value of 2eV and the bulk value of 1eV. Because of this, the net production rate of excimer Xe₂^{*} is high in the region adjacent to the cathode, while by the anode it is negative as shown in Fig.4.

The Xe₂^{*} concentration in the near-electrode region (1mm thickness) is significantly high as shown in Fig.5 because of the high electron temperature brought by the high field.

In this model the a production efficiency of excimer light (172nm) is around 1.5%, which seems reasonable since the value is 10% at atmospheric pressure[6].

4. Conclusion

For the present simulation conditions, the excimer Xe₂^{*} were mainly produced in the near-electrode region (1mm), and the efficiency of excimer production was around 1.5%.

This work was supported in part by a Grant-in-Aid of Scientific Research, Japanese Ministry of Education, Science and Culture.

References

- [1] P. Bergonzo, et al: Appl. Surface Science, 54 (1992) 424
- [2] H. Esrom and U. Kogelschatz: Thin Solid Films, 218 (1992) 231
- [3] F. Kannari, et al: IEEE J. Quantum Electron. QE-19 (1983) 1587
- [4] P. K. Lechner, et al: Phys. Rev. A 13(1976) 1787
- [5] C. Duzy and J. Boness: IEEE J. Quantum Electron. QE-16 (1980) 640
- [6] B. Eliasson and U. Kogelschatz: Appl. Phys. B 46(1988) 299

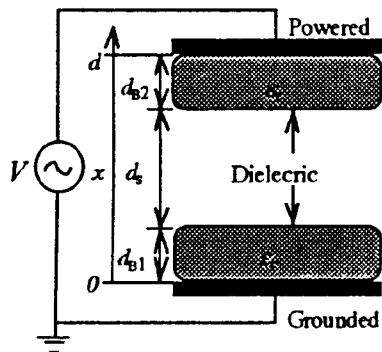


Fig.1 Electrode configuration and external circuit. The electrode distance is $d=10\text{mm}$. The thickness of dielectric barriers are $d_{B1}=d_{B2}=1\text{mm}$ and their dielectric constant $\epsilon_{r1}=\epsilon_{r2}=4$, and $d_s=8\text{mm}$. V_s has an amplitude of 6.375kV and $f=100\text{kHz}$.

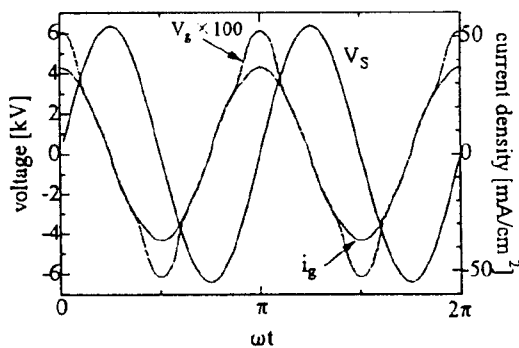


Fig.2 Waveforms for V_g , i_g and V_s .

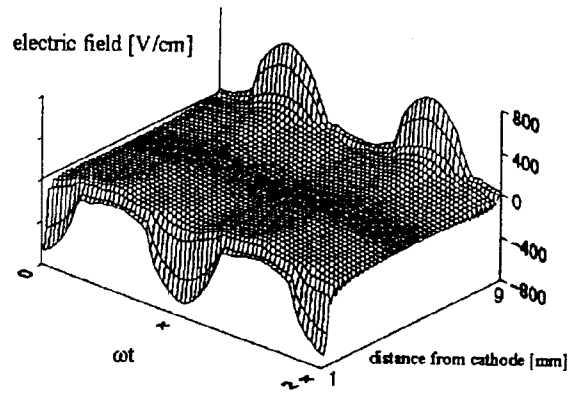


Fig.3 Spatio-temporal evolution of the electric field $E(x,t)$.

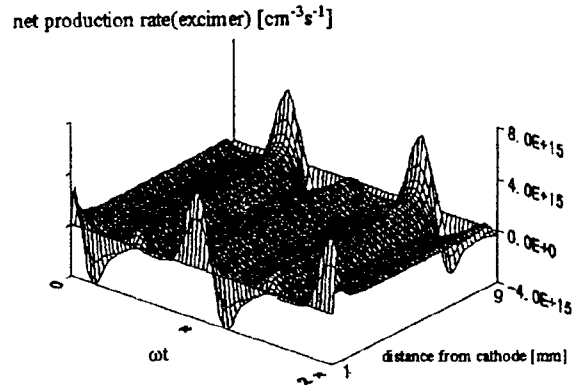


Fig.4 Spatio-temporal evolution of the net generation rate of Xe_2^* .

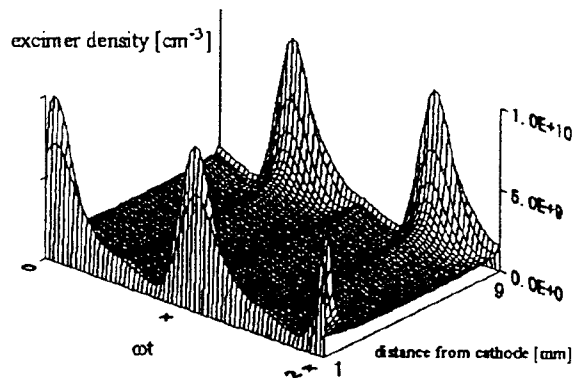


Fig.5 Spatio-temporal evolution of the Xe_2^* concentration.

Numerical Simulation of a Plasma Display Panel Discharge Operated by ac Pulses

Seishiro Hashiguchi and Kunihide Tachibana*

Department of Electronics and Information Science, Kyoto Institute of Technology, Matsugasaki, Sakyo-ku, Kyoto, Japan

Graduate School of Engineering, Kyoto University, Yoshida Honmachi, Sakyo-ku, Kyoto, Japan*

1. Introduction

Plasma display panel(PDP) discharges have been studied for dc type with electrodes and for ac type which is similar to barrier discharges. Modeling were made for both types[1],[2]. One of problems of present PDPs is that efficiency is as low as about 1%. Here, efficiency of UV radiation is defined as the ratio of the intensity of UV radiation on the electrode to the input power per unit area. Higher efficiency will increase brightness of the panel and will make the life time longer. The distribution of electrons in the present PDP's is the same as the one in a usual dc glow discharge; a few but high energy electrons in the cathode region and many but low energy electrons in the region near the anode. The latter is unable to excite atoms. An idea to begin the present study is that how can one energize low energy electrons. If the polarity of the applied voltage is reversed, low energy electrons in a dc PDP may be energized. The present ac PDP is different from this situation; in an ac PDP which has a dielectric layer, the polarity is reversed after the discharge current ceases. Our PDP has two metal electrodes and a rectangular pulse voltage is applied. After a half period, the applied voltage reverses its sign with the same amplitude. The applied voltage changes its sign successively in this way. Numerical study of this PDP cell is described in the following.

2. an ac-PDP cell with metal electrodes

We study the same PDP cell as the one studied in

[1] except the applied voltage. The working gas is He-Xe mixture of 200Torr including 10% of Xe. The electrode distance is 200 μm . The one-dimensional model described in [1] was used to analyze the discharge. Following pulse voltage was used: amplitude was 160V and the pulse width was 50ns for both positive and negative pulses. The discharge was maintained when an appropriate value of initial ion density was chosen. If the dc voltage was applied, 218V was necessary between the electrodes to maintain the discharge. After 50 cycles, change in the discharge current was less than 1% in the next cycle.

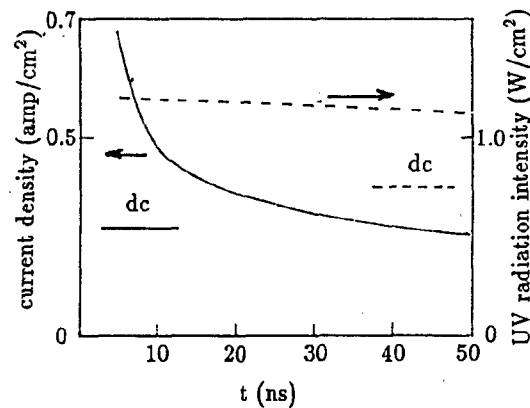


Fig. 1 Current density ——— and UV radiation intensity - - - -. The symbol dc stands for the case of dc voltage of 218V.

Figure 1 shows the discharge current density and UV radiation intensity on an electrode during a pulse. UV radiation was almost constant. Values for dc discharge voltage of 218V were also given in Fig. 1. The larger current for the pulse case gives larger UV radi-

ation intensity than the dc case. The efficiency of UV radiation during a pulse was calculated. This value is 1.5% which is only slightly larger than the value for the dc case of 1.3%.

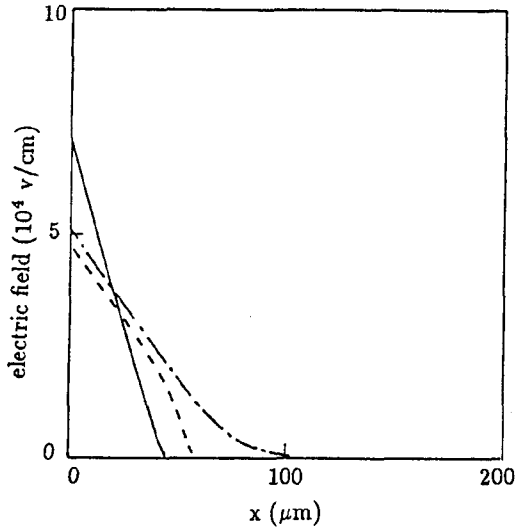


Fig. 2 Electric field at $t=5\text{ns}$ — and at $t=50\text{ns}$ ---- . Electric field for dc case is also given — .

Figure 2 shows the electric field distribution in the cell. The cathode layer becomes thick with increase in time and electrons are driven inward.

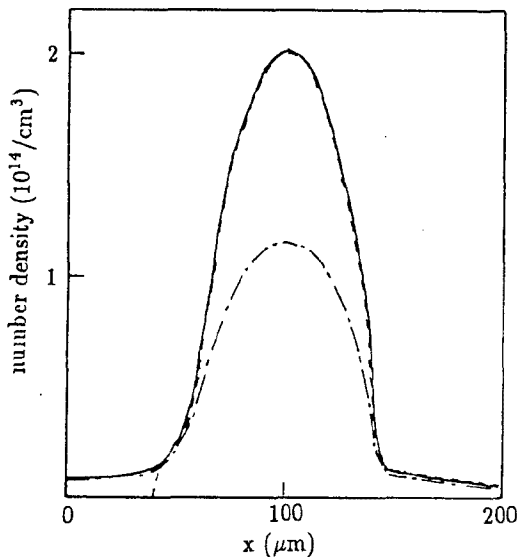


Fig. 3 Density distributions in the cell at $t=5\text{ns}$. Electron ---- , xenon atomic ion — and total ion — .

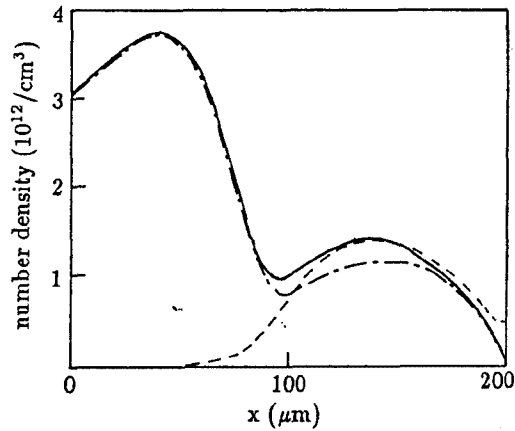


Fig.4 Density distribution in the cell for the dc case. Marks have the same meaning as in Fig. 3.

Figures 3 shows density distributions. High density plasma region exists in the central region and the maximum density is two orders of magnitude larger than the dc case which is shown in Fig. 4.

3. Conclusion

For the ac pulse case studied here, the UV radiation efficiency was almost the same as the dc case. However, if we use smaller pulse amplitude, efficiency may increase. It is necessary to search the most fitted parameters for the ac pulse operation.

4. References

- [1] K.Takahashi, S.Hashiguchi, Y.Murakami, M.Takei, K.Itoh, K.Tachibana and T.Sakai; Jpn. J. Appl. Phys., 35(1996) 251.
- [2] J.Meunier, Ph.Belenguer and J.P.Boeuf; J. Appl. Phys., 78(1995) 731.

DYNAMIC ELECTRICAL CHARACTERISTICS OF FLUORESCENT LAMPS

T.P.C.M. Vos*

F.A.S. Ligthart *

J.A.M. v.d. Mullen**

J. van Dijk**

* Central Development Philips Lighting, Philips Lighting B.V., Building EDW-533,
P.O. Box 80020, 5600 JM Eindhoven, The Netherlands

** Eindhoven University of Technology P.O. Box 513, 5600 MB, Eindhoven,
The Netherlands

INTRODUCTION

An experimental and theoretical study was carried out into the dynamic behaviour of the electrical characteristics of standard T8 fluorescent lamps under high-frequency operation. The development of sophisticated electronic ballasts to operate fluorescent lamps requires a profound knowledge and understanding of the electrical characteristics including not only the static but also the dynamic (transient) aspects. In particular, to reduce the development time for electronic ballasts a reliable electrical model of the lamp is required in order to make possible the use of advanced circuit simulation programs. The aim of the present work is to create a fluorescent lamp model that can be exploited for simulations of the lamp in electronic ballasts.

EXPERIMENTAL

With the help of a frequency variable high-voltage power supply in combination with a near-resonant LCR circuit fast positive or negative discrete changes can be put on the high-frequency electric lamp current resulting in nearly immediate positive or negative responses in the value of the high-frequency lamp voltage. In the steady state the high-frequency voltage-current characteristic shows the familiar non-linear behaviour with a certain degree of hysteresis [1] where the voltage lags somewhat behind the current. See Figure 1, the familiar Lissajous type characteristic. The behaviour of the I-V characteristic under a fast drop the electric current can be described as a superposition of about 70 Lissajous figures moving in clock-wise direction, see Fig.2. In a similar way, a fast increase in lamp current can be described as a superposition of about 10 Lissajous figures moving in counter clock-wise direction.

LAMP MODEL

A three level collision radiative model of the discharge lamp was developed which includes the mercury ground state, a combined excited state and the mercury ion state. This model appears to be capable to describe the dynamic features of the fluorescent lamp in a quantitative way, see Figure 3 for the dynamic I-V behaviour after a sharp current decrease.

CONCLUSIONS

A three level collision radiative model was developed which is capable to describe the main dynamic features of T8 standard fluorescent lamps including the time-scales of the transient phenomena. Using this model the hysteresis in the high-frequency I-V characteristics can be explained as a time and phase lag of the electron temperature behind the electric field.

REFERENCES

- [1] Y. Watanabe and S. Murayama, Jpn. J. Appl. Phys., **32**, 3593, (1993)

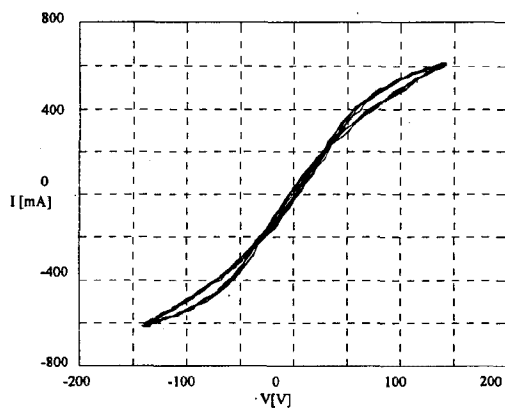


Fig. 1. Experimental voltage/current relation within the high frequency period: the Lissajous curve; measured at room temperature, $f = 96$ kHz and $I = 455$ mA.

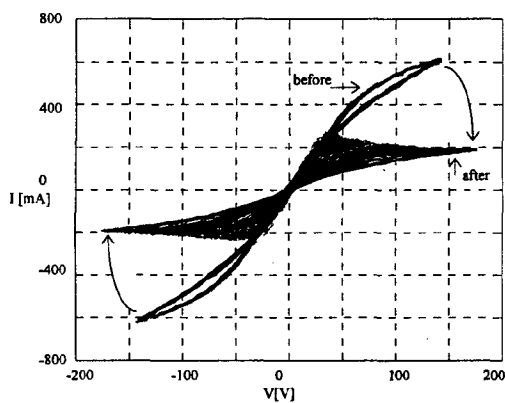


Fig. 2. Experiment: time development of Lissajous curves, after current step-down; $I_{\text{before}} = 455$ mA, $I_{\text{after}} = 155$ mA.

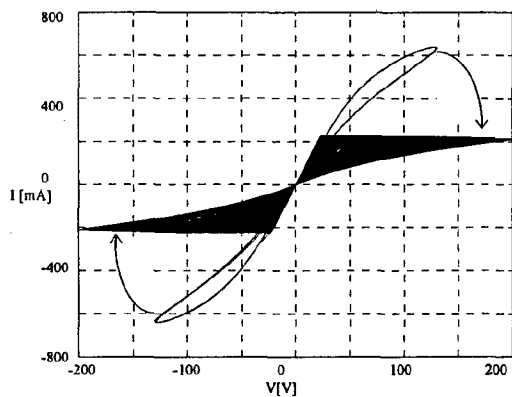


Fig. 3. Model: time development of Lissajous curves, after current step-down; $I_{\text{before}} = 455$ mA, $I_{\text{after}} = 155$ mA.

Investigation of Micro-plasma Source of Radiation

V.A. Gostev, V.V. Mamkovich, V.I. Sysun

Petrozavodsk State University, Department of Physics, Petrozavodsk
185640, Lenin av.33, Karelian Republic, Russian Federation

Interest to the plasma electro-magnetic fields and particles radiating sources increased in the last years because of wide vistas of its applications in many spheres [1]. One of the variants of such sources is given in [2]. In the present work we give the result of the researches of micro-plasma source of radiation (MPSR). The size and form of electrodes were usual for high-pressure discharge pre-ionizing sources [3].

Gas entered the inter-electrode gap by the nozzle in the form of needle, that was the anode. If the pressure on the enter was higher than atmospheric pressure, discharge came out on the outlet of nozzle. Plasma formation had a form of small sphere on the end of sharpened anode. MPSR scheme and micro-plasma formation photo are given on the fig.1.

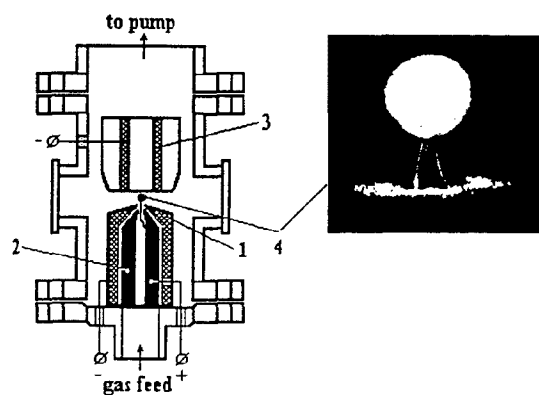


Fig.1 Construction of MPSR. 1-cathode 1, 2-nozzle-anode, 3-cathode 2, 4-micro-plasma formation photo

The investigations were made in helium under the pressure 1,1 - 1,3 Atm. Typical volt-ampere characteristic is given on the fig.2.

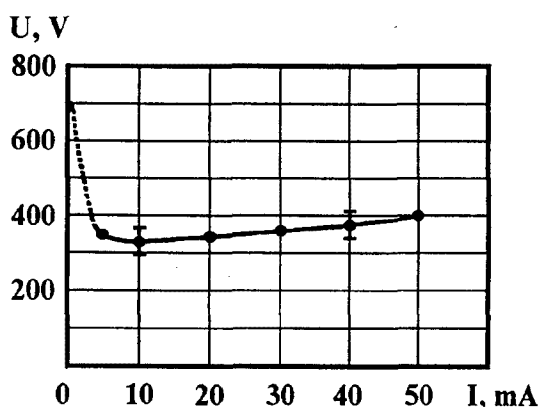


Fig.2 Volt-ampere characteristic MPSR.

The photos of micro-plasma formation were made using microspectrographic installation. Figure 3 depicts the result of spatial distribution of intensity for the line 388,9 nm (HeI). Local values of intensity are derived through Abel transformation [4]: The dependence of distribution width (level 0,1) from discharge current is given on the fig.4.

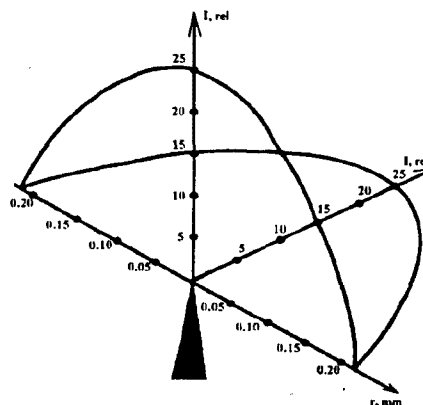


Fig.3 Intensity distribution by MPSR radius.

$\lambda = 388,9 \text{ nm}$, $P = 1,1 \text{ Atm}$, $I = 20 \text{ mA}$

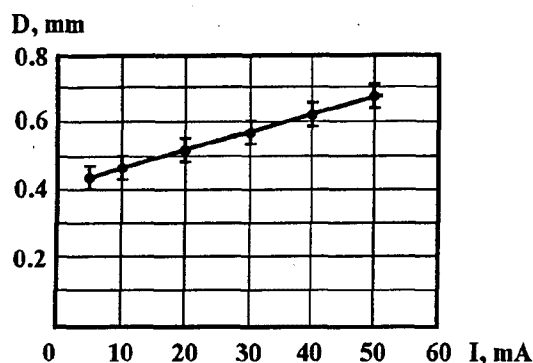


Fig.4 The dependence of distribution width (level 0,1) from discharge current. $\lambda = 388,9$ nm, $P = 1,1$ Atm

References

- [1] I. Brodie and J.J. Muray The Physics of Microfabricants, N.-Y. and London, Plenum Press, 1982
- [2] J.K. Mahoney, J. Perel, A.T. Forrester, Appl. Phys. Lett., v. 38 (1981) 320
- [3] Applied Atomic Collision Physics, v.3, Gas Lasers, Acad. Press, 1982
- [4] L.A.Luisova, Optics and Spectroscopy, v.52 (1982) 690 (in Russian)

Spectral researches of MPSR revealed the number of lines corresponding to transfers in spectra HeI and HeII.

HeI - $ns^1S_0 - 2p^1P_1$ ($n = 3 - 13$)

$np^1P_1 - 2s^1S_0$ ($n = 3 - 20$)

$nd^1D_2 - 2p^1P_1$ ($n = 3 - 18$)

$ns^3S_1 - 2p^3P_j$ ($n = 3 - 11$)

$np^3P_j - 2s^3S_1$ ($n = 3 - 11$)

$nd^3D_j - 2p^3P_j$ ($n = 3 - 12$)

HeII - $nf^2F^0 - 3d^2D$ ($n = 4 - 6$)

We measured the absolute intensities of lines and determined populations of helium atoms excited states in micro-plasma. For atoms with $n = 3 - 4$ values of populations are $10^{10} - 10^9 \text{ cm}^{-3}$. Integral brightness estimated by seeing spectrum range - $5 \cdot 10^4 \text{ kd/m}^2$. The electron temperature was estimated by ratio of line HeI (492,1 and 471,3 nm). The discharge current being 10 mA $T_e = (7 \pm 3) \text{ eV}$, electron concentration - $5 \cdot 10^{13} \text{ cm}^{-3}$. Power density applied to micro-plasma formation is - 10^5 W/cm^3 .

In the poster presentation characteristic experimental results for the different conditions are discussed in more detail.

Topic 17

Numerical modeling.

STABILITY OF LOW-VOLTAGE DISCHARGE IN FINITE MAGNETIC FIELD.

A.A. Temeev, O.S. Sladkov.

Moscow State Aviation Institute, Applied Research Department,

4, Volokolamskoe shosse, Moscow, 125871, Russia.

Phone: 7095-1584098, Fax: 7095-1582977 e-mail: aet@tk.mainet.msk.su

Nowadays in accordance with the latest achievements in the plasma electronics field much attention is paid to the investigations of plasma-beam discharges stability in respect to electromagnetic excitation. The given paper deals with the results of examination of electromagnetic instability excitation in low-voltage plasma beam discharge (LVPBD) at pressure 10^{-10} Pa in external longitudinal magnetic field of finite value. As in papers [1,2] we have examined the model, in which the axial symmetry shaped discharge of ρ -radius and L length is ignited within cylinder shaped electroconducting channel of R radius.

The research of instability process was carried out by analyzing Maxwell equations system in cylindrical coordinates at the boundary conditions:

$$E_z(\rho) - E_{zc}(\rho) = E_\varphi(\rho) - E_{\varphi c}(\rho) = B_z(\rho) - B_{zc}(\rho) = B_\varphi(\rho) - B_{\varphi c}(\rho) = 0; \\ E_{zc}(R) = E_{\varphi c}(R) = 0 \text{ for } \rho < R, \text{ and } E_z(\rho) = 0 \text{ for } \rho = R$$

For the finite external magnetic field \bar{B}_0 dielectric properties of LVPBD plasma for $r \leq \rho$ are characterized by permittivity tensor operator ε_{ij} :

$$\varepsilon_1 = \varepsilon_r = \varepsilon_{\varphi\varphi} = 1 - \frac{\omega^2(\omega + i\nu_e)}{\omega[(\omega + i\nu_e)^2 - \Omega_e^2]} - \frac{\omega^2(\omega - \kappa_3 u)(\omega - \kappa_3 u + i\nu_{be})}{\omega^2[(\omega - \kappa_3 u + i\nu_{be})^2 - \Omega_e^2]}, \\ \varepsilon_2 = \varepsilon_{r\varphi} = -\varepsilon_{\varphi r} = -i \left\{ \frac{\omega^2 \Omega_e}{\omega[(\omega + i\nu_e)^2 - \Omega_e^2]} - \frac{\omega^2 \Omega_e (\omega - \kappa_3 u)}{\omega^2[(\omega - \kappa_3 u + i\nu_{be})^2 - \Omega_e^2]} \right\} \quad (1)$$

$$\varepsilon_{zz} = i \frac{u \omega^2 (\omega - \kappa_3 u + i\nu_{be})}{\omega^2[(\omega - \kappa_3 u + i\nu_{be})^2 - \Omega_e^2]} \frac{\partial}{\partial r} = \varepsilon_4 \frac{\partial}{\partial r}; \\ \varepsilon_r = \varepsilon_4 \frac{1}{r} \frac{\partial}{\partial r};$$

$$\varepsilon_{\varphi\varphi} = \frac{u \omega^2 \Omega_e}{\omega^2[(\omega - \kappa_3 u + i\nu_{be})^2 - \Omega_e^2]} \frac{\partial}{\partial r} = \varepsilon_5 \frac{\partial}{\partial r}; \\ \varepsilon_{\varphi r} = -\varepsilon_5 \frac{1}{r} \frac{\partial}{\partial r};$$

$$\varepsilon_z = 1 - \frac{\omega_e^2}{\omega(\omega + i\nu_e)} - \frac{\omega_{be}^2}{(\omega - \kappa_3 u)(\omega - \kappa_3 u + i\nu_{be})} - \frac{u^2 \omega_e^2 (\omega - \kappa_3 u + i\nu_{be})}{(\omega - \kappa_3 u)[(\omega - \kappa_3 u + i\nu_{be})^2 - \Omega_e^2]} \frac{1}{r} \frac{\partial}{\partial r} \frac{\partial}{\partial r} = \\ = \varepsilon_3 - \alpha_3 \frac{1}{r} \frac{\partial}{\partial r} \frac{\partial}{\partial r};$$

where r, φ, z - cylindrical coordinates; u - directed beam electron velocity; ν_e, ν_{be} - collision frequencies of thermal and beam electrons with plasma particles; ω_e and Ω_e - plasma and cyclotron electron frequencies; $\kappa_3 = \kappa_z$ - wave vector along Z axis.

As it was shown before [1], axially symmetric waves ($d/d\varphi = 0$) are the most unstable. That is why LVPBD instability research is carried out for axially-symmetric field excitations taking into account the fact that their components depend on coordinates and time $A(r, t) = A(r) \exp[i(\kappa_3 z - \omega t)]$. Taking into account

(1) and the following LVPBD parameters values: $\omega_{be}/\omega_e \leq 10^{-2}$; $\Omega_e \gg \nu_e, \nu_{be}$; $\Omega_e < \omega_e$; $\beta = v/c \ll 1$ ($v = \omega/\kappa_3$ - phase velocity) the calculations of Maxwell equations results in the following dependencies for field components after great simplifications at Cerenkov resonance ($\omega \approx \kappa_3 u$):

$$E_r = \frac{-i \sum_{s=1}^2 \varepsilon_s \kappa_s^2 - \kappa_s^2}{\kappa_s} A_s \frac{J_1(\kappa_s r)}{J_0(\kappa_s \rho)}; \quad B_r = \frac{-\varepsilon_1 \sum_{s=1}^2 F_s A_s}{i \varepsilon_s \kappa_s \sum_{s=1}^2 \kappa_s} \frac{J_1(\kappa_s r)}{J_0(\kappa_s \rho)}; \\ E_\varphi = \frac{\varepsilon_1}{i \varepsilon_s \kappa_s \sum_{s=1}^2 \kappa_s} \frac{F_s A_s}{J_0(\kappa_s \rho)} \frac{J_1(\kappa_s r)}{J_0(\kappa_s \rho)}; \quad B_\varphi = -i \kappa \varepsilon_3 \sum_{s=1}^2 \frac{A_s}{\kappa_s} \frac{J_1(\kappa_s r)}{J_0(\kappa_s \rho)}; \quad (2) \\ E_z = \sum_{s=1}^2 A_s \frac{J_0(\kappa_s r)}{J_0(\kappa_s \rho)}; \quad B_z = \frac{\varepsilon_1}{\varepsilon_s \kappa_s \sum_{s=1}^2 \kappa_s} \frac{F_s A_s}{J_0(\kappa_s \rho)};$$

where $J_i(x)$ - Bessel functions ($i=0,1$), $A_s/J_0(\kappa_s \rho)$ ($s=1,2$) - integration constants, $\kappa = \omega/c$ - vacuum wave-number. Maxwell equations solutions for fields components out of LVPBD ($\rho \leq r \leq R$), satisfying the boundary conditions at the conduct cylindrical surface, are as follows:

$$\begin{cases} E_r^c = \frac{i \kappa_3}{\zeta} \frac{\Delta_{10}(r)}{\Delta_{00}(\rho)} B; & B_r^c = \frac{i \kappa_3}{\zeta} \frac{\Delta_{11}(r)}{\Delta_{01}(\rho)} C; \\ E_\varphi^c = -\frac{i \kappa}{\zeta} \frac{\Delta_{11}(r)}{\Delta_{01}(\rho)} C; & B_\varphi^c = \frac{i \kappa}{\zeta} \frac{\Delta_{10}(r)}{\Delta_{00}(\rho)} B; \\ E_z^c = \frac{\Delta_{00}(r)}{\Delta_{00}(\rho)} B; & B_z^c = \frac{\Delta_{01}(r)}{\Delta_{01}(\rho)} C; \end{cases} \quad (3)$$

where B, C - integration constants; $\zeta^2 = \kappa_3^2 - \kappa^2$;

$\Delta_\mu = K_i(\zeta r) I_\mu(\zeta R) - (-1)^{i+\mu} I_i(\zeta r) K_\mu(\zeta R)$; I_i, K_i - modified Bessel functions of the first and second kinds of i -th order.

Using fields components (2,3) and mentioned boundary conditions, the dispersion equation for unlimited along Z axis LVPBD is obtained:

$$\frac{(y_1 + \varepsilon_3 Z_H)(y_2 + Z_H)}{(y_1 + Z_H)(y_2 + \varepsilon_3 Z_H)} = \frac{F_1}{F_2}, \text{ where} \\ y_{1,2} = \frac{\kappa_{1,2} J_0(\kappa_{1,2} \rho)}{\kappa J_1(\kappa_{1,2} \rho)}; \quad Z_H = \frac{\kappa \Delta_{11}(\rho)}{\zeta \Delta_{01}(\rho)}; \quad Z_B = \frac{\zeta \Delta_{00}(\rho)}{\kappa \Delta_{10}(\rho)} \quad (4)$$

iZ_H and iZ_B - H and E waves impedances;

$\kappa_{1,2} = P_1 \pm \sqrt{P_1^2 - P_2}$ - transverse wave-number;

$$P_1 = \frac{1}{2\varepsilon_1} \left[(\varepsilon_1 + \varepsilon_3)(\varepsilon_1 \kappa^2 - \kappa_3^2) + \varepsilon_2^2 \kappa^4 \right];$$

$$P_2 = \frac{\varepsilon_3}{\varepsilon_1} \left[(\varepsilon_1 \kappa^2 - \kappa_3^2) + \varepsilon_2^2 \kappa^4 \right]; F_{1,2} = \frac{\varepsilon_3}{\varepsilon_1} (\varepsilon_1 \kappa^2 - \kappa_3^2) - \kappa_{1,2}^2;$$

For slow waves ($\beta \ll 1$), $\omega \leq \Omega_e$, and LVPBD small parameters values mentioned above the dispersion equation (4) for E-waves will be as follow after same simplifications:

$$\left(\frac{1 - \varepsilon_1 \beta^2}{-\varepsilon_1 \varepsilon_3} \right)^{1/2} \frac{J_0(\kappa_1 \rho)}{J_1(\kappa_1 \rho)} = -\frac{\Delta_{00}(\rho)}{\Delta_{10}(\rho)} \quad (5)$$

H-waves don't interact with beam electrons [1,2].

For electromagnetic wave with $\omega \leq \Omega_e$ from (1) one may concluded, that $|\varepsilon_1 \varepsilon_3| \gg 1$ and equation (5) approximately satisfied, if $|J_1(\kappa_1 \rho)| \ll 1$, i.e. $\kappa_1 = \lambda_{1p}/\rho$, where λ_{1p} is a p^{th} root of equation $J_1(x)=0$. Submitting this value κ_1 and components ε_1 and ε_3 from (1) (because of negligibly small values v_e and v_{be} are ignored) into the expression for $\kappa_1^2 = -\varepsilon_3(\kappa_3^2 - 2\varepsilon_1 \kappa^2 + \kappa^2)/\varepsilon_1$ the following equation is obtained:

$$(2 + N^2)\beta^2 - \frac{\Omega_e^2 - \omega^2}{\omega_e^2 + \Omega_e^2 - \omega^2} + \quad (6)$$

$$+ q \left[2 \frac{\beta^4}{(\beta - \gamma)^2} - \frac{\Omega_e^2 - \omega^2}{\omega_e^2 + \Omega_e^2 - \omega^2} \frac{\beta^2}{(\beta - \gamma)^2} \right] = 0, \text{ where}$$

$$\gamma = \frac{u}{c}; \quad q = \frac{n_b}{n \left(1 - \frac{\omega^2}{\omega_e^2} \right)}, \quad N^2 = \frac{c^2 \lambda^2}{(\omega_e^2 - \omega^2) \rho^2}.$$

Solving equation (6) by perturbation theory method because of $q \ll 1$ ($\omega \ll \omega_e$) in a zeroth approximation ($q=0$) the following is obtained:

$$\beta_0^2 = \frac{\Omega_e^2 - \omega^2}{(\omega_e^2 + \Omega_e^2 - \omega^2)(2 + N^2)} \quad (7)$$

For the first order perturbation theory we suppose $\beta = \beta_0 + \delta$ ($\delta \ll \beta_0$; because of Cerenkov resonance $\omega \approx \kappa_3 u$ and $\beta_0 \approx u/c = \gamma$) and series expanding equation (6), find amendment values:

$$\delta_1 = \beta_0 \sqrt{\frac{qN^2}{2(2 + N^2)}}, \quad \delta_2 = \pm \frac{\beta_0}{2} \sqrt{\frac{qN^2}{2(2 + N^2)}} (\mp 1 + i\sqrt{3}).$$

By the definition of β value the expressions for the numbers $\kappa_j^{(i)}$ in LVPBD are found ($i=1,2,3,4$):

$$\kappa_3^{(1)} = \kappa_3^{(0)} \left(1 - \sqrt{\frac{qN^2}{2(2 + N^2)}} \right); \quad (8)$$

$$\kappa_3^{(2,3)} = \kappa_3^{(0)} \left[1 + \frac{1}{2} \sqrt{\frac{qN^2}{2(2 + N^2)}} (1 \mp \sqrt{3}) \right]; \quad \kappa_3^{(4)} = -\kappa_3^{(0)}.$$

The expression (8) show, that three waves with $\kappa_3^{(1,2,3)}$ propagate along Z axis being accompanied by beam electrons and hence they interact, and the fourth wave travels in the opposite direction and doesn't interact with beam electrons. In this case the wave with $\kappa_3^{(2)}$

amplifies, wave with $\kappa_3^{(3)}$ decays and waves with $\kappa_3^{(1,4)}$ remain neutral. So the solutions (8) show the existence of instabilities in disturbance field wave in LVPBD.

In accordance with [1], expression (8) and reflection coefficient $\chi(\omega)$ in cross section $Z=L$ for limited LVPBD the oscillation spectrum can be calculated ($\omega = \omega + \omega^1$):

$$\omega = \omega_0 - \left(\frac{1}{2} \nu \kappa_3^{(0)} + \frac{\arg \chi}{L} - \frac{2\pi n}{L} \right) \left(\frac{1}{W_s} + \frac{1}{V_s} \right)^{-1}$$

$$\omega^1 = \left(\frac{\sqrt{3}}{2} \nu \kappa_3^{(0)} - \frac{1}{L} \ln \frac{3}{|\chi|} \right) \left(\frac{1}{W_s} + \frac{1}{V_s} \right)^{-1};$$

$$\text{where } \nu = \sqrt{\frac{qN^2}{2(2 + N^2)}}; \quad W_s = \frac{3uV_s}{u + 2V_s};$$

$$\omega_0 = \Omega_0 \sqrt{\frac{1 - \gamma^2(2 + N^2) \left(\frac{\omega_e^2}{\Omega_e^2} + 1 \right)}{1 - \gamma^2(2 + N^2)}}, \quad 1 < \frac{\omega_e^2}{\Omega_e^2} \leq \frac{1}{\gamma^2};$$

$$V_s = u \left\{ 1 + \frac{\Omega_e^2 \left[1 - \gamma^2(2 + N^2) \left(\frac{\omega_e^2}{\Omega_e^2} + 1 \right) \right] \left[1 - \gamma^2(2 + N^2) \right]}{\omega_e^2 \gamma^2 (2 + N^2)^{3/2}} \right\}^{-1}.$$

The condition for the development of instability in LVPBD ($\omega^1 > 0$) may be written as threshold current density of beam electrons:

$$J_{thr} = \omega_e^2 u \frac{16\varepsilon_0 m}{e 3\sqrt{3}} \left(1 + \frac{2}{N^2} \right) \left(\frac{1}{\kappa_3^{(0)} L} \ln \frac{3}{|\chi|} \right)^3 \quad (9)$$

where m , e - mass and charge of electron; ε_0 - permittivity of free space.

When compared the threshold current (9) with the same value for heavy magnetized LVPBD [1,2], the following expression can be obtained $\tau = \omega_e^2 \pi \rho^2 / \mu_{0s}^2 u^2$, where $\mu_{0s} = 2.4$ - for a metal channel completely filled with plasma, and $\mu_{0s} = 3.83$ - for a channel partially filled with plasma. Let's estimate the relation τ for top meanings of LVPBD parameters: $u = 3 \cdot 10^8$ [cm/s]; $\rho = 1$ [mm]; $n = 10^{14}$ [cm⁻³].

The calculation results in $\tau = 7.6 \cdot 10^3$. It shows, that to develop the instability of limited LVPBD in the finite external magnetic field B_0 the current density should be τ times more then in magnetized LVPBD. Hence the intensity of excited waves increases respectively.

REFERENCE

- [1] A.D.Vereshchaco, O.S.Sladkov, A.A.Temeev. Proceedings of XX-th international Conference on phenomena in ionized gases, Pisa, Italy, 1991, p.p. 1373-1374.
- [2] O.S.Sladkov, A.A.Temeev, A.D.Vereshchaco. Proceedings of XXI-th international Conference on phenomena in ionized gases, Ruhr - Universitat Bochum, Germany, 1993, p.p. 401-402.

NEGATIVE CONDUCTANCE BECOMING EXCITED IN MAGNETIZED PLASMA AT HEAVY GRADIENT OF DIRECTED ELECTRON VELOCITY.

A. A. Temeev

Moscow State Aviation Institute, Applied Research Department,

4, Volokolamskoe shosse, Moscow, 125871, Russia

Phone: 7095-1584098, Fax: 7095-1582977 e-mail: aet@tk.mai.net.msk.su

As far as range of problems on plasma flow interactions with magnetic fields is widen, it becomes more clear that the indispensable attribute of these processes are particle oscillation [1,2]. This paper is devoted to the influence of substantial gradients of directed electron velocities on the growth increments of HF oscillations in plasma flow interacting with the transverse magnetic field.

Consider a plasma flow along X-axis which is orthogonal to the external magnetic field B directed along Z-axis (Fig. 1).

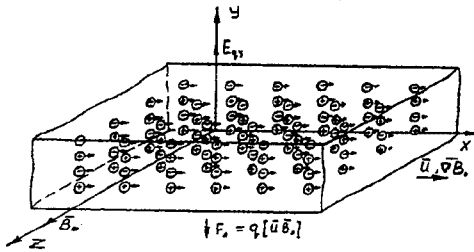


Fig. 1.

At the flow entrance into the magnetic field the Lorentz force leads to charges separation and polarization field component E_y appearance. Consider plasma, in which only electrons are magnetized, i.e.

$$\Omega_e \gg \nu_{ei} \gg \Omega_i \quad (1)$$

where Ω_e and Ω_i are electron and ion cyclotron frequencies. According to inequality (1), when flow enters the magnetic field electrons are so to say "clinking" to the magnetic force lines, whereas ions are moving along X-axis by inertia. As a result (and due to the drifts, leading to polarization disappearance) the longitudinal electric field component E_x arises in the plasma flow. This component is directed opposite to plasma flow motion.

Consider the cool plasma is fully ionized, the phase velocity of HF waves exceeds the thermal electron and the directed velocities $\omega/k \gg v_{Te}$, U_{α}^0 ; the electron-ion collision frequency is less than the electromagnetic oscillation frequency $\omega \gg \nu_{ei}$; all parameters describing plasma have stationary A^0 and varying A^- components: $A = A^0 + A^-$ at $A^0 \gg A^-$ and $A^- = A_m \exp[i(kr - \omega t)]$; HF field does not influence ions in

fact because of their great mass inertia as compared to electrons.

The dispersion equation, describing plasma oscillations for such model will be obtained by the set of linearized electro-magnetic gasdynamic equations.

$$\begin{aligned} i\omega n_e^- + \text{div}(n_e^- \bar{U}_e + n_e^- \bar{U}_e^0) &= 0; \\ -i\omega \bar{U}_e + (\bar{U}_e^0 \nabla) \bar{U}_e + (\bar{U}_e \nabla) \bar{U}_e^0 &= \\ = -\frac{e}{m} \bar{E} - \frac{e}{m} \left\{ \bar{U}_e^0 \bar{B} \right\} + \left[\bar{U}_e \bar{B}^0 \right] - \nu_a \bar{U}_e; & \quad (2) \\ \text{rot} \bar{E} = -\frac{\partial \bar{B}}{\partial t}; \quad \text{rot} \bar{H} = \frac{\partial \bar{D}}{\partial t} + \bar{j}; & \\ \bar{j} = -e(n_e^- \bar{U}_e + n_e^- \bar{U}_e^0). & \end{aligned}$$

Further we shall assume that the stationary value of particle velocity and its gradient have the only component directed along the X-axis. We shall assume also, that electron motion is determined mainly by the electric fields orthogonal to external magnetic field. It allows to simplify the set solution significantly without changing the task qualitatively.

Expanding the determinant and solving the equation obtained relative to $\epsilon = k^2 c^2 / \omega^2$, we obtain dispersion equation for the waves, propagating along the magnetic field:

$$\begin{aligned} \epsilon = 1 - \frac{\omega_p^2}{\omega} \cdot \frac{(\omega \pm \Omega_e)(\omega^2 - \Omega_e^2)}{(\omega^2 - \Omega_e^2)^2 + 2\omega^2(2\nu_a + \nabla_x U_e^0)^2} + \\ + i \frac{\omega_p^2}{\omega} \cdot \frac{(2\nu_a + \nabla_x U_e^0)(\omega \pm \Omega_e)^2}{(\omega^2 - \Omega_e^2)^2 + 2\omega^2(2\nu_a + \nabla_x U_e^0)^2} \end{aligned} \quad (3)$$

The same dispersion equation one can be obtained for discharge with current, external magnetic field and wave vector directed along the plasma column (Z-axis) in cylindrical coordinates (Fig. 2.)

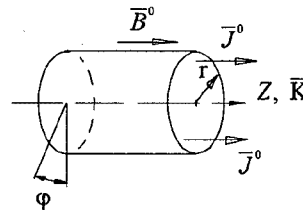


Fig. 2.

taking into account only r and Z stationary components of electron velocity:

$$U_{\alpha}^{-} \frac{dU_{\alpha}^0}{dr} \text{ and } U_{\alpha}^{-} \frac{dU_{\alpha}^0}{dz}$$

The permittivity ϵ is complex value, in which the real part determines intensity of the polarization process, while the imaginary part characterizes the conductivity current density. In the general form ϵ is connected with the conductivity σ by the following relation: $\epsilon = 1 + i\sigma/\epsilon_0\omega$.

It is seen from equation (3), that the imaginary part of permittivity ϵ , determining the plasma conductance, becomes negative when the gradient of particles directed velocity appears to be negative $\nabla_x U_e^0 < 0$ and also when the gradient of absolute value is greater than the double value of electron-ion collision frequency:

$$|\nabla_x U_e^0| > 2\nu_{ei}. \quad (4)$$

The stability analysis of a fluctuating plasmoid in different plasma devices is evidence of electron velocity gradient value realization sufficient for carrying out this condition.

If real values of the wave vector k correspond to the complex values $\omega = \omega_1 + i\gamma$ (dispersion equation (3) describes this very case) then the convective instability takes place in the system. Such systems might be used for oscillations amplification.

The numerical calculation was made for dispersion dependencies construction.

As the analytical definition of the expression for $\nabla_x U_e^0$ is hindered the calculation was made at the parameter $\xi = 2\nu_{ei} + \nabla_x U_e^0$ specification by some constant values: $\xi = -10^7 \div -10^9 \text{ s}^{-1}$.

The calculation was made for three values of electron concentration in plasma: $n_1 = 10^{12} \text{ cm}^{-3}$, $n_2 = 1.74 \cdot 10^{13} \text{ cm}^{-3}$ and $n_3 = 10^{15} \text{ cm}^{-3}$. Besides it was assume that the real part of frequency was $\omega_1 = 2.355 \cdot 10^{11} \text{ Hz}$.

Calculated wave number k and increment of oscillations growth values as functions of parameter $\chi = \Omega_e/\omega_1$ at different parameter ξ values for a case $\omega_1 > 0$ and $\gamma > 0$ are shown at Fig.3 and Fig.4. Function $k = f(\chi)$ is shown by solid lines and $\lg \gamma = f(\chi)$ - by dotted lines.

The calculations results are indicative of following:

1. This wave is propagating at low values of electron concentration in the whole frequency range (excluding the resonance area, where $\omega_1 = \Omega_e$);
2. In the dense plasma the wave might propagate and be amplified in the area $\Omega_e/\omega_1 > 1$ only. The phase velocity of these waves is less than the light velocity which is indicative of the slowed character of their propagation and of the possibility of long-term interaction with plasma.

As it is seen from dispersion dependencies, the traveling waves have growth increments high enough. This is indicative of the possibility of pronounced (by some orders) amplification of these waves energy.

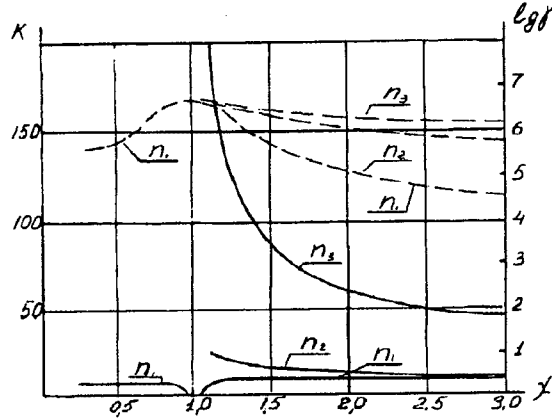


Fig. 3. Dispersion dependence at $\xi = -10^7 \text{ s}^{-1}$

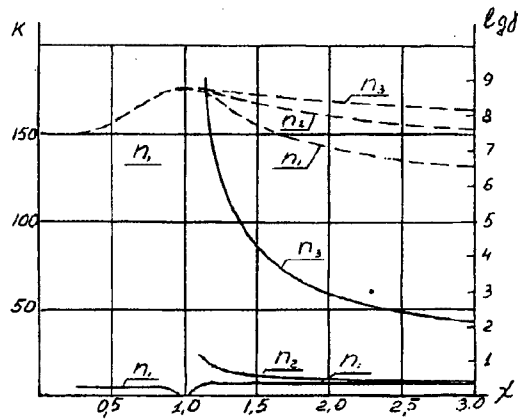


Fig. 4. Dispersion dependencies at $\xi = -10^9 \text{ s}^{-1}$

REFERENCES

- [1] A.B. Mikhailovsky, Theory of Plasma Instabilities. 1, 2, Atomizdat, Moscow, 1977, Russia.
- [2] Fedorenko A.M., Kotsarenko N.Ya., Absolute and convective instability in plasmas and solids. Nauka, Moscow, 1981, Russia.

CAPACITANCE AND CHARACTERISTICS OF THE BOUNDARY SHEATH UNDER VARIOUS CONDITIONS

H.-B. Valentini*, F. Herrmann

Institute of Physics, Greifswald University, Germany

*Address: IPHT, D-07702 Jena, Germany

Abstract: Using a two-fluid model the capacitance and the characteristics of the boundary sheath of a probe or an electrode is given numerically for plane, cylindrical and spherical geometries under steady-state conditions including elastic and inelastic collisions. A collisionless plane model allows analytical solutions. The expressions for the capacitance are a little different under steady-state and low frequency operation conditions due to nonlinear phenomena. Modulating the probe voltage can lead to a hysteresis effect. A quasi-periodic response of the plasma can exist.

1. Introduction

The knowledge of the characteristics and the capacitance of the sheath adjacent to a probe or an other electrode is important for the plasma diagnostics and the plasma technology. To date, the capacitance is mainly calculated for collisionless plasmas in a plane geometry using the quasistationary approximation [1-5]. The goal is to give results for models with plane, cylindrical or spherical symmetry ($\beta=0,1,2$) including elastic and inelastic collisions. Dealing with a plane and collisionless model the nonlinear characteristics is calculated under various variations of the probe voltage and the plasma density with the time.

2. Model and basic equations

The plasma is assumed to consist of cold positive ions (index $s=i$) and electrons ($s=e$) with a constant temperature T_e in an immobile neutral gas. The basic equations are the equations of continuity and of momentum transfer for ions and electrons and the Poisson equation. Under steady-state and one-dimensional conditions they read

$$r^{-\beta} \frac{d}{dr} r^{\beta} n_s v_s = n_e v_{ni}, \quad s=i, e \quad (1)$$

$$n_s m_s v_s \frac{dv_s}{dr} + k T_s \frac{dn_s}{dr} = Z_s n_s e E + (n_s v_{ni} + n_s v_s) m_s v_s \quad (2)$$

$$r^{-\beta} \frac{d}{dr} r^{\beta} E = \frac{e}{\epsilon_0} (n_i - n_e) \quad (3)$$

Here are r the distance from the centre, n the number density, v the drift velocity, E the electric field strength, m the mass, k the Boltzmann constant, e the elementary charge, $Z_i=1$, $Z_e=-1$, ϵ_0 the permittivity of vacuum and in the following ϕ the electric potential. v_{ni} is the ionization frequency, v_s is the collision frequency of ions and electrons, respectively.

We introduce

$$v_B = \sqrt{k T_e / m_i}, \quad I_D = \sqrt{\epsilon_0 k T_e / (e^2 n_e)} \quad (4)$$

and

$$\xi = r / I_D, \quad \eta = -e \phi / k T_e, \quad f = E / E_0 \quad (5)$$

where $f = d\eta / d\xi$.

The so-called sheath scale is used in (5). Dealing with cylindrical or spherical models, r_p is the probe radius and r_w is the wall radius. The resulting boundary and eigen value problem is numerically solved in [5].

3. Results

Using the Gauss theorem under steady-state conditions the capacitance of the sheath around a probe results as

$$C_{st} = (\epsilon_0 A_p / I_D) f(r_p) / \eta(r_p) \quad (6)$$

where A_p is the area of the probe. Numerical results are shown in Fig. 1 where $\beta=2$, $r_w/r_p=30$, $v/v_{ni}=1$ (a), 1000 (b).

An analytical solution exists for the sheath if collisions and the inertia of the electrons are neglected. In this model r is the distance from the sheath edge where

$$n_i = n_e = n_0, \quad v_i = v_e = v_B, \quad f = f_0, \quad \phi = 0$$

is supposed. One obtains [3]

$$f = \sqrt{2(\sqrt{1+2\eta} + e^{-\eta} - 2) + f_0^2} \quad (7)$$

The density of the conductivity current becomes

$$j_c = e n_0 v_B [1 - \exp(\eta_F - \eta)] \quad (8)$$

where $\eta_F = \sqrt{m_i / (2\pi m_e)}$ is the normalized floating potential. The results are different at $\eta \ll 1$ if $f_0 > 0$ or $f_0 = 0$. The thickness of the sheath diverges if the sheath edge is defined by $f_0 = 0$. In Fig. 1 the curve (c) represents C_{st} for this case.

We take into account a time-dependent probe voltage varying with the frequency $\omega/2\pi$ where $\omega \ll \omega_i$. Using

$$j_d = -(C_{qs}/A_p) (d\phi/dt)_p \quad (9)$$

for the density of the displacement current the quasistationary approximation leads to [3]

$$C_{qs} = (\epsilon_0 A_p / l_D) [(df/d\xi) / f]_p. \quad (10)$$

The difference between the equations (6) and (10) is caused by the nonlinear phenomena in the plasma. Eq. (10) is shown in Fig. 1 by function (d).

It is $|j_d/j_c| \ll 1$ if $\omega \ll \omega_i$. The nonlinear characteristics $j(\eta) = j_c(\eta) + j_d(\eta)$ is investigated in [1-4,7]. Both the electrode sheaths and the external circuit are taken into account in [1,4].

The probe voltage is modulated according to $\eta = \eta_0 [1 + a_1 \sin(\omega_1 t)]$ where η_0 and a_1 are constants. Characteristics with a slight hysteresis effect without a node can occur caused by the displacement current (Fig. 2; $\omega/\omega_i = 0.3$).

Additionally, we take into consideration a modulation of the plasma density according to $n = n_0 [1 + a_2 \sin(\omega_2 t - \varphi)]$. The characteristics depend strongly on the frequencies, the amplitudes and the phase angle. If $\omega_2 = \omega_1$ a hysteresis with nodes can exist (Fig. 3; $\omega_1 = 0.012$). If $\omega_1 \neq \omega_2$ quasi-periodic states with period-doubling can occur [8]. An advanced theory would demand the solution of the time-dependent nonlinear equations (1)-(3) under suitable boundary conditions.

References

- [1] A. Metze et al.: J. Appl. Phys. **60** (1986) 3081
- [2] K.-U. Riemann: J. Appl. Phys. **65** (1989) 999
- [3] R. Deutsch et al.: Plasma Chem. Plasma Process. **11** (1991) 501
- [4] R. J. Seeböck et al.: J. Vac. Sci. Technol. A **11** (1993) 682
- [5] R. Godard et al.: Japanese J. Phys. **43**(1995) 7
- [6] H.-B. Valentini et al.: Plasma Sources Sci. Technol. **4** (1995) 353
- [7] K.-D. Weltmann et al.: Contrib. Plasma Phys. **33** (1993) 265
- [8] P. A. Miller et al.: Phys. Rev. Lett. **71** (1993) 863.

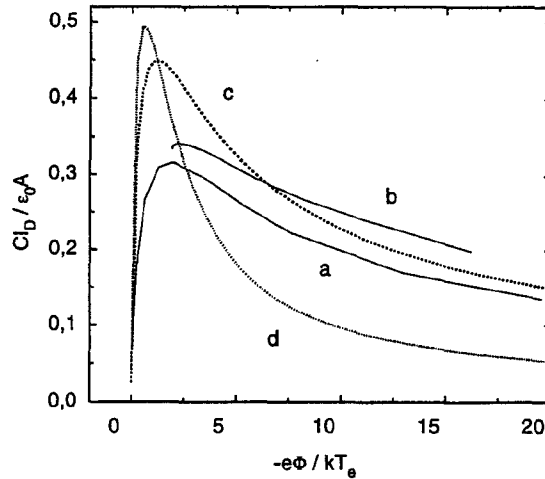


Fig.: 1. Capacitance

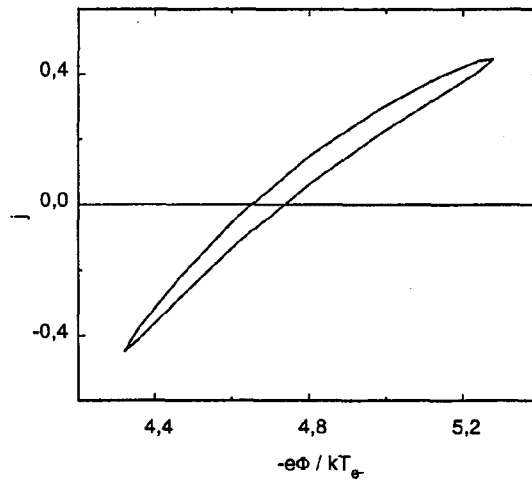


Fig.: 2. Characteristics

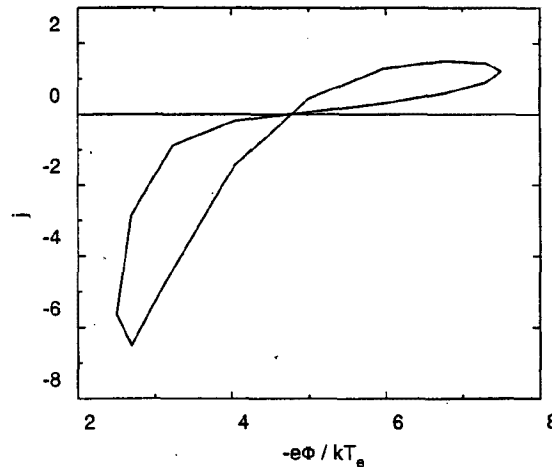


Fig.: 3. Characteristics

Numerical study of the wavelength dependence on the threshold intensity in laser induced breakdown of N₂.

Jamal M. Daoud*, Abdel Naser Abou El-Fotouh* and Yosr E. Gamal**

* Department of Physics, Faculty Of Science, Cairo University, Al-Giza, Egypt.

** National Institute Of Laser Enhanced Sciences, Cairo University, Al-Giza, Egypt.

1. Introduction

In this work we present a numerical investigation of the physical processes which control the breakdown of nitrogen molecule under the effect of a wide range of laser wavelengths. The calculations are carried out at the first four harmonics of a Nd:YAG laser radiation irradiates a nitrogen molecule at atmospheric pressure. These are the experimental conditions of Davis et al.[1]. The numerical analysis is based on a previously developed electron cascade model by Evans and Gamal [2,3] which solves simultaneously the time dependent Boltzmann equation for the electron energy distribution function and a set of rate equations describing the rate of change of the formed excited states population. The model includes the main physical processes which may take place during the interaction of laser radiation with gases. In this analysis the exact correlation between the cross section of each process and the electron energy has been taken into account.

2. Model and basic equation

In this model the rate of energy gain of the free electrons from the laser field is given by:

$$\frac{\partial f}{\partial t} = \frac{1}{3} \epsilon_0 v(\epsilon) \frac{\partial f}{\partial \epsilon} + \frac{2}{3} \epsilon_0 v(\epsilon) \frac{\partial^2 f}{\partial \epsilon^2} + \frac{\partial}{\partial \epsilon} (Q_v f) \quad (1)$$

Where $\epsilon_0 = e^2 E^2 / 2m\omega^2$ is the oscillatory energy of an electron in the laser field with electric field amplitude E and angular frequency ω , $v(\epsilon)$ is the frequency of collision of the electron with the molecule and Q_v is the rate of transfer of energy from an electron of energy ϵ to vibrational levels. In this work we adopted the same molecular structure of the nitrogen molecule as that considered in ref.[2]. Therefore the inelastic processes which are considered in the present work can be summarized as: electron impact ionization of the ground state molecule, electron impact excitation of the considered three excited states, electron impact ionization of the excited states and photoionization of the excited states at energy threshold respectively. In addition to this processes we added in this work the process of molecular dissociation of the nitrogen with its cross section has taken from ref.[4]. We also follows the same functional form of the cross sections and rates for these various processes as those considered in ref.[3]. A breakdown criterion defined as the degree of

fractional ionization $\delta = 0.1\%$ of the neutral gas molecule in the focal volumes is assumed in the present calculations.

3. Results and discussion

The calculations are carried out for molecular nitrogen at atmospheric pressure irradiated with Nd:YAG laser at the wavelengths 1.064 μm , 0.532 μm , 0.355 μm and 0.266 μm with pulse duration 8.5 ns, 7.5 ns, 6.5 ns and 5.5 ns respectively. Figure (1) shows the calculated values of the threshold intensity at these four laser wavelengths and compared with the experimentally measured ones by Davis et al. ref.[1]. From this figure, it is clear that a good agreement is obtained between the calculated values of the breakdown thresholds (solid line) and those experimentally measured ones (open circle). This result also confirms the results obtained for air breakdown at the same four wavelengths under the same experimental conditions given by Simeonsson and Miziolek[5] and shown on figure (1) as shaded circle. We observed an increase in the threshold intensity at wavelength 0.355 μm then a decrease in its value at 0.532 μm follows by another increase at the near IR region (1.064 μm) with the increase for N₂ at this wavelength exceeds that for air. To explain such behavior of the wavelength dependence on the threshold intensity it was necessarily to study in details the electron energy distribution function (EEDF) at each of these wavelengths. Therefore the EEDF at the end of the laser flash is plotted for the four considered wavelengths and shown in figure (2).

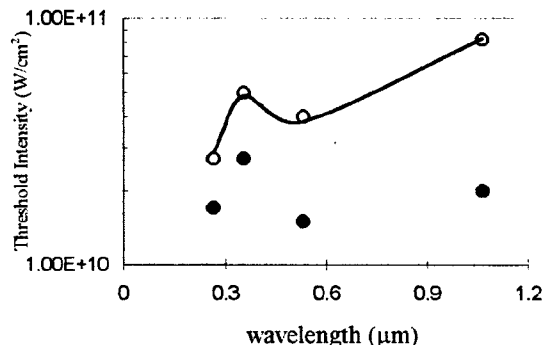


Fig.(1) Comparison between the calculated threshold intensity (solid line) and the measured ones (○ N₂ ref. [1], ● air ref. [5]).

From this figure it is noticed that the EEDF for the four wavelengths undergoes an abrupt drop over the

energy range 1-3 eV. This drop indicates the effect of vibrational losses which in turn acts as a barrier for the electrons to reach the excitation and ionization limits. This in turn results in a retardation of the ionization growth rate of electrons which is noticeably clear at wavelength 0.355 μm where the drop is much deeper and its value over the whole range of electron energy lie below the EEDF for the other wavelengths. In order to study the correlation between the vibrational losses and the laser wavelength a close examination for the EEDF as a function of the laser wavelength over electron energy range from 0-5 eV is plotted and illustrated in figure (3). It is shown from this figure that vibrational losses at 2 eV suffer a sudden decrease over the whole range of the wavelengths with a particular lower value at the wavelength 0.355 μm . Beyond this energy value the EEDF starts to increase gradually over the energy range 3-5 eV for the four wavelengths.

This decrease in the EEDF at 0.355 μm may explain the high rate of vibrational losses at this wavelength which in turn implies the increase of the threshold intensity to overcome these losses. This result interpret the peak appeared in figure (1) at this particular wavelength. On the other hand, the high value of the threshold intensity observed in figure (1) at wavelength 1.064 μm could be explained by the fact that at this wavelength collisional ionization of the excited states is more dominant than photoionization. But because of the coincidence between the amount of energy required to cause ionization of the considered excited states about (5, 8, 9 eV) and those required to produced electron impact excitation for the three excited states (7, 9, 12 eV), therefore this process ceases to take place which result in a slowing down of the ionization growth rate and this in turn explain this increase of the threshold intensity. From the above result it can be shown that at the three first wavelengths, photoionization of the excited states can play an important role in enhancing the ionization growth rate while at the fourth (1.064 μm) wavelength, both photoionization and collisional ionization contribute pronouncely to the breakdown phenomenon. As a confirmation of this result the electron mean energy as a function of time is plotted at these wavelengths and is shown in figure (4). From this figure it is notice that the electron mean energy for the three first wavelengths is almost constant during the whole pulse length with its value for the wavelength 0.266 μm exceeds those for wavelengths 0.532 μm and 0.355 μm , the later values are almost very close to zero which indicates that the whole ionization processes are due to photoionization of the excited states. At the wavelength 0.266, because of the photon energy is considerably high, therefore the newly born electrons can have excess energy higher than zero. For the wavelength 1.064 μm the electron mean energy

follows almost the pulse shape which indicates the importance of collisional ionization processes in particular around the peak of the laser pulse where the rate of energy gain reaches to its maximum value. Beyond the peak electrons can suffer inelastic collision where they lose their energy and hence their mean energy reaches a lower value as shown in figure (4).

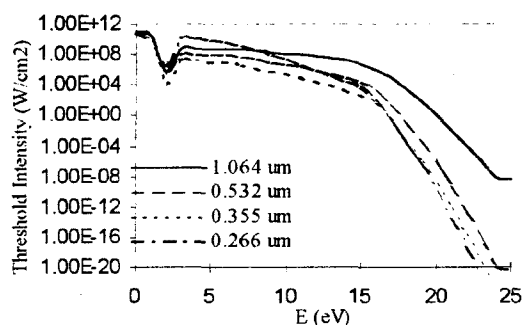


Fig.(2) EEDF for atmospheric N_2 at wavelengths

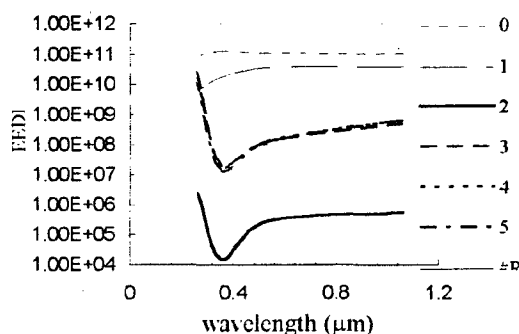


Fig (3) EEDF as a function of wavelength at electron energies 0-5 eV.

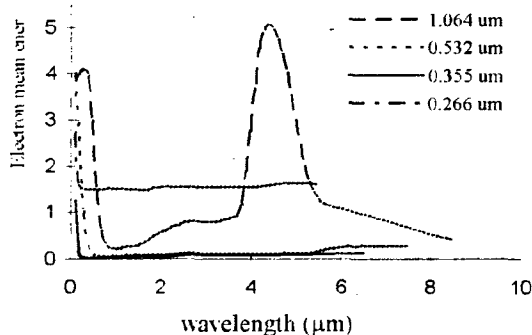


Fig. (4) Electron mean energy as a function of time.

5. References

- [1] J. P. Davis, A. L. Smith, C. Giranda, M. Squicciarini: Appl. Opt., 30 (1991) 4358
- [2] C. J. Evans, Y. EE-D. Gamal, J. Phys. D: Appl. Phys. 16 (1980) 1901
- [3] Y. EE-D. Gamal, N. M. Abdel Moneim, J. Phys. D: Appl. Phys. 20 (1987) 757
- [4] P. C. Cosby, J. Chem. Phys. 98 (1993) 9544
- [5] J. B. Simeonsson, A. W. Miziolek, Appl. Phys. B 59 (1994) 1

Selfconsistent Numerical Modelling of Surface Wave Sustained Discharges

S. Grosse, H. Schlüter

M. Schlüter

Inst. Experiment. Phys. II

Inst. Experiment. Phys. V

Ruhr-University, D-44780 Bochum, Germany

1. Introduction

On the basis of a kinetic model [1] surface wave sustained discharges are studied in the microwave (2.45 GHz) and the radio frequency (100–400 MHz) range for moderate gas pressures ($p \leq 1$ Torr argon, helium) and plasma radii $a \leq 1.4$ cm. Radially a non-local approach is used as a good approximation for sufficiently low values of the product pa . The concept of total (kinetic plus ambipolar potential) energy

$$\varepsilon = \frac{u^2}{2me} - \Phi \quad (1)$$

employed facilitates simplified solutions of the Boltzmann equation and is useful for analysing the structure of particle fluxes even in more general approaches, e.g. of double grid methods, with more complex boundary conditions. For closing the system of equations the ion fluid approach is employed. Maxwell's equations, using a cold plasma permittivity, are solved simultaneously in (zero order) WKB approximation concerning the axial density nonuniformity.

2. Selfconsistency of Field Intensity and Electron Density

Selfconsistency of maintainance electric field intensity $|E|^2$ and electron density is achieved by inclusion of nonlinear effects such as stepwise ionization (taking into account the tendency to saturation towards higher electron densities) [2], electron-electron collisions, radial and axial changes of electron energy distribution functions, changes of radial field and density profiles with axial position. Even though diffusion dominated regimes are considered, a degenerate behaviour in that the field strength becomes independent of the electron density, is avoided which might result from a simplified "linear" particle balance consideration. As a consequence the resultant power loss per average electron (Θ) is a function of axial position, though its axial change turns out to be weak, unless transition to the recombination controlled regime occurs.

3. Radial Electron Density Nonuniformity

The selfconsistent radial density profiles are relatively steep and accentuate the nonuniformity of radial field profiles. The calculations fully account for the consequences in wave dispersion and damping, which largely derive from the decrease of wave penetration along the discharge axis: Towards the discharge end the electron density near the discharge wall gains in relevance as compared to a cross-section averaged electron density. Therefore formation of a maximum in the phase diagrams and the appearance of complex solutions occurs in the collisionless limit ($\nu_c \rightarrow 0$) due to the radial density nonuniformity [3]. Linear mode conversion between forward and backward wave solutions is possible, but only for rather low collisionality [4]. Moreover, a sufficient radial density drop allows resonances between wave frequency ω and local plasma frequencies $\omega_p(r)$ leading to peaks in the intensity of the radial field intensity component $|E_r|$, affecting dispersion as well as damping. These peaks can also be associated with "collisionless" energy transfer as described by quasilinear treatment [5]. The resultant energy diffusion coefficient \mathcal{D}_{ql} —appearing in the heating term of the Boltzmann equation—can be written in the form

$$\mathcal{D}_{ql} = \frac{\pi e}{2m} u^{3/2} \tau \exp\left(-4\pi \frac{\tau}{T}\right) \quad (2)$$

lending itself to an interpretation as transit time heating. The transit time τ of electrons passing the $|E_r|^2$ -peaks takes the rôle of the collision time $\tau_c = 1/\nu_c$ in an expression for the case of Ohmic (DC) heating. The exponent in (2) ensures that the transit time effect is only significant when τ is small as compared to the wave period T . Expression (2) becomes important towards discharge end. The range of significance increases with growing pa , although the ratio of collisionless versus Ohmic heating rate increases with lowered p . The selfconsistent calculations show that in the nonlocal situation the radial density profiles are not so drastically affected as to seriously impede the resonance situation $\omega = \omega_p(r)$, conceivably happening in a local scenario.

4. Ponderomotive Effects

The concept of total energy employed in the nonlocal approximation can be extended to include in the total energy the term $|e||E|^2/4m(\omega^2 + \nu_c^2)$ describing the nonlinear ponderomotive interaction [6]. From this approximation noticeable ponderomotive influence may be expected only for low wave frequencies ω and low gas pressures, as estimates and calculations show.

5. Three-Dimensional Field Calculations

The validity of (zero order) WKB solutions with respect to the axial density nonuniformity can be verified via iterative solutions of the field equations (formulated in integral form) for given radial and axial density profiles. The good accuracy of the WKB results is showing up in spite of the complications such as arising from damping, mode interactions and local plasma resonances. This includes the occurrence of $|E_r|$ -peaks close, but separated, from the plasma boundary, as the example of Fig. 1 demonstrates with a radial profile of normalized $|E_r|$ for a relatively steep density profile $\propto J_0(2.4r/a)$, at $\nu_c/\omega = 0.6$, $\omega/2\pi = 220\text{ MHz}$ and about 20 cm before discharge end. However, this is the case only if the damping is high enough to avoid the appearance of a significant "system resonance" at the discharge end associated with axial density decrease. At relatively low damping (and favourable low wave frequencies) such resonances indeed occur and their properties are then also influenced by the radial density profile. This is in line with the above remark on decreasing radial penetration depth. The radial field distribution is obviously affected, but even the axial position of the resonance is changed. This is ascertained by three-dimensional field computations for given density distributions, incorporating a numerical model of the wave launcher. For the azimuthally symmetric mode considered here, the required computational boundary conditions can be reduced by the use of ideal magnetic boundary conditions with respect to the azimuthal direction [7].

6. Summary/Outlook

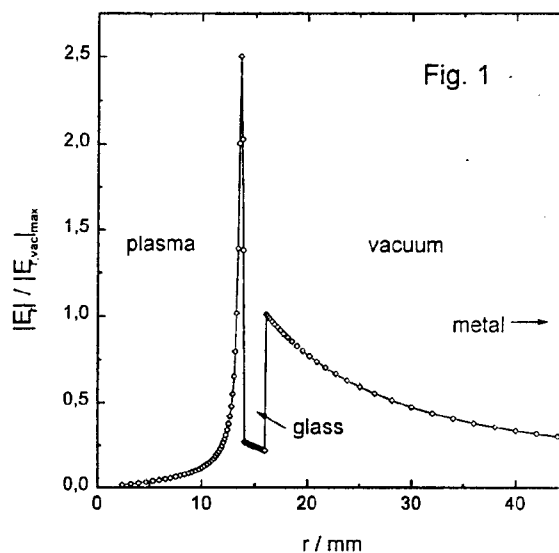
Some experimental evidence for essential features of the modelling has been reported, e.g. [8], though more experimental work remains desirable. There is of course room and need for improvements, in particular by generalization from the nonlocal approximation in a selfconsistent manner and obviously by strengthening the atomic physics data base.

Acknowledgements

The authors are indebted for advice and help to Profs. Yu.M. Aliev, A. Shivarova and L.D. Tsendin. Support by the Volkswagen-Stiftung ist gratefully acknowledged.

References

- [1] Yu.M. Aliev, A.V. Maximov, U. Kortshagen, H. Schlüter and A. Shivarova, *Phys. Rev. E* **51**, 6091-6103 (1995).
- [2] Yu.M. Aliev, S. Grosse, H. Schlüter and A. Shivarova, *Phys. Plasmas* **3**, 3162-3175 (1996).
- [3] S. Grosse, M. Georgieva-Grosse, I. Ghanashev and M. Schlüter, *J. Electromagn. Waves and Appl.* **11**, 609-632 (1997).
- [4] Yu.M. Aliev and H. Schlüter, *J. Phys. D: Appl. Phys.* **29**, 2519-2521 (1996).
- [5] Yu.M. Aliev, V.Yu. Bychenkov, A.V. Maximov and H. Schlüter, *Plasma Sources Sci. Technol.* **1**, 126-131 (1992).
- [6] Yu.M. Aliev, V.Yu. Bychenkov, M.S. Jovanovic and A.A. Frolov, *J. Plasma Phys.* **48**, 167-176 (1992).
- [7] M. Schlüter, "On a Numerical Simulation of 2d Plasma Surface Waves", submitted.
- [8] H. Schlüter, in: *Plasma '95. Research and applications of plasmas. 2nd National Symposium, Warsaw, June 26-28, 1995* (Warsaw, 1995), vol. 2, pp. 135-142.



EFFECT OF KNUDSEN NUMBER ON MOMENTUM, HEAT AND MASS TRANSFER BETWEEN INJECTED PARTICLES AND NITROGEN THERMAL PLASMA

P. Stefanović, D. Cvetinović, P. Pavlović, Ž. Kostić

Institute for nuclear sciences "Vinča" - 11001 Beograd, P.O.Box 522, Yugoslavia

For thermal plasma processing of solid particles injection and mixing i.e. momentum, heat and mass transfer between solid particles and plasma flow is of great importance for quality of the product. This is especially pronounced in plasma processes when powders (for instance Si, Al, Ti etc.) are used as a precursor for the synthesis of ultrafine ceramic nitride or carbide powder (Si_3N_4 , SiC , AlN , TiN , etc.) In those processes metal powders has to be totally evaporated in thermal plasma flow before gas phase chemical reaction take place. Namely, if evaporation is not completed in a high temperature zone of the reactor, the remaining particles become impurities in the product due to short residence period in the reactor for the complete liquid - gas phase synthesis reaction. There are numerous effects involved in plasma-solid particle interaction between which noncontinuum effects have important influence especially in the case of small evaporating particles. Due to difficulties in experimental investigations of two-phase high temperature flows, there is a lack of corresponding experimental data so, numerical modelling of two phase plasma flows and few rather simple diagnostic methods are, in most cases, the main tools for analysis developing and optimizing the plasma reactors and processes.

The paper presents results of numerical analysis of noncontinuum effects influence on interphase momentum, heat and mass transfer, based on computer simulation of two phase (nitrogen plasma - Al or Si or Ti particles) turbulent flow in an axisymmetric reactor schematically shown in Fig. 1. High temperature nitrogen plasma flow enters the vertical chamber of radius R and length L , through the central inlet with radius r_{in} at the top of the reactor. The secondary fluid flow, laden with solid particles at room temperature, is injected from the same side through the conical annular channel with inlet radii r_1 and r_2 and angle α . The products leaves the reactor through a central opening of radius r_{ex} at the reactor bottom. All reactor surfaces are shielded with uncooled high temperature material and all dimensions (L , R) refer to the inside surfaces of the shield. Computer simulation is based on a mathematical model [1] which includes: widely used $k-\epsilon$ model of turbulence for closing equations of motion for two dimensional plasma swirl flow, Lagrangian Stochastic Deterministic model for calculation of particle motion in plasma flow, Particle Source in Cell (PSI-Cell) method for computing particle- plasma interaction and six flux method by De Marco and Lockwood for modeling radiative heat transfer between particles, plasma and reactor wall. Correlations used for interface momentum, heat and mass transfer are based on integral mean values

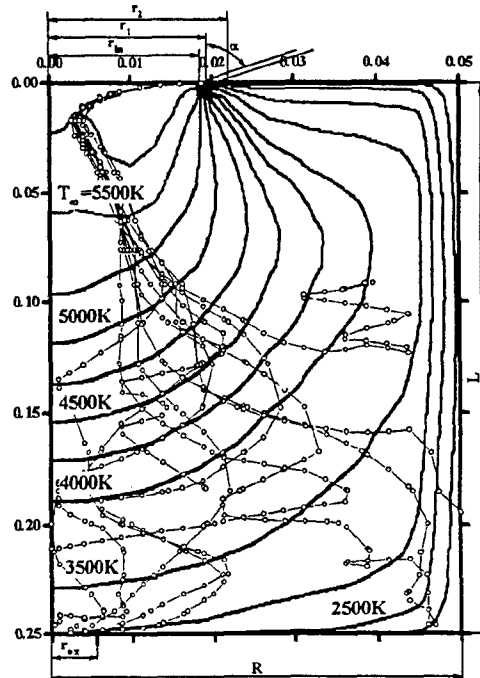


Figure 1. Axial section of the reactor with computed curves of constant plasma temperature with some particles trajectories for the illustrative example

of plasma properties in boundary layer surrounding particles due to high temperature difference in layer, and including corrections due to particle evaporation and Knudsen effect [2].

Presented computed curves of constant plasma temperature with trajectories of some Al particles in the axial section of the reactor refer to the example with the following values of reactor parameters: inlet plasma channel radius $r_1=r_{in}=18.75$ mm, outer radius of injection channel $r_2=21.75$ mm, reactor radius $R=50$ mm, reactor length $L=250$ mm, radius of exit channel $r_{ex}=4$ mm, temperature of the shield $T_w=1500$ K, $T_{w,bottom}=1700$ K, nitrogen plasma flow: $m_n=2.07$ g/s, angle correlating tangential (swirl) W_{in} and axial U_{in} plasma velocity component ($W_{in}=U_{in}\tan\phi_{pl}$) $\phi_{pl}=14^\circ$, inlet plasma temperature $T_{in}=6000$ K, secondary nitrogen mass flow rate $m_{sec}=0.16$ g/s, Al powder mass flow $m_{Al}=0.127$ g/s, initial diameter of Al particles $d_{p0}=50$ μm , angle of injection channel $\alpha=87.5^\circ$. Computed values of modified Knudsen number Kn^* [2] and corresponding correction to particle heat f , momentum transfer $f^{d.45}$ and mass transfer f_m along the same particle trajectories as in Fig. 1 are presented in Fig. 2, 3 and 4, as functions of particle axial position in the reactor. Along the whole particle trajectory effective Knudsen number is in

the range $0.001 < Kn < 0.8$ and calculated corrections are based on theoretical predictions for the "temperature jump" (slip flow) regime modified for the thermal plasma conditions [3]. During the particle "injection" and "penetration" stage, while its diameter is constant, value of Kn rises from ~ 0.006 to ~ 0.03 (Fig. 5) while correction factors f and f_m drops from 1 to ~ 0.92 (Fig. 3 and 4) due to increase of particle temperature. Along the reactor particle Knudsen number rises and correction factor f and f_m decay

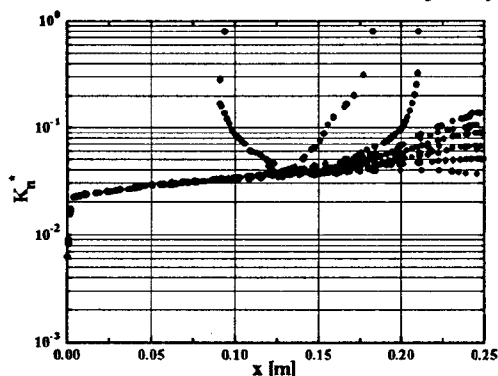


Figure 2. Particle effective Knudsen number as a function of its axial position in the reactor

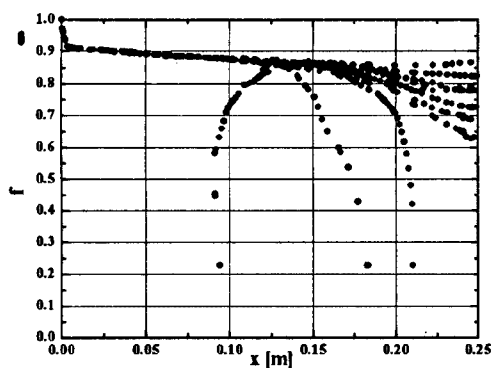


Figure 3. Correction factor f to momentum and heat transfer as a function of particle axial position in the reactor

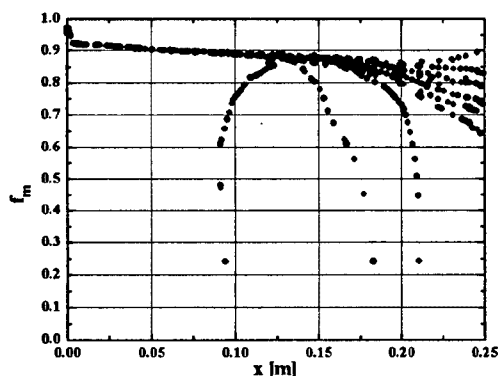


Figure 4. Correlation factor f_m to mass transfer as a function of particle axial position in the reactor

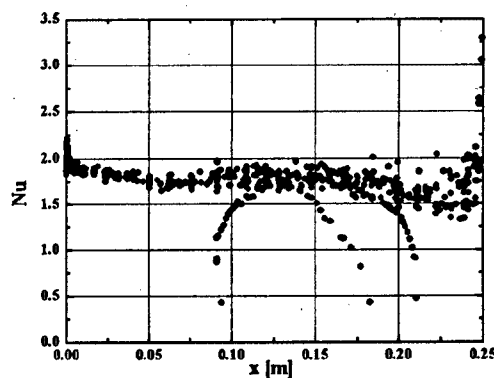


Figure 5. Particle Nusselt number as a function of particle axial position in the reactor

constantly due to particle diameter reduction, and for $d_p \sim 10 \mu\text{m}$ have values: $Kn \sim 0.1$, $f \sim 0.7$ and $f_m \sim 0.7$. Further decrease of particle diameter along its trajectory increases effective Knudsen number up to 0.8 (for $d_p \sim 0.5 \mu\text{m}$) while correction factors are drastically reduced to $f \sim 0.23$ and $f_m \sim 0.24$. It is obvious that effects of Knudsen number on momentum, heat and mass transfer are significant and the corresponding corrections have to be involved in the calculations of small particles ($d_p < 50 \mu\text{m}$ especially for $d_p < 10 \mu\text{m}$) movement, heating and evaporation in nitrogen thermal plasma flows.

Particle Nusselt number, calculated [2] along the trajectories in Fig. 1, is shown in Fig. 5 as a function of particle axial position in the reactor. For $Nu = 2$ the heat transfer to the particle is only by conduction, but in our case of particle evaporation and present noncontinuum effects, Nu number can be less than 2. Due to noncontinuum effect reduction of heat transfer (Fig. 5) is proportional to f (Fig. 3), of momentum transfer to $f^{0.45}$ and reduction of mass transfer to f_m (Fig. 4). From Fig. 5 it is obvious that noncontinuum effect drastically reduces heat flux ($Nu < 1.5$) to small particles ($d_p < 10 \mu\text{m}$). Reduction of momentum, heat and mass transfer from nitrogen plasma to Si and Ti particles due to noncontinuum effect is of the same level as for Al particles presented in Fig. 2, 3, 4 and 5.

ACKNOWLEDGEMENT

This work has been supported by Scient. Fund of Republic of Serbia.

REFERENCES

- [1] Pavlović et al, Supp. au Journal of High Temp. Chem. Processes, Vol.1 N°3, (1992) 381-388,
- [2] Stefanović et al, in Heat and mass transfer under plasma conditions, editor P.Fauchais, Begell House, New York, (1995) 169-176,
- [3] Xi Chen, E. Pfender, Plasma Chem. & Plasma Process., Vol.3 N°3 (1983)351-366

Towards a General Collisional Radiative Model

J. van Dijk, A. Hartgers, J. Jonkers, P.G.J.M. Herben and J.A.M. van der Mullen

Department of Applied Physics, Eindhoven University of Technology,
PO Box 513, 5600 MB Eindhoven, The Netherlands

1. Introduction

Collisional Radiative Models (CRMs) are a widely used tool in the modelling of plasmas. The results of such models appear as source terms in the particle and energy balances of plasma transport models [1].

In case the change of internal energy of the heavy particle is due to electron collisions and radiative processes the Atomic State Distribution Function (ASDF) can be calculated from plasma parameters, such as the electron density and temperature, solving a set of continuity equations. If the electron density is low only a few excited levels have to be taken into account. This holds for e.g. the modelling of conventional fluorescent lamps where, due to an electron density of around $5 \times 10^{17} \text{ m}^{-3}$, a model with only four to six excited atomic mercury levels already gives an accurate description of the discharge [2,3].

If the electron density rises more levels must be taken into account. This is necessary because of the onset of the stepwise excitation and ionization processes [4]. If one would use a purely numerical technique all the levels which are not in partial Local Saha Equilibrium (pLSE) [4] have to be taken into account. Fortunately it is possible to reduce the number of levels that need to be treated numerically by using a so-called Analytical Top Model (ATM) for the densities of the higher excited states [4,5].

2. The Model

The model calculates the Quasi Steady State Solution (QSSS), which means that the spatial and temporal relaxation of the densities of the excited states is neglected. This is valid for a broad variety of plasmas. The trapping of radiation can be treated locally with the introduction of an escape factor.

As stated before in the model both numerical and analytical techniques have been combined. The lowest excited states, which are in Corona Balance (CB) have to be calculated numerically. The highest states are in Partial Local Saha Equilibrium (pLSE). In the case of an ionising plasma, the intermediate levels are in a so-called Excitation Saturation Balance (ESB).

It was shown numerically by Fujimoto [6] and analytically and experimentally by Van der Mullen [4,7] that the deviation from Saha equilibrium of the levels in ESB depends on their effective principal quantum number in a known way. Also these levels can therefore be treated analytically and the number of levels for which the continuity equation has to be

solved can be further reduced. This truncation technique minimizes the numerical effort which is needed and works in the case of recombining plasmas as well.

3. The Program

The program is written in Visual C++. It provides an MS-Windows graphical interface, so all settings can be made via menus and dialogue boxes. A typical screen layout is shown in Figure 2 at the end of this abstract.

The input parameters for the model are the cross sections for the collisional processes, the effective radiative decay frequencies, the electron and heavy-particle temperatures. Further the electron density and the densities of the ion and neutral ground state must be specified. From these data, the program calculates the atomic state distribution function, the net coefficients of ionization and recombination, and the various energy flows in the system. The result of a typical calculation for argon is shown in Figure 1.

The program calculates the rate coefficients of the collisional processes from the collisional cross sections via an integration over the velocity distribution. At this moment the Maxwellian equilibrium distribution is assumed, but the implementation of other velocity distributions is possible.

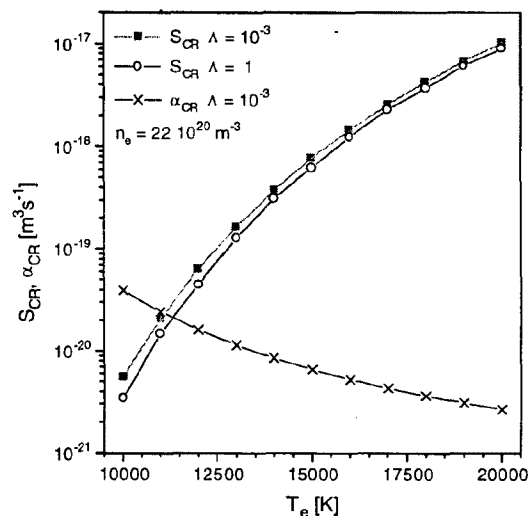


Figure 1: A typical result of the Collisional Radiative Model. Here the ionisation and recombination coefficients (S_{CR} and α_{CR} respectively) are depicted for a fixed electron density. S_{CR} is calculated for two different escape factors Λ for resonance radiation.

Further the program provides default values for the cross sections of the collisional processes involving the higher excited states. These values are calculated from a hydrogen approximation. This approximation is of course not valid for the lower states, for which the cross sections can be entered by specifying the parameters of a chosen fitting function. Special-purpose fitting functions are available.

One may define three interesting points of future investigation,

- applying the model to other elements. At this moment models have been built for atomic argon and mercury;
- extending the model to describe molecules as well;
- allow non-equilibrium velocity distributions;

The results that have been obtained with the current argon and mercury models will be explained and discussed, as well as the plans for the future.

Other research groups are invited to help extending the present model and its applications.

4. References

1. J. van Dijk, M.A. Tas, J. Jonkers, P.G.J.M. Herben and J.A.M. van der Mullen: "Modelling of low pressure argon/mercury discharges", this conference.
2. T.P.C.M. Vos, F.A.S. Ligthart, P.A.P. Zeinstra, J. Jonkers and J.A.M. van der Mullen: "Dynamic Electrical Characteristics of Fluorescent Lamps", this conference.
3. J.F. Waymouth: "Electrical Discharge Lamps", MIT Press, Cambridge MA (1971).
4. J.A.M. van der Mullen: Phys. Rep. **191** (1990) 109.
5. D.A. Benoy, J.A.M. van der Mullen and D.C. Schram: J. Quant. Spectrosc. Radiat. Transf. **46** (1991) 195.
6. T. Fujimoto: J. Phys. Soc. Jap. **47** (1979) 265.
7. J.A.M. van der Mullen, B. van der Sijde and D.C. Schram: Phys. Lett. **79A** (1980) 51.

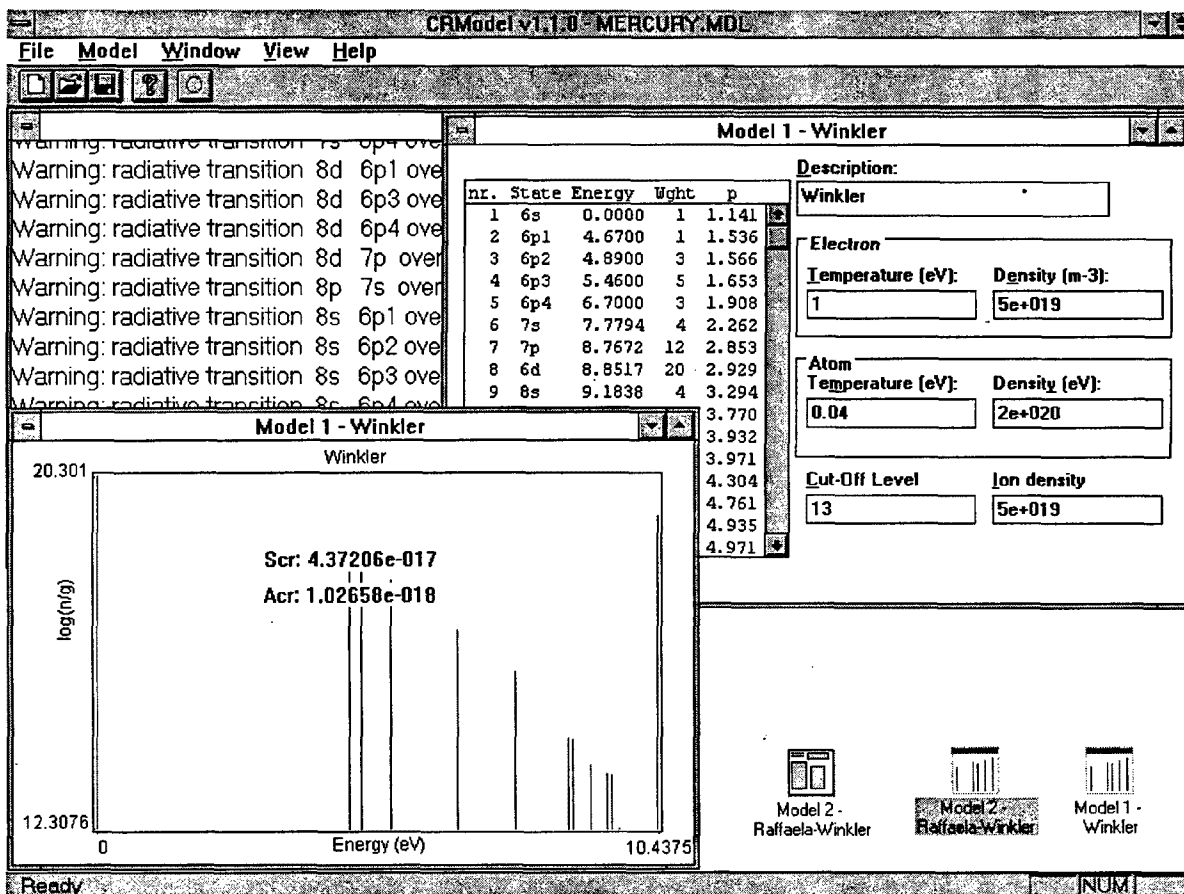


Figure 2: A typical screen of the CRM program.

Numerical Modelling of Low Pressure Argon/Mercury Discharges: an Application of PLASIMO

J. van Dijk, M.A. Tas, J. Jonkers, P.G.J.M. Herben, J.A.M. van der Mullen

Department of Applied Physics, Eindhoven University of Technology,

PO Box 513, 5600 MB Eindhoven, The Netherlands

1. Introduction

In the group Equilibria and Transport in Plasmas at the Eindhoven University of Technology numerical research is being carried out in order to get a better understanding of the relation between the elementary processes and the macroscopic behaviour of various plasma sources. This work has resulted in PLASIMO, a program for the numerical simulation of non-LTE plasmas. In this contribution the results of the application of PLASIMO to the Philips QL lighting system and a high current tube lamp will be discussed. For a description of these lamps we refer to another contribution to this conference [1].

2. Computational aspects

In order to calculate the quantities of interest a control volume method has been applied. An advantage of this technique is that the discretized problem obeys the physical conservation laws exactly.

In principle control volume methods are less suitable for systems with a complex geometry. However, the PLASIMO program is capable of generating a generalized orthogonal grid. All coordinate systems are chosen such that every side of the physical boundary of the gas discharge coincides with one of the coordinate lines. A typical example of a QL-grid has been shown in Figure 1 below.

Further, all physical equations are cast in a standard form (known as Φ -equation), thus allowing a single solution procedure to be used.

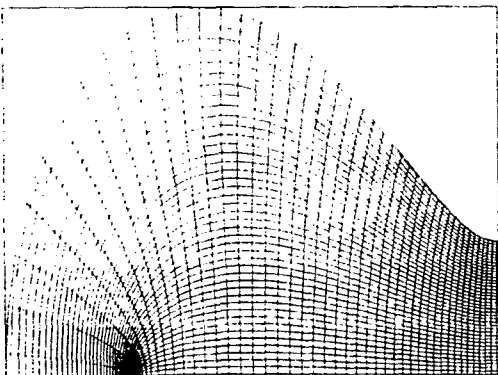


Figure 1: A typical grid for QL simulations

3. Transport equations

The heart of PLASIMO is a Navier-Stokes solver, which is based upon the SIMPLE algorithm, which

simultaneously solves the plasma bulk continuity and momentum equations [2]. The motion of the different species relative to the barycentric velocity is calculated with a self-consistent binary diffusion approximation. Further the possible two-temperature nature of the discharge is taken into account by solving separate equations for the electron and heavy particle energy balances. The energy gain and loss terms due to inelastic processes are treated as sources in the electron energy equation [3].

4. Source terms

The particle production and destruction rates are calculated with a generally applicable collisional radiative model. This is a separate program, which is discussed elsewhere on this conference [4]. It is based upon the assumption of a quasi-stationarity for the excited states [5]. This is valid for a broad variety of plasma, and certainly for the plasmas under study.

5. Results

An overview will be given of the results that have been obtained so far. Voltage-current characteristics for the high current tube lamps have been obtained and will be compared with new experimental values [1] and with previous results of Fang and Huang [6]. Further the depletion of mercury atoms in the centre of these lamps for high currents will be demonstrated and discussed.

6. References

- 1 J. Jonkers, P.G.J.M. Herben, J. van Dijk, D.C. Schram and J.A.M. van der Mullen: "Measurements on a high current conventional fluorescent lamp and comparison with a numerical model", this conference
- 2 S.V. Patankar: "Numerical Heat Transfer and Fluid Flow", Taylor & Francis (1980)
- 3 G.M.W. Kroesen, D.C. Schram and J.C.M. de Haas: Plasma Chem. Plasma Proc., 10 (1990) 531
- 4 J. van Dijk, A. Hartgers, J. Jonkers, P.G.J.M. Herben and J.A.M. van der Mullen: "Towards a General Collisional Radiative Model", this conference.
- 5 J.A.M. van der Mullen: Phys. Rep. 191 (1990) 109
- 6 D.Y. Fang and C.H. Huang: J.Phys.D: Appl. Phys., 10 (1988) 1490

Topic 19a

Special topic at the XXIII ICPIG :
**Highly ionized, low pressure plasmas,
(plasma thrusters, ion sources
and surface treatment).**

MICROWAVE SURFACE DISCHARGE THRUSTED HYPERSONIC FLIGHT IN THE ATMOSPHERE

Glaskov V.V., Sinkevich O.A.

Moscow Power Engineering Institute, Heat Phys. Dept.,
Krasnokazarmennaja, 14, Moscow, 111250, Russia, fax (095)3611620

Serious efforts have been undertaken in the field of microwave thrust engine development [1]. The use of microwave beamed power (MBP) for payload delivery from the Earth to low-Earth orbit (LEO) is, however, highly questionable: the simplest estimate shows that even if the total MBP transmitted is of the order $Q \sim 100$ MW, the resulting engine thrust can station into LEO a payload mass of only a few dozen kilogram. This drives into conclusion that a classical microwave - driven rocket scheme for orbital payload delivery is unproductive and new ideas are needed.

Recent MBP systems development makes the prospects of new microwave systems, generating beams of 1-10 MW power with 5-10 m aperture, move likely in the near term. These MBP systems will be capable of causing powerful discharges in the upper layers of the atmosphere and this possibility should be examined for practical uses.

There are two ways of using MBP for aircraft and spacecraft propulsion in the upper atmosphere: 1) microwave discharge air heating inside the engine onboard the aircraft; 2) microwave discharge external air heating on the surface and at the bottom of the aircraft. In the case of internal microwave discharge, the engine could be a ram-jet with a microwave transparent external duct wall. Such concept is very attractive as the conversion efficiency of MBP to aircraft thrust is high. However, it is difficult to find a material transparent for MBP influxes of $q \sim 100$ W/cm² at gas flow temperatures of $T \sim 2000$ K, so the prospects of this MBP thrust generation scheme look doubtful.

The case of microwave discharge air heating on the surface has a direct relation with external burning chemical engines, intensively studied in late 60-s and 70-s [2-4], with fuel burning near the aircraft's

surface. The experiments demonstrated sufficient efficiency only at high Mach numbers. Before further development of this concept, three critical questions have to be answered:

A) At what speed and flight altitude of aircraft can the near-surface external microwave discharge be expected at reasonably low MBP influxes? B) What is the likelihood of microwave discharge propagation along the beam, screening the aircraft neighborhood from the MBP and decreasing the thrust? C) How big a thrust can be expected if the total power deposited in the discharge is some $Q \sim 10$ -50 MW?

Considerable experimental data for microwave discharges in the atmosphere [6] and external burning chemical engines [3,4,5] are available, so we can get the answers.

A) A microwave power influx of $q \sim 100$ -100 W/cm² is sufficient for near-surface microwave discharge development for all altitudes higher than 20 km [5]. Up to an altitude of 80 km the Langmuir frequency of the discharge plasma is greater than the microwave frequency expected ($n \sim 10$ c), and the surface will be effectively shielded from MBP. B) In the pressure region of $P \sim 20$ -200 Pa, (altitudes 50-80 km), for an MBP influx of 100 W/cm² the microwave discharge front propagation speed along the beam can be expected to be $v \sim 5000$ m/s. The most probable discharge propagation mechanism in this pressure regime is the resonance photon transfer from the microwave discharge front to gas ahead of the front. The front propagation speed value is too great for microwave discharge location on the surface. However, there are two reasons why the examination has to be continued: Primarily, the real speed value, most probably, is not so high, because the experimental data was seriously affected by experimental chamber

walls configuration and the microwave mode composition, which led to various resonance effects. The second reason is that not a single but some dozen of microwave beams will be targeted on the surface. In each beam power influx will be no more than $q_1 \sim 5-10 \text{ W/cm}^2$ and only some meter apart from the aircraft's surface microwave power influx diminishes from the total value of 100 W/cm^2 to q_1 . The microwave discharge propagation speed will accordingly drop from 5000 m/s to 500 m/s . If the flight Mach number is more than 2, the latter figure is less than the aircraft speed and microwave discharge is located on the surface. C) For a thrust estimate, the results obtained for chemical fuel external burning can be used [2-4]: The thrust magnitude F is derived from the equation $F=L/(Mc)$, where $L = \eta Q$, and η - efficiency of microwave power conversion, Q - total microwave discharge power, c - speed of sound, M - flight Mach number at static gas temperature. For a flat wing, rhombic in cross section with an acute leading edge angle θ , we get the equation $\eta \approx (k-1)M^2 \theta$ [4], where k - the polytropic coefficient of the gas flow, M - flight Mach number at stagnation gas temperature. If we have $Q \sim 20-30 \text{ MW}$ and $\theta \sim 18^\circ$ we obtain thrust $F \sim 2-3 \text{ kN}$. This value is relatively small, but sufficient for further examination. So at altitudes of $50-80 \text{ km}$ the microwave discharge has to burn on the aircraft surface and the thrust level expected is some kN . The following applications can be imagined:

1) to facilitate the aerodynamic maneuver of spacecraft and satellites in the atmosphere; 2) to push hostile warheads away from their trajectory at re-entry into the atmosphere; 3) to create a light spacecraft acceleration system from low supersonic speed up to $6-7 \text{ km/s}$. This option is the most promising, so some estimates can be made: If to take the spacecraft lift-to-drag ratio expected $K = 1-5$ [6], one can easily conclude that microwave discharge surface gas heating can be used for acceleration of vehicles with a total mass of $500-1000 \text{ kg}$. The MBP system can probably consist of individual stations, capable of microwave beams generation, with a power $1-3 \text{ MW}$ and an aperture, $D \sim 5 \text{ m}$. The stations themselves can be placed along the

perimeter of a circle, with a radius of 2000 km , at intervals of $50-70 \text{ km}$ from each other, so the scheme deals with some 200 MBP single stations. Simultaneously, some 10-15 stations can be targeted on each spacecraft, so it is possible to accelerate it up to 7 km/s in 20-30 minutes, provided its mass is no greater than 500 kg , and to place it in LEO with practically any desired inclination. Approximately 5-10 spacecraft can be launched by the system simultaneously. Their initial conventional aircraft such as the SR-71 can be used.

CONCLUSION

The simple estimates demonstrate the possibility of a microwave beamed power acceleration system, capable of placing in LEO dozens of small spacecraft a day. The key elements of the system would be located on the Earth's surface, thus are safe in case of malfunction during launch. The ecological consequences are expected to be benign, as in the microwave discharge ozone will be generated.

REFERENCES

- 1 Glaser, P.E., "Microwave Power Transmission for Use in Space," *Microwave Journal*, Vol.29, N 12, 1986, pp.44-58.
- 2 Bartlma, F., "Gasdynamik der Verbrennung", Springer-Verlag, Wien, 1975, pp.279.
- 3 Mehta, G.K. and Strahle, W.C., "Analysis of Axially Symmetric External Burning Propulsion," *AIAA Journal*, Vol.17, N 3, 1979, pp.269-270.
- 4 Zieper, J., "Ähnlichkeits Gesetze für Profilstromungen mit Wärmezufuhr," *Acta Mechanica*, Vol 1, N 1, 1965, pp.60-70.
- 5 Bethke, G.W. and Ruess, A.D., "Microwave-Induced Plasma Shield Propagation in Rare Gases," *Phys. of Fluids*, Vol 12, N 4, 1969, pp.822-835.
- 6 Kuchemann, D., "The Aerodynamic Design of Aircraft," Pergamon Press, New York, 1978, pp.564.

TRANSITION TO THE SUPERSONIC ION FLOW IN STATIONARY PLASMA THRUSTER

K. MAKOWSKI

Institute of Fundamental Technological Research PAS
Świętokrzyska 21, 00-049 Warsaw, Poland

M. DUDECK

Laboratoire d'Aerothermique du CNRS
4-ter route des Gardes, F-92190 Meudon, France

Among many versions of plasma thrusters designed for future application and exploited now in space, the Stationary Plasma Thrusters (SPT) appears as very promising solution of the jet propulsion for spacecrafts. In SPT the discharge is excited and sustained in the annular channel (see e.g. [1]) of typical dimensions of the order of some cm. The radial magnetic field of maximal value of the order of some hundreds Gauss is applied. In all examples B increases when coming toward exit and approaches its maximum value at the exit. Axial electric field is generated by the anode situated at the entrance to the channel, where it coexists with gas supply system, and cathode positioned outside the channel, which compensates the electron outlet.

Our aim is to formulate the simple onedimensional SPT plasma fluid model, which allow us to overcome the singularity appeared in fluid equations [2] when ions are passing the ion sound velocity. This can be achieved by analyzing plasma separately in the anode vicinity (ionization zone) and in the the region of exit (acceleration zone). These two zones are separated by the transition layer.

At the nearest vicinity of the anode we have the electrons flowing toward anode with the axial drift velocity of the order 10^6 m/s. Hence we can expect the appearance of ion sound instability of the plasma fluctuations [see e.g. 3], since then we have the electron fluid penetrated by the ion beam with the supersonic velocity. It was proved in [4], that in such a case the non-

linear phenomenae and collisional dissipation can provide to the shock-like solutions. The equations modeling the SPT plasmas are:

$$\partial n_e / \partial t + \partial(n_e U_{ez}) / \partial z = \alpha n_e,$$

$$\partial n_i / \partial t + \partial(n_i U_i) / \partial z = \alpha n_i,$$

$$\partial W_i / \partial t + W_i \partial W_i / \partial z = e E_z / M -$$

$$\alpha(n_e / n_i)(W_i - V_A)$$

$$\partial n_e / \partial z + E_z + v_2 U_{ez} - \omega_b n_e U_{e\phi} = 0$$

$$\partial U_{e\phi} / \partial t + U_{ez} \partial U_{e\phi} / \partial z + \omega_b U_{ez} + v_2 U_{e\phi} = 0$$

$$\varepsilon_0 \partial E_z / \partial z = e(n_i - n_e)$$

where the indices $\{e, i, a\}$ denote electrons, ions and atoms, while $\{z, \phi\}$ axial and azimuthal components respectively. n_x , U_x , W_x and V_x are the respective densities and velocity components. ω_b is the electron cyclotron frequency and v_2 is the effective electron-dielectric wall collision frequency (the diffusion reflection was assumed following [5]).

These equations were solved by applying the singular perturbation method, where in the range of transition layer the length scale were shortened in order to describe the shock profile. Outside the transition layer $\partial E_z / \partial z$ were taken ≈ 0 in this approximation. Here we present the examples of solutions (Fig. 1 ÷ 4). Calculations were performed for the following values of Stationary Plasma Thruster parameters

inner radius = 4.5 cm;

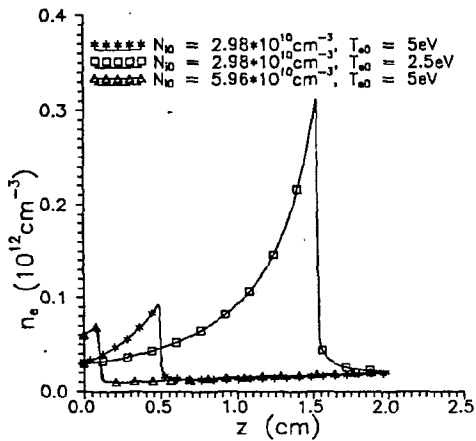
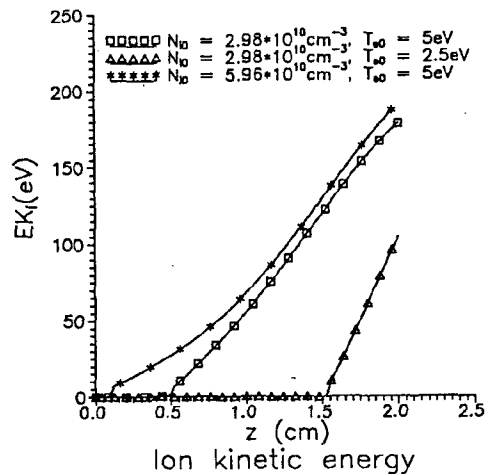
outer radius = 6.5 cm;

length = 2.0 cm;
 electric current = 4.5 A,
 mass supply = 3.5 mg/s;
 $B_{\max} = 130$ Gauss (at the exit);
 neutral atom velocity = 500 m/s;

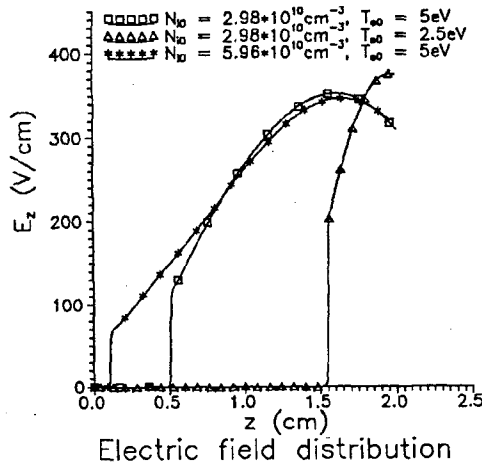
and initial conditions (plasma parameters at the anode):

electron temperat.(z=0) $2.5 \div 5$ eV
 ion density(z=0) $2.5 \div 6.0 \times 10^{10} \text{ cm}^{-3}$
 ion velocity(z=0) 500 m/s

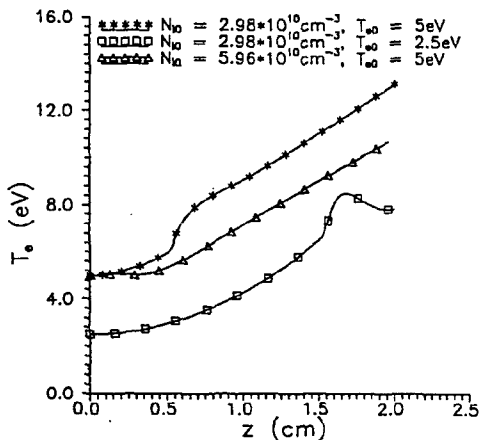
It is worthwhile to point out that that in case of lower initial values of ion density and temperature the transition layer is moved to the region of larger B and as a result the ion density just before the layer strongly increases.



Electron density distribution



Electric field distribution



Electron temperature distribution

References:

- 1) A.I. Morozov, Yu.V. Esinchuk, G.N. Tilinin, A.V. Trofimov, Yu.S. Sharov, G.Ya. Shchepkin, Sov. Phys. Tech. Phys. **17**, 38 (1972).
- 2) N.A. Krall, A.W. Trivelpiece "Principles of Plasma Physics", McGraw-Hill Inc. N.Y. 1973.
- 3) K. Makowski, Rapport NT-96 Laboratoire d'Aerothermique du CNRS, Meudon.
- 4) T. Kakutani, T. Kawahara, Jour. Phys. Soc. of Japan **29**, 1068, (1970).
- 5) A.I. Morozov "Physical foundations of spacecraft electric thrusters" (in russian), Atomizdat ed. Moscow 1978.

ERRATUM : IV-244

USE OF DYNAMIC ACTINOMETRY FOR THE DIAGNOSTICS OF A MICROWAVE H_2 - CH_4 - N_2 PLASMA FOR DIAMOND DEPOSITION

Hassan CHATEI*, Jamal BOUGDIRA, Michel REMY and Patrick ALNOT

Laboratoire de Physique des Milieux Ionisés (CNRS URA 835); Université Henri Poincaré - Nancy I, BP 239, F- 54506 Vandoeuvre les Nancy Cedex, France. Fax : + 33 3 83 27 34 98.

Microwave plasma assisted chemical vapour deposition is widely used for the growth of diamond films. Among the parameters that can affect the process the total gas pressure is an important one. It is known that at high pressure the discharge is a small plasma ball situated just above the substrate holder, without contact with the wall of the reactor and the carbon film is made of diamond [1]. At low pressure the discharge take up a larger volume, limited by the wall of the reactor (quartz tube) and the deposited film is made of graphite. We will point out, using dynamic actinometry, that the plasma chemistry in the gas phase as well as in the plasmas-film system is also modified by the pressure change.

The experimental device has been described elsewhere [2] and for each experiment a diamond film of standard quality is present on the substrate holder in the microwave discharge. The gas mixtures sustaining the discharge are : 98.6% H_2 - 0.4% CH_4 - 1% N_2 at 1.5 Torr and 98% H_2 - 1% CH_4 - 1% N_2 at 60 Torr. The dynamic actinometry [3] consists in the study of the evolution with time of the relative concentration of some species after one of the gas lines feeding the reactor (CH_4 or N_2) has been cut off. The evolution of [H], [CH] and [CN] are shown respectively on figures 1, 2 and 3 at 1.5 Torr and on figures 4, 5 and 6 at 60 Torr.

At low pressure the cut off of nitrogen in the gas mixture induces a decrease of the concentration of atomic hydrogen (fig. 1a). We can speculate that vibrational excited states of nitrogen, as they have a sufficiently high energy, can promote the dissociation of the hydrogen molecule. After methane cut off [H] increases sharply and after 1 minute remains constant with a value 40% higher than its initial value. We have already observed [4], that at low pressure the introduction of methane in the discharge induces a sharp decrease in the electronic density. The elimination of methane from the discharge can thus be responsible of an increase of the density of electrons and, as electronic collisions is the main process for atomic hydrogen production, of an increase of [H].

At high pressure (fig. 4) the evolution of [H] is different. The atomic hydrogen concentration increases after nitrogen cut off and decreases after methane cut off. In this case the effect of the gas mixture changes on the electronic density is not so drastic and chemical effects are more important than direct electron collisions in the process.

The relative concentration of the CH radical after cut off of nitrogen increase sharply and then stays constant (fig. 2a and 5a). The atomic nitrogen reacts with carbonated species such as CH in order to produce CN, which is more strongly bound. Introducing nitrogen in the discharge results in a decrease of the relative concentration of carbon deposition precursors. After

the cut off of methane, [CH] decreases sharply but, depending on the pressure, it vanishes (fig. 5b) at high pressure, but stays constant at 40% of its initial value at low pressure (fig. 2b). Even if no gaseous carbon source is present in the reactor, CH can be produced by interaction of H with carbon films. At high pressure the plasma is close to the diamond film and far from the walls, as H is not an etchant of diamond the production of CH vanishes. At low pressure the plasma can interact with the walls of the reactor where non diamond carbon is unvoluntary deposited, which is etched by H to produce CH.

After the cut off of nitrogen, the relative concentration of CN decreases sharply and vanishes (Fig. 3a and 6a). This result shows that N or CN are not present on the carbon film : adsorption or incorporation of nitrogen in the film is thus not detectable.

After the cut off of methane, [CN] decreases sharply and then remains constant. Thus CN results both of interactions of nitrogen with carbonated species in the gas phase and of the etching of the carbon films by nitrogen. Contrary to hydrogen, nitrogen can etch both diamond and non diamond phases.

In order to prove our assumptions concerning the production of carbonated species without methane in the discharge by plasma-surface interactions, we have carried out an experiment at 60 Torr, after the cut-off of methane, and after removing the substrate holder out of the discharge (Fig. 6c). In this case neither gaseous nor solid sources of carbon are present in the device. In this case the CN concentration decreases sharply during two minutes, corresponding to the elimination of the methane, the decrease is slow during 10 minutes corresponding to the elimination of solid carbon pollution in the reactor and then vanishes.

The dynamic actinometry is complementary to other diagnostics methods and allows us to point out the participation of plasma surface interactions in the production of some species, leading to a better knowledge of the global process of diamond deposition.

- [1] C.P. Klages; Applied Physics A, 1 (1993) 513
- [2] H. Chatei, J. Bougdira, M. Rémy, P. Alnot, C. Bruch, J. K. Krüger; Diamond and Related Materials, in press
- [3] S.F. Durrant, E.C. Rangel, M.A. Bica de Moraes; J. Vac. Sci. Technol. A, 13 (1995) 1901
- [4] J. Bougdira, H. Chatei, C. Simon, M. Rémy, P. Alnot; Le Vide : Sci. Techn. Appl., Suppl 275 (1995) 305

* On leave from LPTP, Faculté des Sciences, Université Mohamed I, Oujda, Morocco.

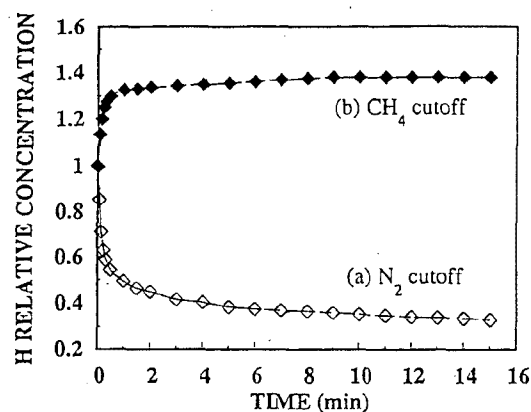


Fig 1: Evolution with time of [H] after cut off of
a) nitrogen b) methane at 1.5 Torr.

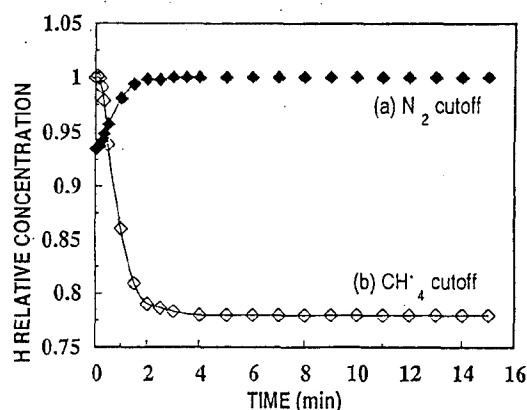


Fig 4: Evolution with time of [H] after cut off of
a) nitrogen b) methane at 60 Torr

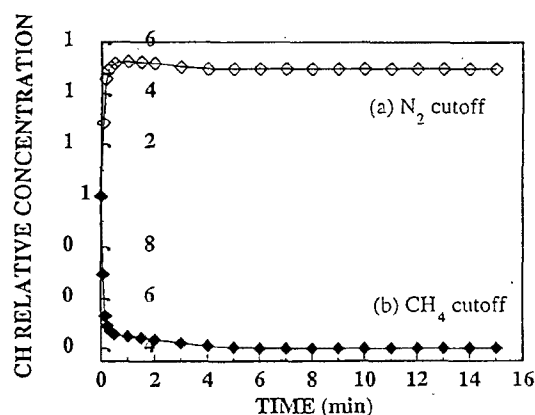


Fig 2: Evolution with time of [CH] after cut off of
a) nitrogen b) methane at 1.5 Torr.

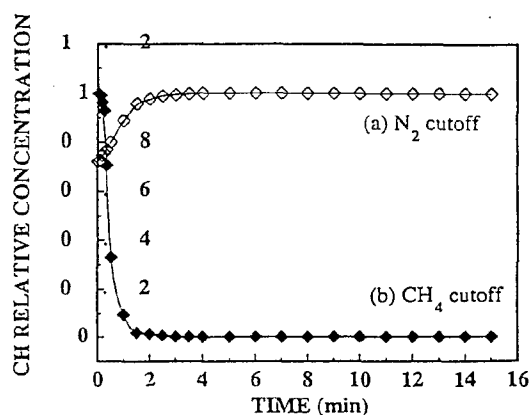


Fig 5: Evolution with time of [CH] after cut off of
a) nitrogen b) methane at 60 Torr

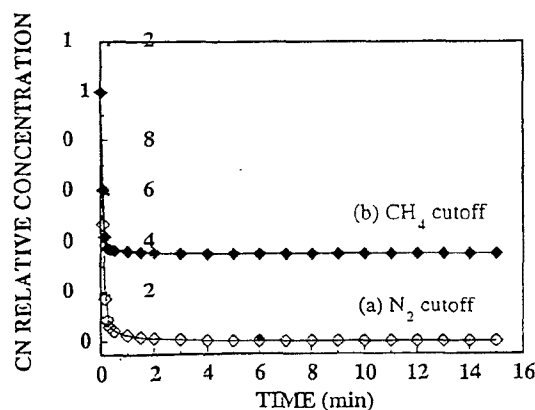


Fig 3: Evolution with time of [CN] after cut off of
a) nitrogen b) methane at 1.5 Torr

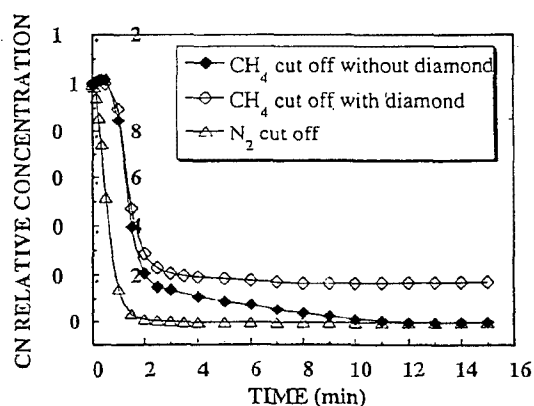


Fig 6: Evolution with time of [CN] after cut off of
a) nitrogen b) methane with substrate c) methane without
substrate at 60 Torr.

Authors Index

A

- | | | | | | |
|------------------------|---------|-----------------|--------|--------------------|---------|
| Abbaoui M. | I-4 | Annaratone B.M. | I-116 | Baksht F.G. | I-12 |
| Abbas A. | V-12 | | I-132 | | IV-138 |
| | V-14 | | I-192 | Baldwin M. | IV-194 |
| Abdel-Maksoud A.S. | V-14 | | I-194 | Baltog A. | I-94 |
| Abdelli S. | IV-264 | Anschutz B. | II-204 | Bano G. | III-96 |
| Abdullin I.Sh. | IV-72 | Anschutz F.B. | II-202 | | IV-212 |
| Ablitzer D. | IV-200 | Antoni V. | II-262 | Baranov I.E. | IV-224 |
| Abramzon N. | I-62 | | IV-134 | Baravian G. | IV-232 |
| Adachi K. | I-246 | Antonova T.B. | III-88 | Barinov Yu.A. | III-104 |
| Adler H.G. | III-22 | Arai T. | IV-86 | Barj M. | IV-142 |
| Afanas'ev V.P. | III-104 | | IV-88 | Bartlova M. | II-80 |
| Ahedo E. | I-2 | | IV-90 | Basha T. S. | V-12 |
| | I-204 | Arnal Y. | IV-230 | | V-14 |
| Akaishi K. | IV-156 | Arnas-Capeau C. | I-202 | Bashutin O.A. | IV-112 |
| Akhmedzhanov R.A. | I-272 | | II-164 | Basner R. | IV-196 |
| | I-274 | Arriaga C. | I-18 | Basurto E. | I-18 |
| Alcaide I. | II-2 | Asselman A. | III-24 | Batanov G.M. | I-138 |
| Aldea E. | IV-254 | Atipo A. | II-170 | Bauchire J.M. | II-120 |
| Alekseeva L.M. | I-206 | Aubes M. | III-16 | | II-136 |
| | II-156 | | IV-64 | | II-206 |
| Alexandrov A.F. | I-44 | Aubrecht V. | II-78 | Baude S. | III-86 |
| | I-108 | | II-80 | Baumbach J.I. | V-30 |
| | III-88 | | II-82 | Bayle P. | I-252 |
| Alexandrov L.S. | I-208 | Aubreton J. | I-4 | | II-220 |
| Alexandrovich B. | IV-76 | | IV-102 | | IV-154 |
| Alexeff I. | III-102 | | IV-220 | Becker K. | I-62 |
| Al-Hassan A. A. | V-44 | Auday G. | I-58 | | I-64 |
| Al-Hussany A. | II-216 | Averyanov V.P. | I-188 | | IV-196 |
| | II-218 | Awakowicz P. | I-60 | Behnke J. | IV-226 |
| Alkaa A. | II-260 | | II-202 | | II-4 |
| Allen J.E. | I-116 | | II-204 | Behnke J.F. | II-4 |
| | I-132 | | | | II-6 |
| | I-192 | B | | | II-8 |
| | I-194 | Babaeva N.Yu. | II-246 | Beilis I.I. | I-14 |
| Almeida R.M.S. | V-32 | Babartitskiy A. | IV-224 | | II-84 |
| Almi A. | I-254 | Babich I.L. | II-154 | Belenguer Ph. | I-100 |
| Alnot P. | V-102 | Babich L.P. | I-6 | Belhaouari J.B. | II-86 |
| Alvarez I. | I-18 | | I-8 | Belmonte T. | IV-66 |
| Alves L. | I-120 | | I-10 | | IV-198 |
| Amakawa T. | I-246 | | IV-2 | Ben Gadri R. | IV-44 |
| Amemiya H. | I-110 | Babich M.L. | I-10 | Benabdessadok M.D. | I-252 |
| | IV-60 | Babicky V. | I-248 | Benilov M.S. | V-32 |
| | IV-62 | | IV-14 | | V-34 |
| Amirov A.H. | IV-262 | Bacal M. | I-12 | | V-72 |
| Ammelt E. | II-182 | | III-78 | Bernard J.F. | IV-130 |
| Amorim J. | IV-232 | Bachev K. | I-160 | Berreby R. | III-92 |
| Andre P. | I-4 | | I-162 | Berthomieu D. | I-148 |
| | III-104 | Baclawski A. | II-110 | Bevilacqua C. | V-2 |
| Andreazza P. | IV-252 | Badie J.M. | IV-192 | Bezborodko P. | IV-68 |
| Andreazza-Vignolles C. | IV-252 | Baeva M. | V-52 | Bezemer J. | II-224 |
| Andrieux M. | IV-192 | Bagatin M. | II-262 | Bhattacharjee S. | I-110 |
| Anikin N.B. | IV-48 | | IV-134 | Biborosch L. | II-190 |
| | | Bagautdinov A. | IV-222 | Biel W. | II-226 |
| | | | | Bilikmen S. | I-172 |

Billing G.D.	V-10	Brunet H.	I-58	Chevolleau T.	III-90
Bindemann Th.	II-6		III-100	Chevrier P.	II-100
Birau M.	III-46	Bruno D.	II-242		II-102
Bisch C.	IV-192	Bugrova A.I.	II-76	Chinnov V.F.	II-94
Blaise G.	III-86		III-68		IV-262
Blanc E.	III-10	Bultel A.	II-90	Chiodini G.	V-2
Blois D.	IV-142	Burke R.	IV-230		V-70
Blundell R.E.	II-150	Burm K.T.A.L.	II-108	Chirkin M.V.	I-208
Bobrov Yu.K.	II-166	Bursikova V.	IV-260		II-174
	II-168	Busov B.	II-78	Chizhik A.	III-110
	II-208	Buzzi J.M.	III-46	Choi P.	II-12
	II-210	Bykanov A.N.	IV-72		III-28
	IV-4			Choi W.K.	III-88
	IV-6	C		Chorazy J.	I-82
Bobrova L.N.	IV-6	Cacciatore M.	V-10	Christoffersen E.	V-10
Bockel S.	IV-200	Cachoncinlle C.	III-30	Christophorou L.G.	I-68
Boeuf J.P.	I-112		III-32	Chuaqui H.	II-12
	II-56		III-44		III-28
	II-228	Cahoreau M.	IV-220	Chumak G.M.	IV-206
	II-252	Caillez Y.	III-46	Chutov Yu.I.	V-64
	II-254	Cajal D.	II-92	Cicconi G.	II-176
	III-42		IV-74	Cicman P.	IV-250
	III-70	Calderon M.A.G.	II-112	Cinelli M.J.	IV-102
Bogaerts A.	II-10	Capitelli M.	I-24		IV-220
Bonhomme G.	II-16		I-26	Ciobanu S.S.	II-100
	II-170		I-66		II-102
Bonifaci N.	IV-10		II-116		IV-150
	IV-12		II-242	Ciocca M.	V-22
Booth J.P.	IV-70	Cardinaud C.	III-90	Cisneros C.	I-18
	IV-202	Carman R.J.	II-258	Clavreul R.	III-94
Borcia C.	II-172	Cartry G.	II-70	Clenet F.	II-212
Bordage M.C.	IV-44		II-72	Clupek M.	I-248
Borisenko A.G.	I-38	Caspani D.	V-70		IV-14
	IV-248	Catherinot A.	IV-102	Coitout H.	II-96
Borodin V.	III-18		IV-220		IV-78
Bouaziz M.	II-88	Cenian A.	I-16	Collins G.	IV-194
Boubert P.	IV-152		III-18	Colombo V.	II-214
Boucher I.	III-2	Censor D.	I-234	Conde L.	I-70
Bouchoule A.	I-200	Cercek M.	IV-162		II-2
	III-66	Cernak M.	I-248	Coppa G.G.M.	II-214
Boudjella A.	IV-16		IV-8	Cormier J.M.	II-122
Boufendi L.	IV-204	Cernogora G.	I-102	Coste C.	I-268
Bougdira J.	V-102		II-70	Coulombe S.	II-98
Bougrov G.E.	III-88		II-72	Courtois L.	II-42
Boxman R.L.	II-84	Chabert P.	IV-202	Csambal C.	II-8
Bozin J.V.	I-98	Chaker M.	I-166	Cuk M.	V-48
Brablec A.	I-128		I-168	Cunge G.	IV-202
	IV-226	Champain H.	IV-94	Cvetinovic D.	V-92
Bragin V.E.	IV-72	Chapelle J.	II-122	Czerwec T.	IV-66
Braginskiy O.V.	III-76	Chapput A.	IV-142		IV-198
Brasile J.P.	II-42	Charles C.	IV-252	D	
Bratescu M.A.	I-92	Chatei H.	V-102	D'yachkov L.	I-188
Brault P.	IV-252	Chebotarev A.V.	IV-110		I-190
Bretagne J.	III-80	Chenevier M.	IV-70	Daoud J.M.	V-88
	IV-184	Cheredarchuk A.I.	II-154	Damelin court J.J.	III-16
	IV-210	Chernukho A.	III-18		III-24
Brethes S.	I-268	Chernyshev A.V.	I-176	Darnon F.	III-66
Briaud Ph.	II-212	Cheron B.G.	II-90	Dauchot J.P.	IV-210
	III-72	Chervy B.	II-104		
Bruhn B.	II-200				

David M.	II-226	Donko Z.	II-64	Fang M.T.C.	II-148
Davies A.J.	II-216	Dony M.F.	IV-210		II-150
	II-218	Doreswamy C.V.	II-146	Fattorini L.	V-2
De Benedictis S.	I-72	Dorning J.	I-210	Fauchais P.	I-4
	IV-14	Dors M.	I-250		II-158
	IV-80	Dorval N.	IV-216	Fauconneau J.	IV-68
De Graaf A.	IV-254	Doveil F.	I-202	Faure G.	III-104
De Hoog F.J.	I-152	Draghici-Lacoste A.	I-120		IV-78
	IV-246	Drallos P.J.	I-30	Favre M.	II-12
De Souza A.R.	IV-46	Druetta M.	III-92		III-28
De Urquijo J.	I-18	Ducarroi M.	IV-192	Fedorovich O.A.	IV-240
Debal F.	IV-210	Dudeck M.	III-78	Fergusson E.E.	I-84
Decomps Ph.	III-106		V-36	Ferguson D.C.	II-146
Deegan C.M.	I-114		V-100	Fernsler R.	II-30
Degond P.	III-64	Dumitrescu-Zoita C.	III-28	Ferreira C.M.	I-120
Deha I.	IV-116	Dupont G.	IV-208		I-122
Delaporte Ph.C.	I-48	Durand J.	I-148		I-124
	III-26	Dussart R.	III-44	Fetisov I.K.	II-24
	IV-52	Dussoubs B.	II-158	Fewell M.	IV-194
Delhaes P.	IV-236	Dwarkanath K.	V-28	Fiala A.	III-86
Denat A.	IV-10	Dyatko N.A.	I-24	Fiermans V.	I-20
	IV-12		I-66	Fievet C.	II-102
Derouard J.	I-150		II-116		IV-150
	IV-202	Dyomkin S.A.	IV-224	Filippov A.A.	II-142
Deschamps N.	IV-46	Dyson A.E.	I-116	Fitaire M.	IV-28
Desideri D.	II-262	Dzermanova N.	II-192	Fitzgerald T.J.	III-10
	IV-134			Flamant G.	II-124
Desoppere E.	I-20	E		Flazi S.	IV-16
	I-106	Eby S.D.	I-50	Fleddermann C.B.	IV-214
	III-38	Egli W.	II-236	Fleurier C.	II-100
Despax B.	IV-208	Ehrich H.	II-118		II-102
Dessaux O.	IV-142	Eichwald O.	I-252		III-44
Destombes V.	III-100		II-220		IV-150
Deutsch H.	II-4		IV-154	Flieser J.	IV-124
	II-6			Fliesser W.	IV-122
	II-74	El Bezzari M.	I-190		IV-126
	II-200	El Shaer M.	I-118	Fodrek P.	IV-128
	IV-188	El-Fotouh A. N.	V-88	Foest R.	IV-196
Devyatov A.M.	I-44	El-Habachi A.	V-22	Fontaine B.	III-26
Dewald E.	II-50	Elakskar F.F.	V-44	Fontanesi M.	V-2
	II-52	Elchinger M.F.	I-4		V-46
Diamy A.M.	IV-218	Eldevik T.	I-32		V-68
Dias F.M.	I-122	Elloumi H.	IV-64		V-70
Dilecce G.	I-72	Entlicher M.	II-232	Fortov V.	I-212
	IV-14	Epifanie A.	II-160	Fortov V.E.	I-176
	IV-80	Ercilbengoa A.E.	III-84		I-178
Dinescu G.	IV-254	Eremenko Yu.	IV-222	Frank K.	II-52
Dinklaga A.	II-200	Erraki A.	II-106	Franke St.	II-74
	IV-188	Ershov A.P.	II-60	Franklin R.N.	II-14
Djakov A.F.	II-166	Escarguel A.	I-174	Frost R.M.	I-60
	II-168	Essolbi R.	III-94	Fujii S.	V-56
	II-208	Etievant C.	IV-224	Fujioka H.	IV-88
	II-210	Etoh A.	IV-104		IV-90
	IV-4	Evdokimov P.A.	V-50	Fukuchi Y.	I-74
	IV-6	Ezubchenko A.N.	II-162	Fukuda M.	IV-168
Djermoune D.	IV-94	F		Fulcheri L.	II-124
Dolgolenko D.A.	II-162	Fabry F.	II-124	Funato Y.	IV-156
Domingo P.	II-238	Fanack C.	III-2	Furukawa M.	V-58
Dominguez I.	I-18				

G			Gombert M.M.	I-22	Hanacek P.	II-78
Gajic D.Z.	I-222		Gomes A.M.	I-254	Hangai N.	I-144
	I-224			II-160	Hanitz F.	I-266
Galofaro J.T.	II-146	Gonzalez J.J.		II-86	Hansel A.	I-84
Galy J.	I-58			II-120		I-260
	III-100			II-136	Harendt A.	I-126
Gamal Y.E.	V-88			II-140	Hartgers A.	III-108
Gamberale L.	V-2	Gonzalez-Aguilar J.A.	II-112	II-206		V-94
	V-70	Gorbachev A.M.	I-272		Hartmann G.	IV-94
Ganciu M.	II-50		I-274			IV-96
	II-52	Gorbunov N.A.	I-80		Hartmann W.	IV-164
Garamoon A.A.	V-44		I-82		Hashiguchi S.	V-76
Garanin S.F.	IV-158	Gordeev O.A.	IV-136		Hassouba M.A.	V-44
Gardou J.	I-104	Gordiets B.F.	I-124		Hassouni K.	II-116
Garrigues L.	III-70	Gorse C.	I-26			IV-70
Gary F.	II-92		II-116		Hatano Y.	I-74
	IV-74	Gortchakov S.	III-58		Haug R.	III-98
Gasteiger S.	III-36	Gostev V.A.	V-80			IV-96
Gavrilenko V.P.	IV-82	Goto M.	I-96			IV-166
Gavrilov N.V.	II-32		IV-86		Hava O.	II-18
Gavrilova T.	I-188		IV-88		Hayashi N.	I-216
Gerasimov D.N.	V-20		IV-90			II-198
Gerova E.	IV-120	Goudmand P.	IV-142		Haydon S.	IV-194
Gerteisen E.	II-238	Goulet J.C.	I-218		Hbid T.	I-152
Gherman C.	II-172	Gousset G.	I-120			IV-246
Gicquel A.	IV-70		III-80		Hebner G.A.	IV-214
Gigant L.	IV-114		IV-92		Hecq M.	IV-210
Gijbels R.	II-10		IV-184		Helbig V.	II-8
Gillispie K.	III-102	Grabowski D.	III-50		Held B.	I-268
Giordano D.	I-26	Graham W.G.	IV-151			III-84
Girard A.	I-140	Granier A.	III-72			IV-180
	II-256		III-74			IV-236
Glanschnig M.	I-84	Gregor J.	II-30			IV-238
Glaskov V.V.	V-98	Gresser L.	IV-180		Heldt J.	III-50
Gleizes A.	II-86	Gross B.	II-82		Hemmati M.	I-214
	II-88	Grosse S.	V-90		Hemmers D.	II-226
	II-104	Grosswendt B.	I-78		Hempel F.	IV-196
	II-106	Grozev D.	I-156		Henneberger K.	I-40
	II-126		II-192		Hennig A.	II-8
	II-136	Grozeva M.	II-130		Henrion G.	II-16
	II-140	Gryaznov V.	I-212		Herben P.G.J.M.	III-63
Glisic S.	IV-42	Gubsch S.	II-200			V-94
Glosik J.	III-96	Guerra V.	IV-160			V-96
	IV-212	Guerrini G.	III-78		Herrmann F.	V-86
Godyak V.	IV-76	Guiberteau E.	II-16		Hertl M.	IV-216
Goedheer W.J.	II-108	Guillot Ph.	I-58		Heuraux S.	III-2
	II-222		III-100		Higaki H.	I-230
	II-224	Gyergyek T.	IV-162		Hipp M.	IV-122
Goldman A.	III-98					IV-126
Goldman M.	III-98				Hirech A.	II-230
Goldsmith S.	II-84	H				III-100
Golly A.	II-110	Ha S.C.	V-4		Hirota A.	I-228
Golosnoy I.O.	IV-84	Hacquin S.	III-2		Hitz D.	III-92
Golubev A.	I-212	Hadi H.	IV-16		Hlina J.	V-60
Golubovskii Yu.B.	I-36	Hadjadj A.	IV-204		Hoang T.G	III-94
	II-4	Hajek V.	IV-258		Hoffmann D.H.H.	I-212
	II-6	Hallil A.	IV-62			II-52
	II-54	Hamada T.	IV-118		Hoffmann V.	I-146
	II-62	Hamers E.A.G.	II-224		Holzinger R.	I-260

Hong D.	III-44 IV-150	Jauberteau J.L.	IV-102 IV-220	Kettlitz M.	II-114 IV-108
Hopkins M.B.	I-114	Jelenkovic B.M.	I-98	Khacef A.	III-30
Horiike Y.	V-56 V-58	Jeon B.H.	V-4		III-32
Horikoshi K.	IV-88 IV-90	Jivotov V.K.	IV-222 IV-224	Khadka D.B.	I-74
Horvath M.	II-232	Johnston C.	III-62	Kharchevnickov V.K.	II-76
Hosokawa T.	IV-16 IV-168	Jolly J.	IV-190 IV-216	Khodachenko G.V.	II-24
Houska A.	II-82	Jones J.E.	IV-18 IV-20	Khodataev K.V.	IV-24
Hrach R.	II-230 II-232 IV-128 IV-218		IV-22	Khodja H.	I-140
Hrachova V.	II-18 II-20 IV-218	Jonkers J.	III-62 III-63 III-108	Kidalov S.V.	III-54 III-56
Hubicka Z.	I-130 IV-228	Jordan A.	V-94 V-96	Kimura T.	I-76 II-22
Huet S.	IV-204	Jovanovic T.	I-260 V-16 V-18	Kindel E.	III-34 IV-108
Hugon R.	II-16	Jugroot M.	II-220 IV-154	Kinoh Y.	IV-104
Hure L.	III-44	Jung H.J.	III-88	Kirillin A.	I-184
I				Kirnev G.S.	II-26
Ieda Y.	II-22			Kirov K.	I-156 II-192
Ignatov A.M.	I-180	K		Kiyooka C.	IV-156
Inagaki K.	IV-140	Kaklugin A.S.	V-66	Klima M.	I-128 IV-226
Inomata T.	IV-26	Kalachov I.	IV-222	Kling R.	III-36
Ion L.	IV-236 IV-238	Kalinin A.V.	II-60	Klockow D.	V-30
Isakaev E.H.	II-94	Kameta K.	I-74	Klopovskiy K.S.	I-86 I-88 II-28 II-234 III-40
Iserov A.D.	II-94	Kaminska A.	V-36		I-164
Ishida A.	IV-118	Kandah M.	IV-176	Kobayashi Y.	IV-144
Ivanov M.S.	II-242	Kando M.	IV-104	Koch A.W.	IV-54 IV-56
Ivanov O.A.	I-272 I-274	Kaneda T.	IV-168		II-200
Ivanov V.G.	I-12	Kanka A.	II-18 II-20	Koch B.P.	III-50
Ivanov V.V.	I-86 I-182 II-28 II-234 III-40		I-128 IV-226 IV-228	Kocik M.	IV-58
J		Kapicka V.	III-104 I-130 IV-228	Kof L.M.	I-216
Jacobsen L.M.	III-4 IV-122 IV-124 IV-126	Kaplan V.B.	IV-228	Koga K.	I-244 I-244
Jager H.	I-256 IV-98 IV-100 IV-260	Kapoun K.	II-162 IV-106 I-132 IV-234	Kogelschatz U.	II-236
Janca J.	III-88 IV-226 IV-228	Karchevsky A.I.	I-134 II-34 IV-132	Kogoma M.	IV-26
Jang H.G.	IV-220	Karderinis S.N.	I-136 I-216 I-244 II-198	Koh S.K.	III-88
Jastrabik L.	IV-102 IV-220	Katkalo A.A.	IV-106 I-132 IV-234	Kolenic F.	IV-128
Jauberteau I.		Kawaguchi M.	I-134 II-34 IV-132	Kolisko A.L.	I-272 I-274
				Kolosov V.Yu.	I-170 IV-172
		Kawai Y.	I-136 I-216 I-244 II-198	Kondranin S.G.	III-88
		Kawakami R.	IV-266	Konjevic N.	IV-146
		Kawamura K.	IV-144 IV-186 V-58	Konstantinov E.	IV-222
			I-14 II-226 IV-264	Kopytin A.A.	III-40
		Keidar M.		Korbel A.	II-132
		Kempkens H.		Korge H.	III-110
		Kerdja T.		Korolev Yu.D.	IV-174
				Korotaev K.N.	V-62
				Korshunov O.V.	IV-262
				Kosbagarov A.	IV-222
				Kosecek A.M.	IV-128
				Kossyi I.A.	I-138 IV-110

Kostic Z.	V-92	Latyshev Ph.E.	I-82	Lorthioir S.	III-86
Kouchi N.	I-74	Laufer B.	V-36	Louhibi D.	II-244
Kovalev A.S.	III-76	Laure C.	IV-252	Loureiro J.	I-90
Kovalev E.V.	V-50	Laurent A.	II-92		I-102
Kozyrev A.V.	III-54		IV-74		IV-160
	III-56	Law D.A.	I-192		IV-232
	IV-174		I-194	Louvet G.	I-186
Krajcar-Bronic I.	I-78	Laz'ko V.S.	II-162	Loza O.T.	III-46
Kralkina E.A.	III-88	Le Brizoual L.	III-72	Lozneau E.	II-184
Krasa J.	IV-272	Le Guen C.	I-188		II-186
Krasilnikov M.A.	III-46	Leborgne L.	I-218	Luca A.	IV-212
Kravchenko A.Yu.	V-64	Leclert G.	III-2	Lungu C.P.	I-94
Krcma F.	IV-100	Le Coeur F.	IV-230	Luo X.	V-52
Krenek P.	II-104	Lecot C.	II-256	Lyapin A.I.	IV-234
Kriha V.	I-266	Le Duc E.	IV-28	Lyszyk M.	III-66
Kriulina O.V.	V-8	Lee Z.H.	IV-112		
Kroesen G.M.W.	I-152	Lefort A.	I-4	M	
	IV-246		III-104	Machala Z.	I-262
Krylov V.I.	V-8	Legrand J.C.	IV-218	Maftoul J.	IV-74
Ksiazek I.	II-110	Lemaire P.	IV-114	Mage L.	III-74
Kuba P.	IV-128	Lemur F.	II-90	Magne L.	II-70
Kubota Y.	IV-156	Lemperiere G.	II-214		II-72
Kudelcik J.	IV-8	Leon L.	I-70	Maheu B.	II-90
Kudrle V.	IV-28	Leprince P.	I-120	Mahony C.M.O.	IV-151
Kudryavtsev A.Yu.	I-6		IV-92	Makasheva K.	I-156
	I-10	Leroux A.	II-238	Makowski K.	V-100
	IV-2	Leroy O.	IV-216	Malek S.	IV-264
Kudu K.	IV-34	Lesage A.	I-174	Malinowsky G.Y.	I-48
Kulikovskiy A.A.	I-258	Leu F.	II-118	Malovic G.N.	I-98
	IV-30		II-188	Maluckov C.	V-16
Kulish M.	I-212	Leu G.	II-184		V-18
Kumar S.	IV-194		II-186	Malykh N.I.	I-138
Kuraica M.M.	IV-146	Leukens A.	V-54	Mamkovich V.V.	V-80
Kurilenkov Yu.K.	I-186	Levchenko V.D.	I-220	Mandache N.B.	II-50
	I-188		II-240		II-52
	I-190	Leys C.	III-38	Manheimer W.	II-30
Kurnaev V.A.	II-24	Li Bo	I-52	Mankelevich Yu.A.	II-234
	II-26	Li Y.M.	III-20	Maouhoub E.	II-96
	IV-112	Lighthart F.A.S.	V-78	Marchal F.	I-104
Kurunczi P.	I-64	Lindinger W.	I-84	Margot J.	I-166
Kutsyk I.M.	I-6		I-260	Mark T.D.	IV-250
	I-8		IV-212	Markovic V.Lj.	II-46
	IV-2	Lino J.	IV-232		IV-178
Kuwae H.	II-198	Lipaev A.M.	I-178	Marliere C.	I-148
Kuzelev M.V.	III-46	Lipatov A.S.	II-76	Marode E.	IV-46
Kuzovnikov A.A.	I-154	Lister G.G.	III-22	Martines E.	IV-134
		Loffhagen D.	III-34	Martus K.	I-64
L			III-58	Marty-Dessus D.	IV-236
Laan M.	IV-32	Loiseau J.F.	III-84		IV-238
Lagstad I.H.	IV-34	Lomakin B.N.	IV-262	Masek J.	II-78
Lamoureux M.	I-140	Londer J.I.	II-144		II-82
Lancellotti C.	I-210	Longo S.	I-24	Masek K.	IV-272
Lange H.	IV-36		I-26	Mashino S.	IV-88
Lapuerta V.	I-204		II-116		IV-90
Laroussi M.	III-102		II-242	Massines F.	III-106
Lasgorceix P.	IV-102	Lopaev D.V.	I-86		IV-44
Laska L.	IV-272		I-88	Matejcik S.	IV-250
Latocha V.	III-64		II-28	Matheron P.	IV-116
Latyshev Ph.E.	I-80		III-40	Mathew J.	II-30
			III-76		

Matsui T.	I-142	Monin M.P.	I-270	Ness K.F.	I-54
Matsumoto M.	I-238	Moreno J.	II-12	Neuilly F.	IV-202
	II-58		III-28	Nichipor G.V.	I-250
Matsuoka M.	I-134	Mori A.	II-34	Nicolazo F.	III-74
	II-34	Mori I.	IV-266	Nienhuis G.J.	II-224
Matsuoka M.	IV-132	Morimoto T.	IV-266	Niessen W.	I-264
Matveev A.A.	I-138	Morozov A.	IV-124	Nikulín S.P.	II-36
Maury J.	IV-114	Morozov A.I.	II-76	Nishioka T.	II-58
Maximov A.I.	I-256		III-68	Nistor M.	II-50
Mayoux C.	III-106	Morozov D.A.	I-208		II-52
McFarland J.	IV-151	Morrow R.	II-258	Nogaki M.	IV-40
Meger R.	II-30		IV-38	Norman G.E.	V-66
Melin G.	I-140	Morvova M.	I-262	Novak M.	IV-226
Melnig V.	II-172	Mouadili A.	III-24		IV-228
Melnikov A.S.	I-80	Movtchan I.A.	I-80	Novak S.	II-248
Mentel J.	II-130	Mozgovoi A.L.	I-6		IV-128
	II-132	Mozgrin D.V.	II-24	Novakovic N.V.	I-28
	III-48	Muller H.J.	IV-54	Nunomura S.	I-196
	III-50	Muller I.	II-182	Nur M.	IV-10
Merad A.	I-112	Muller S.	IV-120		IV-12
Mercier M.	II-92	Murata T.	III-82		
	IV-74	Muromkin Yu. A.	II-162	O	
Merel P.	I-168	Murphy D.	II-30	Oda A.	V-74
Mesyats G.A.	II-32	Musa G.	I-92	Odagiri T.	I-74
Meunier J.L.	II-98		I-94	Ohe K.	I-76
	IV-176		II-118		II-22
Mezhiba A.	I-212		II-188		II-66
Michaut C.	III-78	Mushiaki M.	IV-156		IV-140
Michel H.	IV-66	Musikowski H.D.	II-128	Ohno N.	I-196
	IV-198	Musinov S.	IV-222	Ohtani K.	IV-86
	IV-200	Musiol K.	II-122	Oien A.H.	I-32
Michishita T.	I-230	Mustata I.	II-118		III-4
Mikheev L.D.	I-48		II-188	Oishi H.	I-230
	IV-52	Myamoto K.	I-92	Okada T.	I-96
Mikikian M.	I-202			Okazaki S.	IV-26
Milenin V.M.	III-54	N		Okita Y.	III-82
	III-56	Nagahama T.	I-228	Olthoff J.K.	I-68
Milic B.S.	I-28	Naghizadeh-Kashani Y.	II-106	Ono M.	IV-186
	I-222	Nagorny V.P.	I-30	Onoda H.	II-68
	I-224	Naidis G.V.	II-246	Onose H.	I-144
	I-226	Naito Y.	I-144	Otorbaev D.K.	IV-110
Millet P.	I-104	Nakamura M.	I-76	Otte M.	II-38
Milosavljevic V.	V-48		I-196		II-40
Mimura M.	IV-118	Nakamura Y.	I-242	Overchuk K.	IV-222
Minami K.	I-144		I-244		
	I-228		V-4	P	
Minea T.M.	III-80	Nandelstädt D.	II-132	Pacheco J.	II-120
Mintsev V.B.	I-212	Napartovich A.P.	I-24	Paillol J.	II-42
Mitrofanov N.K.	II-134		I-66		II-250
	IV-138	Nefedov A.P.	I-176	Panchenko V.G.	II-178
Mizeraczyk J.	I-250		I-178		II-180
	II-130	Neger T.	IV-122		IV-240
	III-50		IV-124		IV-248
Mobasher M.	I-118		IV-126	Pancheshnyi S.V.	IV-48
Modreanu G.	II-50	Neiger M.	I-264	Panciatichi C.	II-214
Mohri A.	I-230		II-36	Pardo C.	II-112
Moisan M.	I-168	Nekuchaev V.O.	I-36	Paris P.	IV-32
Mokhtari A.E.	II-244		II-54	Parizet M.J.	II-96
Molotov V.I.	I-178	Nerushev O.A.	I-198	Parys P.	IV-272
Mond M.	I-236				

Pashkovsky V.G.	II-162	Pitchford L.C.	III-86	Raynaud P.	I-148
Passoth E.	II-8	Pivkin V.V.	V-8		III-74
Pauna O.	I-166	Placinta G.	IV-242	Razafinimanana M.	II-88
Pavlenko V.N.	I-232	Pogora V.	II-138		II-120
	II-178	Pointu A.M.	II-50		II-126
	II-180		II-52		II-136
	IV-240	Pokrzywka B.	II-122	Redon R.	IV-116
	IV-248	Ponomarev N.S.	I-36	Reess T.	II-250
Pavlik J.	IV-128		II-54	Remscheid A.	IV-148
Pavlik M.	IV-250	Popa G.	II-66	Remy M.	V-102
Pavlov V.B.	III-88		IV-242	Revel I.	II-56
Pavlovic P.	V-92	Popescu A.	II-118	Riad H.	II-106
Pawelec E.	II-122		II-188	Ricard A.	I-168
Pealat M.	IV-216	Popescu I.I.	II-50		IV-66
Pechacek R.	II-30		II-52		IV-198
Pedoussat C.	II-252	Popov A.M.	II-28		IV-200
Pegoev I.N.	V-50	Popov N.A.	I-88		IV-210
Pejovic M.M.	II-46	Poppe F.	III-38	Riccardi C.	V-2
	IV-178	Porokhova I.A.	II-4		V-46
Pekarek S.	I-266		II-6		V-68
Pellerin S.	II-122		II-62		V-70
Pelletier J.	IV-230	Porras D.	III-60	Richou J.	I-174
Peres G.	II-254	Postel C.	I-270		IV-116
Perret C.	II-256	Potantin E.P.	IV-106	Rivaletto M.	II-42
Perrin J.	IV-190	Potapkin B.V.	IV-224	Robert E.	III-30
Peska L.	II-78	Pousse J.	II-126		III-32
	II-82	Pouvesle J.M.	III-30	Robin L.	IV-152
Petit L.	III-98		III-32	Robson R.E.	I-52
Petrov G.	II-266		III-44		I-54
Petrov O.F.	I-176	Praessler F.	I-146	Roca i Cabarrocas P.	IV-204
	I-178	Prazeller P.	I-260	Rodriguez-Yunta A.	II-112
Petrov T.	II-130	Proshina O.V.	I-88	Rohlens K.	IV-272
Petrova Ts.	V-40		II-234	Rohmann J.	II-38
Petrovic Z.Lj.	I-34	Protuc I.	II-138		II-40
	I-98	Proulx P.	II-206	Romeas P.	I-186
	II-44	Puech V.	I-270	Rosatelli C.	II-176
	II-46	Punset C.	III-42	Rosenfeld W.	III-44
	IV-42	Puric J.	V-48	Rosenkranz J.	I-266
	IV-178	Purwins H.G.	II-182	Rosum I.N.	II-178
Peyrous R.	I-268				II-180
	III-84	R		Roth M.	I-212
	IV-180	Rabehi A.	IV-44	Rousseau A.	IV-92
Pfau S.	II-38	Radovic M.	V-16	Roussel J.	IV-130
	II-40		V-18	Roussel-Dupre R.T.	III-6
Phelps A.V.	II-48				III-8
Piejak R.	IV-76	Rahal H.	I-22		III-10
Pierre Th.	II-164	Rahel J.	IV-250		III-12
	II-170	Rakhimov A.T.	I-86		III-52
	V-46		I-88		IV-162
	V-68		II-28	Rovtar J.	IV-162
Pierson J.F.	IV-198		II-234	Rozoy M.	I-270
Pignolet P.	II-42		III-40	Rozsa K.	II-64
Pinheiro M.J.	IV-232	Rakhimova T.V.	I-86	Rudakowski S.	IV-148
	I-124		I-88	Rudnitsky V.A.	I-38
Pintassilgo C.D.	I-102		I-182	Rukhadze A.A.	I-172
Pitchford L.C.	I-100		II-28		III-46
	II-56		II-234		III-88
	II-252		III-40	Rulev G.B.	I-86
	III-42	Rao B.N.	V-28	Rusanov V.	IV-222
	III-70	Ravary B.	II-124	Rusanov V.D.	IV-224
				Rusnak K.	IV-258

Rutkevich I.	I-234	Scheibner H.	IV-188		V-58
	I-236	Schein J.	II-132	Shishkin A.G.	V-38
Ryazantsev E.I.	IV-224	Scheiring Ch.	I-84	Shishkin G.G.	V-38
Rybakov A.B.	IV-138	Scherbakov Yu.V.	II-210	Shimizu K.	IV-62
Rybakov V.V.	I-240	Schepe R.	I-40	Shiozaki A.	I-144
S		Scheubert P.	II-202	Shiratani M.	IV-190
			II-204	Shivarova A.	I-156
		Schimke C.	III-34		I-158
			IV-108		II-192
		Schluter H.	V-90	Shkol'nik S.M.	I-12
		Schluter M.	V-90		II-134
		Schmidt E.	III-48		III-104
		Schmidt M.	IV-196		IV-138
		Schmoll R.	IV-164	Shkvarunets A.G.	III-46
		Schoenbach K.H.	V-22	Short K.	IV-194
Sadeghi N.	I-150	Schopp H.	II-114	Si-Bachir M.	IV-264
	I-152		IV-108	Sicha M.	I-130
	IV-202	Schram D.C.	II-108		IV-226
	IV-246		III-62		IV-228
Saenko V.A.	I-38		III-63	Siddagangappa M.C.	V-28
	IV-182		III-108	Siegel R.	I-62
	IV-248		IV-254	Sigeneger F.	II-62
Saidane K.	II-126	Schram P.J.J.M.	V-64	Sigmond R.S.	IV-34
Sakai T.	IV-16	Schruft R.	I-264	Sigov Y.S.	I-220
Sakai Y.	I-92	Schulze J.	II-130	Silakov V.P.	I-138
	V-74		III-48		IV-110
Sakamoto S.	IV-186		III-50	Simek M.	I-72
Salabas A.	II-118	Schumann J.	II-118		IV-14
Salamero Y.	I-104	Schumann M.	II-132		IV-80
Salierno M.	V-46	Schwarzenbach W.	I-150	Simko T.	II-64
	V-68		IV-202		IV-184
Samarian A.	I-184	Segui Y.	I-148	Simonet F.	III-16
Sando K.	I-164		III-74	Singaevsky I.F.	I-108
Sanduloviciu M.	II-172	Segur P.	II-260	Singh D.P.	I-44
	II-184		IV-44		I-154
	II-186	Selen L.J.M.	III-108		II-60
	II-188	Sentis M.L.	I-48	Singh N.	II-136
	II-190		III-26	Sinkevich O.A.	V-20
Sapozhnikov A.V.	I-138		IV-52		V-42
Sarrette J.P.	I-254	Sergeichev K.F.	II-196		V-98
	II-160	Serianni G.	II-262	Sirghi L.	II-66
Sarroukh H.	III-24		IV-134	Si-Serir F.	II-244
Sarytchev D.V.	II-26	Servant S.	II-92	Skalny J.D.	IV-250
Sasada T.	IV-132	Sery M.	I-130	Skowronek M.	I-186
Sato K.	IV-118		IV-228	Skrynnikov A.V.	IV-256
Sato S.	I-242	Sewraj N.	I-104	Skvortsov V.A.	III-14
Sato T.	I-164	Shakhatov V.A.	I-16		IV-270
Sato H.	I-238		I-42	Sladkov O.S.	V-82
	II-58		IV-136	Slavicek P.	I-128
Satoh K.	II-260		IV-256		IV-226
Saulle C.	III-46	Sharafutdinov R.G.	I-212	Smakhtin A.P.	I-240
Savinov V.P.	I-108	Sharkov B.	IV-186	Smirnov V.V.	I-42
Savjolov A.S.	II-24	Shibamoto M.	V-22		IV-136
	II-26	Shi W.	I-44	Smirnov V.M.	V-62
	IV-112	Shibkov V.M.	I-154	Smurov I.	I-80
	V-62		II-60	Snell J.	II-14
Sawa Y.	V-58		I-44	Snyder D.B.	II-146
	V-56	Shibkova L.V.	I-154	Solntsev I.A.	II-208
Sayler G.S.	III-102		II-60	Solonin V.V.	II-174
Scepanovic M.	V-48	Shindo H.	V-56	Sonnenschein E.	I-234
Schaefer J.H.	V-52				
Scheibe H.J.	II-128				

Soppart O.	V-30	Symbolisty E.	III-52	Touzeau M.	II-70
Sorokin A.V.	II-166	Sysun V.I.	V-80		II-72
	II-168				IV-46
Sosnin V.E.	V-42	T			IV-160
Soukup L.	IV-226	Tabbal M.	I-166	Tramontin L.	II-262
	IV-228		I-168	Trepanier J.Y.	I-50
Soulem N.	III-84	Tachibana K.	V-76	Treshchalov A.	III-110
Spector N.O.	II-94	Taddei F.	II-214	Trinquecoste M.	IV-236
Spyrou N.	III-84	Takamura S.	I-196	Trusca A.	II-140
	IV-180	Takayama K.	IV-144	Tsuda N.	IV-268
Stacewicz T.	I-82		IV-186	Tsuda S.	I-142
Stamate E.	IV-140	Talsky A.	IV-160	Tsukabayashi I.	I-242
Stan C.	II-188	Tamme D.	I-40	Tsvetkov T.S.	II-192
Stanciu T.	II-138	Tanaka H.	I-230	Turban G.	II-212
Stanojevic M.	IV-162	Tanaka K.	I-228		III-74
Starikovskaia S.M.	IV-48	Taniguchi K.	II-198		III-90
	IV-50	Taranenko Y.	III-8	Tusaliu D.	V-24
	IV-58		III-12		V-26
Starikovskii A.Yu.	IV-48		III-52	Tusaliu M.	V-24
	IV-50	Tarnev Kh.	I-158		V-26
	IV-58	Tas M.A.	V-96	Tusaliu P.	V-24
Stark R.	II-52	Tatarova E	I-122		V-26
Steel W.H.	I-192		I-160	Tusaliu V.	V-24
	I-194		I-162		V-26
Stefanovic I.	II-44	Tcheremiskine V.I.	I-48	U	
Stefanovic P.	V-92		IV-52	Udrea M.	II-50
Stefka J.	II-78	Tchuyan R.K.	II-268	Ueda Y.	I-136
Stepanov V.A.	I-208	Teboul E.	IV-92	Uhlenbusch J.	II-226
	II-174	Telbizov P.	II-130		V-52
Stepanovic O.	V-16	Telegov K.V.	II-240	Uhrlandt D.	II-74
	V-18	Temeev A.A.	V-82	Ukai M.	I-74
Stockl C.	I-212		V-84	Ulyanov D.K.	III-46
Stojanovic V.D.	I-34	Tendys J.	IV-194	Ulyanov K.N.	II-142
Stojilkovic S.M.	I-28	Terai K.	III-82		II-144
Stoykova E.	I-160	Tereshkin S.A.	II-94	Uneyama T.	IV-118
	I-162	Tesar C.	IV-98	Ustalov V.V.	IV-240
Strelkov P.S.	III-46	Tessier P.Y.	III-90	Ustinov A.L.	II-162
Strinic A.I.	IV-42	Teuner D.	II-130	Uteza O.	III-26
Suchaneck G	I-146		III-48		
Suchy K.	V-6	Theroude C.	II-254	V	
Sugawara H.	V-74	Thomann A.L.	IV-252	Vacque S.	II-120
Sugawara M.	I-96	Thomaz J.	IV-232		II-126
	I-164	Tichonov M.G.	IV-262	Valentini H.B.	II-202
	II-68	Tichy M.	IV-226		V-86
Suginuma Y.	IV-40	Tiirik A.	IV-32	Vallee C.	III-74
Sukhinin G.I.	I-46	Timofeev N.A.	III-54	Vallone F.	IV-134
	I-198		III-56	Valuev A.A.	V-66
Sukhomlinov V.S.	IV-170	Tioursi M.	IV-96	Van Bever T.	I-106
	IV-172		IV-166	Van de Grift M.	I-152
Sultan G.	IV-232	Toader E.I.	IV-151		IV-246
Sunarchin A.A.	IV-262	Toedter O.	IV-54	Van de Sanden M.C.M.	IV-254
Sunka P.	I-248		IV-56	Van der Mullen J.A.M.	II-108
	IV-14	Tokumasu H.	I-228		III-62
Supiot P.	IV-142	Toma M.	II-190		III-63
Surda V.	IV-8	Tominaga K.	IV-266		III-108
Sychov I.A.	II-194	Tonegawa A.	IV-144		V-78
	II-196		IV-186		V-94
Symbolisty E.	III-8	Torchinskii V.M.	I-178		V-96
	III-10	Tous M.	IV-226		
	III-12				

Van Dijk J.	III-63 V-78 V-94 V-96
Van Egmond C.	III-38
Van Ootegem B.	I-218
Vardelle A.	II-158
Vardelle M.	II-158
Vaselli M.	I-44 I-154 II-60
Vasenkov A.V.	I-56 IV-256
Vasilieva A.N.	III-76
Vaulina O.	I-184
Vayner B.V.	II-146
Veis P.	III-98
Veklich A.N.	II-154
Velikanov S.D.	V-50
Velleaud G.	II-92 IV-74 V-74
Ventzek P.	V-74
Verdes D.	IV-242
Vereshchagin K.A.	I-42 IV-136
Vervisch P.	I-218 II-238 IV-152
Vervloet M.	III-74
Vesselovzorov A.N.	III-78
Vialle M.	II-70 II-72
Videlot H.	IV-190
Videnovic I.R.	IV-146
Viel V.	IV-130
Vikharev A.L.	I-272 I-274
Viladrosa R.	III-30 III-32 III-44
Vill A.	III-110
Vitel Y.	I-188 I-190
Vivet F.	I-200
Vizgalov I.V.	II-26
Vlcek J.	IV-258
Vogel N.I.	III-14 IV-270
Voitik M.	III-26
Vos T.P.C.M.	V-78
Vovchenko E.D.	IV-112
Vrba P.	II-264
Vrhovac S.B.	II-44
Vul A.Ya.	III-54 III-56

W

Wachutka G.	II-204
Wakabayashi Y.	II-58
Wang Yicheng	I-68
Watanabe T.	I-244
Watanabe Y.	I-170
Wautelet M.	IV-210
Wendt R.	IV-36
Wetzig K.	I-146
White R.D.	I-52 I-54 I-20
Wieme W.	I-20
Wiesemann K.	IV-148
Wilke C.	II-74 II-200 IV-188
Winkler R.	II-62 II-266 III-58
Winter J.	V-54
Wiolland R.	III-46
Wolf O.	I-264
Wolowski J.	IV-272
Woryna E.	IV-272
Wujec T.	II-110
Wuttmann M.	I-118
Wyndham E.	II-12 III-28

Y

Yagi Y.	IV-134
Yakovetsky V.S.	V-64
Yamada J.	IV-268
Yamada K.	I-74 I-142
Yamazawa Y.	I-230
Yan J.D.	II-148 II-150
Yasuda M.	I-170
Yasui S.	I-246
Yatsu M.	II-68
Yilmaz A.	I-172
Yoshida M.	I-134
Yoshimura S.	I-244
Yousfi M.	I-252 II-220 IV-154
Yukhimuk V.	III-6 III-8 III-12 III-52
Yumoto M.	IV-16
Yurghelenas Yu.V.	II-208 II-210
Yuyama T.	I-230

Z

Zahoranova A.	IV-8
Zahraoui A.	II-260
Zajickova L.	IV-260
Zakouril P.	III-96
Zambra M.	II-12 III-28
Zapol'sky A.F.	V-50
Zaretsky E.	I-236
Zatsepin D.V.	IV-50
Zhang Z.	V-52
Zhelyazkov I.	I-160 I-162
Zheng X.	I-228
Zhovtyansky V.A.	II-152 II-154
Zicha J.	II-18
Zigman V.J.	I-226
Zissis G.	III-60
Zivkovic J.V.	IV-42
Zobnin A.V.	II-94
Zoller V.	IV-222
Zuev V.S.	IV-52
Zvonicek V.	IV-160